博士論文

AN EXPERIMENTAL STUDY ON THE EFFECT OF MACRO-STRUCTURED SURFACE ON CHF IN DOWNWARD-FACING FLOW BOILING

（下向伝熱面沸騰における表面形状効果の実験的研究）

Abdul R. Khan

カーン　アブドゥル　レーマン

AN EXPERIMENTAL STUDY ON THE EFFECT OF MACRO-STRUCTURED SURFACE ON CHF IN DOWNWARD-FACING FLOW BOILING

A Thesis
by
ABDUL R. KHAN

Submitted to
The University of Tokyo
in partial fulfillment of the requirements for the degree of

Doctor of Philosophy

September 2015

Department: Nuclear Engineering & Management

Committee Chair:
Dr. Koji OKAMOTO, Professor, Head of Department (Nuclear Professional School)

Committee Members:
Dr. Hirofumi DAIGUJI, Professor, Department of Mechanical Engineering
Dr. Naoto KASAHARA, Professor, Department of Nuclear Engineering and Management
Dr. Satoshi SOMEYA, Visiting Associate Professor, Department of Human and Engineered Environmental Studies
Dr. Shoji MORI, Associate Professor, Yokohama National University

for my family

TABLE OF CONTENTS

ABSTRACT

Current ex-vessel cooling capability may be insufficient to prevent vessel failure during a severe accident for next generation larger-powered Light Water Reactors. An issue arises for the integrity of the Reactor Pressure Vessel as boiling occurs on the vessel surface. Excessive boiling conditions on the exterior of the vessel surface may cause Critical Heat Flux (CHF), which may eventually lead to vessel failure. A modified or structured surface design utilizing fins is proposed for the exterior of the vessel surface. Pressure vessel failure may be prevented if the CHF safety margin can be increased through the structured surface design. Thus, experiments were performed to assess the impact of a pin-fin on the heat transfer and CHF from a boiling surface. Subcooled and saturated flow boiling experiments were performed with separate facilities to investigate the effect of a pin-fin from a downward-facing boiling surface. Subcooled experiments were performed at approximately constant subcooling while varying the flow rate. Three mass flux were applied: 244, 215, and 177 kg/m^2-s. CHF was observed only for 177 kg/m^2-s. Saturated experiments were performed at a reduced pressure of approximately 0.050 MPa at which the saturation temperature was approximately 81ºC. Different mass flux, ranging from 202 – 1456 kg/m^2-s, were applied in the saturated experiments. Positive and negative effects were observed from both experiments when comparing the results of bare and finned surfaces. An average enhancement of 4 – 5% in the heat transfer was obtained with a finned surface for the subcooled experiments. For the saturated experiments average enhancements of 19% and 61% were obtained in the heat transfer and CHF, respectively. In the saturated experiment, approximately three times greater CHF enhancement was obtained compared to the heat transfer at approximately the same excess heat temperature. Negative effects, such as reduction in the heat transfer and CHF, were also observed from both experiments. Moreover, greater fin-downstream location temperatures may become an issue as they may cause surface damage. It was found that the fin can enhance the CHF significantly at relatively high flow rates. From the work performed as part of this thesis, the proposed finned structured surface is an applicable design to improve the heat transfer and CHF from a boiling surface. It is believed that such a design can be applied on the outer surface of the pressure vessel to improve CHF during ex-vessel cooling.

ACKNOWLEDGEMENT

I am very thankful that I was able to interact with people who made my time and studies in Japan very enjoyable.

I would like to thank Professor Koji Okamoto for helping me throughout my studies at the University of Tokyo. I am very grateful for his help, assistance, and guidance during my studies.

I would like to thank my committee members for taking the time out of their busy schedules to attend my presentations and for providing suggestions regarding the thesis material.

I would like to thank Assistant Professor Nejdet Erkan and Dr. Byeongnam Jo for all their comments and suggestions during my studies.

I would like to thank all my friends and colleagues who gave their time to help me during my experiments, especially Mr. Genki Fujikawa, Mr. Haiguang Gong, Mr. Hongyang Wei, Mr. Laishun Wang, and Mr. Hector Lopez.

I would like to thank the staff at the department of Nuclear Engineering and Management at the University of Tokyo for all their help with various procedures, and in making life at the university and in Japan very comfortable.

Finally, I am very thankful and grateful to my family for providing their support and encouragement during my time in Japan.

LIST OF FIGURES

LIST OF TABLES

NOMENCLATURE

Symbols

°C	Degrees Celsius
μ	Liquid viscosity
ρ_g	Gas (vapor) density at saturation [kg/m^3]
ρ_l	Liquid density [kg/m^3]
σ	Liquid surface tension [N/m]
τ_S	Reactor operating time [s]
Δh	Distance between T_{TOP} and T_{BOT} [m]
ΔT_{SAT}	Excess heat [°C or K]
$\Delta T_{SAT,CHF}$	Excess heat at CHF [°C or K]
ΔT_{SUB}	Degree of subcooling [°C or K]
A_{bare}	Surface area of bare boiling surface [m^2]
A_c	Cross-sectional area of the flow geometry [m^2]
A_{fin}	Surface area of finned boiling surface (including fin) [m^2]
Bo	Boiling number
c_p	Liquid specific heat (at constant pressure)
$CHF_{measured}$	CHF given by experimental data [MW/m^2]
$CHF_{predicted}$	CHF given by a correlation [MW/m^2]
D	Diameter [m]
D_h	Hydraulic diameter [m]
G	Mass flux [kg/m^2-s]
h	Heat transfer coefficient [W/m^2-K]
h_{bare}	Experimental HTC for bare surface [W/m^2-K]
h_{BOT}	Distance of bottom thermocouple from the boiling surface [m]
$h_{downstream}$	Experimental HTC for downstream (finned surface) [W/m^2-K]
h_{exp}	Experimental heat transfer coefficient [W/m^2-K]
h_{fg}	Latent heat of vaporization
h_{fin}	Finned surface HTC [W/m^2-K]
$h_{measured}$	HTC given by experimental data [W/m^2-K]
$h_{predicted}$	HTC given by a correlation [W/m^2-K]
$h_{ratio,\ downstream}$	Heat transfer coefficient ratio for the finned surface downstream location

$h_{ratio,\ upstream}$	Heat transfer coefficient ratio for the finned surface upstream location
h_{TOP}	Distance of top thermocouple from the boiling surface [m]
$h_{upstream}$	Experimental HTC for upstream (finned surface) [W/m^2-K]
Ja^*	Modified Jacob number
k	Thermal conductivity [W/m-K]
k_l	Liquid thermal conductivity
l	Length of heater [m]
L	Length [m]
Nu	Nusselt number
Nu_l	Single-phase (non-boiling) Nusselt number
Nu_{tp}	Two-phase (boiling) Nusselt number
P	Power from decay heat [MW]
P_0	Reactor operating power [MW]
P_H	Heated perimeter [m]
P_W	Wetted perimeter [m]
Pr	Prandtl number
q''	Surface heat flux [MW/m^2]
q''_{conv}	Heat flux by convection on boiling surface [MW/m^2]
q_{CHF}	Critical heat flux [MW/m^2]
$q_{CHF,\ Bare}$	Bare surface CHF [MW/m^2]
$q_{CHF,\ Fin}$	Finned surface CHF [MW/m^2]
Re	Reynolds number
t_S	Time after shutdown [s]
T_S	Extrapolated surface temperature [°C]
T_{BOT}	Temperature of the thermocouple closest to the boiling surface [°C]
T_{film}	Average temperature between T_S and the bulk water temperature [°C]
T_{SAT}	Fluid saturation temperature for Shlikov et al. correlation [K]
T_{SAT}	Fluid saturation temperature [°C]
T_{TOP}	Temperature of the thermocouple farthest from the boiling surface [°C]
We	Weber number

Acronyms

BWR	Boiling Water Reactor
CHF	Critical Heat Flux

CRGT	Control Rod Guide Tube
DAQ	Data Acquisition
DS	Downstream location on finned surface
ERVC	External Reactor Vessel Cooling
HTC	Heat transfer coefficient
IRWST	In-containment Refueling Water Storage Tank
IVR	In-Vessel Retention
LWR	Light Water Reactor
NRC	Nuclear Regulatory Commission
PEEK	Polyether ether ketone
PIV	Particle Image Velocimetry
PWR	Pressurized Water Reactor
RISA	Radiation Induced Surface Activation
RPV	Reactor Pressure Vessel
SA	Severe Accident
SAMG	Severe Accident Management Guideline
UCSB	University of California – Santa Barbara
US	Upstream location on finned surface

1. INTRODUCTION

1.1 Background

In the past few years focus has been centered again on strengthening current safety systems or adding improved systems to enhance the safety level required during severe accidents. As safety is vital in nuclear power plants, much effort has been made in existing and new reactor designs to incorporate procedures part of the Severe Accident Management Guidelines (SAMGs). Applying procedures part of SAMGs will help to minimize the effects of severe accidents and control their progression. Recently new reactor designs are implementing passive safety systems, which are designed to work without any electrical power requirement. The benefit of such systems is, for example, to supply water required in a certain location by gravity (no pumps necessary) or remove heat from a certain component by natural circulation. If such systems are available during severe accidents, they may provide sufficient time during which other longer-lasting systems can be applied. Other improvements include mobile-type generators i.e. transportable electric generators placed on vehicles in order to provide electricity to necessary locations under emergency conditions. Similarly, vehicles able to transport water during emergency conditions are also available at some plants.

Consider the following severe accident scenario at a nuclear power plant: due to an unforeseen incident and certain sequence of events, the reactor core has melted and relocated to the lower plenum inside the Reactor Pressure Vessel (RPV). After boiling off the remaining water in the lower plenum the corium (melted core materials) will begin to heat the lower head of the RPV. The heat transferred to the RPV is the decay heat generated by the radioactive materials present in the original reactor core which have melted and relocated into the lower plenum along with other materials inside the RPV. As the heat is transferred from the corium to the RPV lower head, eventually the lower head temperatures will begin to increase. The lower head temperatures will continue to rise in the event that no cooling is applied from the outside of the RPV. After a certain amount of time the lower head temperatures will reach the melting point of carbon steel (type of steel used to manufacture RPVs). Upon reaching the melting point temperatures, RPV failure may occur by thermal stresses and/or creep (Theofanous et al., 1997). If vessel failure occurs the corium will be released from the vessel into the containment area. Since the corium contains highly radioactive materials which will be released into the

containment, any leakage paths from the containment may allow the radioactive materials to escape into the environment. For environmental and public safety, the leakage into the environment must be prevented.

There may be two ways to prevent the leakage of the radioactive materials into the environment: prevent the leakage from the RPV or prevent the leakage from the containment. Completely enclosing the containment and preventing any leakage may be difficult. On the other hand, preventing the leakage or release of the corium from the RPV may be a less difficult task. The RPV is designed to be a closed system, since during normal reactor operation no leakages from the primary cooling system are desired. Due to the closed RPV design the fission products can be retained inside the vessel even if the core has melted and the fission products have been released. The remaining issue would be to prevent the overheating of the vessel surface which may lead to vessel failure. By ensuring the integrity of the pressure vessel during severe accident conditions the melted core and fission products can be kept inside the RPV. A particular severe accident management strategy that may prevent the failure of the RPV is termed In-Vessel Retention (IVR). The following section explains the concept of IVR and an issue that may arise for its applicability in future larger-powered Light Water Reactors (LWRs).

1.2 IVR & Possible Issues for Future Reactors

1.2.1 IVR

The concept of IVR can be seen in Fig. 1-1. During the IVR process, the reactor cavity (area outside the RPV) is flooded with water supplied by the In-containment Refueling Water Storage Tank (IRWST). Once the water is supplied to the reactor cavity, heat will be transferred to the water from the heated pressure vessel surface. As a result, boiling will occur on the outer vessel surface. The water temperature will rise as the boiling process continues, decreasing the density of water and leading to natural circulation conditions. Once natural circulation begins, convection will cause the water to flow between the insulation and the vessel surface (Theofanous et al., 1997). As water contacts the heated RPV wall, heat transfer will reduce the wall temperature. It is expected that higher heat transfer from forced convection during the IVR scenario will assist in preventing failure of the RPV wall from overheating. It should be

clarified that the term “in-vessel” is implied for corium. Actually, IVR is accomplished by cooling the vessel from the outside of the RPV. Thus, another name found in the literature to describe the IVR concept is External Reactor Vessel Cooling (ERVC).

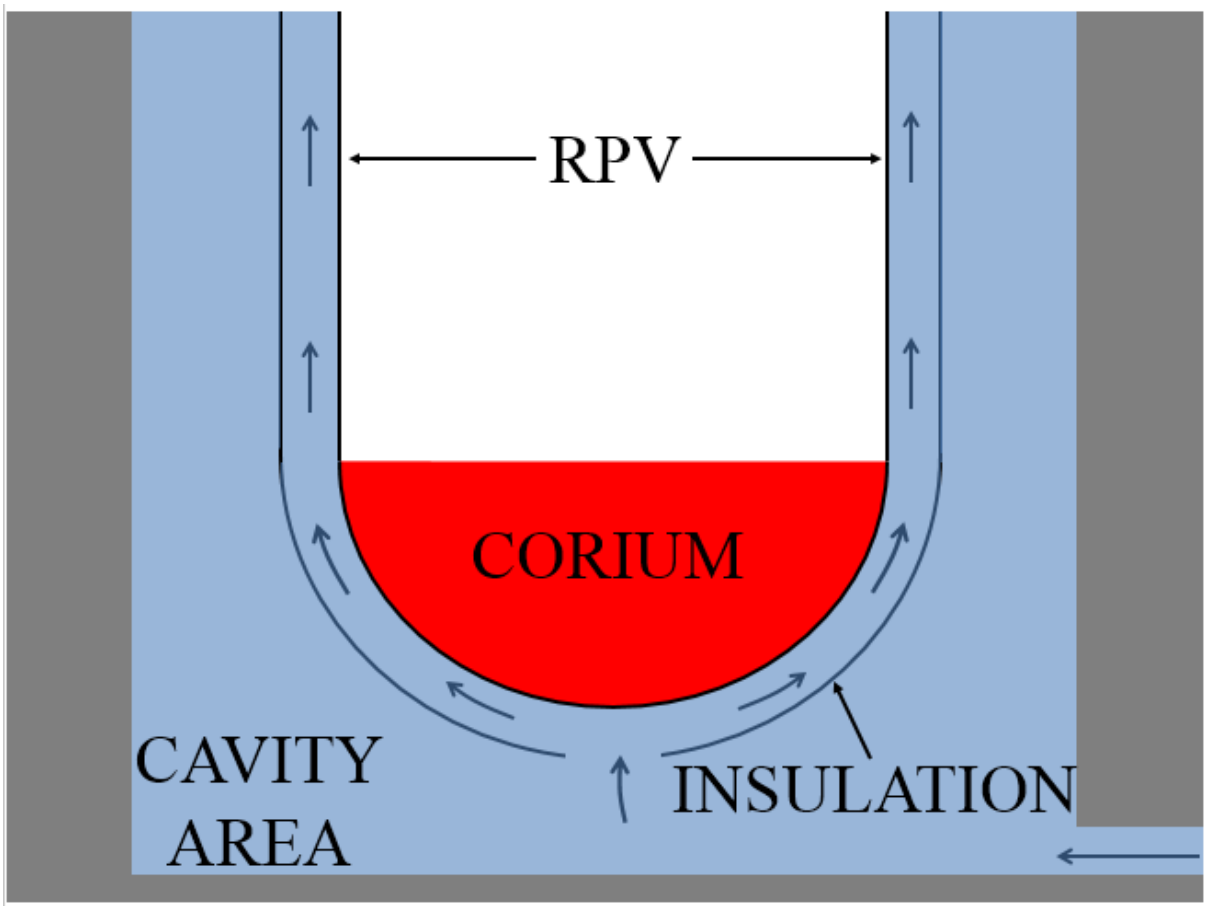

Figure 1-1: Concept of IVR showing cavity area flooded and the path of fluid flow.

Cavity flooding is not a new concept, and had been considered previously by Tong (1968). Although his analysis may have been simple, he showed that heat transfer from different parts of the RPV was able to prevent vessel failure. The idea of IVR through ex-vessel cooling became an important concept as a potential severe accident management strategy for some reactor designs in the past few decades. For example, the AP-600, AP-1000, VVER-440 (Loviisa), APWR-1400, and AREVA’s 1000MWe (BWR) reactor designs have implemented IVR as part of their accident management strategies (Sehgal, 2012). To the best of the authors

knowledge work is still ongoing regarding the enhancement of IVR in the APR1400 due to the larger power of the Korean reactor (Park et al., 2006; Park et al., 2012).

There have been many studies performed related to the idea of IVR. For brevity, only the work related to the ULPU facility performed at University of California – Santa Barbara (UCSB) will be briefly mentioned. At first it was designed to investigate IVR for the Loviisa plant, but afterwards was used for the AP600 (Kymalainen et al., 1997) and AP1000 designs (Dinh et al, 2003). The ULPU experiments were performed with five (V) different configurations (Figs. 1-2 and 1-3).

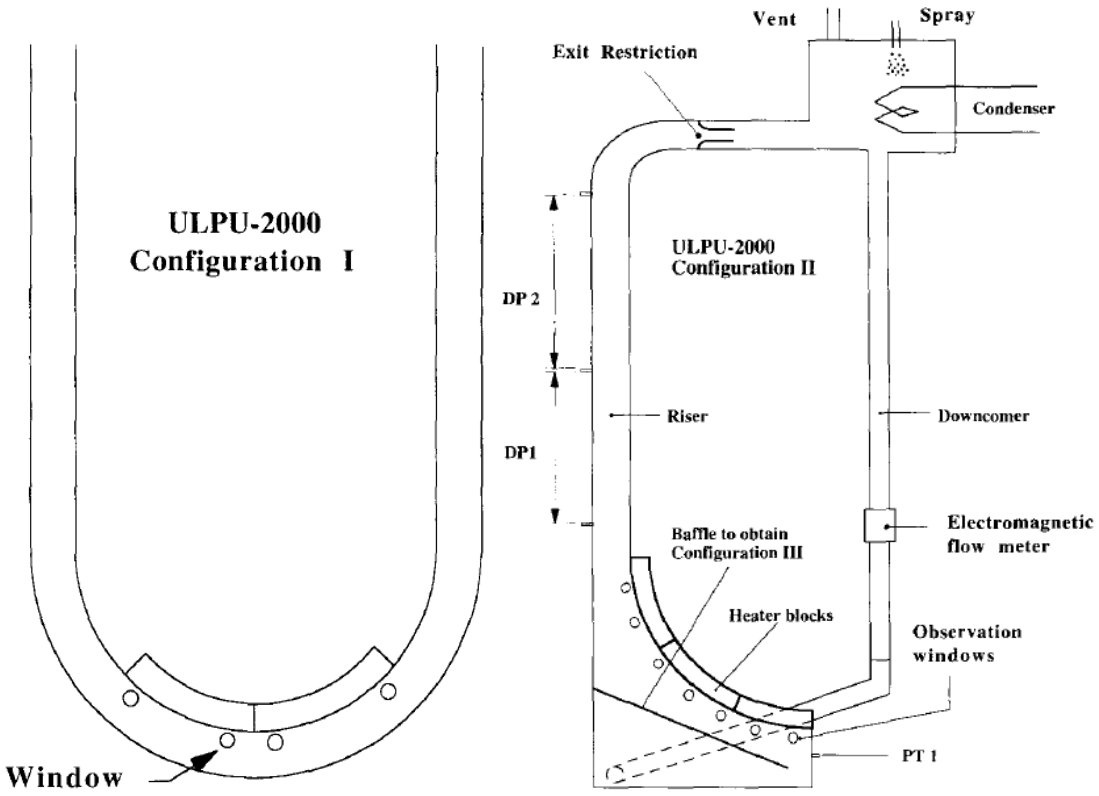

Figure 1-2: Configurations I-III of ULPU (images: Theofanous & Syri, 1997).

Although in configuration I the full curvature was not considered (only 0-30°) and pool boiling conditions were present, experiments were performed with the full curvature of the lower head (0-90°) in configurations II and III along with flow conditions (Theofanous & Syri, 1997). The difference between configurations II and III is the baffle inserted in the latter to represent the

thermal insulation. The two configurations (II and III) were used to investigate IVR for the AP600. Afterwards, the AP1000 IVR experiments were performed with the modified designs of configurations IV and V. In configuration V, the design was slightly modified to represent the AP1000 flow path correctly and the reliability of IVR was tested at higher heat flux (~2.4 MW/m^2) (Dinh et al., 2003).

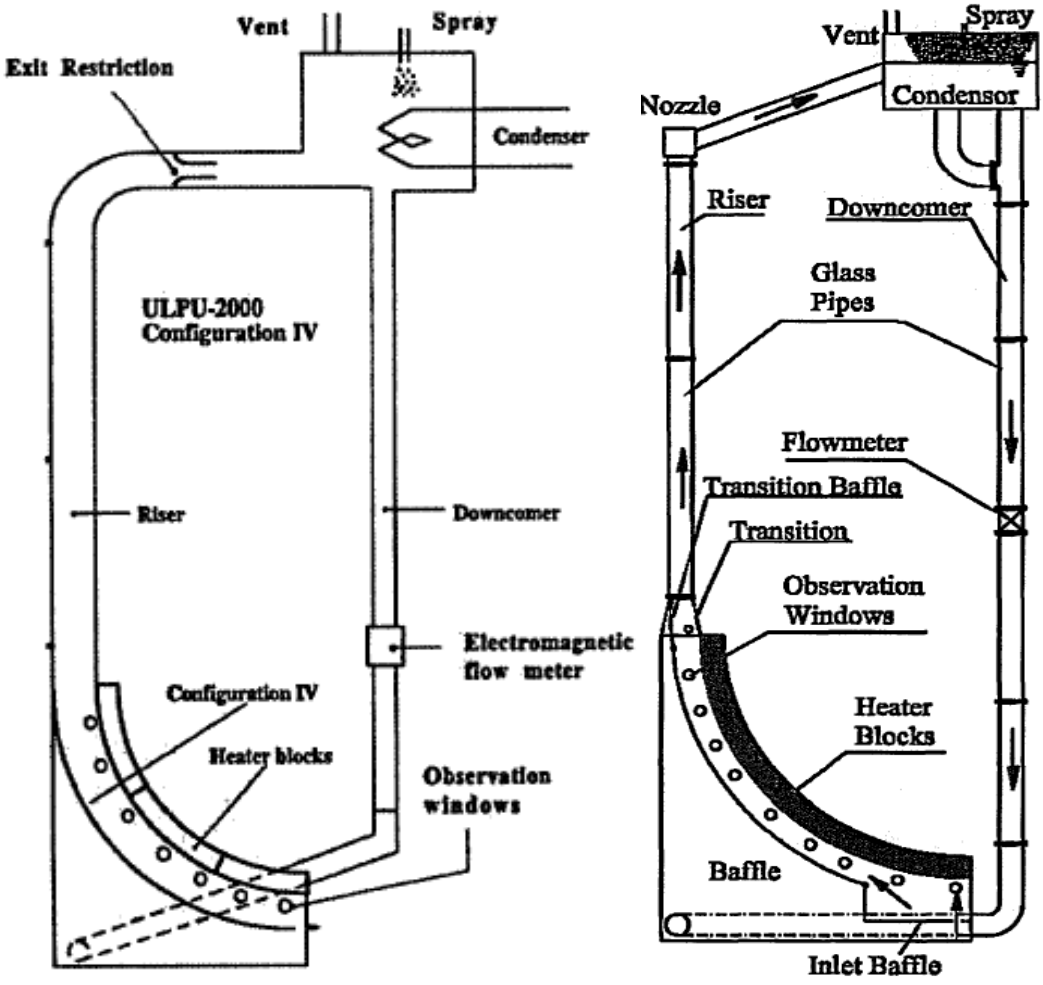

Figure 1-3: Configurations IV and V of ULPU experiments (images: Dinh et al., 2003).

1.2.2 Current Status: IVR

The general concept of IVR is such that if the lower head of the RPV is submerged, failure of the vessel may be prevented due to cooling of the exterior surface by the water (ERVC).

Although this concept may prevent RPV failure, another problem may arise. As the decay heat from the corium heats the RPV lower head the water temperature will start to increase, eventually causing boiling on the vessel surface. Therefore, excessive boiling conditions leading to Critical Heat Flux (described in the next section) may pose a risk for the RPV integrity. As a result, a channel-like design was proposed to increase the flow conditions on the exterior wall of the RPV surface. The channel-like geometry was created between the RPV and the thermal insulation (Fig. 1-1). Extensive work at UCSB through the ULPU experiments have helped to establish IVR for the AP600 and AP1000 reactor designs. Issues that may arise for future larger-powered reactors are mentioned in the next section.

1.2.3 Possible Issue for Future LWRs

As mentioned in the previous section, the ULPU studies at UCSB have well established the applicability and reliabiltiy of IVR as a accident management strategy, since both the AP600 and AP1000 licenses have been approved by the Nulcear Regulatory Commission (NRC). The issue that may arise is whether IVR can be utilized as an accident management strategy for future larger-powered LWRs? A larger-powered reactor will contain more fuel in the reactor core. Considering a hypothetical severe accident with core melt and relocation into the lower plenum, the melted core from a more powerful reactor will produce more decay heat compared to a less powerful one. As a comparison, consider three different reactors: AP-1000, APR-1400, and CAP-1700. Note that the CAP-1700 is a proposed design based on the CAP-1400 (Zheng, 2013). The decay heat after shutdown of a reactor can be approximated by (Todreas & Kazimi, 1990)

$$\frac{P}{P_0} = 0.066\left[t_S^{-0.2} - \left(t_S + \tau_S\right)^{-0.2}\right] \tag{1-1}$$

where

P = power from decay heat [MW]

P_0 = reactor operating power [MW]

t_S = time after shutdown [s]

τ_S = reactor operating time [s]

The reactor operting power is the thermal output power (MWt). Assuming a very long operating time at a nuclear power plant, the term $(t_S + \tau_S)^{-0.2}$ becomes negligible and the power can be estimated by

$$P = 0.066\, P_0\, t_S^{-0.2} \tag{1-2}$$

Equation (1-2) was plotted for the three reactors mentioned earlier. An operating power of 3400 MWt was used for the AP-1000 (see References) and 3983 MWt for the APR-1400 (see References). Since the CAP-1700 is proposed design, the information from the CAP-1400 (Tian, 2013) was used to calculate the operating power for the CAP-1700.

Figure 1-4 shows the decay heat curve for the three reactor designs. Since the typical passive cooling duration is approximately 72 hours, the decay heat curve is only shown for that duration in Fig. 1-4. Due to the complexities of the phenomena involved, the time required for full core melt and relocation to the lower plenum is unknown. While performing severe accident calculations for the AP-1000, Zhang et al. (2010) found relocation times of 1.7 hours with the MAAP code and 2.6 – 3.7 hours with MELCORE code. Based on their analysis, three relocation times were chosen to compare the three reactor designs mentioned earlier with equation (1-2): 1.7 hours, 2.7 hours, and 3.7 hours. These values are depicted with vertical lines in Fig. 1-4. The decay heat at the different relocation times for the three reactor designs is shown in Table 1-1.

Table 1-1: Decay heat at different relocation times for three reactor designs.

Relocation Time	**AP-1000**	**APR-1400**	**CAP-1700**
1.7 hours	39.2 MW	46.0 MW	57.0 MW
2.7 hours	35.7 MW	41.9 MW	51.9 MW
3.7 hours	33.6 MW	39.3 MW	48.8 MW

The greater amount of decay heat generated may lead to higher heat flux on the outer surface of the vessel lower head. If the IVR method remains unchanged, higher heat flux will lead to

excessive boiling conditions on the vessel surface. This may pose to be a potential risk, as Critical Heat Flux (CHF) may occur due to the rigorous boiling on the vessel surface.

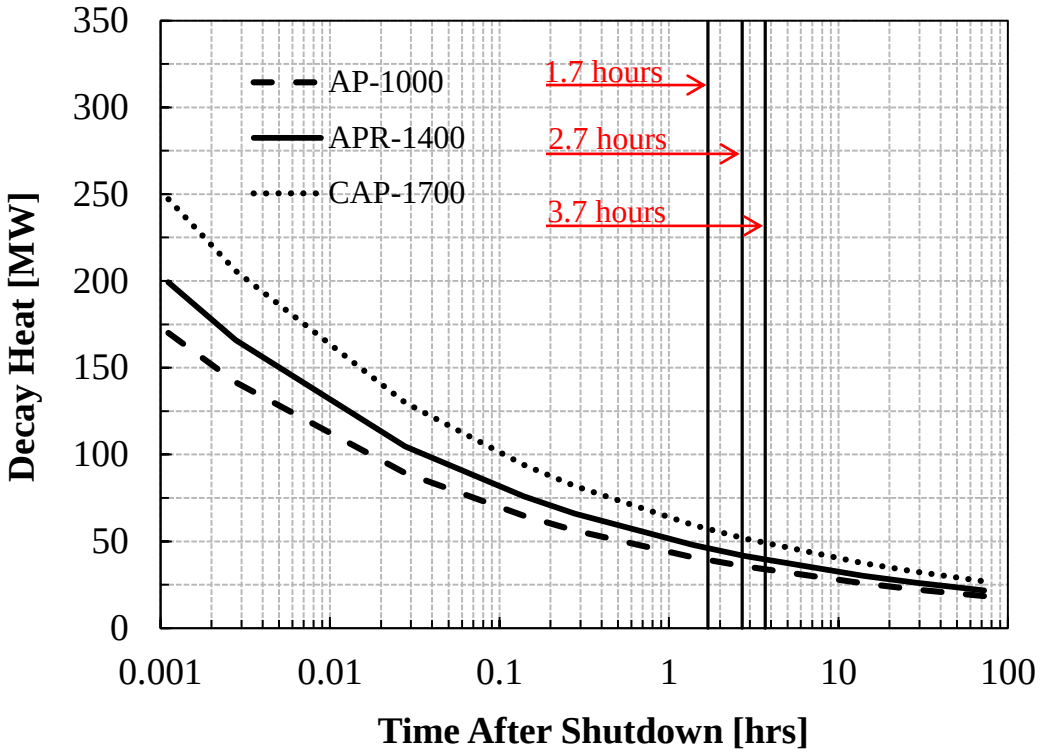

Figure 1-4: Decay heat power after shutdown for AP-1000, APR-1400, and CAP-1700.

CHF is the value at which even a small increment in the heat flux will cause a sudden increase in surface temperature. When CHF conditions are present on a surface bubble generation does not allow for the surrounding liquid to directly contact the heated surface, since a vapor film usually forms on the surface. If such conditions persist, the surface will become damaged and RPV failure may eventually occur. Therefore, it is important to consider such an issue for future larger-powered LWRs implementing ex-vessel cooling as an accident management strategy.

2. OBJECTIVE

2.1 Final Goal

As explained in the previous section, IVR has been established for some existing reactor designs. The experimental work has shown that the current IVR technique allows for effective cooling of the outer vessel surface during accident scenario conditions. Depending on power requirements some next generation advanced LWRs are designed to output more power than previous reactors, and the current IVR method may not be sufficient for future larger-powered reactor designs. Therefore, increasing the safety margin for the CHF limit is an important aspect that should be considered for larger-powered LWRs.

The problem statement of this thesis is presented as follows: how can the CHF safety margin be increased for future larger-powered LWRs planning to adopt ex-vessel cooling as a severe accident management strategy? The work performed in this thesis investigates the effect of physically altering a boiling surface in order to improve heat transfer during flow boiling (forced convection) conditions. Since the work performed in this study is related to heat transfer in general, it can be applicable for ex-vessel cooling as well.

2.2 Proposal

One method to improve the heat transfer from a surface can be accomplished by modifying, or changing, the surface. The modification proposed in this work is a structured surface design. The proposal made is if a structured design is applied on a heated surface, the surface characteristics can be changed to enhance the heat transfer. Therefore, the hypothesis is that an enhancement in CHF may also be observed.

2.3 Objective

The proposal made in this thesis is to investigate the effect of a certain type of structured surface on CHF. Although many different methods or techniques may exist to improve heat transfer,

the one considered in this thesis is very simple. A pin fin is used in the current work to investigate the heat transfer effect from a boiling surface during forced convection conditions in the downward-facing direction.

While fin heat transfer in not a new subject, studies relating to flow boiling fin heat transfer have not been found in the literature by the author. From experiments performed in the past the fin is known to enhance the heat transfer from a heated surface. The hypothesis is that the fin may also enhance the CHF in flow boiling conditions. Therefore, the objective of this thesis is to investigate the effect of a fin on CHF from a downward-facing boiling surface in forced convection conditions.

2.4 Differences in Current Experiments and Past Studies

It was observed from previous works that downward-facing boiling studies were not as common as other orientations e.g. upward for vertically-facing boiling surfaces. Fin boiling heat transfer studies were also limited. Pool boiling experiments with fin(s) have been performed in the past, some of which showed CHF enhancement. Many of the flow boiling experiments utilizing fins are micro and mini-scale experiments related to electronic chip cooling. The current study investigates large-scale (macro) fin flow boiling, and such studies were not found in the literature. Details of some previous works related to the current study are described in Chapter 4.

3. FOCUS OF CURRENT WORK

3.1 Downward-facing Forced Convection Conditions

It is worthwhile mentioning why this study is focused on forced convection boiling conditions in a downward-facing position. The reason to apply forced convection is due to similar conditions present during a severe accident scenario employing ex-vessel cooling as an accident management strategy. Water supplied to the reactor cavity will submerge the RPV. Water will initially remain as stagnant liquid. It will gain momentum when heat is transferred from the vessel surface, causing density differences in the water. Once the temperatures on the vessel surface increase to such an extent as to cause boiling the generated vapor (bubbles) will rise, condense, and cooler water will be supplied back to the cavity. Even though this process of natural circulation does not use forced convection, similar flow conditions applied (using pumps) represent the presence of flow between the RPV and the insulation. Therefore, experimental work studying heat transfer in flow boiling conditions, such as in the current study, usually apply forced convection by using pumps rather than working with natural circulation flow conditions.

There were mainly two reasons for studying heat transfer from a downward-facing surface: difficulty in bubble removal, and scarcity of data for such geometry. For a downward-facing surface the buoyancy of the bubble will cause the bubble to rise, except it will not be able to do so (Fig. 3-1). Since the heated surface is directly above the bubble, the only way to remove the bubble is through forced convection. In the downward-facing direction, buoyancy is likely to cause more damage since the bubble cannot be removed by the buoyancy force. At relatively low flow conditions, bubble accumulation may become an issue for the heat transfer in the downward-facing heated surface case. In other directions (vertically or upward-facing heated surfaces in Fig. 3-1), buoyancy may help to alleviate bubble removal from the boiling surface since no disturbance exists to prevent the bubbles from escaping the surface. In such cases, accumulation may not be an issue in preventing the release of the bubbles from the heated surface even at low flow conditions. Another reason for studying the downward-facing direction is to obtain data for such type of geometry, since there is shortage of data for downward-facing flow boiling studies. Experimental work investigating downward-facing boiling has not been studied as extensively as other surface orientations.

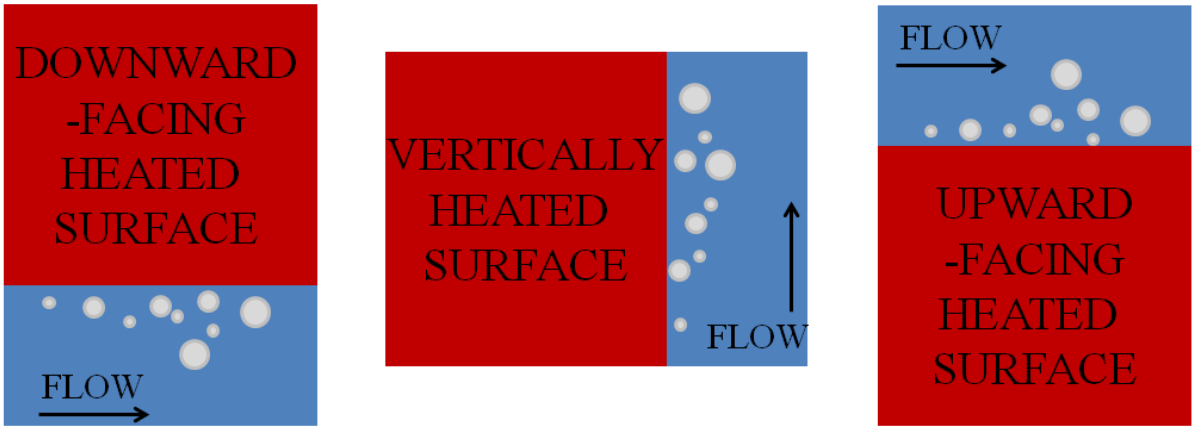

Figure 3-1: Different orientation of heated surfaces with forced convection conditions.

3.2 Fin Representation

There were two purposes for studying the finned surface design. One of the purposes was the proposed structured surface design. The fin acted as the modified surface design that may be applied on the exterior of the RPV surface. The other purpose of the fin was to represent the Control Rod Guide Tube (CRGT) in the BWR lower head, although it was a simplified depiction.

Majority of the studies related to IVR investigated heat removal from a plain surface i.e. no protrusions existed on the boiling surface. For example, the ULPU experiments were performed by heating three large copper blocks. Since each block covered approximately 30°, arranging the three blocks together covered the full angular range of the lower head. Although that was beneficial for a full-scale study, the effect of lower head penetrations was not studied in those experiments. It may be crucial to study and understand the effect of the lower head penetrations during a severe accident with the RPV submerged, especially for the Boiling Water Reactors (BWR). Pressurized Water Reactors (PWR) have few penetrations in the lower head when compared to the BWRs (Fig 3-2).

The concept of cavity flooding is not only limited to the PWR. It is also being considered for accident management in new BWR containment designs (Sato and Kojima, 2007, Sato et al., 2009). Even though the reason for the cavity flooding may not be for IVR purposes, consider

for a BWR the previously mentioned accident scenario in which a severe accident leads to core melt and its relocation to the lower plenum. Moreover, consider the application of cavity flooding during this process. The heat will be transferred from the BWR lower head vessel wall to the water and boiling will initiate on the vessel surface. One main difference between PWRs and BWRs is the CRGT penetrations in the lower head of the BWR (Fig. 3-2). The CRGTs may play a crucial role in determining the integrity of the vessel during the accident. Since the CRGTs housing extends outward from the lower head of the vessel, they may act as heat sinks for the decay heat generated by the corium inside the vessel. Although that may seem to enhance the heat transfer and reduce the temperatures on the outer surface, there may be a drawback for such a scenario. With the vessel submerged and releasing heat to the water, boiling will initiate on the outer surface. Due to the existence of few penetrations in the lower head of PWRs, bubbles generated from boiling on the vessel can travel along the curved vessel surface. On the other hand, there are a great many CRGTs in the lower head of a typical BWR. The images in Figs. 3-3 and 3-4 emphasize the congested space below the BWR RPV. As fluid flows along the surface of the vessel, it will interact with the penetrations. Consequently, the fluid flow and heat transfer may be affected. Thus it is important to understand the effect of the lower head penetrations on the integrity of the RPV during severe accident conditions.

Although the work performed in this thesis has no direct relation with the BWR lower head penetrations, some issues may be revealed during the experimental work performed herein that may be extrapolated to the conditions present for a submerged BWR involving the lower head penetrations during a severe accident.

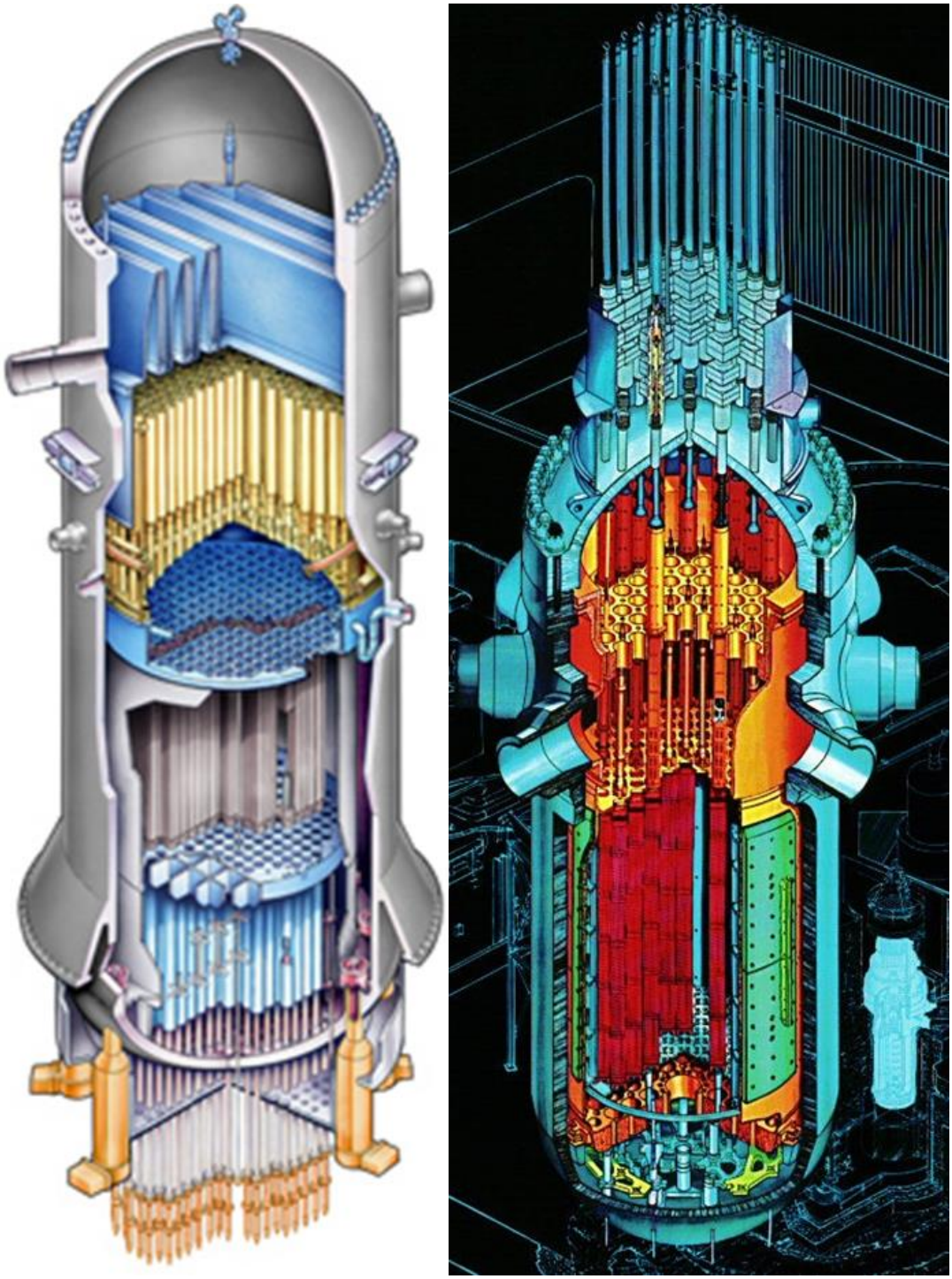

Figure 3-2: Designs of BWR (left) and PWR (right) showing the difference between the lower head penetrations (images: see reference section).

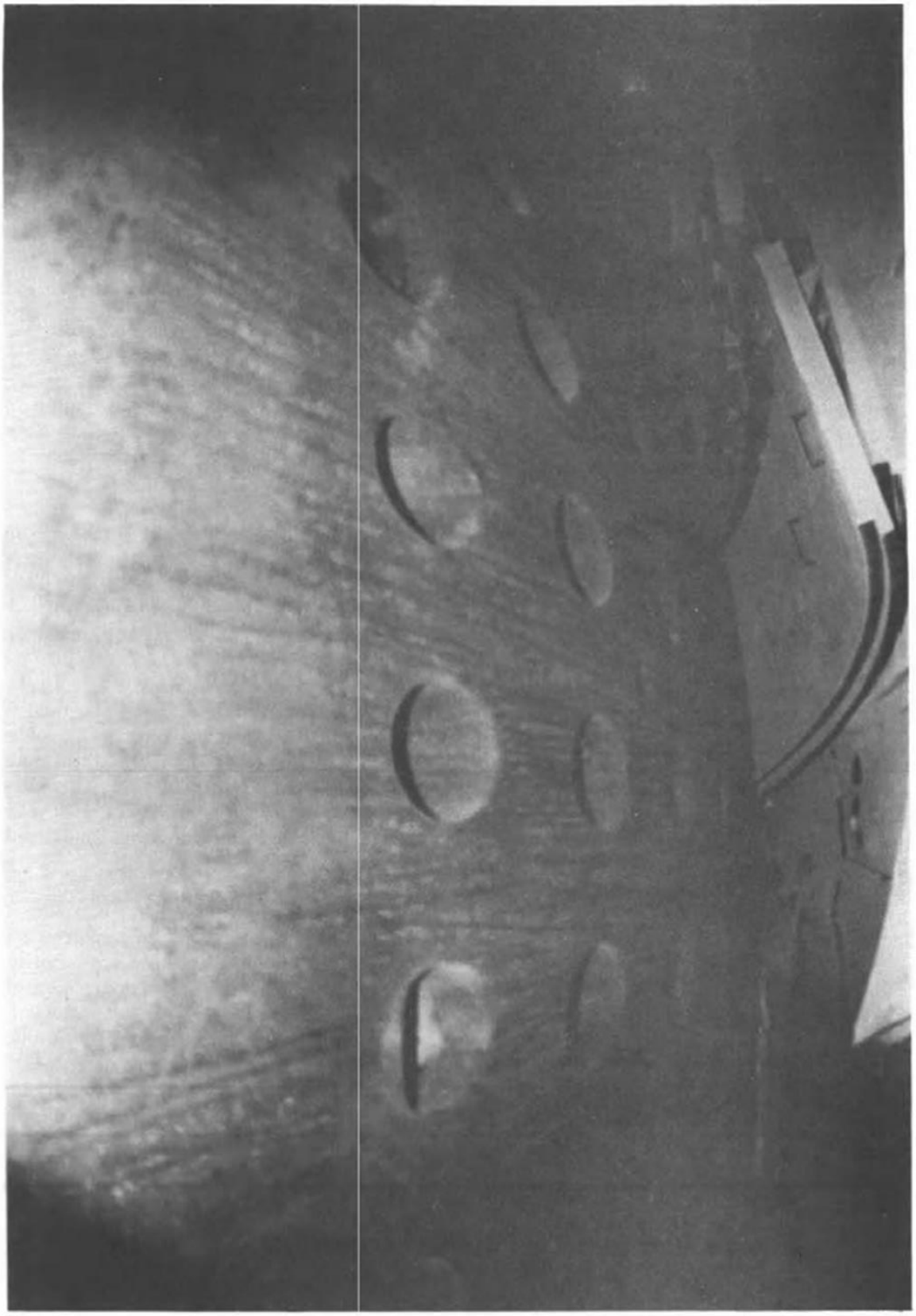

Figure 3-3: Lower head of BWR without CRGTs (image: Hodge et al., 1992).

Figure 3-4: Image showing CRGTs housing (large stainless steel cylinders on right side).

3.3 Conditions Chosen for Experimental Work

This section explains why certain conditions were chosen for the experiments. Consider the subcooling of the water supplied to the cavity area for ex-vessel cooling. Since the exact temperature of the water is unknown, for simplicity it is assumed that the water is stored at room temperature in the containment building before it is drained into the cavity. Moreover, convection conditions are assumed during ex-vessel cooling as mentioned in section 3.1 and seen from previous experiments (ULPU). As a result, the above two conditions (subcooling and some form of velocity) established the base for the current experiments. It was desired to place the ULPU configuration V experimental conditions on a graph including the above-mentioned conditions, since the ULPU experimental conditions are assumed to be the real ex-vessel cooling conditions. Two assumptions were necessary in order to calculate the required parameter for the ULPU experiments. The first assumption was that the mass flow rate at the location of the flow meter (Fig. 1-3) was the same as in the region of the curved heated copper blocks. This assumption was necessary because no fluid velocity information was available at the location of the curved heated section. The second assumption was related to the geometrical information about the ULPU configuration V design. It was assumed that the dimensions given by Dinh et al. (2003) were correct and applicable for a simple flow analysis in the curved section of the ULPU design. Additionally, flow rates approximately ranging from 590 – 715 L/min were shown by Dinh et al. (2003) for the ULPU configuration V experiments. With the above stated assumptions, flow rate information, and a three-inch baffle configuration, the approximate ULPU mass flux ranged from 750 – 1050 kg/m^2-s. Figure 3-5 presents a graph showing the water subcooling as a function of its mass flux. The subcooling of the water ranges from saturation (0 degrees) to room temperature (-80 degrees). Note the conditions of the ULPU experiments towards the top of the graph. Again, the ULPU conditions were assumed to be the real (final, end state) conditions of ex-vessel cooling.

Next, two hypothetical severe accident scenarios involving cavity flooding were considered. In Scenario 1, the cavity is flooded before the corium relocates into the lower plenum of the RPV. When relocation occurs and the decay heat begins to heat the lower head, the water is available to remove the heat from the exterior of the vessel surface. As time progresses the heat transferred to the water will increase its temperature, causing density differences. As a result, natural circulation will exist which will allow for flow conditions. In this scenario the water is

stagnant at very high subcooling in the beginning of the cavity flooding, and nearly saturated having some flow conditions long after the accident started. Scenario 2 is the opposite of Scenario 1, with the corium relocating to the lower plenum before the cavity is flooded. In this scenario the exterior of the vessel surface will be heated by the decay heat from the corium when the cavity is flooded. This is similar to the quench phenomenon. Rigorous boiling may occur as the water contacts the heated vessel surface. As the heat is transferred to the water, its temperature will increase leading to natural circulation conditions. Although the boiling conditions may be different for the two scenarios, the water subcooling and flow conditions for Scenario 2 are assumed to be similar to Scenario 1 i.e. the water has high subcooling and low flow conditions in the beginning of the cavity flooding and low subcooling and relatively higher flow conditions long after the cavity is flooded.

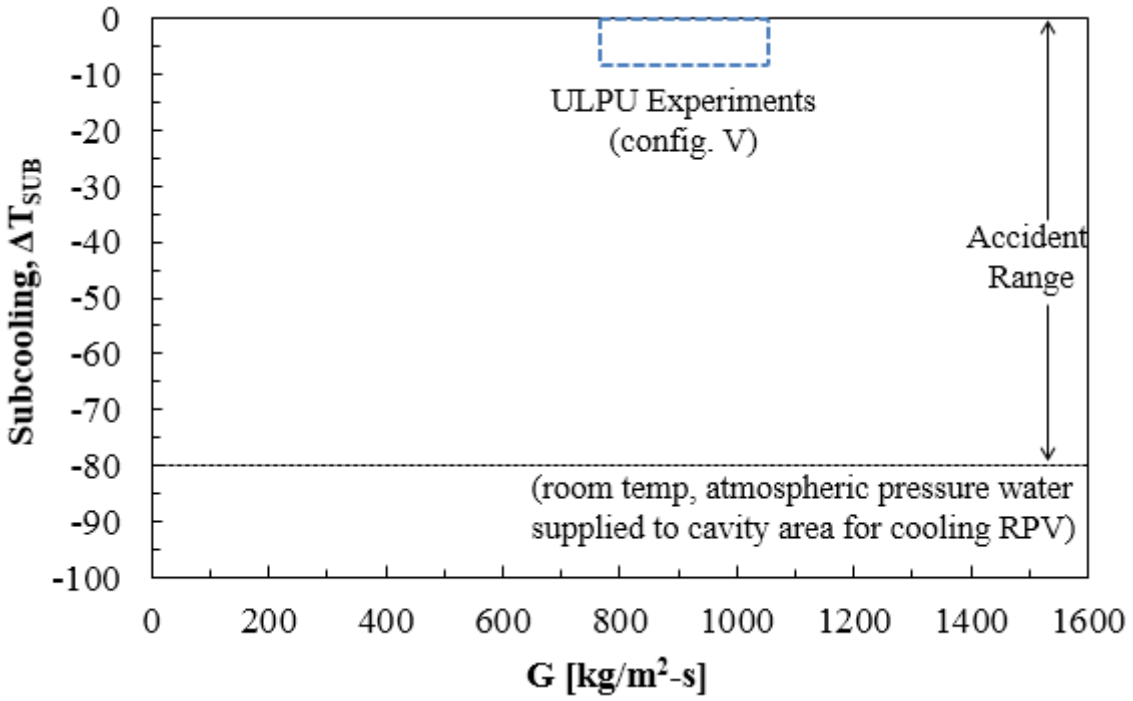

Figure 3-5: Graph of water subcooling vs its mass flux when supplied to the cavity area, including the ULPU experimental conditions.

Based on the conditions in the beginning and long after cavity flooding of the above two scenarios and combining them with Fig. 3-5, two particular conditions were chosen. The first condition is high subcooling and relatively low flow rates. This may be considered as the initial

condition of the water supplied to the cavity area. The second conditions is low subcooling (saturated or nearly-saturated) and relatively high flow rates, which may be considered as the final or the end state of ERVC. The two conditions were taken as the parameters for the experiments performed in this thesis. As a result, flow boiling phenomenon was investigated in subcooled and saturated conditions. The approximate subcooling and mass flux for the experiments performed in this study are shown in Fig. 3-6.

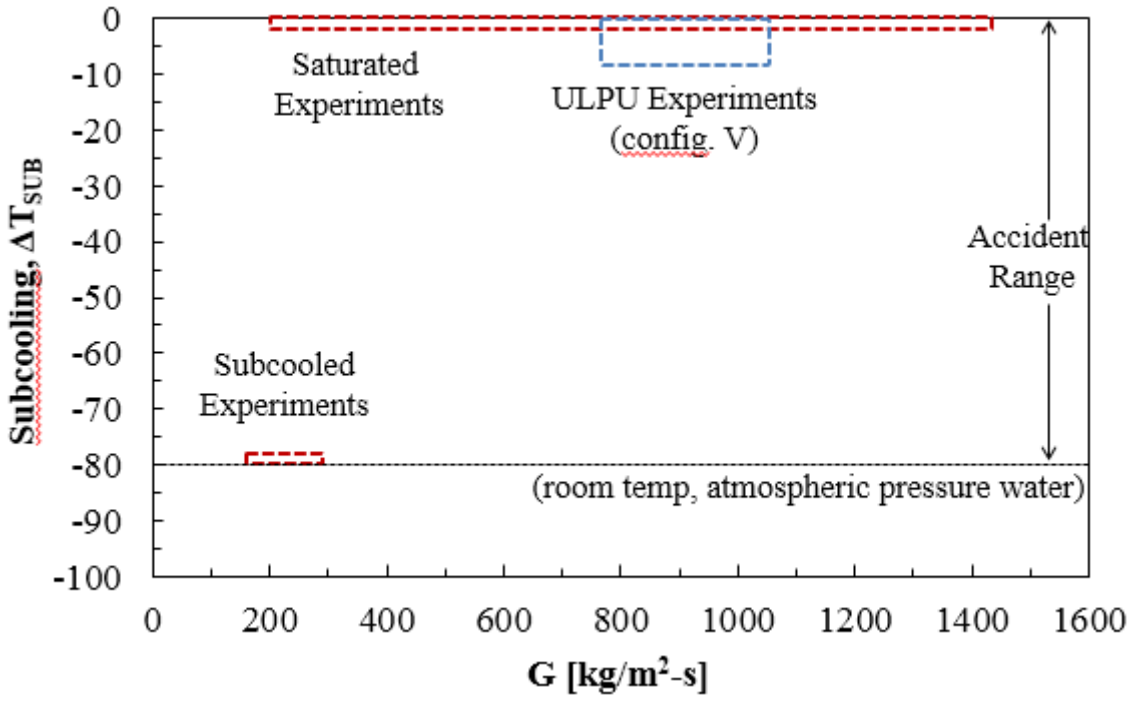

Figure 3-6: Graph of water subcooling vs its mass flux when supplied to the cavity area, including the current and ULPU experimental conditions.

For the purposes stated in the previous sections as well as this section, an experimental study was performed to address the heat transfer enhancement capability from a finned surface in downward-facing flow boiling. The experiments were also performed to study fundamental issues existing in a downward-facing boiling phenomenon with a fin. While many separate studies have been performed relating to downward-facing boiling and cylinder in cross-flow, studies on the combination of the two during boiling conditions have not been found in the literature. Therefore, the current study will provide insight on the boiling phenomenon for such

type of geometry and conditions. From the results of this study, important aspects relevant to heat transfer and boiling are evaluated.

The experimental work was separated into two parts. First, experiments were performed at highly subcooled conditions. The subcooling could not have been varied during the experiments due to the experimental facility. The facility was not designed to handle high fluid temperatures. After the subcooled experiments had been completed, a new experimental facility was designed in which saturated conditions were applied for the flow boiling experiments. In the new facility, the pressure was reduced to reach saturated conditions at lower temperatures. The reduced pressure of approximately 0.050 MPa allowed for saturated water conditions at approximately 81°C. As will be shown later, the boiling phenomenon was different when comparing the two experiments.

4. PREVIOUS STUDIES

In this chapter, some previous works relevant to the current study will be mentioned. Since the focus of this thesis is to observe the effect of a finned surface in downward-facing flow boiling conditions, the experiments mentioned in this chapter have been limited to such studies. It should be clarified that this chapter does not provide a comprehensive review of all related works available in the literature.

4.1 Boiling from Finned Surfaces

A fin, also known as an extended surface, is well known to enhance the heat transfer from a heated surface with convection conditions. While the heat transfer coefficient of a finned surface may be constant for slow-moving liquids, it cannot be considered a constant when boiling conditions are involved (Haley &Westwater, 1964). Therefore, experimental work is needed to understand boiling heat transfer from a finned surface.

Pool boiling experiments were performed to understand the boiling phenomenon on a fin (Fig. 4-1) by Liaw and Yeh (1994). They investigated boiling from a horizontally placed pin fin 2.5 cm in diameter by 10 cm in length. The fin was attached to a base plate heated by cartridge heaters. Thermocouples along the centerline of the fin allowed for temperature monitoring during the boiling process. One of the conclusions from their study stated that there was a significant increase in the burnout temperature by attaching the fin to the surface.

Experiments performed by Guglielmini et al. (1996) used an array of square fins in a dielectric liquid, with the heated surface oriented horizontally (fins facing upward) and vertically (fins facing to the side). The fin spacing was varied and different pressures were used in the experiments. They concluded that better boiling performance was achieved with the fins compared to a plane surface. Yu and Lu (2007) also investigated the effect of an array of fins in FC-72 (Fig. 4-2), varying the fin spacing and length. They obtained the highest CHF value with the longest fin length and shortest fin spacing.

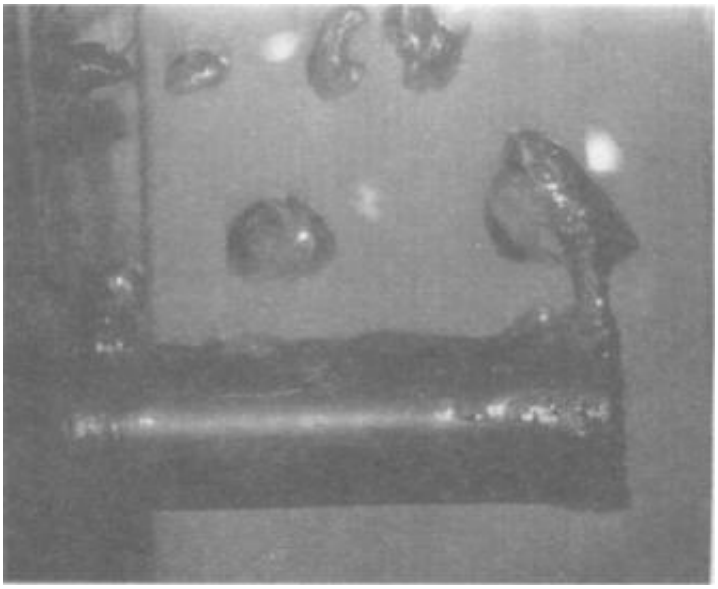

Figure 4-1: Boiling occurring on a horizontal fin in Liaw and Yeh's (1994) experiment.

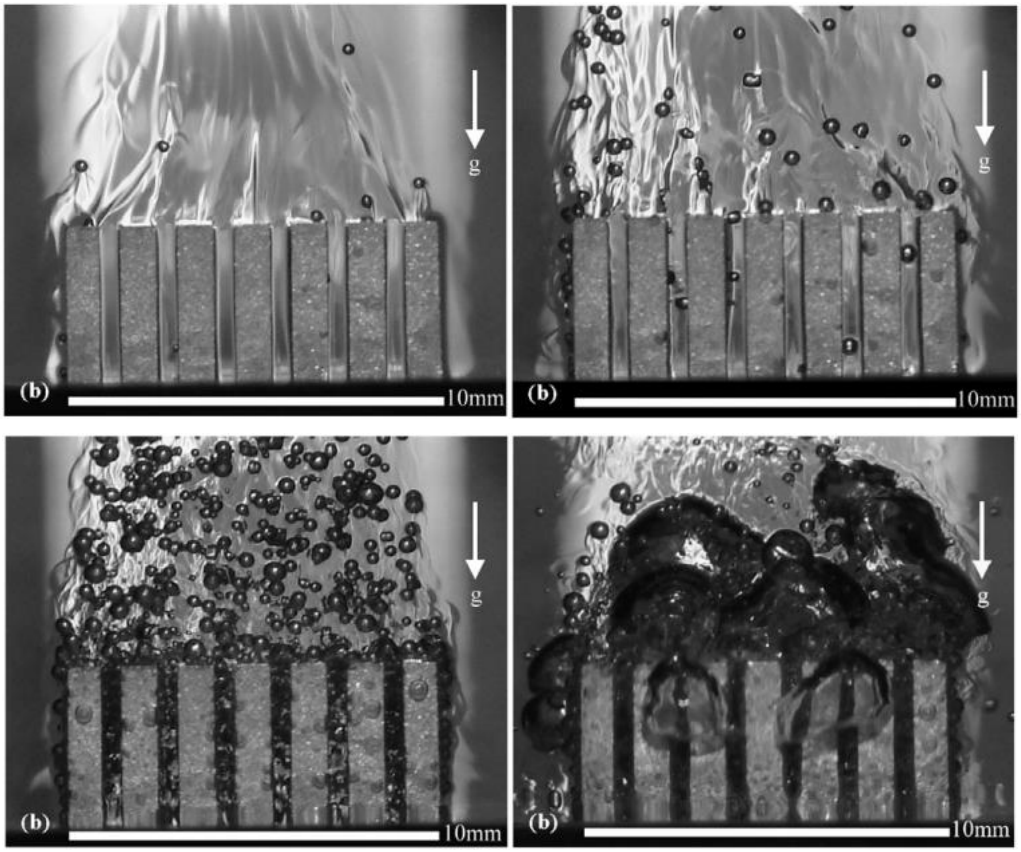

Figure 4-2: Heat flux from top left image is 1.1 % of CHF, 23.3 % of CHF, 56.8 % of CHF, and 81.3 % of CHF; fin spacing of 0.5 mm and length of 4 mm (Yu and Lu, 2007).

Similar to Yu and Lu, Chan et al. (2010) varied the fin spacing, thickness, and height. They performed experiments with water as the working fluid, but in reduced pressure conditions. For a given fin spacing and height they observed moving boiling curves for different fin thicknesses, with 0.75 mm thickness being the optimal one. While varying the fin spacing only, different pressures resulted in slightly different boiling curves. No optimal fin spacing was stated. The fin height also resulted in overlapping boiling curves, and no optimal fin height was stated.

Many of the fin-related studies found in literature have been performed with a refrigerant or coolant as the working fluid. In addition, some of those studies utilize fins to investigate cooling for electronic devices and the test sections are on the scale of millimeters or micrometers. For brevity, they will not be mentioned here. If the reader is interested in such studies, they may refer to the following works for more information: Wei and Honda (2003), Wei et al. (2005), Launay et al. (2006), Zhang and Lian (2008), and Balasubramanian et al. (2013).

Macro-scale fin studies in convection conditions are rarely found in the literature. Moreover, no study found has performed separate-effect tests on a single fin during flow boiling conditions. It is desired that the results of the current study will provide a better understanding on that matter.

4.2 Downward-facing Boiling

Even though surfaces with different orientations can be found in the literature, downward facing flow boiling experiments are scarce. Some pool boiling experiments conducted in the past will be mentioned.

El-Genk and Guo (1993) performed pool boiling quenching experiments on a copper surface at different inclination angles, one of the angles being 0° (downward-facing). Pressure conditions were slightly sub-atmospheric at 0.086 MPa. From their results, an average CHF value of approximately 0.25 MW/m^2 was reported from 0° experiments. They presented an illustration showing the reason why the CHF will be lower for the downward-facing orientation compared to other orientations (Fig. 4-3). In a downward-facing position the bubbles will

coalesce and cover the heated surface. There can no bubble removal only from buoyancy itself. For an inclined surface bubble buoyancy will cause movement of the bubbles from the heated surface, possibly increasing CHF.

Yang et al. (1997) performed pool boiling experiments in two different phases on stainless steel surfaces, varying the heater orientation. For the first phase experiment, the angles ranged from -90° (downward-facing) to -40°. For the second phase experiment, the ranged had increased from -90° to 90° (upward-facing). First phase experiments resulted in average CHF values of 0.776 MW/m^2 and 0.504 MW/m^2 for two downward-facing different sized surfaces. From the second phase experiments average CHF values of 0.591 MW/m^2 and 0.469 MW/m^2 were reported. When comparing with other angles, the downward-facing CHF values were the lowest ones reported. They concluded that heater size had an impact on CHF, since it would be more difficult for bubbles to escape from a larger heated surface.

Investigation of gap cooling was performed by Noh and Suh (2014) in which pool boiling experiments were conducted at different angles. Gap sizes of 1, 2, 5, and 10 mm were applied for one of the experiments. For the gap experiments, they stated that the bubbles are able to escape from the gap if their size is large than the size of the gap. A comparison of the gap sizes with no gap condition (open heated surface) resulted in higher CHF values for the latter.

Other studies that have also included downward-facing boiling are those that use hemispherical geometry. Such experiments try to investigate the boiling phenomenon on the exterior of a RPV surface. Some of those studies, along with the ones mentioned in this section are summarized in Table 4-1.

A flow boiling experiment focusing on CHF at different orientations was conducted by Zhang et al. (2002a, 2002b). Experiments were performed in a small 5 mm x 2.5 mm cross-section channel with different velocities and saturated FC-72 as the working fluid. Their results showed that for the downward-facing position, CHF increased as the velocity was increased. The downward-facing position showed the lowest CHF value even at the highest flow rate of 1.5 m/s.

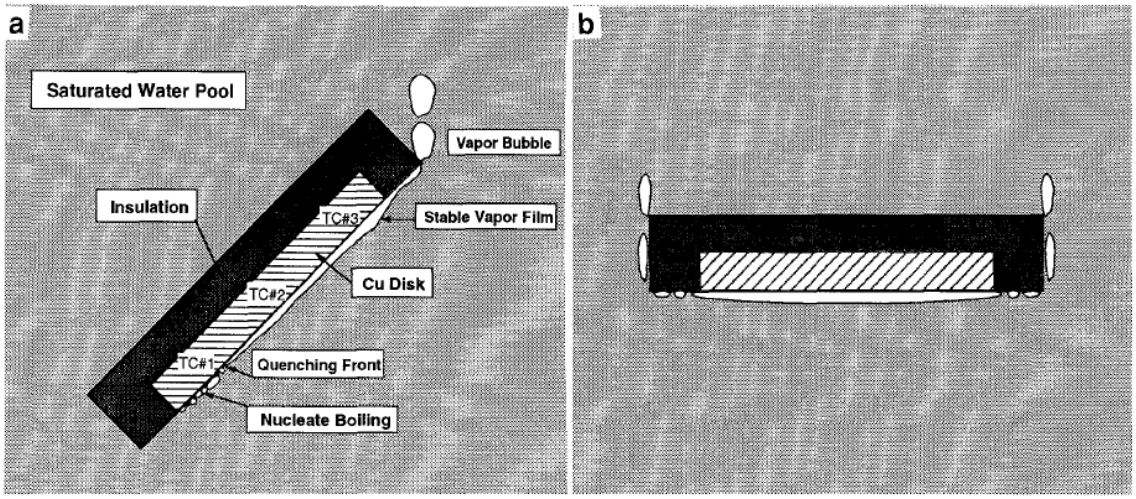

Figure 4-3: Illustration from El-Genk and Guo (1993) showing boiling for different orientation: a) inclined surface, b) downward-facing surface.

Table 4-1: Summary of some downward-facing pool boiling experiments found in literature.

INVESTIGATOR	**ORIENTATION**	**CHF (downward-facing)**
El-Genk and Guo (1993)	0° to 90°	0.25 MW/m^2
Yang et al. (1997)	-90° to -40°	0.776 & 0.504 MW/m^2
	-90° to 90°	0.591 & 0.469 MW/m^2
Noh and Suh (2014)	90° to 180°	0.95 MW/m^2 (no gap)
Theofaneous and Syri (1997)	-30° to 30°	0.35 MW/m^2 (≈4°)
Cheung et al. (1997)	Hemisphere (quench)	0.40 MW/m^2
Yang et al. (2005)	Hemisphere (steady-state)	0.40 MW/m^2
	Hemisphere (quench)	0.45 MW/m^2

5. DOWNWARD-FACING SUBCOOLED FLOW BOILING WITH BARE AND FINNED SURFACES

In this chapter, the experiments performed at highly subcooled conditions will be explained in detail. A small scale experiment was performed to study the heat transfer effect from a finned surface in downward-facing subcooled flow boiling.

5.1 Experimental Loop

The experimental loop used in the subcooled experiments was not designed specifically for the current study. It was originally designed for flow visualization studies. One benefit of the loop was it allowed for a new test section to be replaced with the older one in the long acrylic flow channel. Figure 5-1 shows an illustration of the current experimental loop. Each part of the flow loop will be explained in the following subsections.

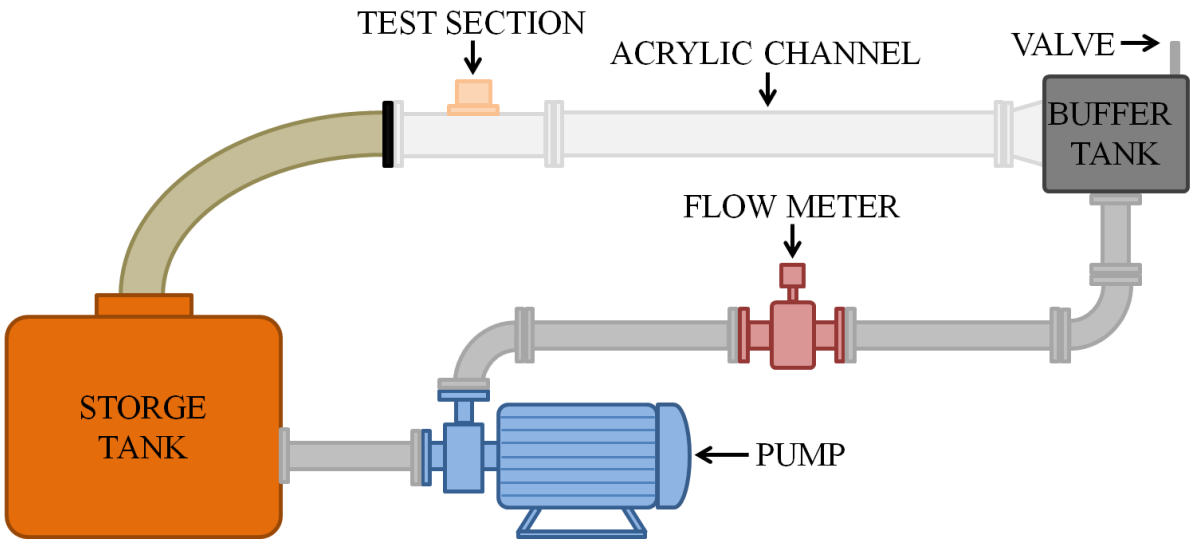

Figure 5-1: Schematic of the overall flow loop used in the subcooled experiments.

5.1.1 Storage Tank

The storage tank (Fig. 5-2) was simply a normal tank that contained the water required for the subcooled experiments. The maximum capacity of the tank was labeled at 300 Liters. The upper portion of the tank was open to the laboratory environment. After performing many experiments, it was necessary to replace the water inside the tank. A drain was located on the one of the shorter sides of the tank in order to replace older water with fresh water. Holes were created on one of the longer sides of the tank to attach piping leading to the pumps.

Figure 5-2: Image of water storage tank shown with the drain and pump connection.

5.1.2 Pumps

Two magnetic pumps (Fig. 5-3) were arranged in parallel to provide powerful flow conditions. Both pumps were manufactured by Iwaki Co., Ltd. (Japan). Both pumps employed a three phase induction motor (manufactured by Hitachi). The specifications of each pump was slightly different (Table 5-1), one pump more powerful than the other. The current experiments did not

require very high velocities, so only one of the pumps was operated during the experiments. Both pumps were separately connected to a power box. Each pump was controlled and operated individually by separate control boxes (Fig. 5-4).

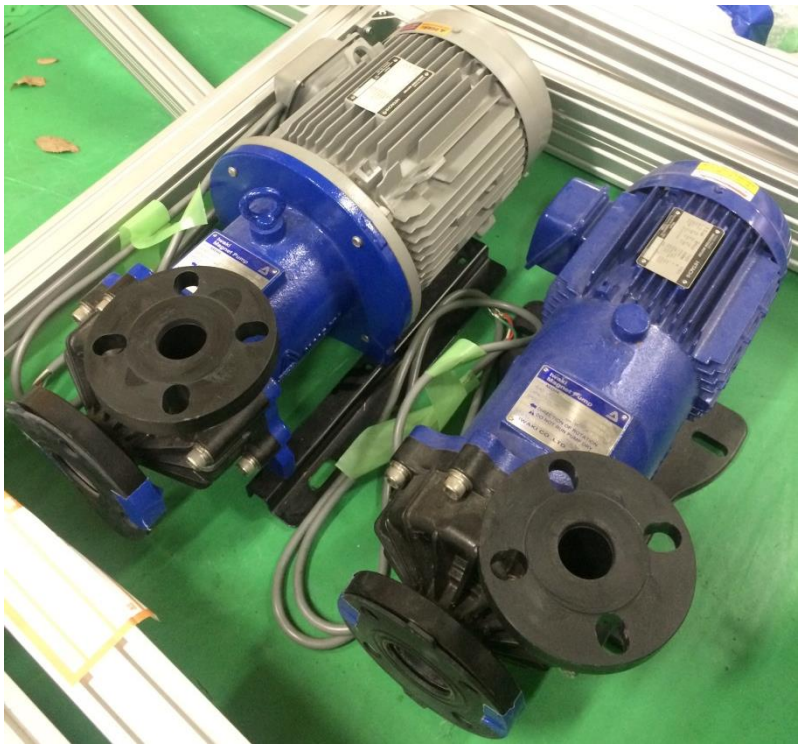

Figure 5-3: Image of the magnetic pumps used in subcooled experiments.

Table 5-1: Specifications of the magnetic pumps used in the experiments.

MODEL NO.	MDH-425CV6C-D	MDH-422CV5-D
MOTOR POWER	3.7 kW	1.5 kW
SPEED	3500 RPM	2900 RPM
HEAD	26.5 m	18 m
CAPACITY	400 L/min	200 L/min

Figure 5-4: Individual controllers for each pump (not connected to pump when image taken).

5.1.3 Pipes/Tube Connections in Flow Loop

All pipe connections were made with PVC pipes to connect the different components in the flow loop. The pipe connections included: 1) storage tank to pumps, 2) pumps to flow meter, and 3) flow meter to buffer tank. All accompanying flanges were also PVC material. Gaskets were inserted between interconnected parts to prevent water leakage. A large, flexible tube was connected at the exit of the acrylic channel to return water back into the storage tank. A portion of the PVC piping connecting the pumps and the flow meter is shown in Fig. 5-5.

Figure 5-5: A portion of PVC piping in the loop.

5.1.4 Flow Meter

An electromagnetic flow meter (Fig. 5-6) was placed after the two magnetic pumps in the flow loop to measure the flow rate during the experiments. The volumetric flow rates were displayed on the flow meter screen, and were monitored visually. No connections were available on the flow meter to record flow rate measurements through a Data Acquisition (DAQ) system. Table 5-2 summarizes the specifications for the flow meter.

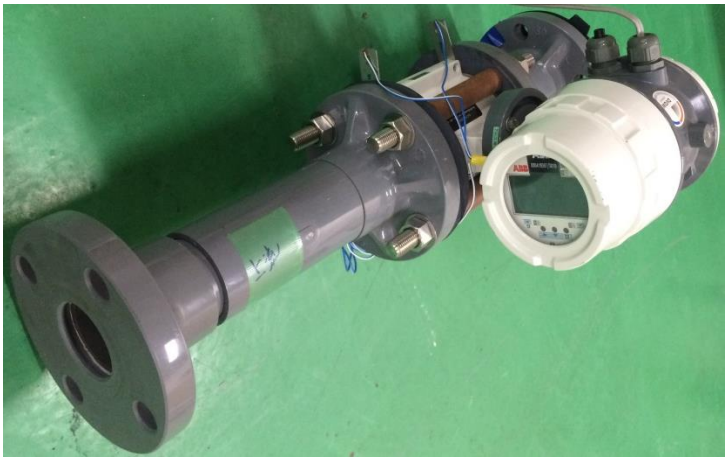

Figure 5-6: Image of electromagnetic flow meter used in experimental loop.

Table 5-2: Specifications of electromagnetic flow meter.

MODEL NO.	DE43W
ACCURACY	0.5 % of full scale
FLOW RANGE	20-400 L/min
FLUID TEMP. RANGE	-25 – 130°C

5.1.5 Upstream Buffer Tank

The upstream buffer tank was smaller in size than the water storage tank, and was manufactured with stainless steel (Fig. 5-7). The flow entered from the bottom of the tank and exited from

the front (left image in Fig. 5-7). Two valves on the top allowed for air to escape when filling the tank with water. One valve was fitted with a tube in case some water also was released along with air. The tube exit was placed back into the storage tank. The valves were closed once the air had escaped from the buffer tank. Inside the tank, a funneling design was created to smoothly allow water to flow into the acrylic channel (right image in Fig. 5-7).

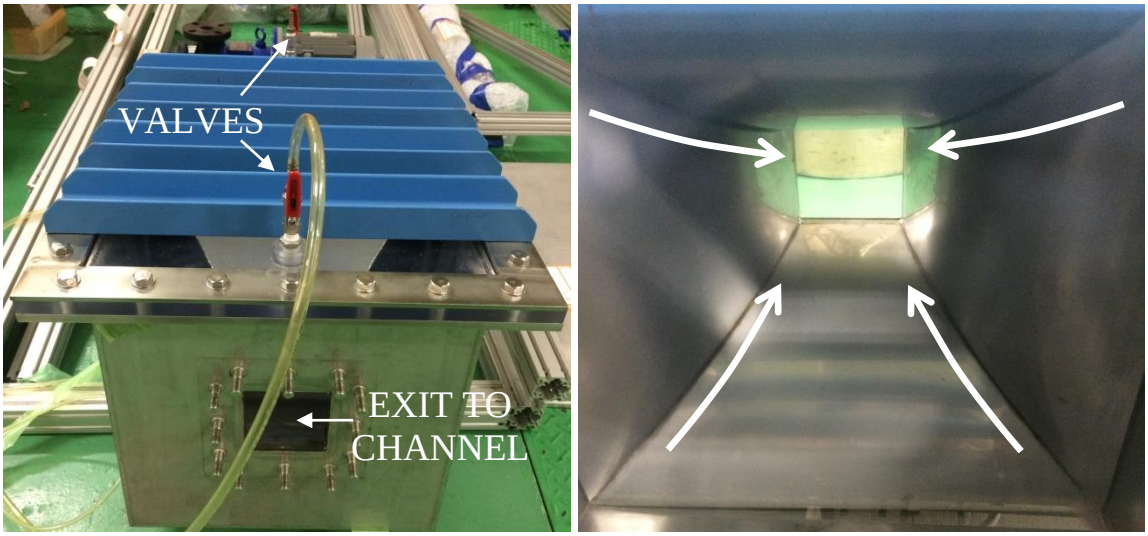

Figure 5-7: Upstream water buffer tank (left) and funneling design inside tank (right).

5.1.6 Acrylic Channel

The channel consisted of two parts (Fig. 5-8): the longer portion attached to the buffer tank and the shorter portion which contained the test section. All parts of the channel were manufactured from acrylic. The longer portion had a total length of 100 cm, which included 2 cm thick flanges. The shorter portion of the channel had a total length of 53 cm with 1.5 cm thick flanges. The sides of the channel for both portions were 1 cm in thickness. Both portions also had the same square cross-section of 5 cm x 5 cm inside the channel. The shorter portion of the channel was designed to fit the test section. Thus, the top of the channel was modified to do so. The CAD design of the shorter portion is shown in Fig. 5-9.

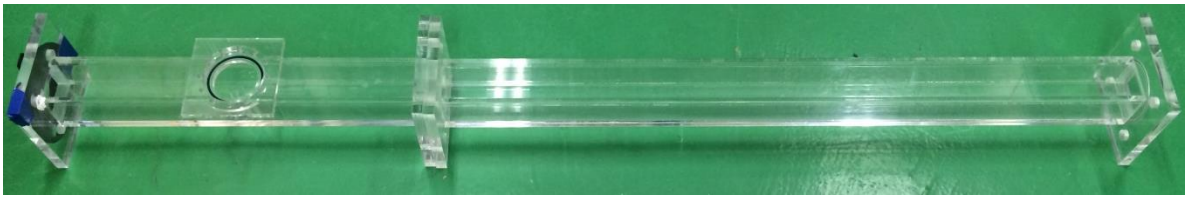

Figure 5-8: Longer portion (right) & shorter portion (left) of acrylic channel.

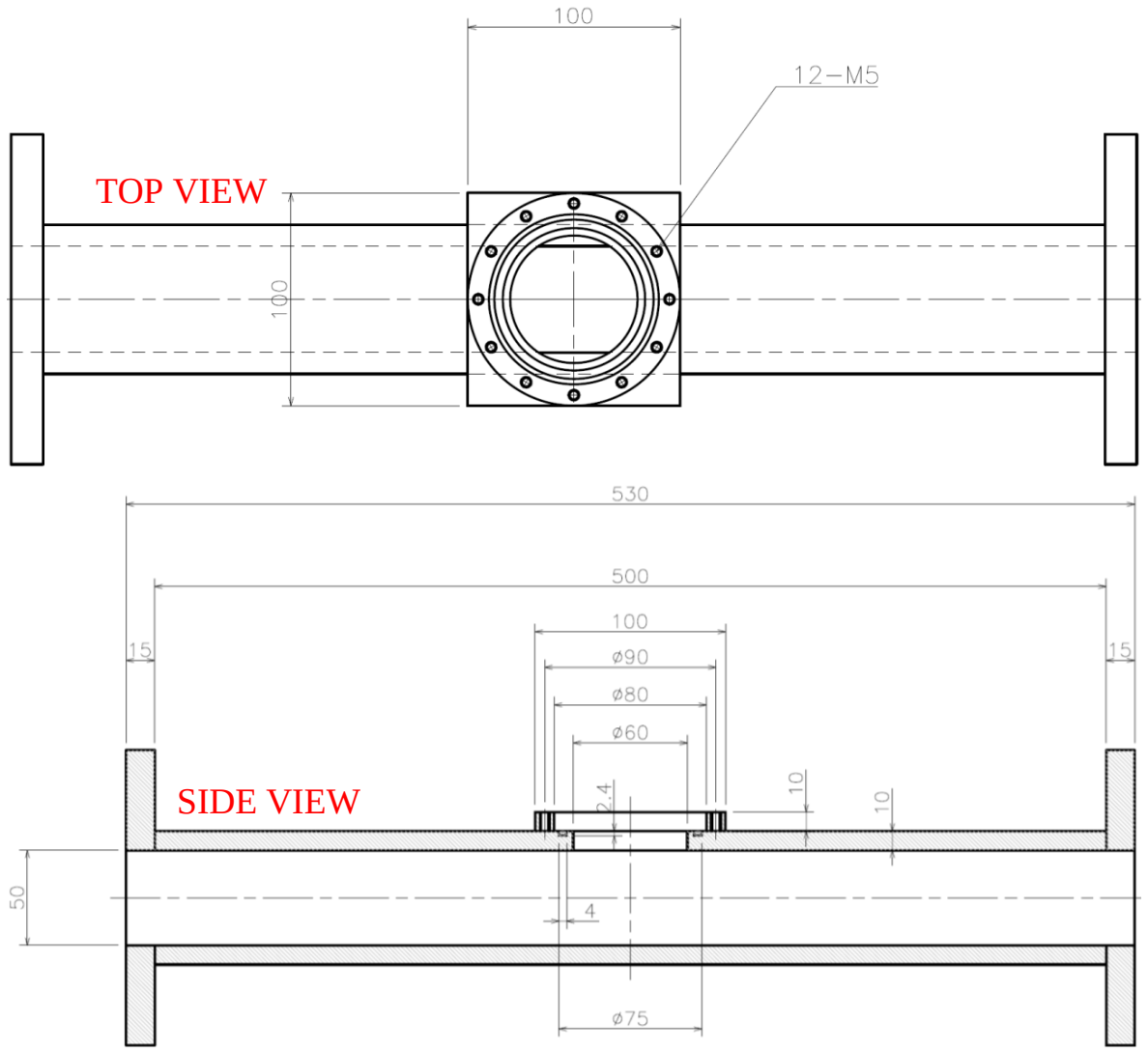

Figure 5-9: CAD drawing of shorter portion of channel (dimensions in mm).

5.1.7 Test Section

The test section placed in the acrylic channel comprised of a copper block and the insulation. Copper was chosen as the heating material applied in the experiments due to its excellent thermal conductivity. Two cylindrical copper blocks (Figs. 5-10 to 5-12), separately used in the experiments, had similar designs except for the boiling surface. One block was designed with a bare (flat) surface and the other with a pin fin on the surface. It was essential to compare results from the two surfaces to observe the heat transfer effect by the pin fin. The full height of the copper blocks was 60 mm. The top portion of the blocks was 40 mm in diameter, with the bottom portion (boiling surface) narrowed down to a diameter of 20 mm. The fin, with a diameter of 4 mm and a length of 10 mm, was centered on the 20 mm diameter boiling surface.

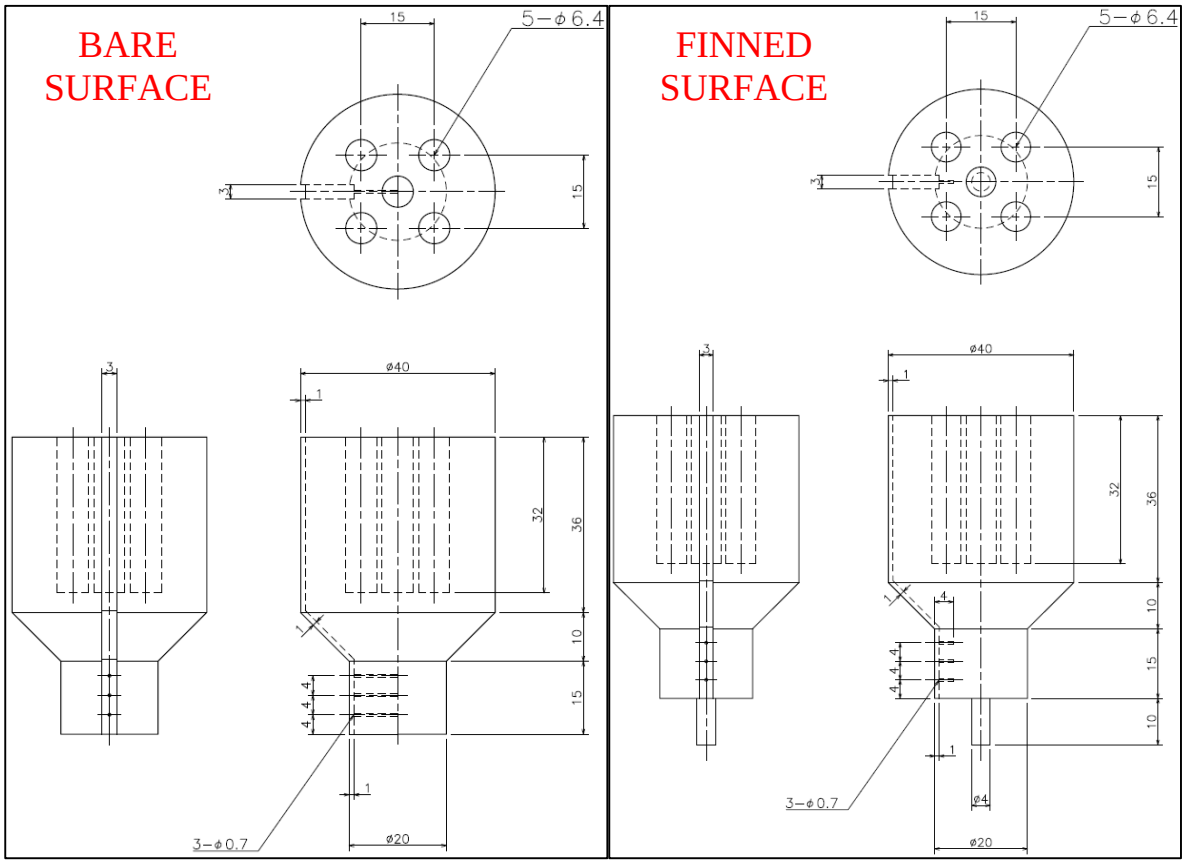

Figure 5-10: CAD drawings of bare and finned copper blocks (dimensions in mm).

PEEK (polyether ether ketone) was chosen for its low thermal conductivity as the insulation material for both copper blocks. The insulation surrounds the blocks mainly on the sides to reduce heat loss. During the placement of the copper block inside the PEEK, silicone was applied (in the lower 15 mm height portion of copper block) in between the two materials to prevent water leakage (Fig. 5-11). Table 5-3 lists some typical properties of copper and PEEK materials. Figure 5-13 shows the test section fitted into the channel.

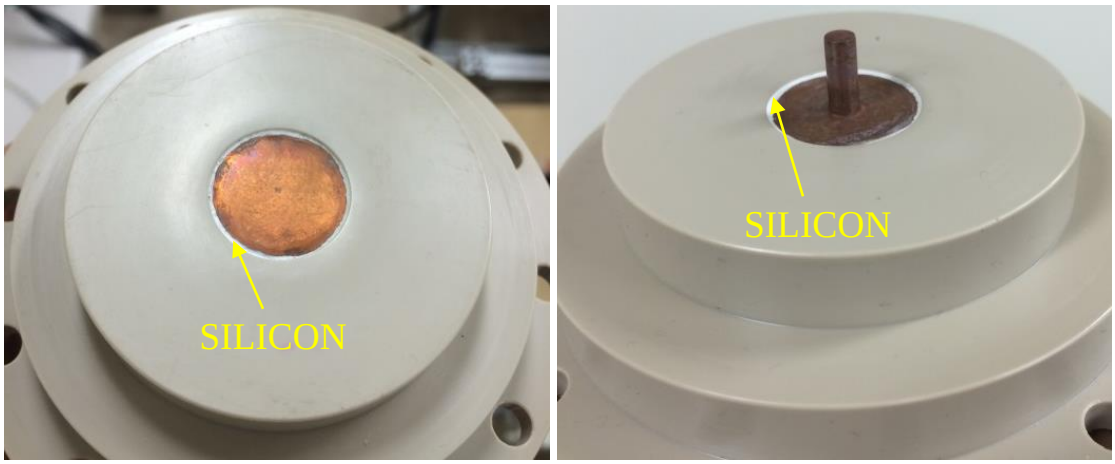

Figure 5-11: Bare (left) and finned (right) copper blocks inside PEEK.

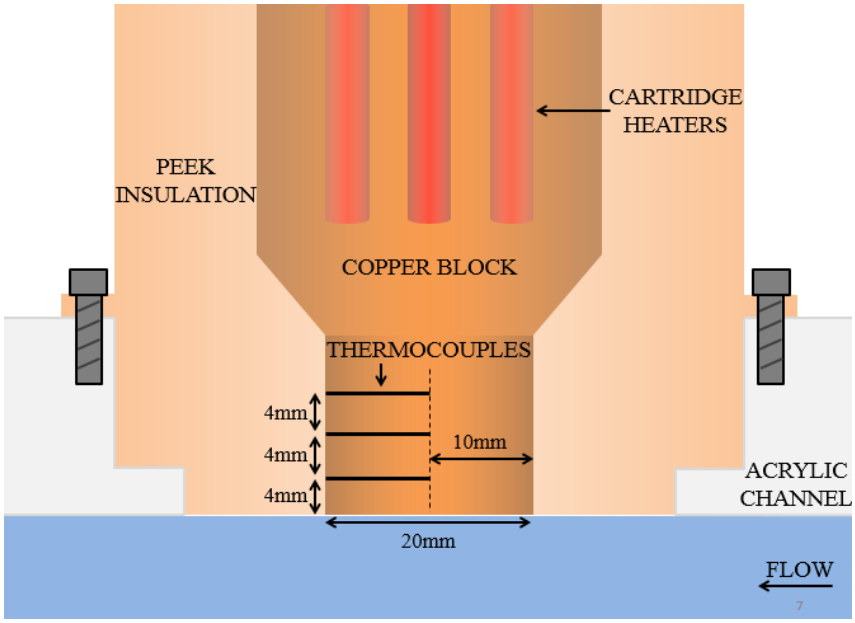

Figure 5-12: Mid-section schematic of bare surface copper block test section.

Table 5-3: Typical properties of copper[1] and PEEK[2] at room temperature.

	COPPER	PEEK
DENSITY	8940 kg/m^3	1260-1320 kg/m^3
THERMAL CONDUCTIVITY	391 W/m-K	0.25 W/m-K
SPECIFIC HEAT	385 J/kg-K	1340 J/kg-K
MAX. OPERATING TEMP	–	250 °C

[1,2] See Reference section.

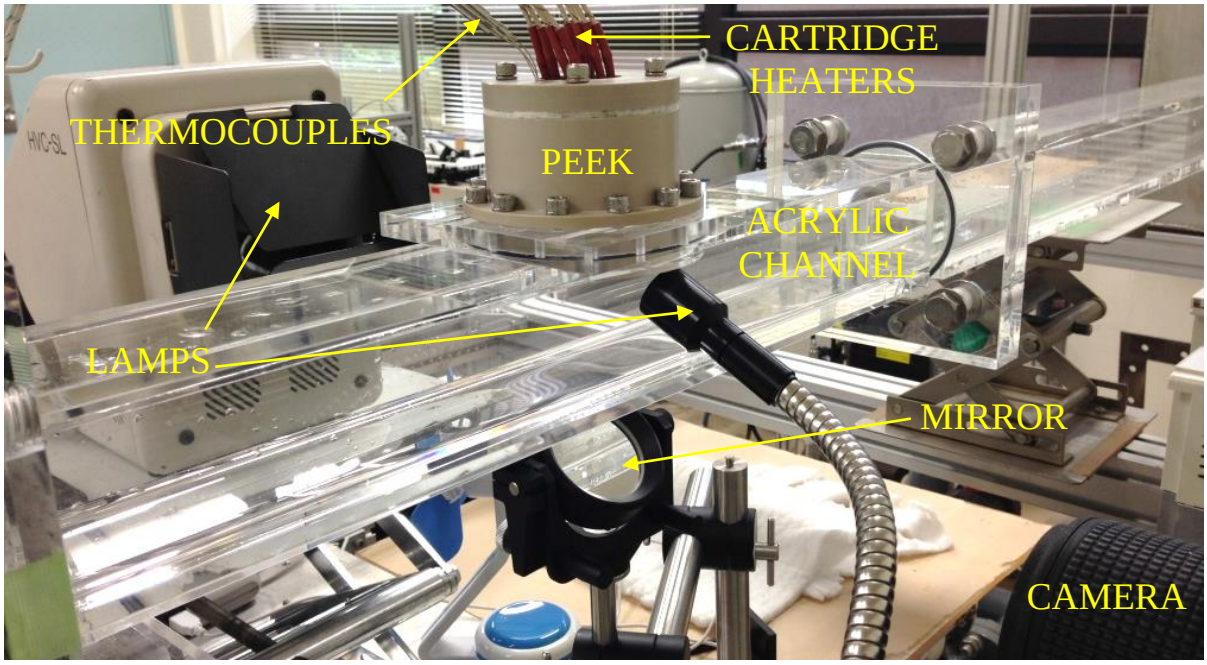

Figure 5-13: Test section placed in shorter portion of acrylic channel during experiments.

5.1.8 Cartridge Heaters

Cartridge heaters were used to apply heat in the copper blocks. Five 200V Watlow Firerod cartridge heaters, each heater rated at 225W, were inserted in the top portion of the copper blocks (Figs. 5-10 and 5-12).The heater diameter and length were 6.25 mm and 31.8 mm, respectively. The electrical leads of the cartridge heaters were connected to a slidac (variable

transformer), which was directly connected to the main power box. The voltage levels ranged from 0-240V on the slidac.

5.1.9 Temperature Measurement

In order to obtain temperature data required for surface temperature and heat flux calculations, 0.5 mm diameter K-type thermocouples were inserted in the lower region of the copper blocks (Fig. 5-10 and 5-12). The measurement uncertainty for the thermocouples was ± 0.75% of the measured temperature. The thermocouple distance was set at a height of 4 mm from the boiling surface for both copper blocks. The same height was kept between consecutive thermocouples. Three thermocouples measured the temperatures in the center of the bare copper block. The location of the pin-fin would not allow for the calculation of the surface temperature and heat flux in the center of the block. As a result, the thermocouples were kept at a location of 4 mm from the outer edge of the cylindrical region of the block (close to PEEK in Fig. 5-12). The distance was chosen based on simple simulations performed with ANSYS software. The purpose of the simulations was to obtain the location at which the temperature inside the copper block would be undisturbed and allow for proper calculations without the effects of the fin. The combination of boiling heat transfer and flow around the fin resulted in the measurement of upstream and downstream temperatures for such type of geometry. Therefore, three thermocouples were inserted before (upstream) and an additional three thermocouples were inserted after (downstream) the fin. The two-sided thermocouple design is not shown in Fig. 5-10. Grooves were manufactured on inside of the PEEK to provide sufficient space between the copper block and PEEK. The grooves allowed the thermocouples to exit the top of the test section.

5.1.10 Experiment Visualization

Visualization of both block types was performed mainly for qualitative analysis of the boiling process from below the channel (Fig. 5-13). The visualization during the experiments was performed by a Photron SA5 camera. Only the 200 mm lens attached to the camera is shown in Fig. 5-13. The boiling surface was illuminated from the sides by two halogen lamps. The

resolution and frame rate were 1024 pixels x 1024 pixels and 1000 frames per second, respectively.

5.1.11 Experimental Conditions

The experimental conditions are summarized in Table 5-4, along with a comparison of ULPU experiments and postulated accident conditions for the BWR. The water temperature and pressure for the subcooled experiments were room temperature and atmospheric pressure, respectively. The experiments were performed at different flow rates. Equivalent values of the flow rates are presented in Table 5-5. The highest flow rate was initially applied, but was reduced in order to reach CHF conditions. CHF was observed only for the lowest flow rate. Note that in the BWR case, a channel size cannot be applied because the boiling would occur on the open vessel surface. BWR insulation is not similar to that of the PWR, where a gap is created between the vessel surface and the insulation. Also, the flow conditions for the BWR accident scenario are unknown since no large-scale or full-scale experiments have been performed for the BWR lower head with CRGT penetrations.

Table 5-4: Conditions of subcooled experiments vs accident conditions.

	Subcooled Experiment	**ULPU(Conf. V)***	**BWR SA Scenario**
Fluid Temperature	≈20°C	≈90-100°C	≈90-100°C
Fluid Pressure	Atmospheric	> Atmospheric	> Atmospheric
Boiling Surface	Downward facing: Bare & Fin	Curved (0-90°), 3 Blocks	Curved (Hemisphere)
Surface Size	Bare & Fin: 20mm dia. Fin: D=4mm, L=10mm	W=152mm, L≈2500mm	Lower Head with CRGT Penetrations
Channel Size	50mm x 50mm	152mm x 76mm	Not Applicable
Reynolds No.	See Table 5-5	2.56×10^5	Unknown

* From Dinh et al. (2003).

Table 5-5: Equivalent flow rates for the subcooled experiments.

Volumetric Flow	Mass Flux	Reynolds No.*	Velocity
37 L/min	244 kg/m^2-s	3.02x10^4	0.24 m/s
33 L/min	215 kg/m^2-s	2.68x10^4	0.22 m/s
27 L/min	177 kg/m^2-s	2.14x10^4	0.18 m/s

* Based on hydraulic diameter.

5.2 Experimental Procedure

5.2.1 Boiling Surface Preparation

Prior to performing the experiment, the boiling surface of each block type was polished. From trial experiments, heavy damage to the surface was observed when the boiling surface was subjected to continuous experiments without polishing (Fig. 5-14). It was necessary to polish the surface since only one copper block was available for each type of surface. Without polishing the surface, the surface conditions may have led to incorrect temperature and heat flux calculations due to a change in the surface characteristics. Both boiling surfaces (including fin itself) were polished with fine (P1200) sandpaper.

The following summarize the preparation for the boiling surface:

1) Remove previously applied silicone on surface.
2) Apply new silicone on the boundary of boiling surface, ensuring to cover the gap between the edge of the copper boiling surface and the edge of PEEK.
3) Remove excess silicone inadvertently applied on the boiling surface and PEEK.
4) Apply lubricating oil on the boiling surface.
5) Cut a small portion of the P1200 sandpaper (required for polishing the surface).
6) Polish boiling surface (and fin) completely.
7) Wipe off excess oil and surface products (from polishing).
8) Clean surface with alcohol (ethanol/acetone).

9) Fit test section back onto acrylic channel for experiments.

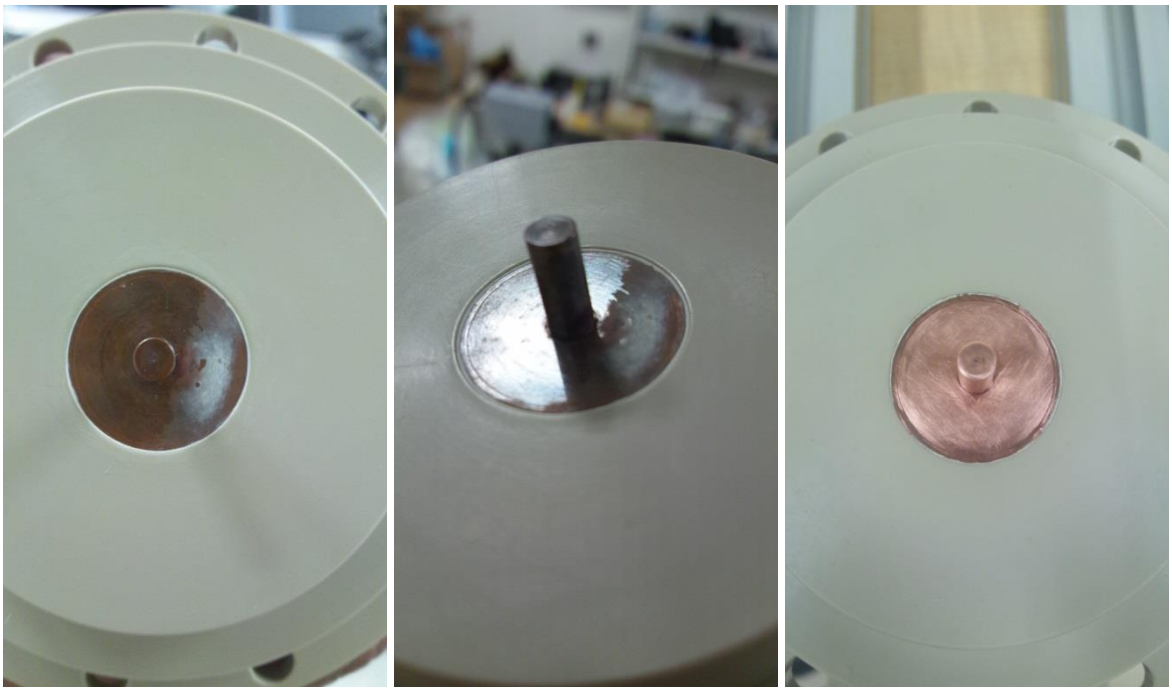

Figure 5-14: Surface damaged after continuous use of finned copper block (left and middle image). Surface is clean after polishing (right image).

5.2.2 General Experiment Procedure

Once the test section was placed and secured in the channel, the main power box was turned on to supply all the equipment with power. Afterwards, the pumps were started to circulate and fill the entire loop with water. During this process the valves on the buffer tank were left open to allow the air inside to escape while the water filled the tank. The valves were closed when the buffer tank was filled.

When the flow loop was completely filled with water, the desired flow rate was set by controlling the pump speed with the pump controllers. A waiting time of approximately a few minutes was required after setting the flow rate. The experiments began once steady flow conditions were achieved.

The power supplied to the cartridge heaters was adjusted using a slidac. The voltage on the slidac ranged from 0 to 240V, with 240V providing maximum power to the heaters. From test experiments performed earlier, a range of 120V to 220V was adequate for both copper blocks. Due to the possibility of damaging the insulation, maximum power was not applied.

The first voltage level applied was 120V, and the following levels were incremented in intervals of 10V until 220V. When the desired voltage was applied, steady state temperatures were measured before proceeding to the next voltage level. The video observations of the boiling phenomenon were performed during this period. The power was increased to the next voltage level, steady state temperatures were reached, and the power was increased again. This process continued until the final voltage level. All experiments were repeated twice for repeatability purposes, and the averaged results are presented. Figure 5-15 shows an example of a temperature profile for one of the bare experiments.

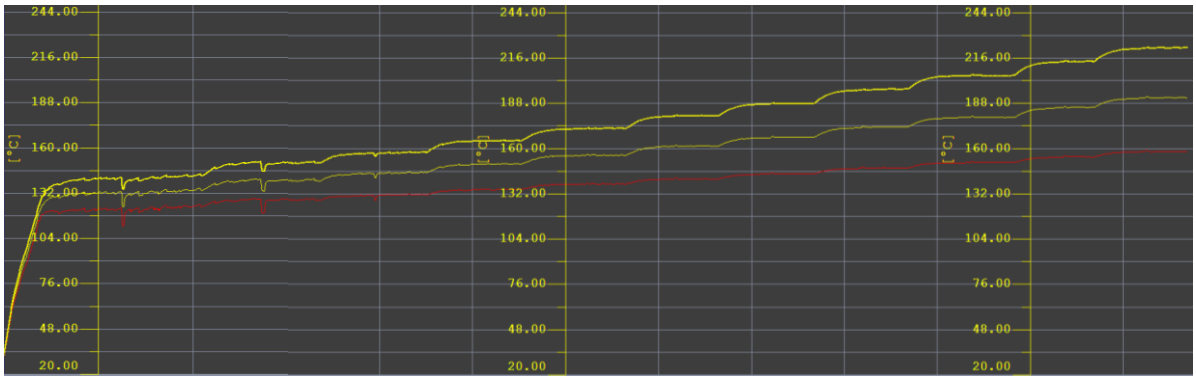

Figure 5-15: Typical temperature profile during experiments (vertical division: 5 minutes).

The shutdown procedure started after the measurements finished at the last voltage level. The voltage level was brought back down to zero after completion of the experiments. The pumps were stopped when the copper block had cooled down to room temperature. The valves on the buffer tank were opened in order to drain the flow loop. At the end of the experiments all the water in the loop had accumulated in the water storage tank. Although all electrical equipment had been turned off, the main power box was turned off for additional safety.

The above conditions were slightly different for the lowest flow rate case (177 kg/m^2-s). CHF conditions occurred due to the reduced flow conditions. The voltage level at which CHF occurred was lower compared to the voltage levels of the other experiments. As shown in Fig. 5-16, the temperatures increased rapidly at CHF. At that point the voltage was suddenly turned to 0V and the flow rate was increased quickly to reduce the surface temperatures. This was done to prevent any damage to the components of the test section, specifically the PEEK insulation. The maximum operating temperature of PEEK was approximately 250°C (Table 5-3), and temperatures exceeding that value may damage the material.

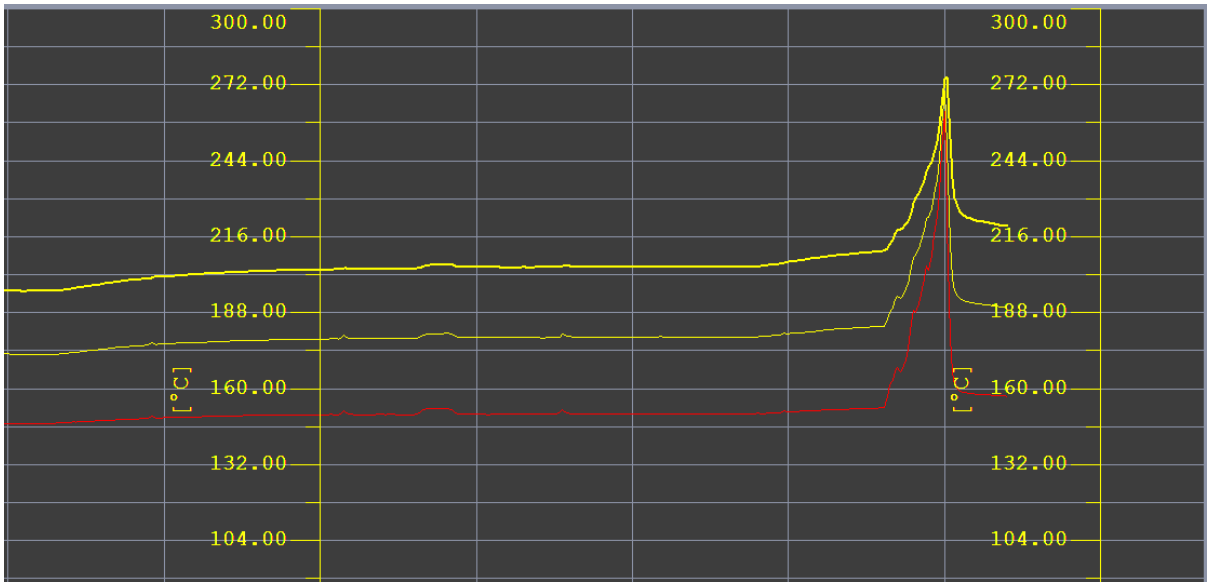

Figure 5-16: Rapid temperature rise at CHF for 177 kg/m^2-s (vertical division: 1 minute).

5.3 Data Post-processing

The thermocouples provided the temperature data required for the surface temperature and heat flux calculations. Steady state temperature data obtained after voltage adjustment was used to calculate the average temperature at each thermocouple location. The time-averaged temperature at each of the three thermocouple locations (six locations for finned surface) was calculated for the different power levels. The top and bottom thermocouple data is used for the surface temperature and heat flux calculations. The central (middle) thermocouple was used to verify the linearity of the data for heat flux calculations. The process of surface temperature

extrapolation is illustrated in Fig. 5-17 with data from the experiment. The top and bottom thermocouple data provide two values, which are then used to extrapolate the surface temperature. Using the general extrapolation formula,

$$\frac{T_{TOP} - T_{BOT}}{h_{TOP} - h_{BOT}} = \frac{T_{BOT} - T_S}{h_{BOT} - 0mm} \tag{5-1}$$

where

T_S = extrapolated surface temperature [°C]

T_{TOP} = temperature of the thermocouple farthest from the boiling surface [°C]

T_{BOT} = temperature of the thermocouple closest to the boiling surface [°C]

h_{TOP} = distance of top thermocouple from the boiling surface [m]

h_{BOT} = distance of bottom thermocouple from the boiling surface [m]

Rearranging equation (5-1) and inserting the heights, the surface temperature is given by

$$T_S = T_{BOT} + \frac{1}{2}(T_{BOT} - T_{TOP}) \tag{5-2}$$

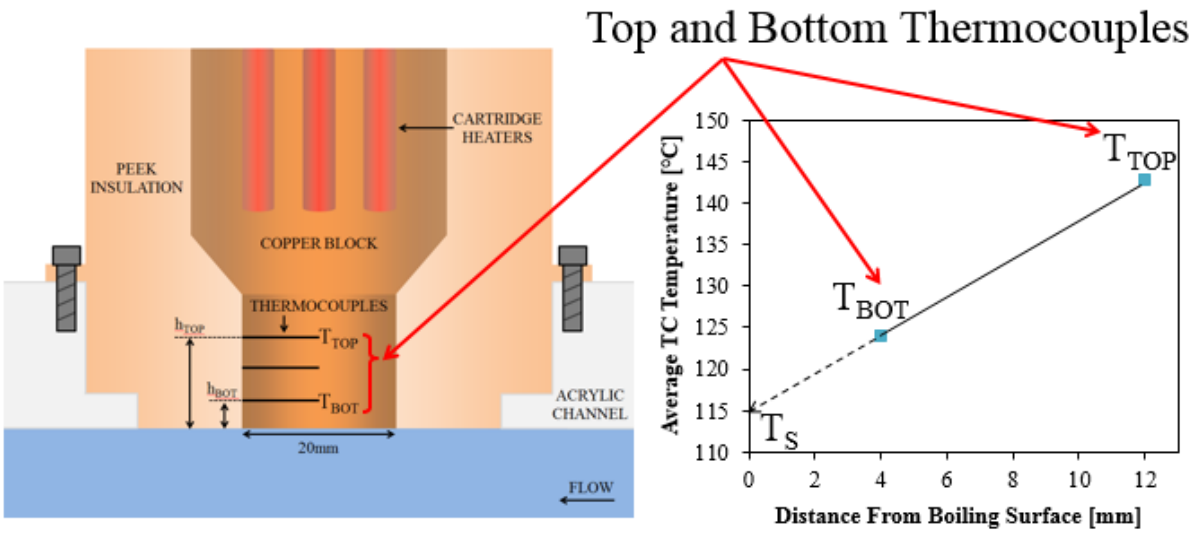

Figure 5-17: Illustration of surface temperature extrapolation.

The average temperatures were also used to calculate the surface heat flux. One-dimensional steady state heat conduction is assumed to be the main mechanism of heat transfer to the boiling surface. The assumption was confirmed by the linear temperature profile of the thermocouple data at the three different locations. Therefore, an approximate average surface heat flux can be estimated by the temperature data from T_{TOP} to T_{BOT}. The surface heat flux was calculated as

$$q'' = k\frac{\Delta T}{\Delta h} = k\frac{T_{TOP} - T_{BOT}}{h_{TOP} - h_{BOT}} \tag{5-3}$$

where

q'' = surface heat flux [MW/m^2]

k = thermal conductivity of copper [W/m-K]

Δh = distance between T_{TOP} and T_{BOT} [m]

The surface temperature and heat flux for the different voltages were used to create boiling curves for the two different types of blocks. It should be clarified that the surface temperature and heat flux are local estimations.

As a comparison the extrapolation method was compared to the least squares method, which uses all three thermocouple data. The extrapolated temperatures and simplified heat flux are shown above in equations (5-2) and (5-3), respectively. The least squares methods provides the equation for the line of best fit using the three thermocouple data, from which the surface temperature can be obtained. The heat flux can be calculated by multiplying the thermal conductivity (k) with the slope (dT/dh) of the least squares equation. The comparison of both methods is shown in Fig. 5-18 for 215 kg/m^2-s bare surface case. As the figure shows both methods show quite similar results. The average relative errors between the two methods for the surface temperatures and heat flux are approximately 0.25 % and 3.44x10^{-3} %, respectively. Similarly, the upstream location average errors for the temperatures and heat flux of the finned surface are approximately 0.98 % and 4.80x10^{-4} %, respectively. The downstream location average errors for the temperatures and heat flux of the finned surface are approximately 2.02 % and 6.27x10^{-4} %, respectively. Since both methods show approximately similar heat flux and a relatively small difference exists between the temperatures, as a simplification the extrapolation method was used for the data analysis.

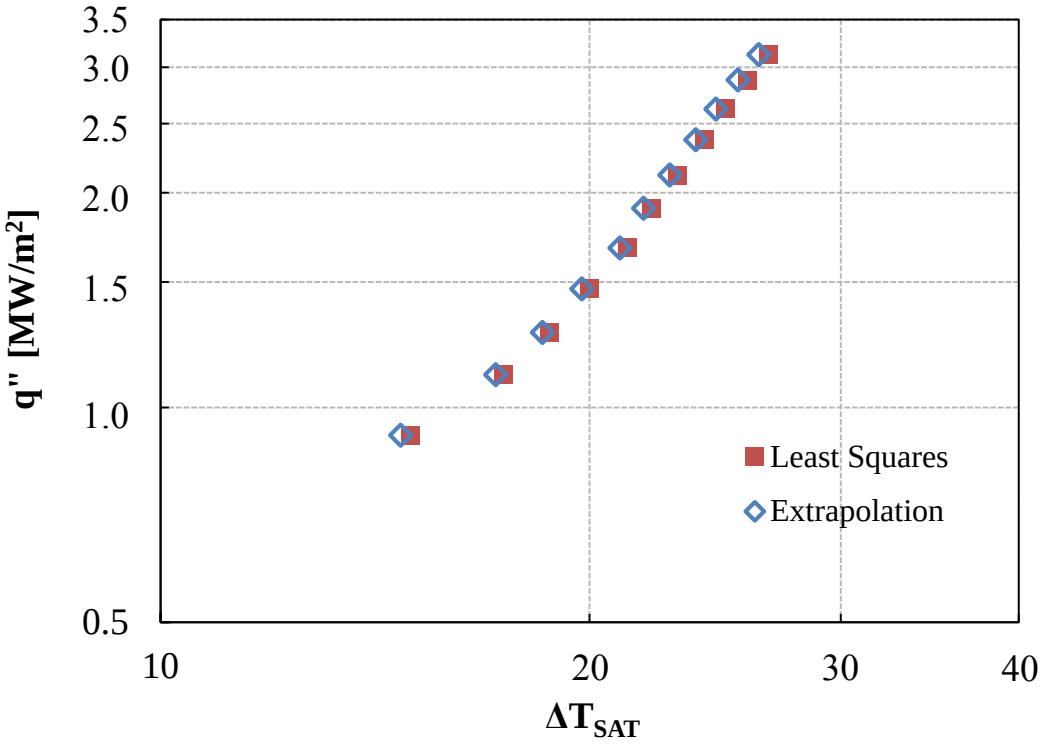

Figure 5-18: Difference in bare surface analysis between different methods for 215 kg/m^2-s.

A simple calculation for the local heat transfer coefficient was performed by considering an energy balance at the boiling surface. The heat flux conducted through the copper block is removed by convection on the surface. As a result, the local heat flux by conduction to the boiling surface equals the local heat flux by convection. The heat flux by conduction is given by equation (5-3). The heat flux by convection is calculated by Newton's law of cooling,

$$q''_{conv} = h\,\Delta T = h\,(T_S - T_{film}) \tag{5-4}$$

where

q''_{conv} = heat flux by convection on boiling surface [MW/m^2]

h = heat transfer coefficient [W/m^2-K]

T_{film} = average temperature between T_S and the bulk water temperature [°C]

Rearranging equation (5-4) while setting the equivalent heat flux at the surface, the local experimental heat transfer coefficient (h_{exp}) was calculated as

$$h_{exp} = \frac{q''}{(T_S - T_{film})} \tag{5-5}$$

Again, the heat transfer coefficient in equation (5-5) is a local value and should not be taken as the overall heat transfer coefficient.

5.4 Bare Surface Results

The results of the bare surface will be presented first, since the bare surface is the reference case to which a comparison will be made for the finned surface. Again, three mass flux were applied in the experiments: 177 kg/m^2-s, 215 kg/m^2-s, and 244 kg/m^2-s. For convenience, the mass flux from hereon will be referred to as low, medium, and high flow rates, respectively. The emphasis of the results is on the higher heat flux values. Of the three flow rates mentioned above, CHF was observed only for the low flow rate. Due to reducing the flow rate, CHF occurred at a lower heat flux in the low flow rate experiment compared to the medium and high flow rates. Therefore, fewer data is presented. The highest heat flux data point was calculated before CHF had occurred. At CHF the boiling surface was completely covered by a large bubble (Fig. 5-19), which caused elevated temperatures (Fig. 5-16).

The boiling curves obtained for the bare surface experiments are shown in Fig. 5-20. The high and medium flow rates show similarity in data, with small differences in the excess heat (ΔT_{SAT}) and heat flux. The low flow rate case shows slightly reduced surface temperatures compared to the high and medium flow rates. The figure shows that all three flow rates present typical boiling curve trends. Even though the experiments were performed at subcooled conditions, the excess heat is plotted in the boiling curves. The liquid temperature must reach saturation for boiling to occur. Thus, saturated liquid must be present. It was assumed that while the bulk fluid was at room temperature conditions, the liquid very near to the boiling surface had reached saturated conditions to cause bubble generation.

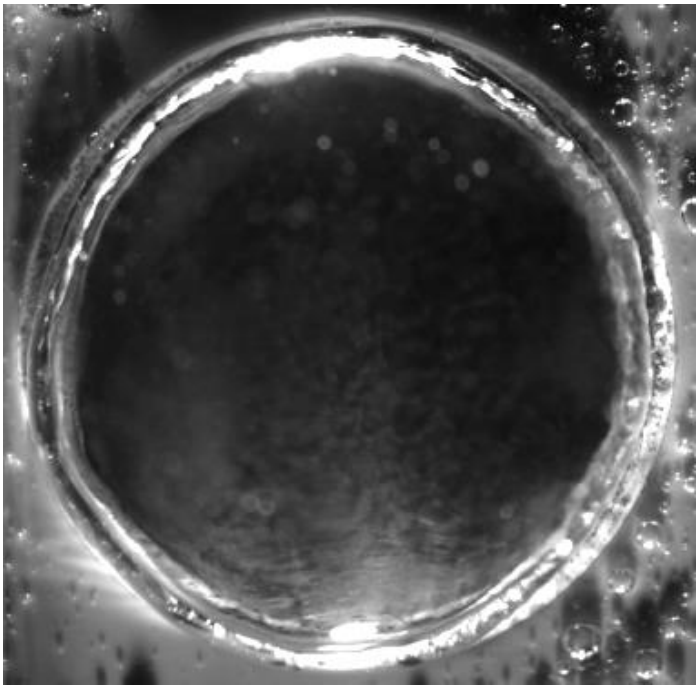

Figure 5-19: Bubble covering entire boiling surface at CHF for 177 kg/m^2-s case.

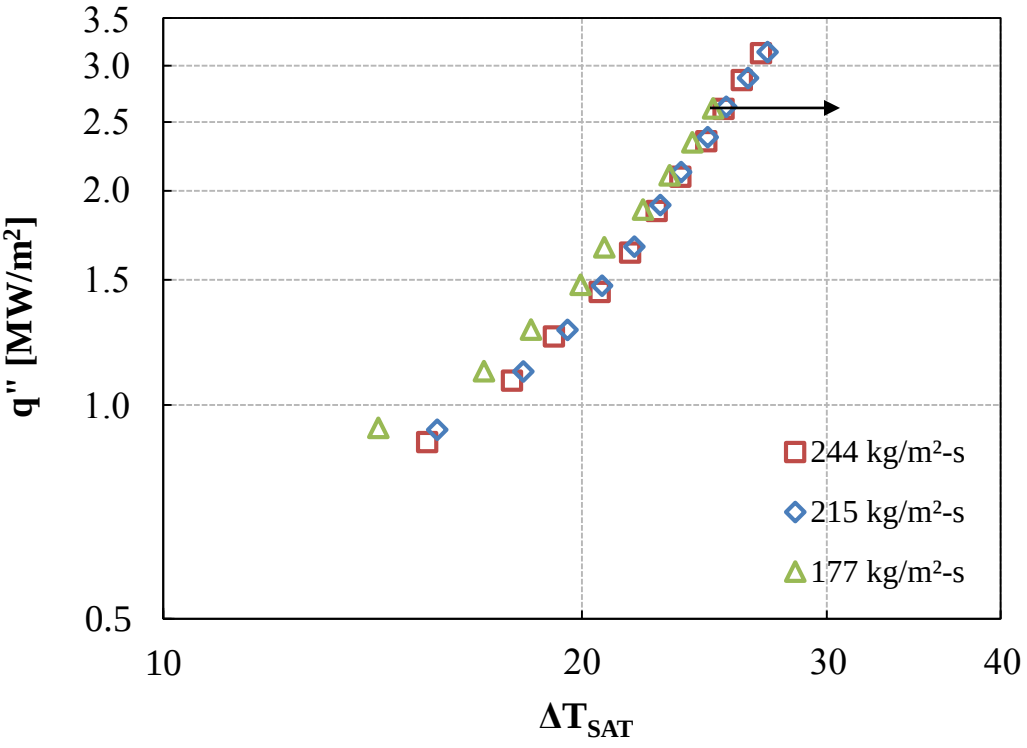

Figure 5-20: Boiling curves for the bare surface at high, medium, and low flow rates.

Visualization performed from the bottom of the channel looking upward at the bare boiling surface is shown in Figs. 5-21 to 5-23 for the high, medium, and low flow rates, respectively. An interesting observation occurred at CHF. A transition from the nucleate boiling to film boiling occurs by oscillation of a large bubble, which eventually covered the entire surface. The large bubble that covered the surface in Fig. 5-19 began downstream (left side of image). As the boiling added more vapor to the large bubble, the volume of the bubble increased and the bubble front traveled towards the upstream direction. Once it initially covered the surface, it was pushed back. This may occur due to the volume being insufficient to remain on the surface as the inertia of the flow pushes the bubble front towards downstream. When the large bubble is pushed back downstream, the above process repeats. The oscillation continues to occur until the volume of the bubble is sufficiently large to remain on the surface and overcome the inertial force of the flow. The above process can be visually seen in Fig. 5-24.

The relatively large heat flux values are the result of the high subcooling. At higher subcooled conditions, a larger heat flux is necessary to generate boiling conditions. If the heat flux is relatively low, no boiling will occur on the surface. Consider the heat flux value of approximately 1.16 MW/m^2 for the ULPU Configuration V (for AP1000) experiments at the closest point to downward-facing position (Dinh et al., 2003). While the flow conditions are quite different, comparing ULPU CHF with the CHF value of 2.61 MW/m^2 for the bare surface of current experiments shows ULPU results to be lower than half of the obtained results. Again, this is due to one of the limitations of the current experiments: highly subcooled conditions.

A comparison was made with a subcooled CHF correlation to check the reliability of the experimental CHF data. While describing correlations for subcooled flow boiling, Divavin et al. (1996) shows a CHF correlation obtained by Shlikov et al. given as

$$q_{CHF} = 0.0412\, G^{1/2} \Delta T_{SUB}^{1/3} \left(1 - \frac{\rho_g}{\rho_l} \right)^{1.8} \tag{5-6}$$

where

q_{CHF} = critical heat flux [MW/m^2]

G = mass flux [kg/m^2-s]

ΔT_{SUB} = subcooling (saturated water temperature (T_{SAT}) minus bulk fluid temperature) [°C]

ρ_g = gas (vapor) density at saturation [kg/m^3]

ρ_l = liquid density [kg/m^3]

The valid ranges of parameters as stated in the work of Divavin et al. are given in Table 5-6. The pressure and velocity of the current experiments are within the range of the Shlikov et al. correlation. Even though the velocity is out of range in the current experimental work, Fig. 5-25 shows the experimental data to be within 12% of the correlation.

Table 5-6: Valid range of parameters for Shlikov et al. correlation.

Corr. Parameters	**Range**
Pressure	0.05 – 0.30 MPa
Velocity	16 – 25 m/s
Subcooling	15 – 85°C

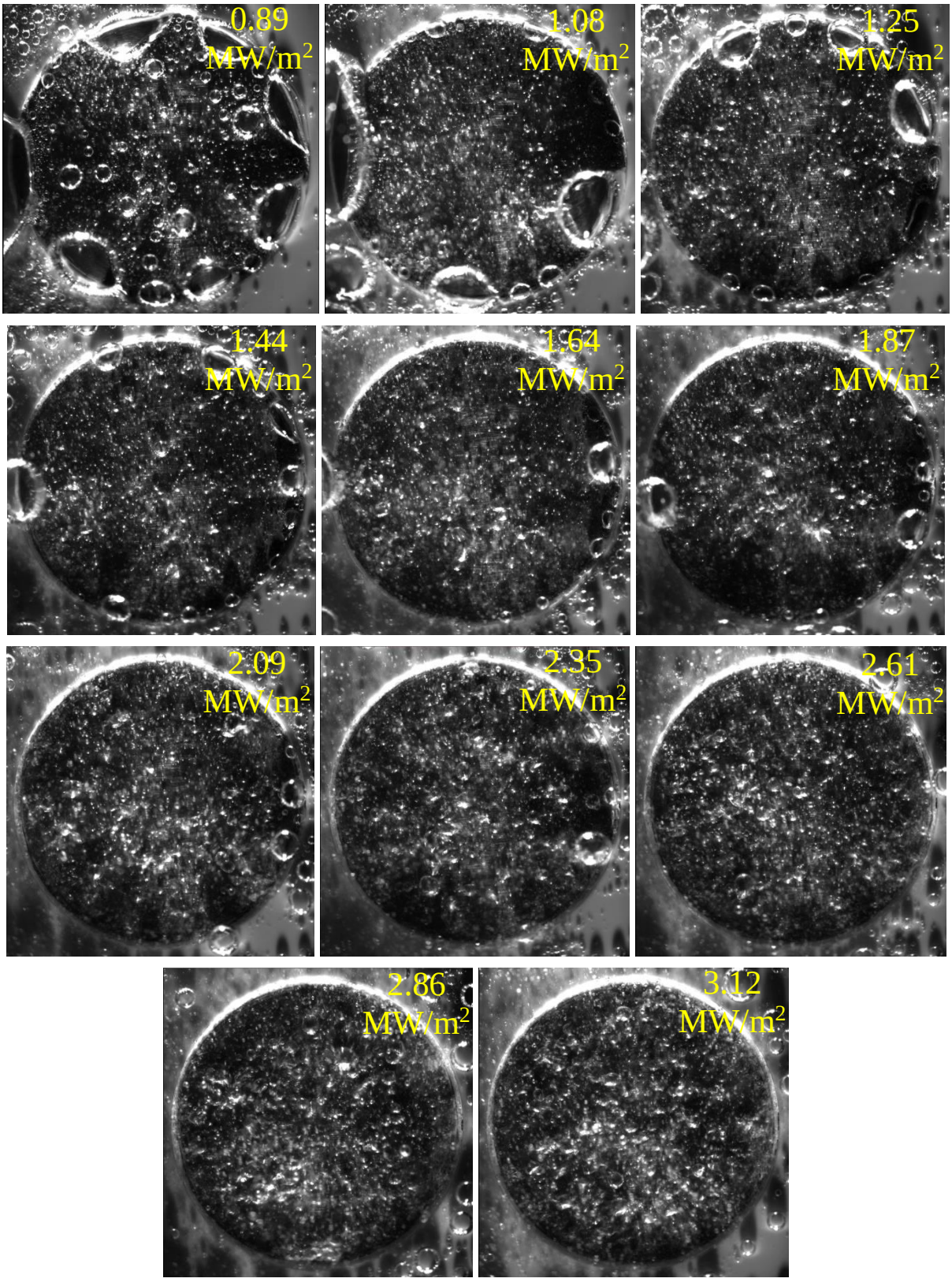

Figure 5-21: Visualization of 244 kg/m^2-s bare surface experiment.

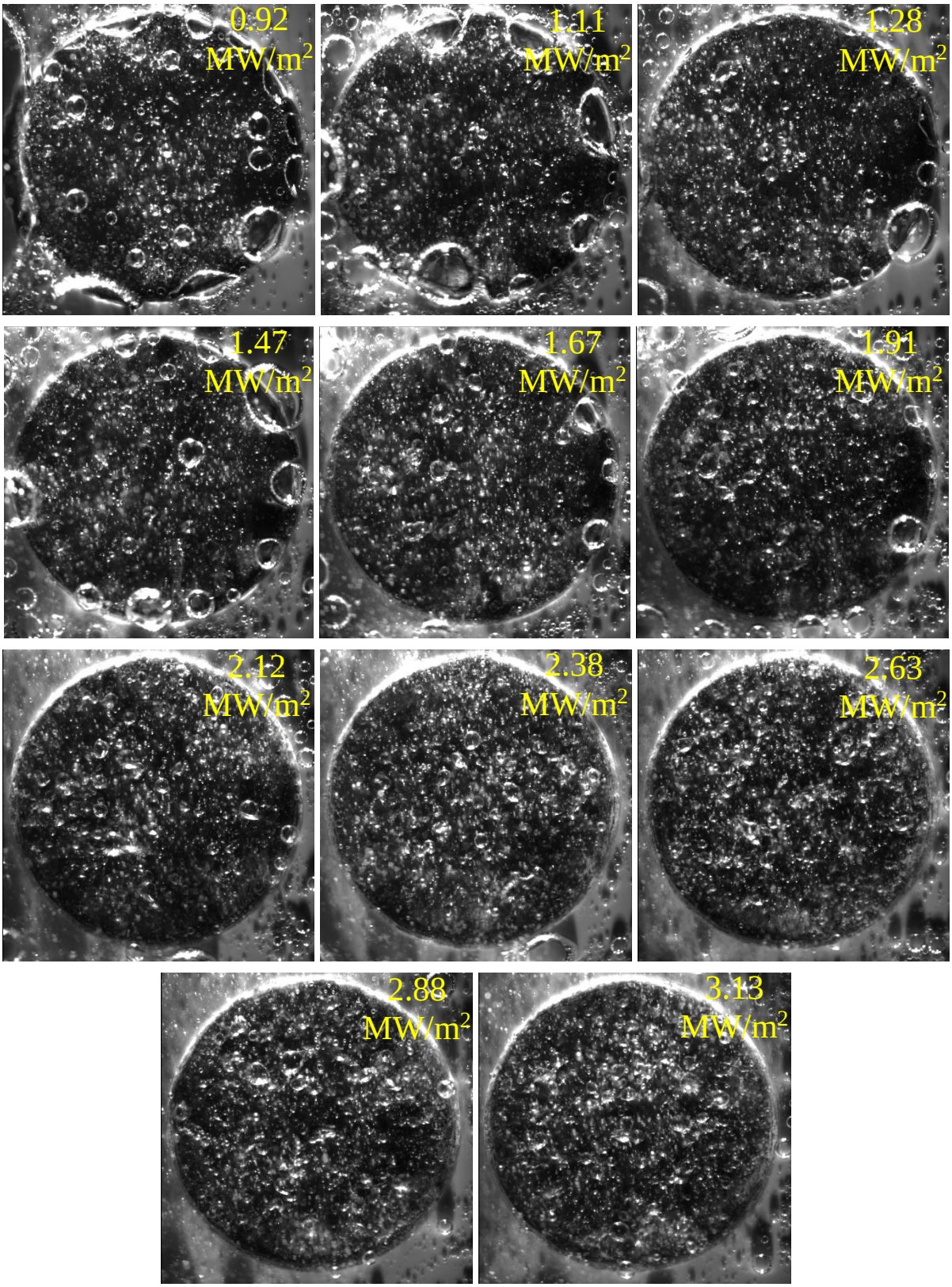

Figure 5-22: Visualization of 215 kg/m^2-s bare surface experiment.

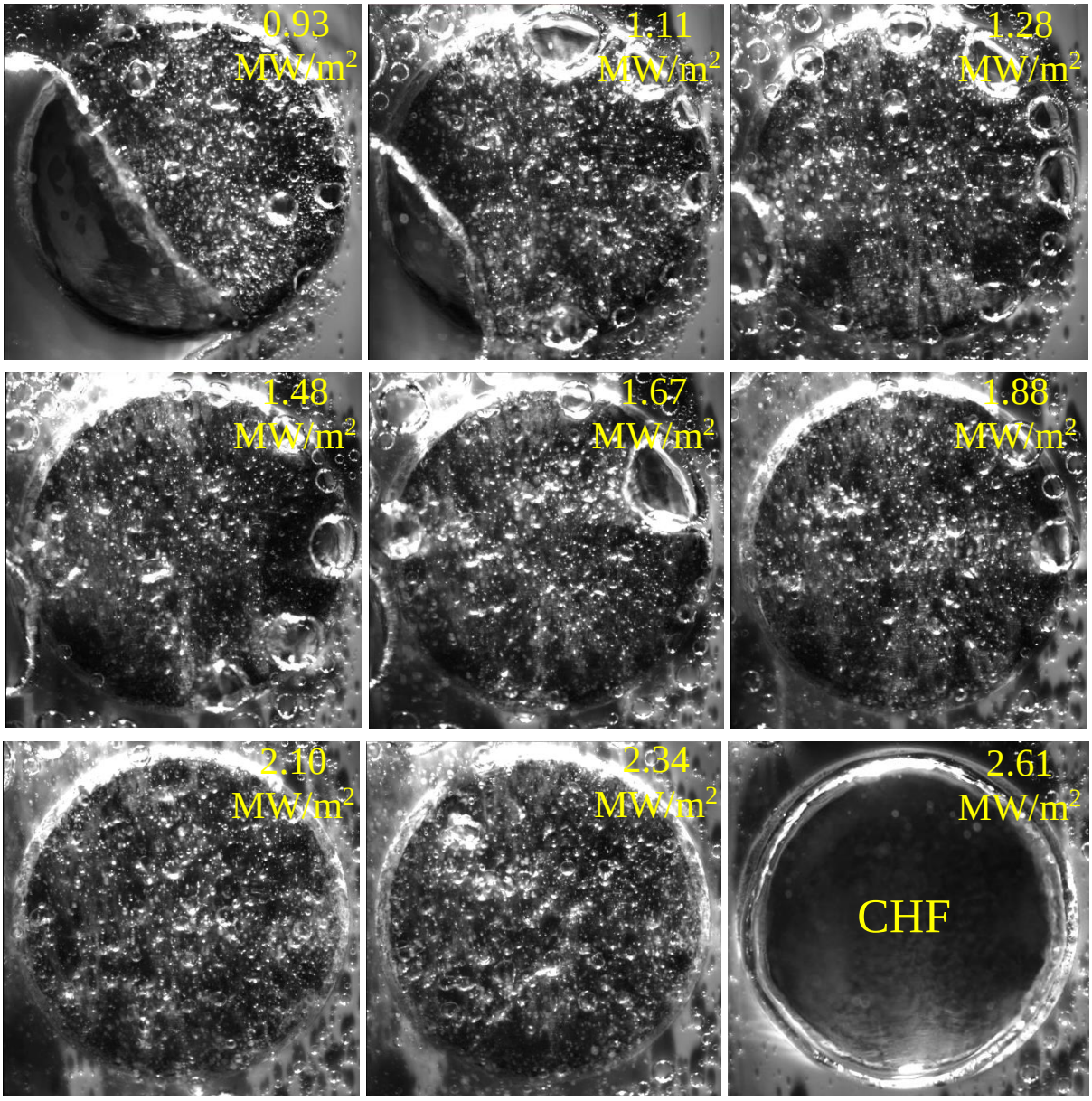

Figure 5-23: Visualization of 177 kg/m^2-s bare surface experiment.

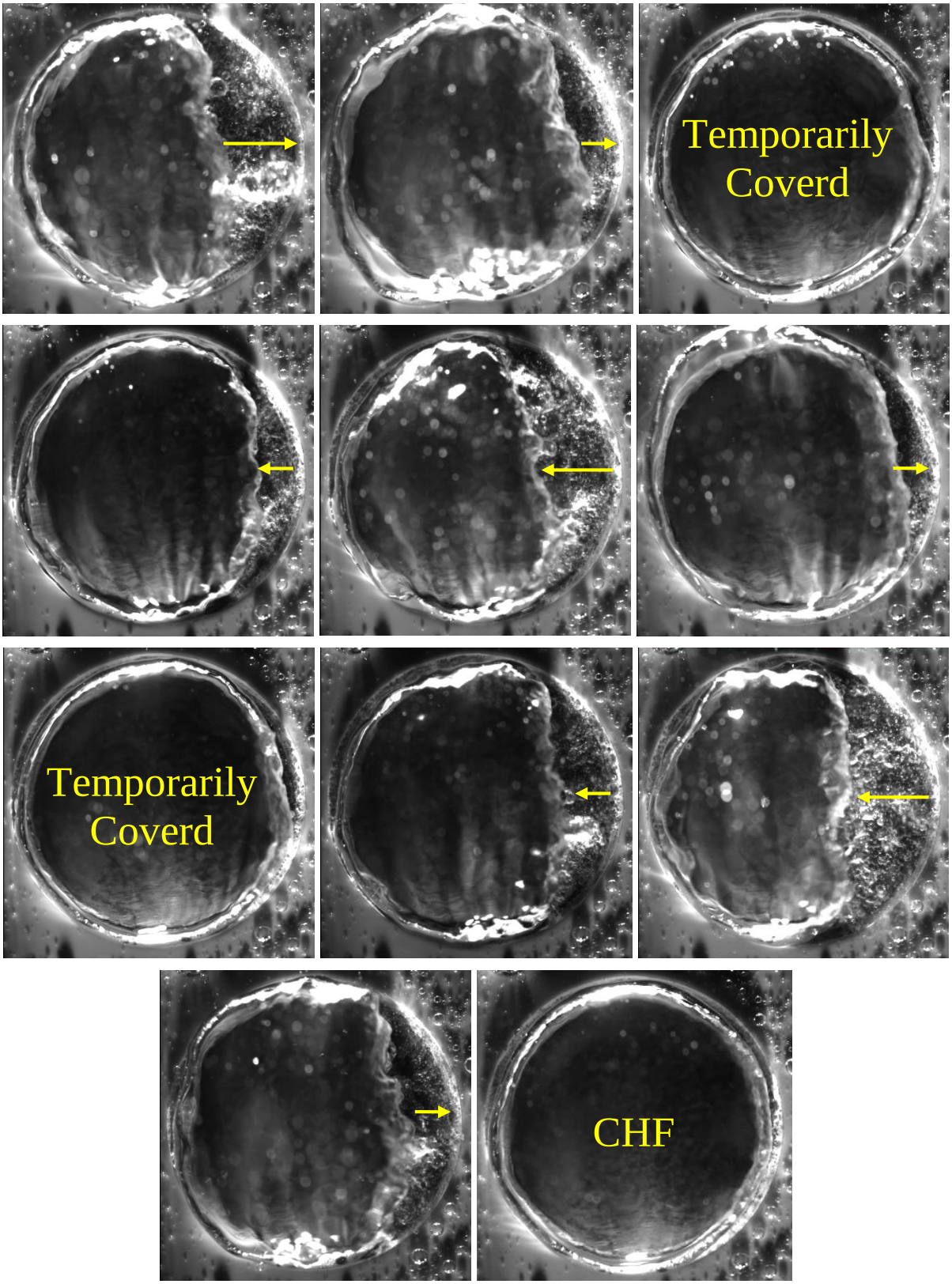

Figure 5-24: Oscillation of large bubble before CHF (starts from top left, goes right).

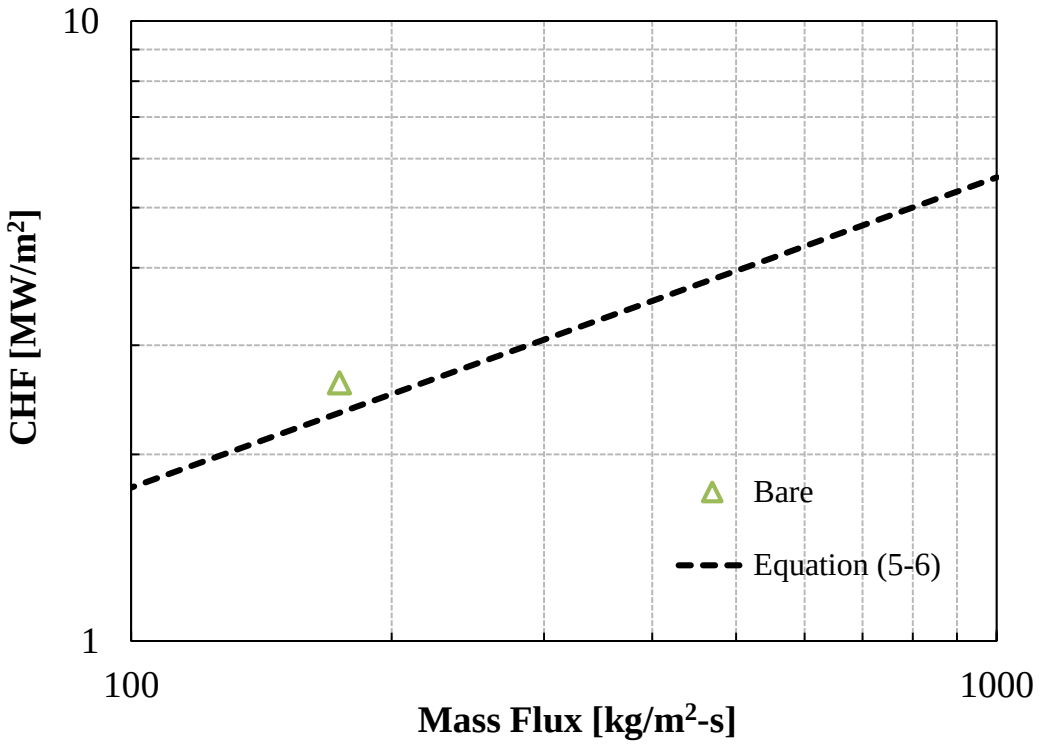

Figure 5-25: Comparison of bare surface subcooled CHF data and Shlikov et al. correlation.

5.5 Finned Surface Results

In this section the finned surface results are presented, and simultaneously compared with the bare surface case. The conditions, procedures, and analysis of sections 5.1.11, 5.2, and 5.3 for the bare surface experiments were the same applied for the finned surface experiments. Only the test section differed slightly (Fig. 5-26): the fin protruded from the surface, and upstream (US) and downstream (DS) temperatures were measured. It should be clarified that the fin was not separately attached to a bare copper block, but was machined to be part of the block.

5.5.1 Initial Observation

From an observation made in the beginning of the experiments, a comparison between the bare and finned surfaces showed accumulation of a bubble on the boiling surface downstream in the finned surface experiments. In the image on the right hand side in Fig. 5-27 the bubble

accumulation occurs immediately after the fin, which is located in the center of the image. The flow direction in the figure is towards the left side of the images. The effect of the bubble buildup on the heat transfer was of interest. Hence, monitoring the upstream and downstream temperatures was essential to better understand the effects of the accumulation on the heat transfer.

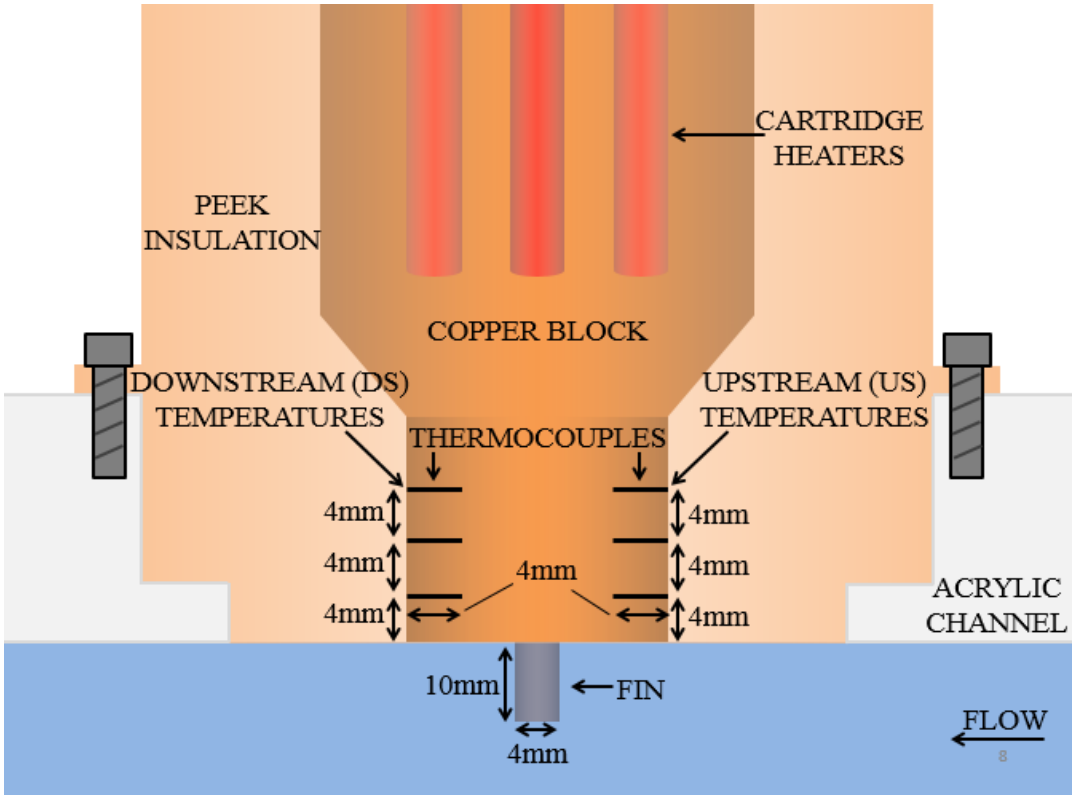

Figure 5-26: Mid-section schematic of finned copper block test section.

5.5.2 Heat Transfer from Both Surfaces

The boiling curves for both types of surfaces and all three flow rates are shown in Figs. 5-28 to 5-30. For the finned surface data the upstream and downstream are denoted as US and DS, respectively. Again, CHF conditions were observed only for the low flow rate.

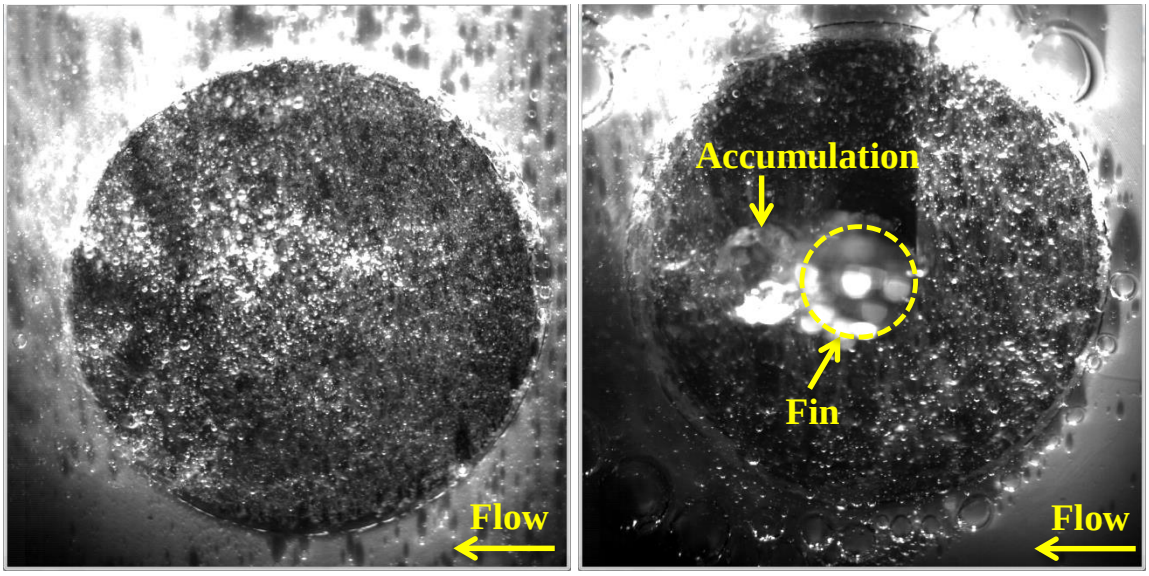

Figure 5-27: Comparison of bare (left) and finned (right) surfaces.

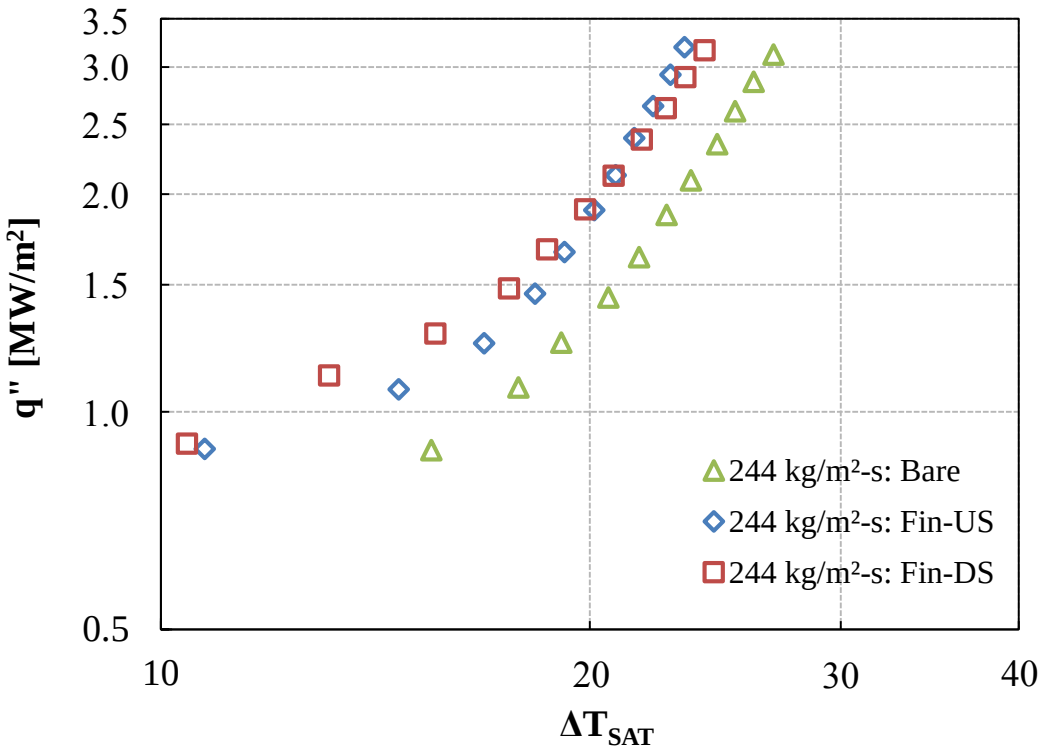

Figure 5-28: Boiling curves of bare and finned surfaces at 244 kg/m^2-s case.

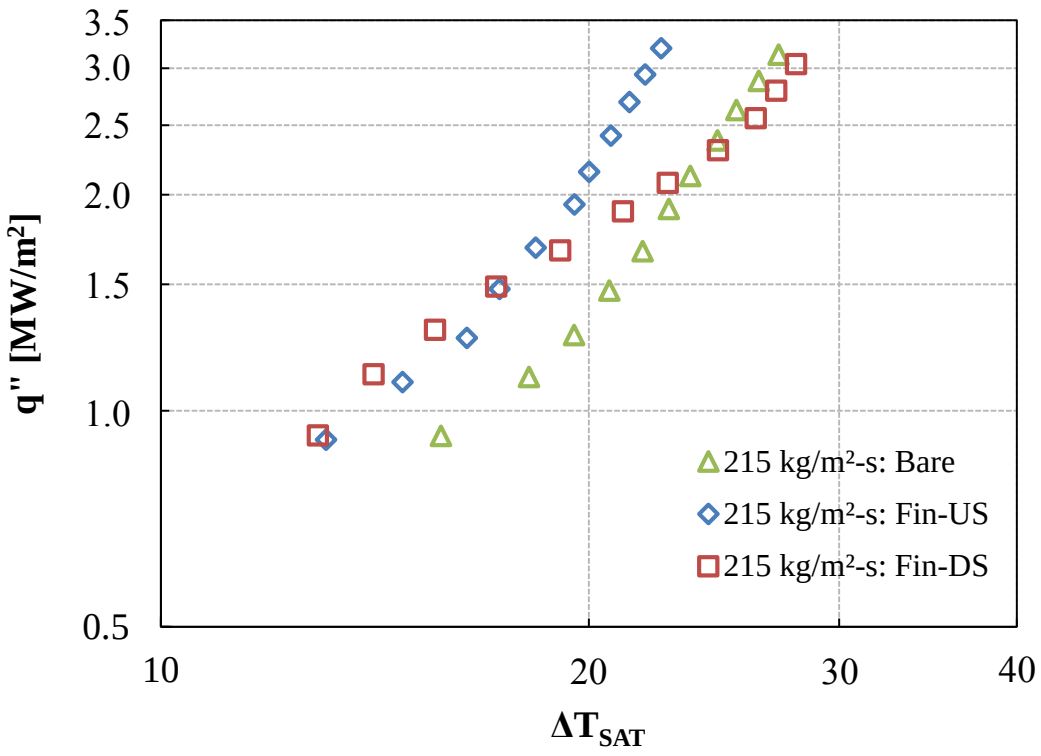

Figure 5-29: Boiling curves of bare and finned surfaces at 215 kg/m^2-s case.

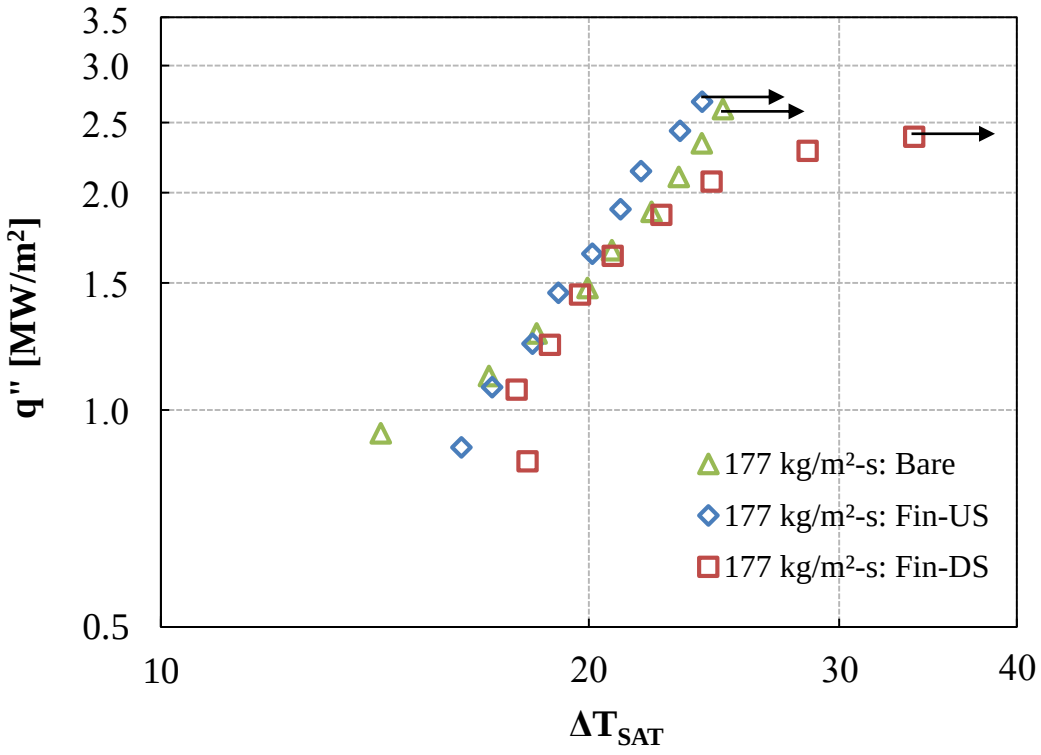

Figure 5-30: Boiling curves of bare and finned surfaces at 177 kg/m^2-s case.

The emphasis of the results is towards the higher heat flux levels. In the high flow rate experiments (Fig. 5-28), the surface temperatures for the bare surface are greater than the upstream and downstream temperatures of the finned surface. An advantage of the fin for the high flow rate case is observed: a reduction in the surface temperatures. Notice that for the finned surface, the downstream temperatures are slightly greater than the upstream temperatures. Although the upstream temperatures for the finned surface are still lower compared to the bare surface temperatures for the medium flow rate, the downstream temperatures slightly exceed the bare surface temperatures (Fig. 5-29). For the medium flow rate case, the advantage of surface temperature reduction is only seen for the upstream data. When the flow rate is reduced further, the downstream temperatures rise significantly compared to the medium and high flow rates (Fig. 5-30). Even for the low flow rate case, the reduction in the surface temperatures for the upstream location is still observed. The entire boiling surface was completely covered by a bubble at the occurrence of CHF (Fig. 5-31). Note that only the portion of the fin base close to the boiling surface was covered by the bubble, and not the entire fin along its length. Figure 5-32 shows the maximum heat flux from the boiling curves of Figs. 5-28 to 5-30. At the high flow rate, the surface heat flux on the finned surface is greater than the bare surface. As the flow rate decreases, only the Fin-DS heat flux decreases below the bare surface heat flux. From the figure it is evident that a reduction in the heat flux occurs for Fin-DS compared to the bare surface as the flow rate is reduced. This implies that a phenomenon is occurring only in the downstream location disturbing the heat transfer. Notice that the Fin-DS CHF has been reduced compared to the Bare and Fin-US CHF. Visualization of the boiling phenomenon on the finned surface is shown in Figs. 5-33 to 5-35 for the three flow rates.

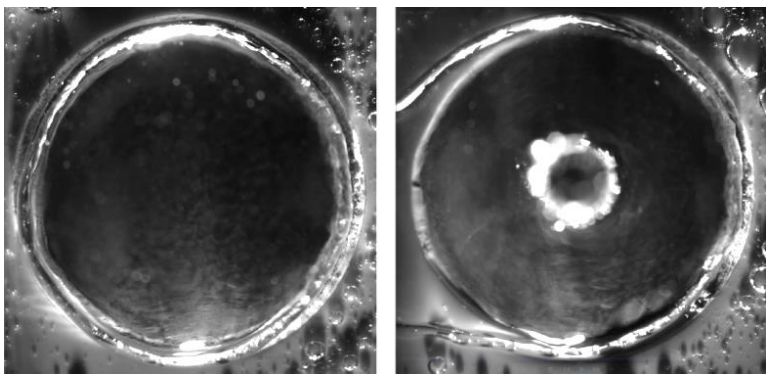

Figure 5-31: Bubble covering the bare surface (left) and the finned surface (right) at CHF.

As mentioned earlier, bubble accumulation was observed at the fin-downstream location in the initial observation of the experiments. The accumulation may cause disturbance in the heat transfer in the downstream location. There is no obstruction in the flow path for the upstream location on the finned surface. This allows the liquid to contact the heated surface directly. For the downstream location, the flow has been affected due to the presence of the fin. In a way, the flow for the finned surface experiment may be described as flow around a cylinder. As the fluid flows around the cylinder, a wake produced downstream after the cylinder. Besides fluid flow, boiling is also present in the experiments. As a result, the bubbles will be entrained in the flow and accumulate in the wake. In some cases, the bubble accumulation on the surface occurs for a significant amount of time. Furthermore, the liquid velocity is reduced considerably compared to the bulk flow in the wake region (Warui and Fujisawa, 1996). The bubble accumulation and low velocity in the downstream location will affect the heat transfer by causing inadequate cooling of the surface. The accumulation of bubbles will not allow the liquid to contact the boiling surface and the low velocity will decrease the heat transfer from the boiling surface to the liquid. The accumulation in the downstream location may cause a hotspot at that location, and the temperatures can increase significantly during the accumulation. The bubble accumulation and reduced velocities in the wake region are believed to have caused increased temperatures downstream.

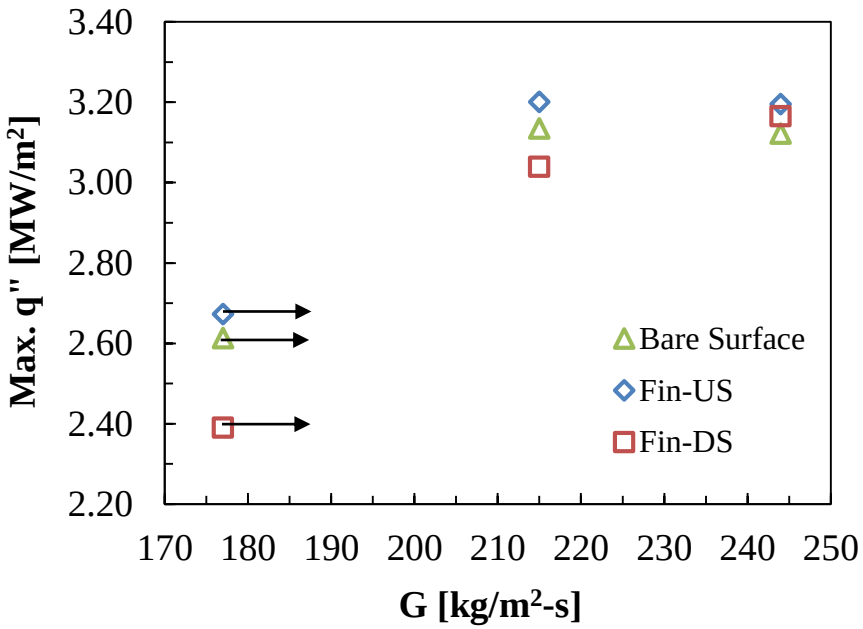

Figure 5-32: Maximum heat flux at 244 kg/m^2-s, 215 kg/m^2-s, and 177 kg/m^2-s (CHF).

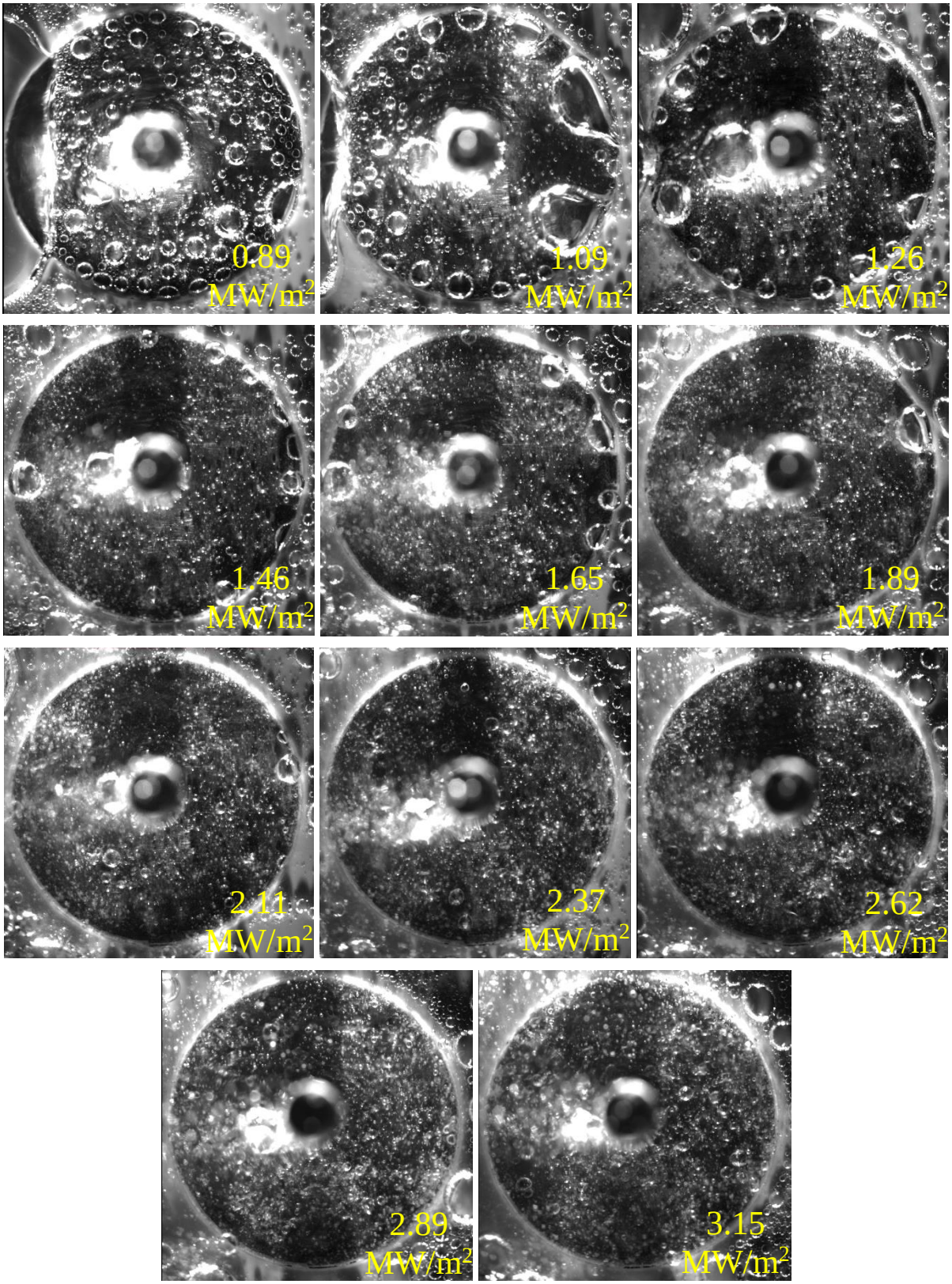

Figure 5-33: Visualization of 244 kg/m^2-s fin surface experiments.

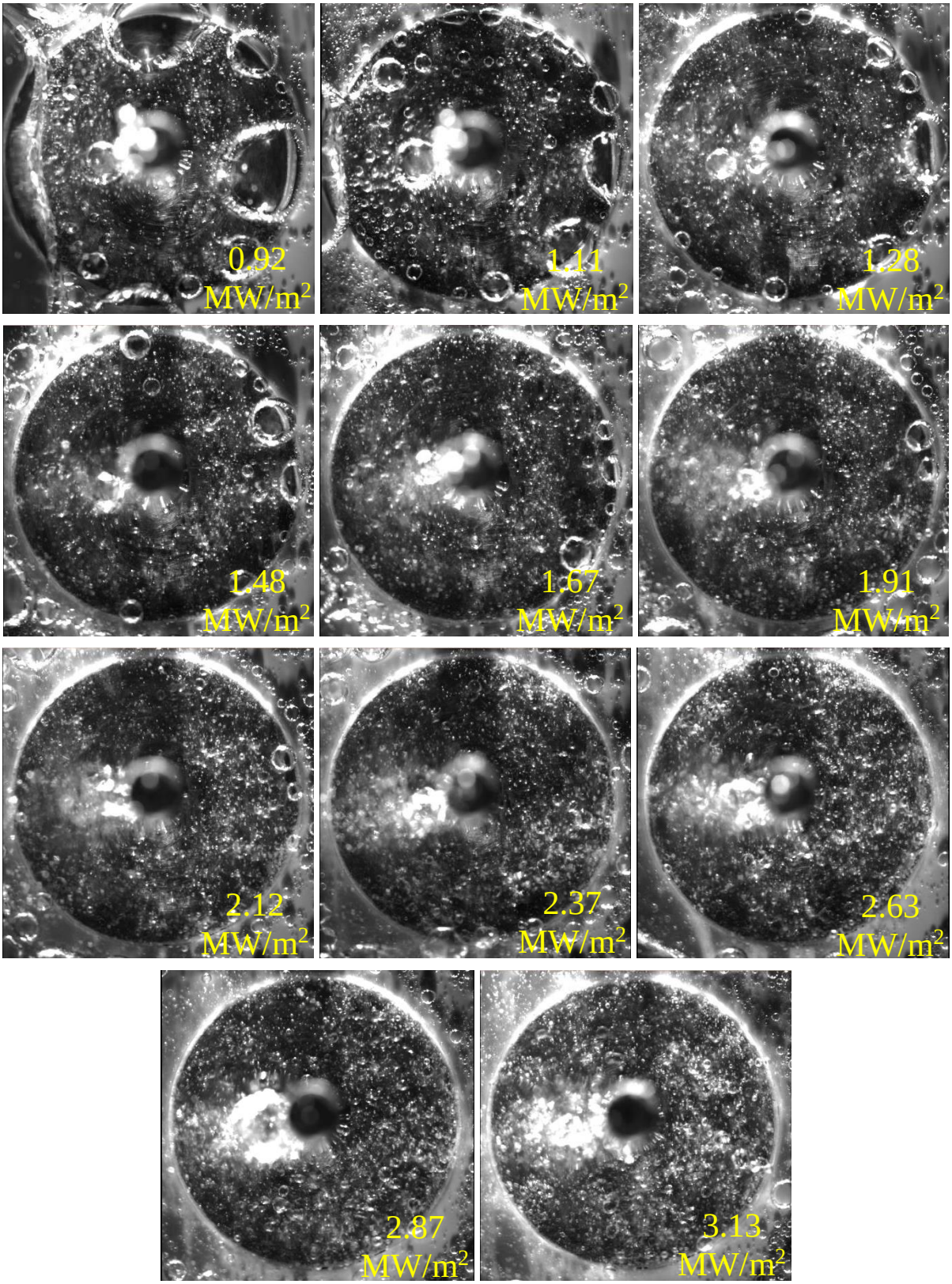

Figure 5-34: Visualization of 215 kg/m^2-s fin surface experiments.

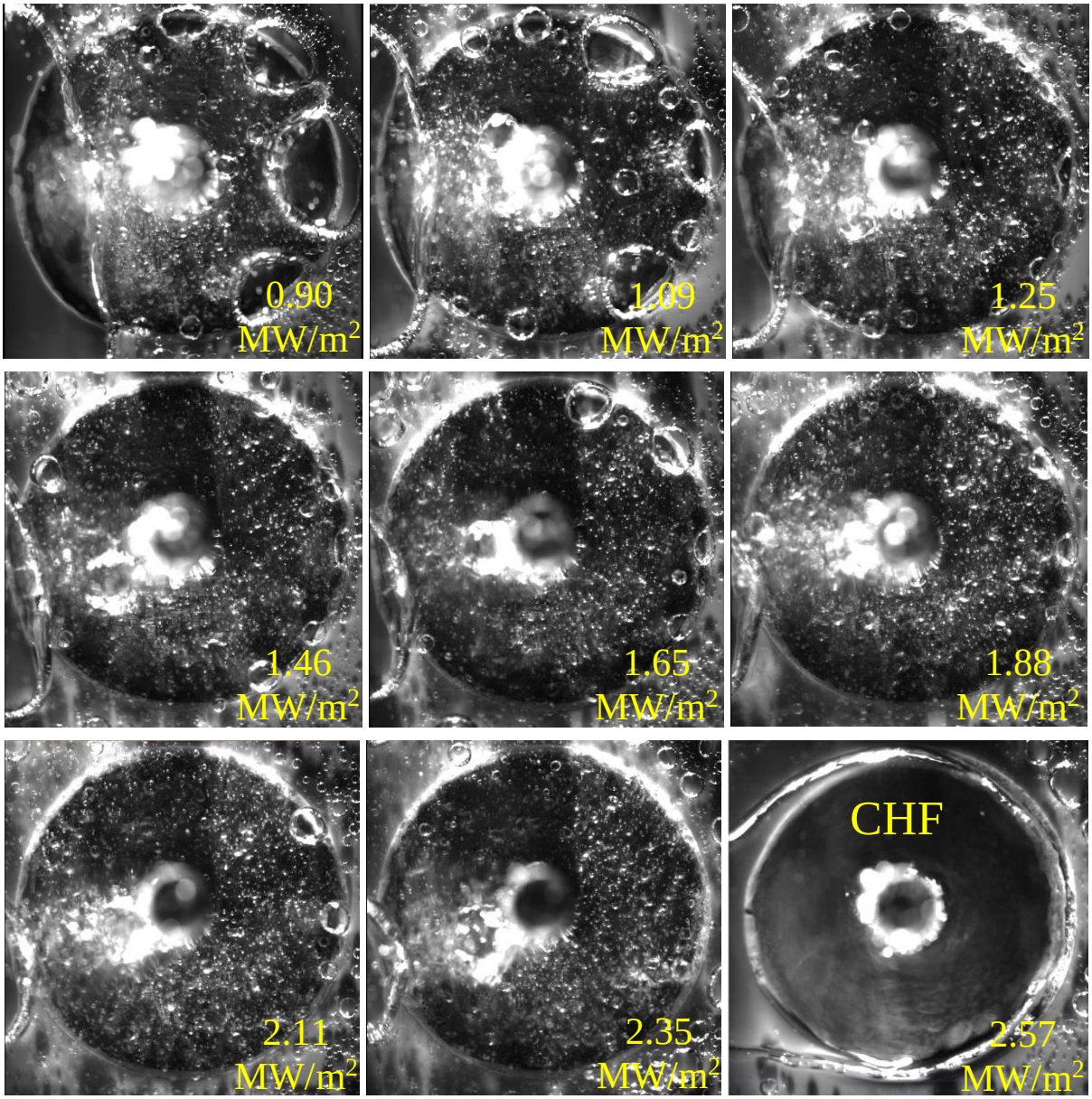

Figure 5-35: Visualization of 177 kg/m^2-s fin surface experiments.

A simple Particle Image Velocimetry (PIV) experiment was performed to verify the flow around the fin. The PIV experiment was performed for the high flow rate case only. In Fig. 5-36 it can be clearly seen that there is no disturbance in the majority of the flow except after the fin in the wake region downstream, and Fig. 5-37 confirms the same.

Figure 5-36: Super-imposed images from particle tracking experiment for 244 kg/m^2-s case.

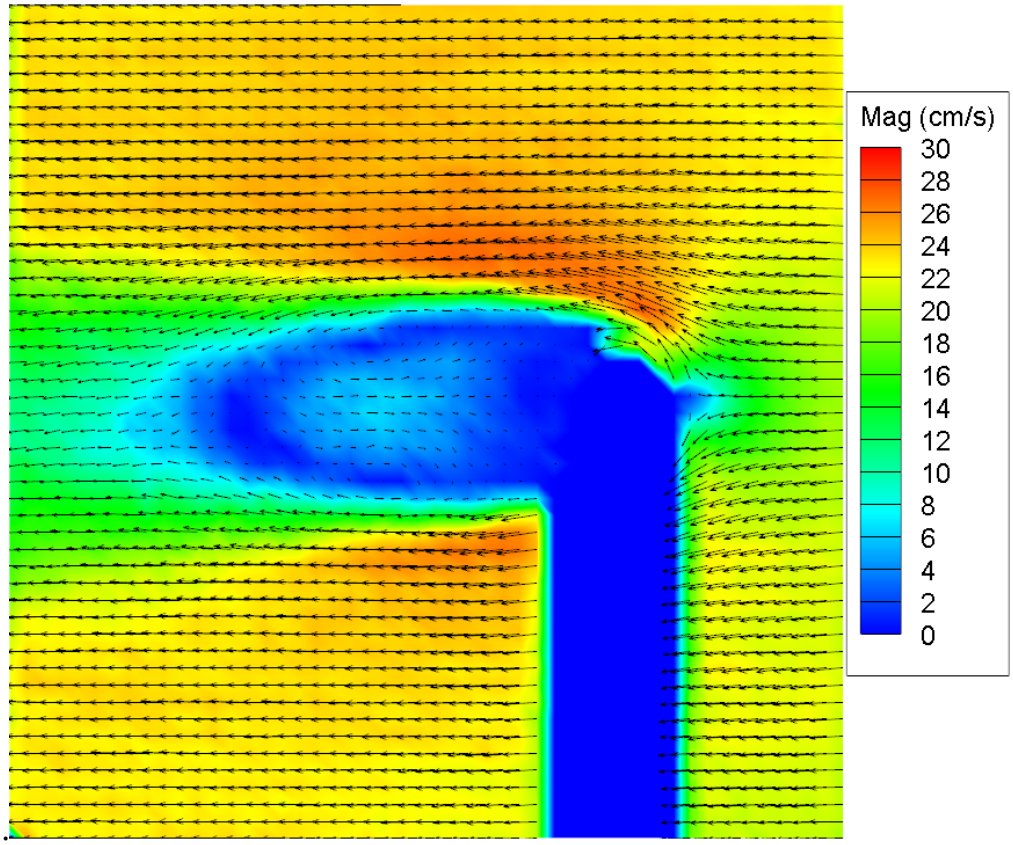

Figure 5-37: Low velocity region after fin in the particle tracking experiment for 244 kg/m^2-s case. Flow is from right side of the image to the left.

The experimental heat transfer coefficient (HTC) was calculated using equation (5-5). In order to observe the improvement in the heat transfer due to the addition of the fin, a ratio was taken of the finned surface heat transfer coefficient (both locations) to the bare surface heat transfer coefficient. The heat transfer coefficient ratio was defined as

$$h_{ratio,uptream} = \frac{h_{upstream}}{h_{bare}} \tag{5-7}$$

where

$h_{ratio,\ upstream}$ = heat transfer coefficient ratio for the finned surface upstream location

$h_{upstream}$ = experimental HTC for upstream (finned surface) [W/m^2-K]

h_{bare} = experimental HTC for bare surface [W/m^2-K]

The ratio $h_{ratio,\ upstream}$ compares the improvement in the heat transfer for finned surface upstream location against the bare surface. Similarly,

$$h_{ratio,downtream} = \frac{h_{downstream}}{h_{bare}} \tag{5-8}$$

where

$h_{ratio,\ downstream}$ = heat transfer coefficient ratio for the finned surface downstream location

$h_{downstream}$ = experimental HTC for downstream (finned surface) [W/m^2-K]

Equation (5-8) compared the improvement in the heat transfer for finned surface downstream location against the bare surface. The ratios in equations (5-7) and (5-8) are plotted for all three flow rates in Figs. 5-38 and 5-39, respectively. Again, the emphasis of the results is on higher heat flux levels. Values above 1.00 imply improvement in the heat transfer on the finned surface compared to the bare surface. In Fig. 5-38 the ratio is greater than 1.00 at high and medium flow rates for all heat flux, meaning that the heat transfer has improved for the upstream location on the finned surface. The low flow rate initially shows a ratio below 1.00, but the heat transfer improves as the heat flux increases. An overall improvement in the heat transfer is observed for the upstream location, since there is no obstruction in the flow path. The average improvement in the heat transfer for the high and medium flow rates is

approximately 5%, and approximately 3% for the low flow rate. On the other hand, Fig. 5-39 shows improvement only for the high flow rate. A transition from improvement to reduction of the heat transfer occurs for the medium flow rate. For the low flow rate case the ratio starts to increase, but reduces as the heat flux increases to CHF. The low flow rate does not show any improvement in the heat transfer compared to the bare surface. In Fig. 5-39, a reduction in the heat transfer is observed as the flow rate is reduced.

The heat transfer on the downstream location for the finned surface (Fig. 5-39) has been enhanced locally for the high flow rate, but the heat transfer reduction is increasing as the flow rate decreases i.e. the difference between each flow rate is increasing as the flow rate is decreasing. The addition of an extended surface may enhance the overall heat transfer due to the increase in the surface area. The current experiments show that a reduction in the local heat transfer is also possible by addition of a finned surface.

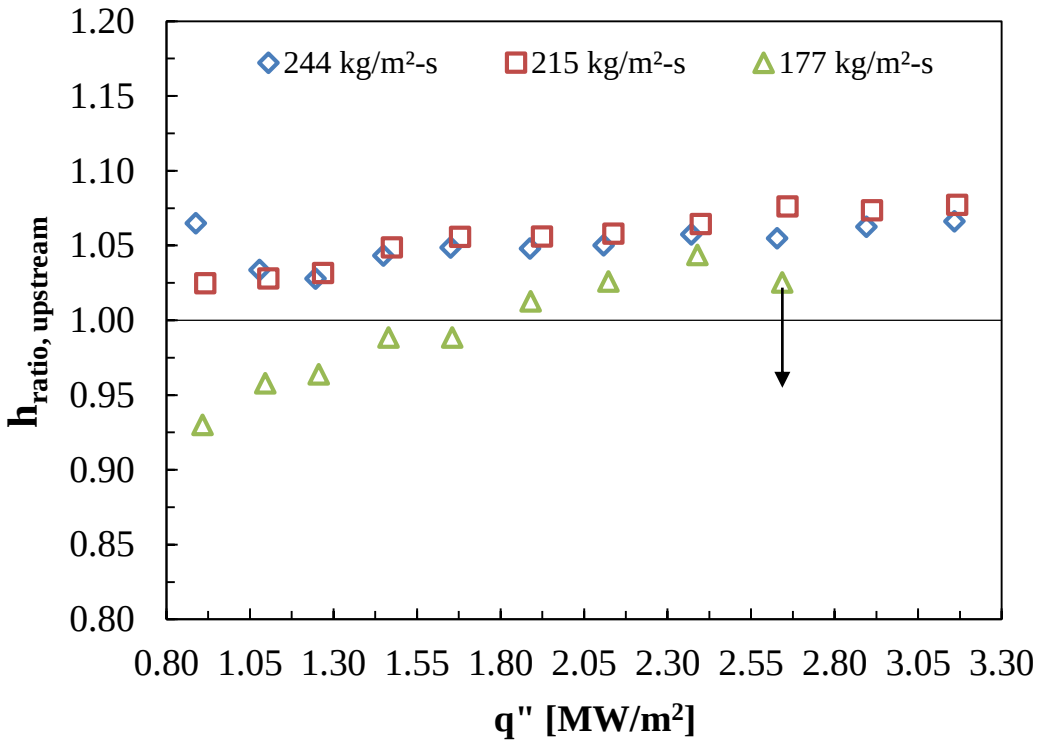

Figure 5-38: Heat transfer coefficient ratio of fin (upstream location) to bare surfaces.

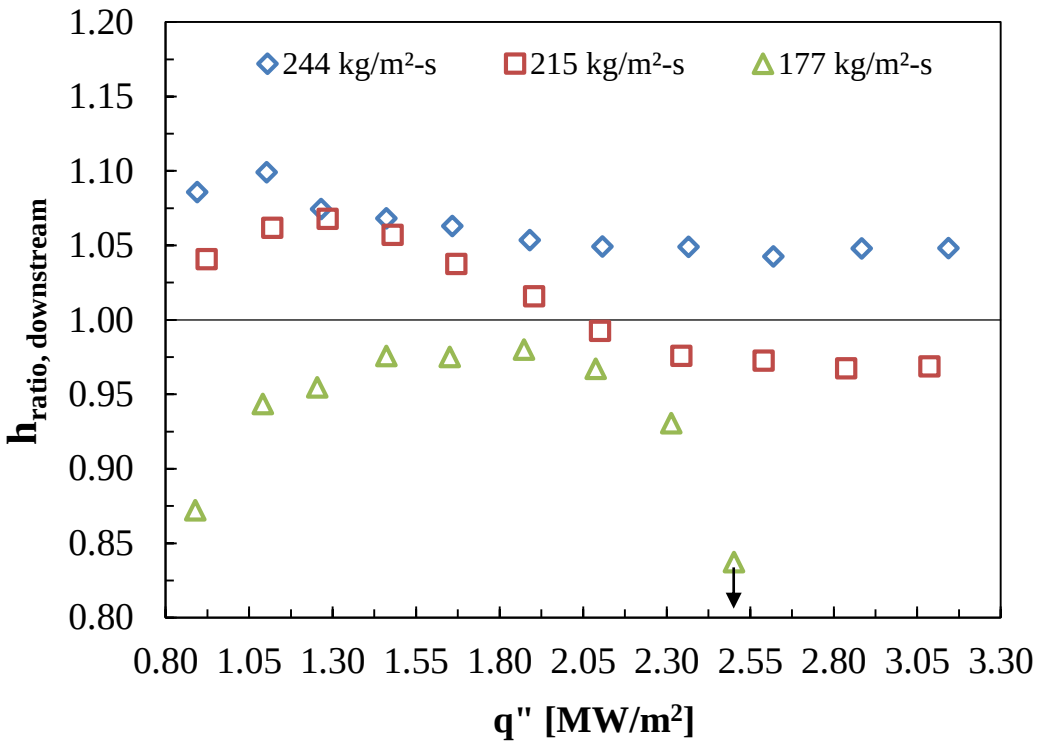

Figure 5-39: Heat transfer coefficient ratio of fin (downstream location) to bare surfaces.

5.5.3 Heat Transfer Coefficient Comparison: Experiment & Correlation

In the previous section, the finned and bare surface heat transfer coefficients were compared. In this section, the finned surface heat transfer coefficient is compared with a subcooled flow boiling correlation.

A literature search for flow boiling heat transfer correlations has shown that most of the correlations found were developed from experiments performed at saturated conditions. Frequently studied experiments involve flow boiling inside heated tubes at saturated conditions. Since majority of the correlations are for saturated conditions, correlations for subcooled conditions are not commonly available. Moreover, the correlations developed from experiments performed at saturated conditions cannot be applied for experiments performed at subcooled conditions because the former do not account for the subcooling. Additionally, some parameters cannot be applied for experiments performed at subcooled conditions.

In previously proposed correlations, some important parameters found were

- some form of fluid velocity: Reynolds number (Re), mass flux (G), velocity
- some form of geometry: length or diameter (L or D), boiling surface diameter
- liquid density: ρ_l
- gas density: ρ_g
- liquid viscosity: μ
- liquid thermal conductivity: k_l
- liquid specific heat (at constant pressure): c_p
- latent heat of vaporization: h_{fg}
- heat flux: q''
- excess surface heat: ΔT_{SAT}

The subcooling is an important parameter for subcooled flow boiling, in addition to the parameters mentioned above. The following may be considered for subcooled flow boiling

$$h = f(velocity, geometry, \rho_l, \rho_g, \mu, k_l, c_p, h_{fg}, q'', \Delta T_{SUB}) \tag{5-9}$$

Correlations often employ dimensionless parameters, which are composed of some individual parameters or characteristics. Some dimensionless parameters used in boiling correlations are

- Reynolds number: $Re = \dfrac{\rho_l v D}{\mu} = \dfrac{G D}{\mu}$
- Prandtl number: $Pr = \dfrac{\mu c_p}{k_l}$
- Boiling number: $Bo = \dfrac{q''}{G h_{fg}}$
- Nusselt number: $Nu = \dfrac{h \mathrm{L}}{k_l}$

Subcooled flow boiling correlations shown in the work of Prodonovic et al. (2002) provide three general heat transfer coefficient correlations (not for CHF). Only one of the three correlations provided in the paper incorporates a subcooling parameter. The correlation originally proposed by Badiuzzaman is

$$\frac{Nu_{tp}}{Nu_l} = 178 Bo^{0.75} Ja^{*-0.9} \left(\frac{\rho_g}{\rho_l}\right)^{-0.06} \left(\frac{\Delta T_{SUB}}{T_{SAT}}\right)^{0.45} \tag{5-10}$$

where

Nu_{tp} = two-phase (boiling) Nusselt number

Nu_l = single-phase (non-boiling) Nusselt number

T_{SAT} = fluid saturation temperature [°K]

Ja^* = modified Jacob number

The modified Jacob number is given by (Prodonovic et al., 2002)

$$Ja^* = \frac{c_p \, \Delta T_{SUB}}{h_{fg}} \tag{5-11}$$

The original Jacob number includes ΔT_{SAT} instead of ΔT_{SUB}. The Nusselt number (Nu) is an important dimensionless parameter in heat transfer problems. The Nusselt number is defined as the ratio of convection to pure conduction heat transfer (Incropera, 2007), and can be calculated as

$$Nu = \frac{h \, L}{k_l} \tag{5-12}$$

where

h = heat transfer coefficient [W/m^2-K]

L = characteristic length [m]

In equation (5-10) the parameter desired is Nu_{tp}, from which h_{tp} can be calculated by equation (5-12). The single-phase Nusselt number (Nu_l) is obtained from the Dittus-Boelter equation (Incropera, 2007):

$$Nu_l = 0.023 Re^{0.8} Pr^{0.4} \tag{5-13}$$

Equation (5-10) was calculated and compared with the experimental data. Instead of plotting the upstream and downstream correlation separately, the average correlated values are plotted since the experimental data for the upstream and downstream locations are quite similar. The results are presented in Figs. 5-40 to 5-42. It is evident from the figures that the correlation

overestimates the experimental data, and the same is confirmed by Fig. 5-43. Therefore, the correlation was slightly modified to try to estimate the current experimental data. Two modifications were made to the correlation: 1) a hydraulic diameter was calculated based on the heated surface and channel dimensions in the current experiment, and 2) the constant in the correlation was altered. In equation (5-10), the geometry information required for Nu_{tp} and Nu_l is different. The two-phase Nusselt number uses the diameter of the boiling surface (20 mm). The single-phase Nusselt number uses the size of the channel (50 mm) in equation (5-13). Due to the different dimensions used in the different Nusselt numbers, a hydraulic diameter applied to both Nusselt numbers was calculated based on the heated surface and channel dimensions.

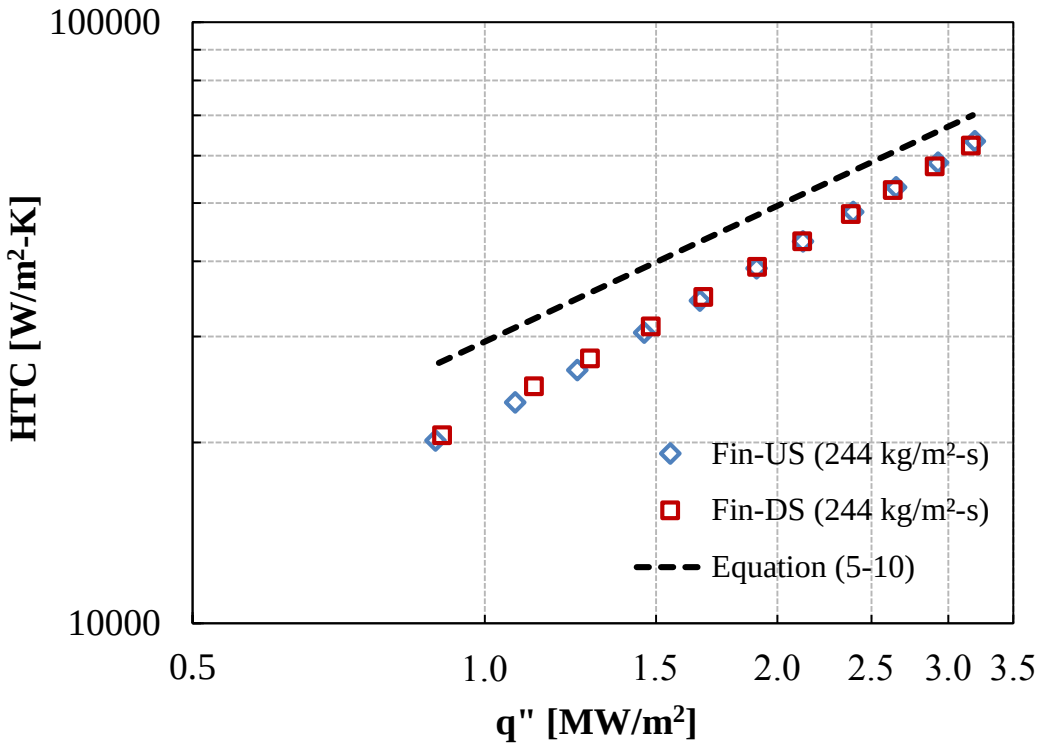

Figure 5-40: Comparison of subcooled correlation and experimental data (244 kg/m^2-s).

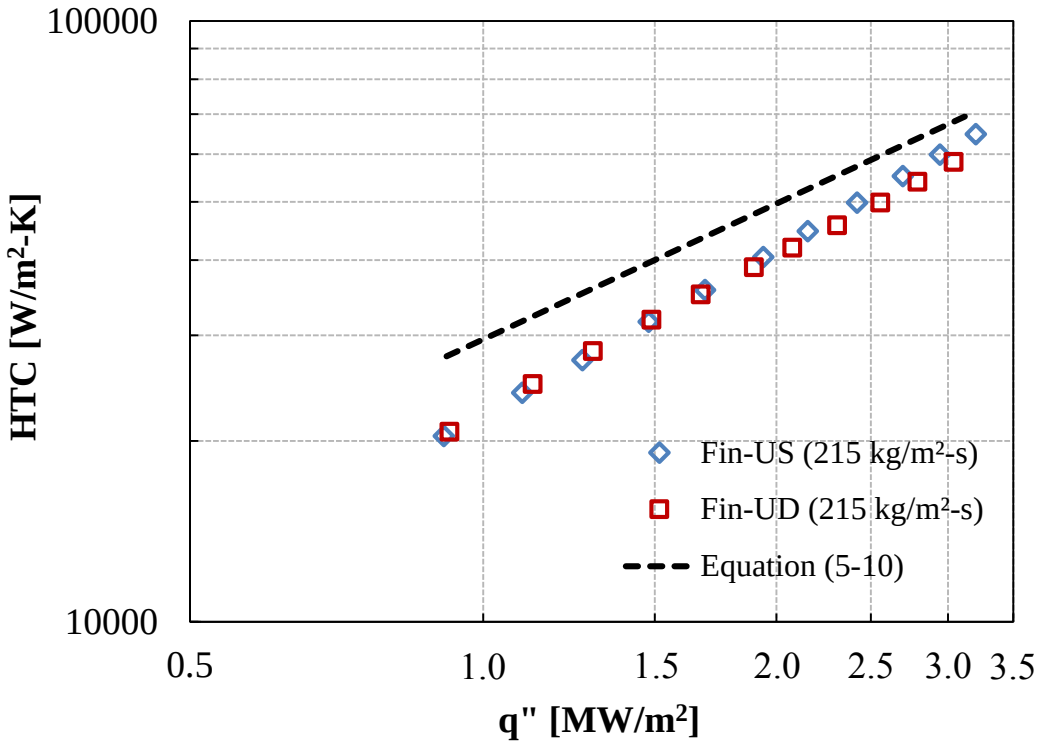

Figure 5-41: Comparison of subcooled correlation and experimental data (215 kg/m^2-s).

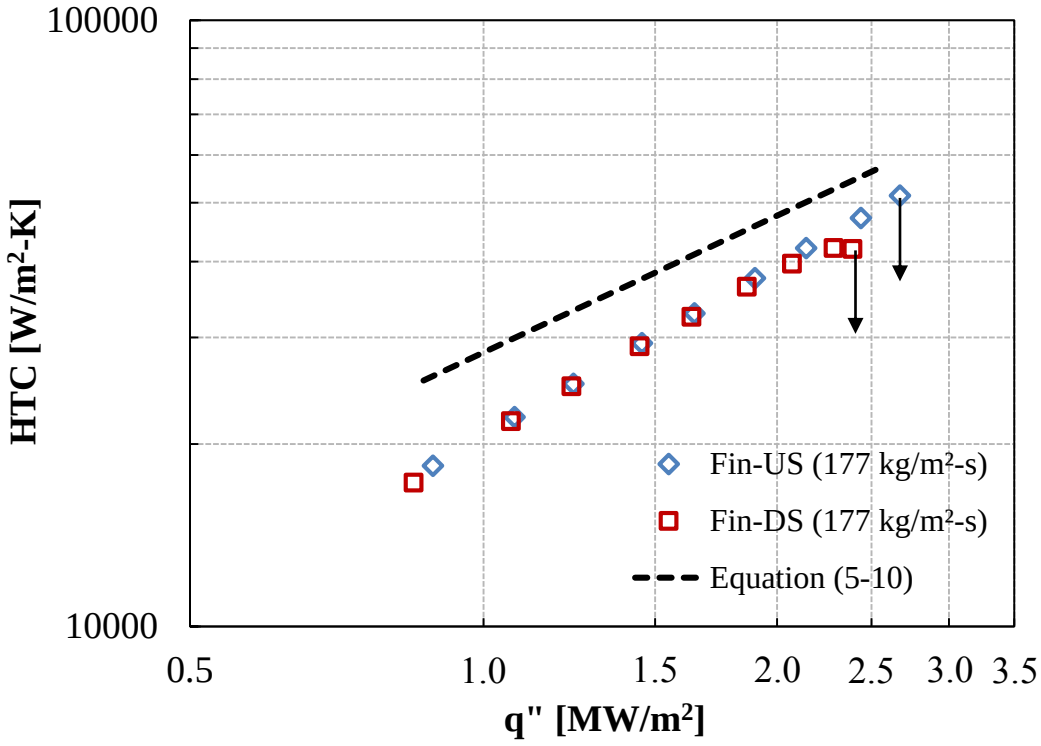

Figure 5-42: Comparison of subcooled correlation and experimental data (177 kg/m^2-s).

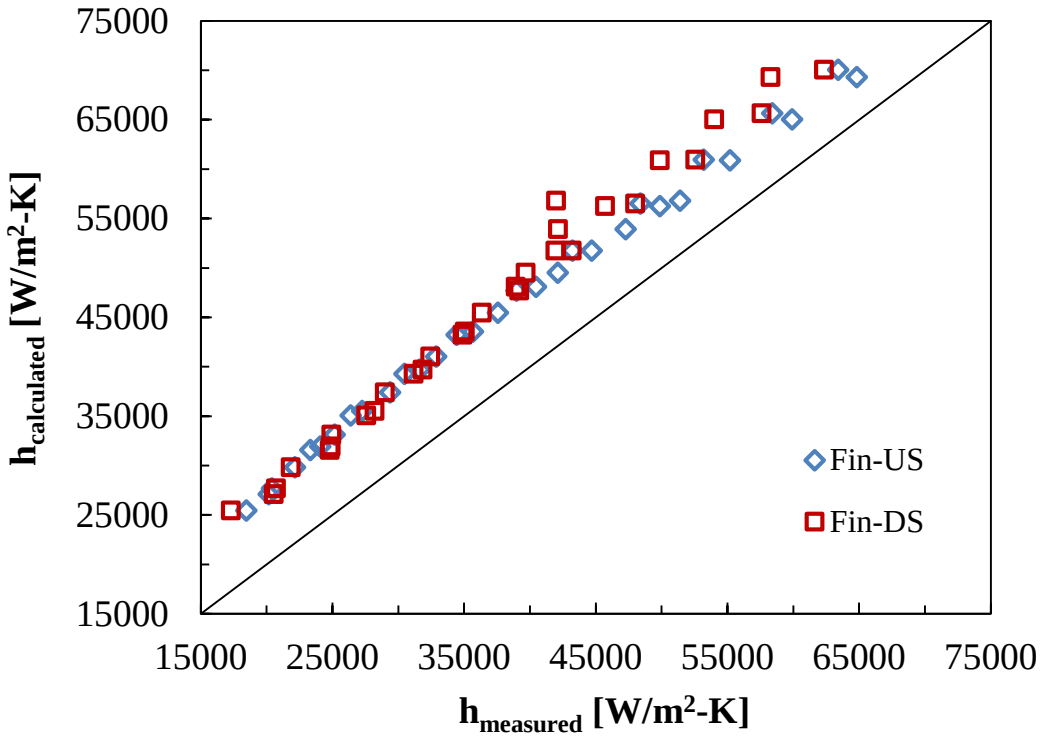

Figure 5-43: Comparison of predicted (Equation (5-10)) and measured HTCs.

Consider the heated surface geometry in a tube compared to the current experimental conditions (Fig. 5-44). Experiments for flow inside tubes often apply uniform heating on the tube. In those conditions, the heated surface and flow surface inside the tube are equivalent. Hence, the hydraulic diameter is the tube diameter. On the other hand, the diameter of the boiling surface in the current experiments cannot be considered as the hydraulic diameter due to the smaller size compared to the flow channel geometry.

The hydraulic diameter is defined as (Incropera, 2007)

$$D_h = \frac{4A_C}{P_W} \tag{5-14}$$

where

D_h = hydraulic diameter [m]

A_c = cross-sectional area of the flow geometry [m^2]

P_W = wetted perimeter [m]

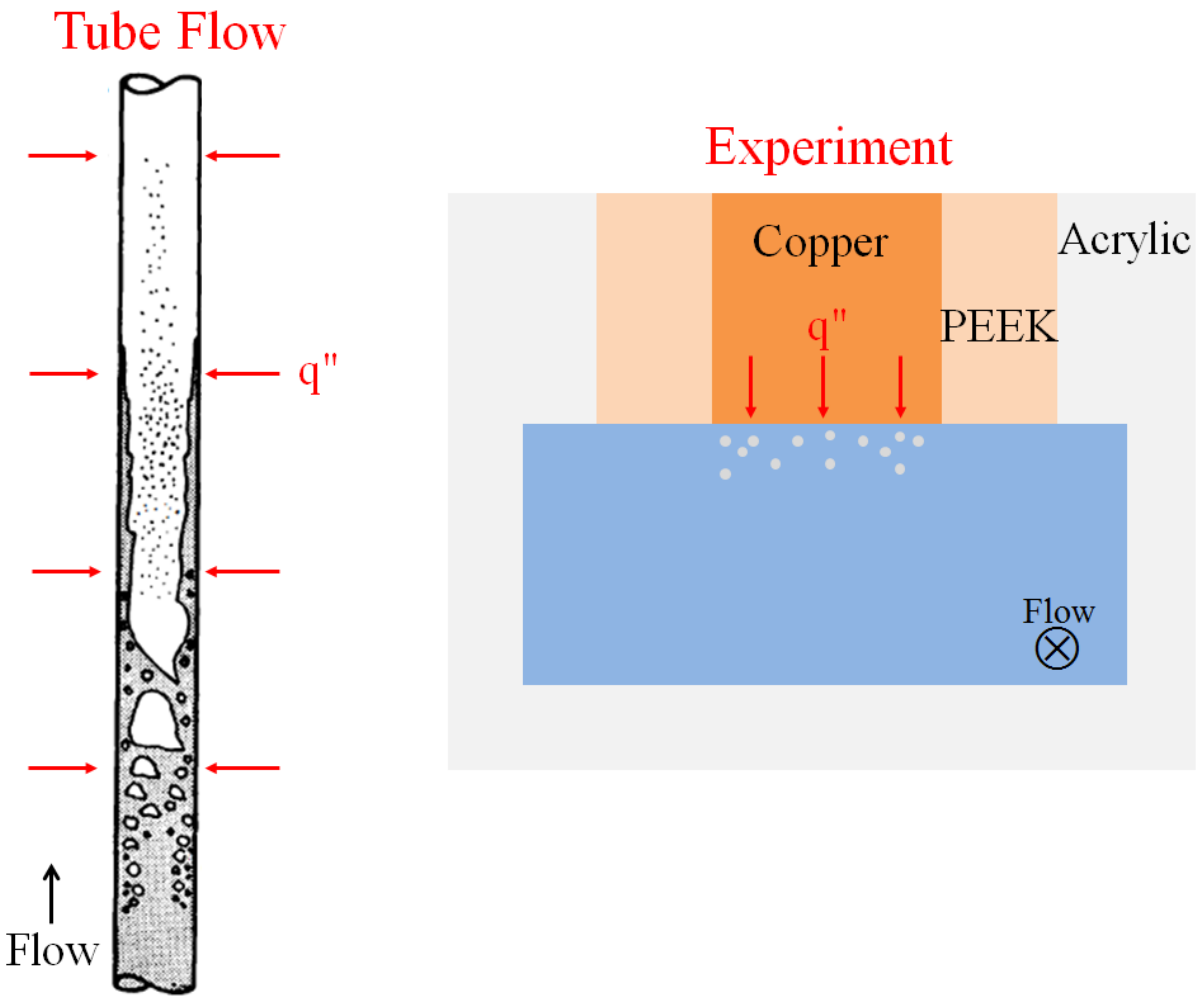

Figure 5-44: Difference in tube and current geometries (tube image: Collier, 1994).

Instead of using the wetted perimeter, a cross-sectional heated perimeter (P_H) equivalent to the diameter of the boiling surface was applied in equation (5-14). The hydraulic diameter calculated for the current experiment and used in both Nusselt numbers in equation (5-10) is

$$D_h = \frac{4A_C}{P_H} \tag{5-15}$$

As mentioned earlier, the other modification was made to the constant in equation (5-10). The constant was increased by a factor of 3.5. The modified correlation was calculated as

$$h_{tp} = 623 Bo^{0.75} Ja^{*-0.9} \left(\frac{\rho_g}{\rho_l}\right)^{-0.06} \left(\frac{\Delta T_{SUB}}{T_{SAT}}\right)^{0.45} h_l \qquad (5\text{-}16)$$

where h_l is calculated from equation (5-12), after using equation (5-13) to solve for Nu_l. The new comparison of h_{tp} and h_{exp} is shown in Figs. 5-45 to 5-47. Although there is some difference between the modified correlation and the experimental data, equation (5-16) shows better agreement compared to the original correlation from equation (5-10). Comparison of Figs. 5-43 and 5-48 also shows that equation (5-16) better estimates the experimental values compared to equation (5-10).

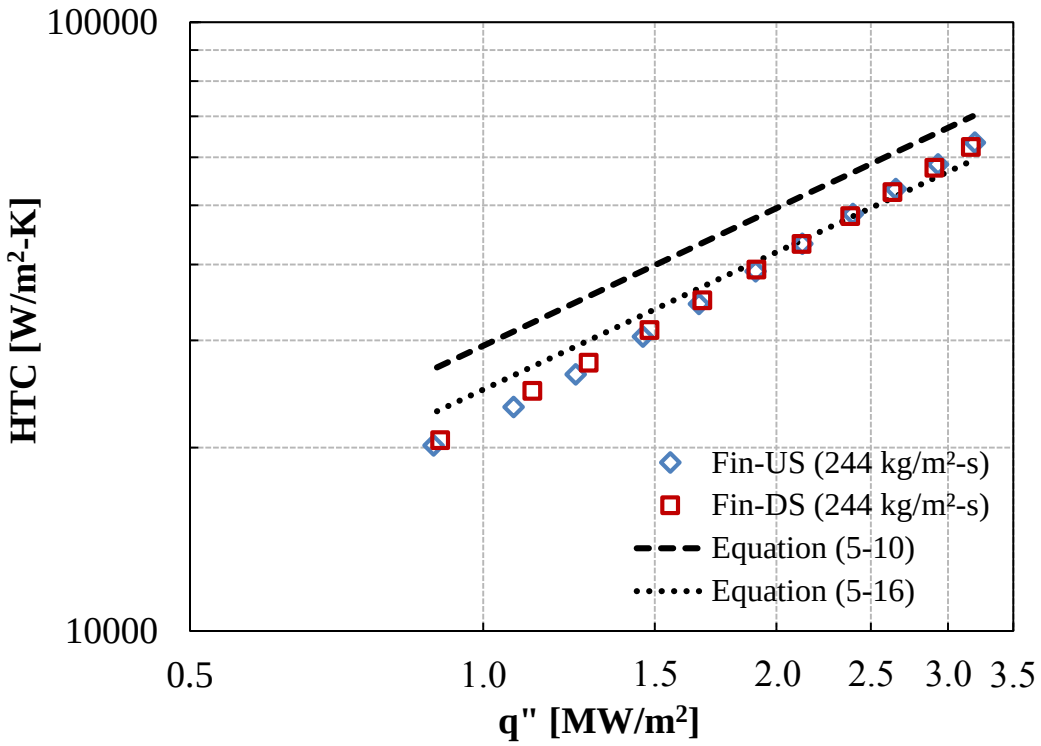

Figure 5-45: Comparison of modified correlation and experimental data (244 kg/m^2-s).

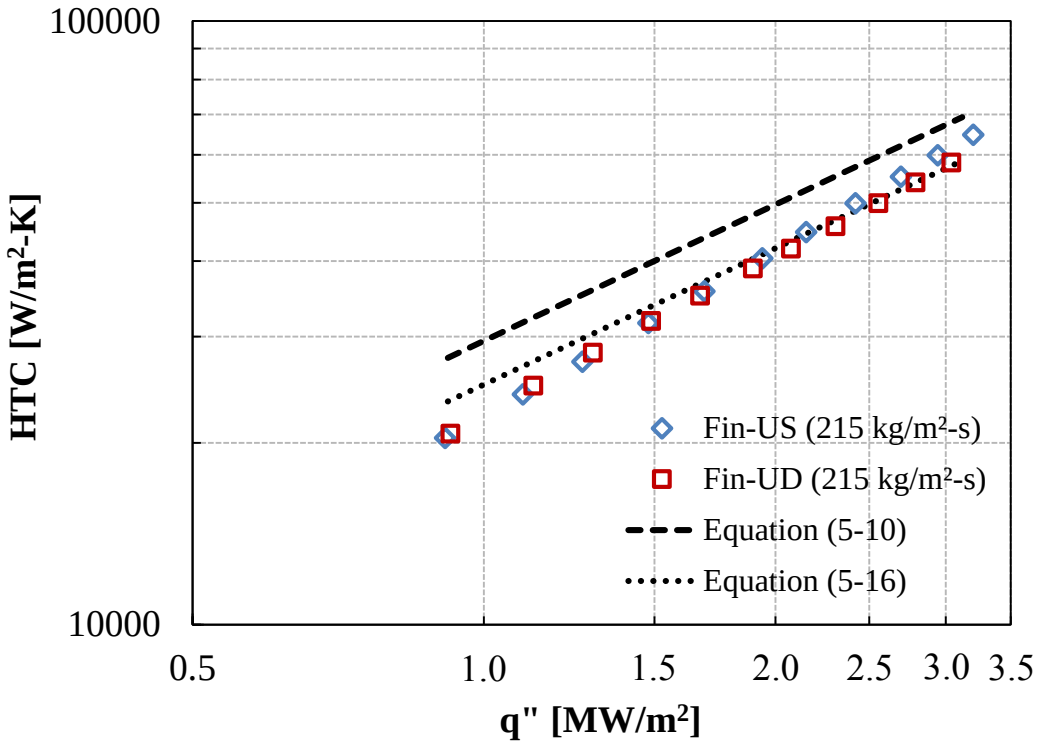

Figure 5-46: Comparison of modified correlation and experimental data (215 kg/m^2-s).

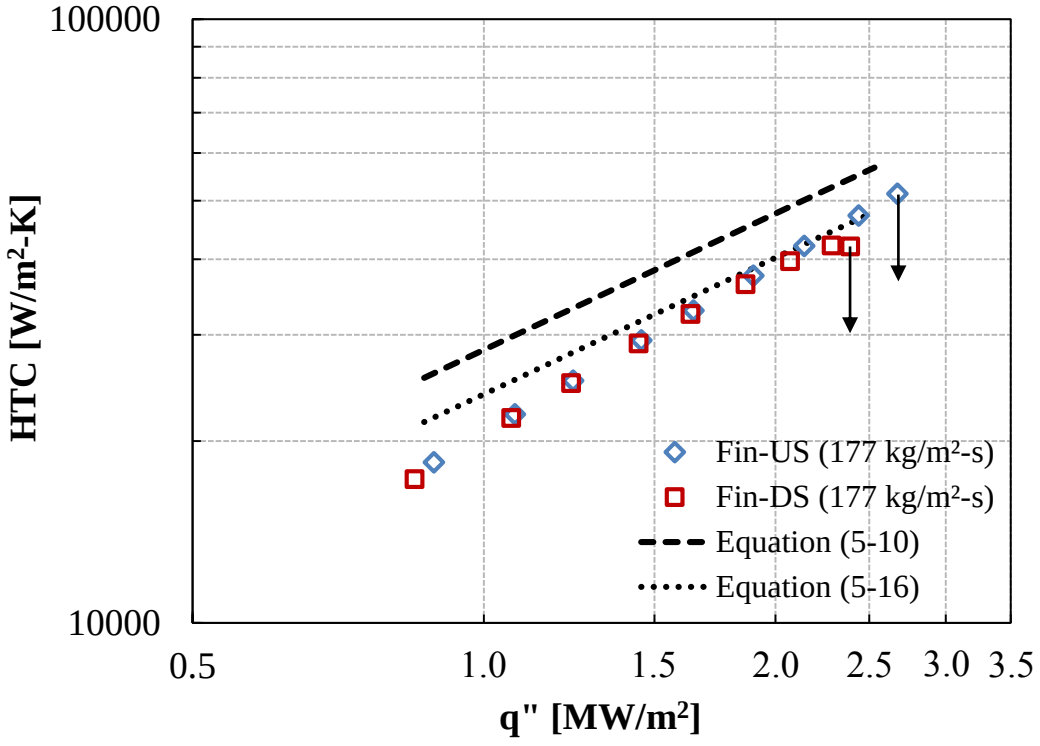

Figure 5-47: Comparison of modified correlation and experimental data (177 kg/m^2-s).

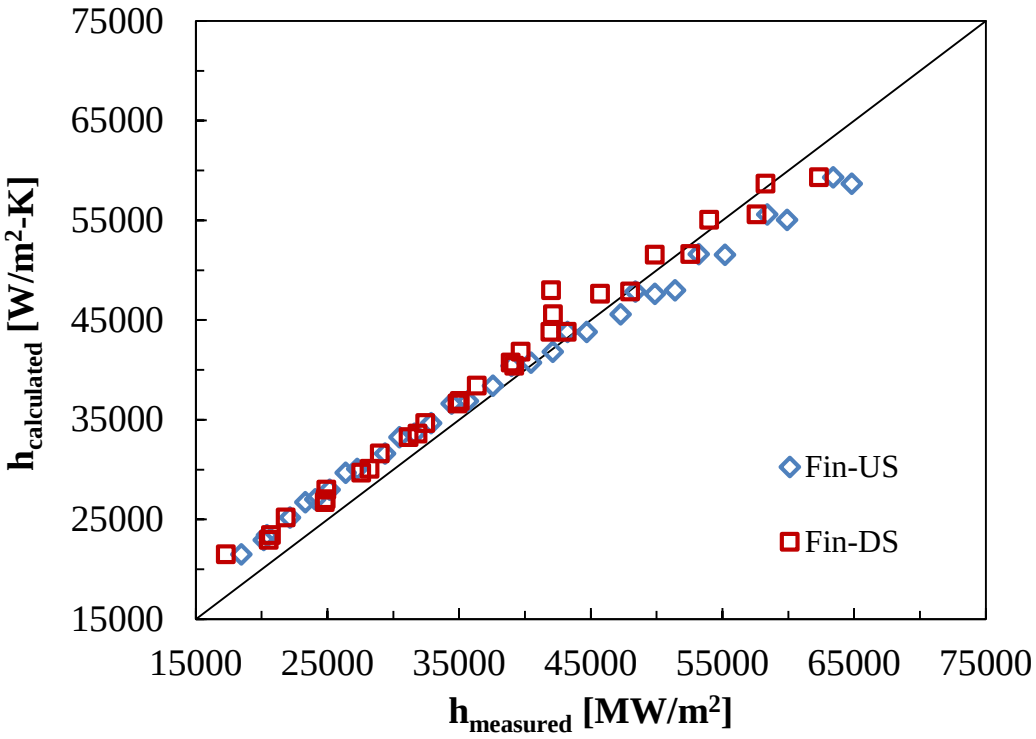

Figure 5-48: Comparison of predicted (Equation (5-16)) and measured HTCs.

5.5.4 Bubble Accumulation Frequency

The effect of the bubble accumulation on the heat transfer has been mentioned in previous sections. In this section, the frequency of the bubble accumulation is described. To clarify, this analysis was performed only for the finned surface. In the downstream location the bubbles were found to accumulate, depart from that location, and accumulate again. In some cases the bubble presence is prolonged on the boiling surface. In order to calculate the frequency, a longer visualization time was required to observe the phenomenon. The camera speed was reduced to the lowest frame rate which permitted the longest recording time available. The experiments were performed at the highest heat flux for 244 kg/m^2-s and 215 kg/m^2-s.

The bubble accumulation was defined from the beginning of the accumulation of a bubble downstream until its complete departure from the boiling surface. Visually the process can be seen in Fig. 5-49. A condition was applied for the analysis: bubbles having an accumulation time of one second or more were considered. The reason for the condition is that smaller accumulation times may not affect the downstream temperatures significantly. The recorded

data was converted to individual images, which totaled 5,457 images. The images were then analyzed manually to obtain the frequency.

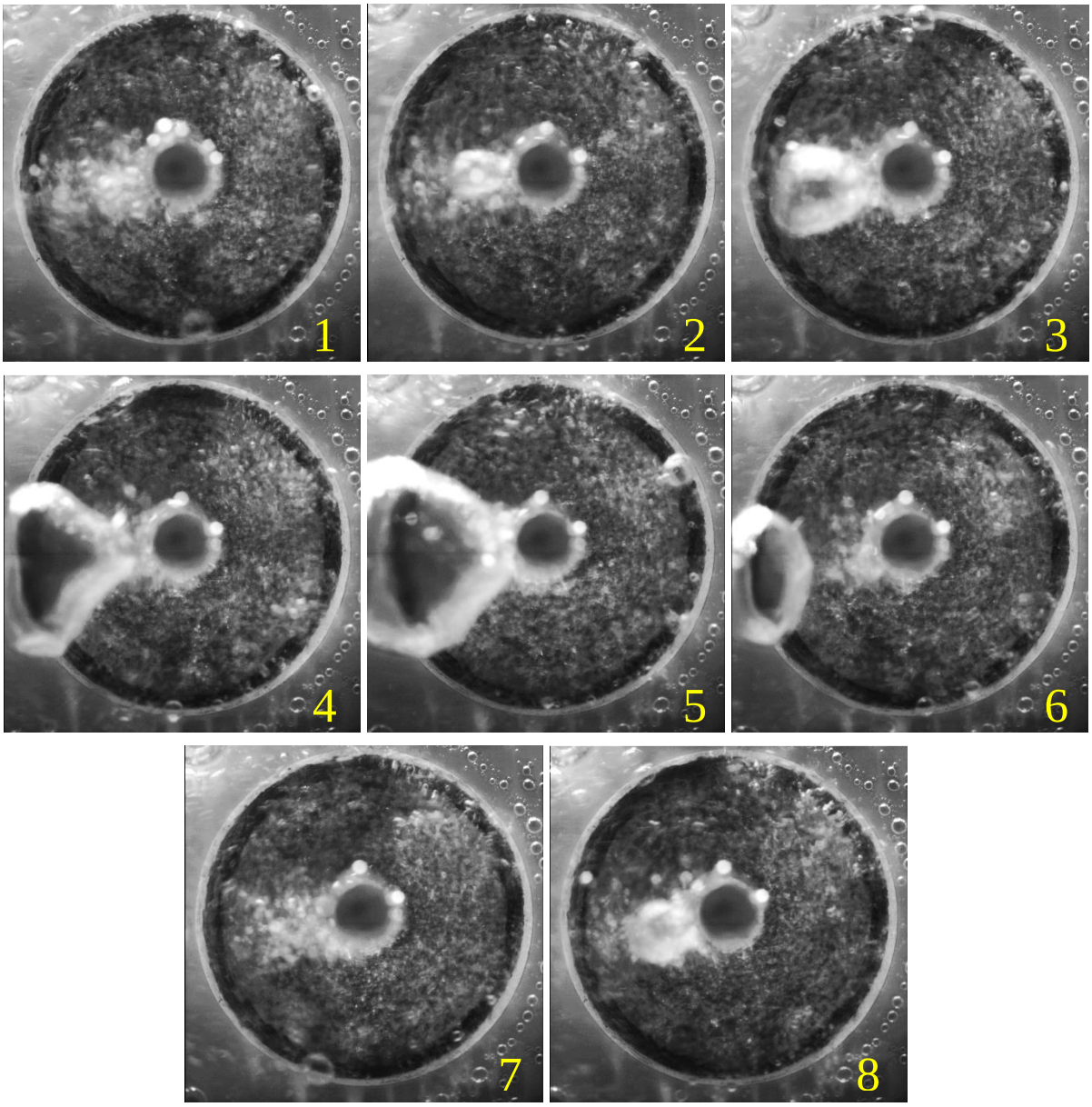

Figure 5-49: Process of bubble accumulation downstream of fin: accumulation starts (1-2), bubble grows in size (2-5), bubble departs from surface (5-7), and process starts again (7-8).

Two important quantities were defined from the obtained data: the bubble accumulation frequency and the bubble presence ratio. The bubble accumulation frequency was simply defined as the number of accumulations that occurred on the surface per minute. The bubble

presence ratio was defined as the total time of all bubble presence on the surface divided by the total observation time. In other words, the bubble presence ratio is the temporal ratio of the total time of all the bubble accumulations to the total recorded time.

The results of the manual analysis of the images are shown in Fig. 5-50 for 244 kg/m^2-s and in Fig. 5-51 for 177 kg/m^2-s. The x-axis in the figures represents the visualization time, and the y-axis shows the state of bubble presence. A value of 0 was assigned when there was no bubble accumulation occurring on the surface. A value of 1 was assigned when accumulation was observed. In the Figs. 5-50 and 5-51 a sudden change of the bubble presence on the surface from 0 to 1 implies the start of the accumulation, and a sudden drop implies removal of the accumulation from the surface. In some cases the removal of an accumulated bubble and the starting of another accumulation occur very rapidly, and is shown by a rapid transient from a value of 1 to 0, and again to 1.

The results are summarized in Table 5-7. As the table shows, a frequency of 16 bubbles per minute was obtained for the high flow rate and was reduced to 12 bubbles per minute for the medium flow rate. While the bubble frequency decreased from high to medium flow rate the bubble presence ratio increased. As the flow rate decreases less bubbles accumulate on the surface, but remain on the surface for a longer period. This can be seen in Figs. 5-50 and 5-51. In Fig. 5-50 there are a greater number of incidents for the bubble presence that reach a value of 1 compared to Fig. 5-51. On the other hand, when a bubble presence incident reaches a value of 1 it remains at that value for a longer time in Fig. 5-51 compared to Fig. 5-50. This presents a potential risk for the heat transfer. The longer a bubble remains on the surface, the higher the surface temperatures will become for that duration. Figure 5-52 shows the thermocouple temperature data during the bubble frequency experiments. The sharp peaks are clearly visible in the figure. They represent a rapid temperature increase due to the inadequate cooling of the surface when bubble accumulation occurs. If the bubble presence is prolonged, the temperature increase will become larger. Also, the surface may possibly become damaged with a higher presence ratio.

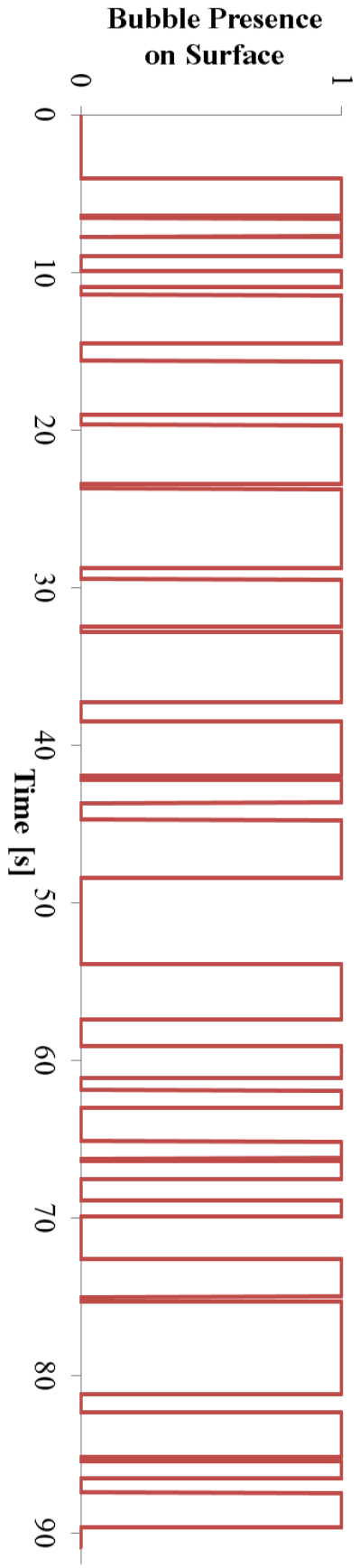

Figure 5-50: Manual analysis of the bubble presence for 244 kg/m^2-s.

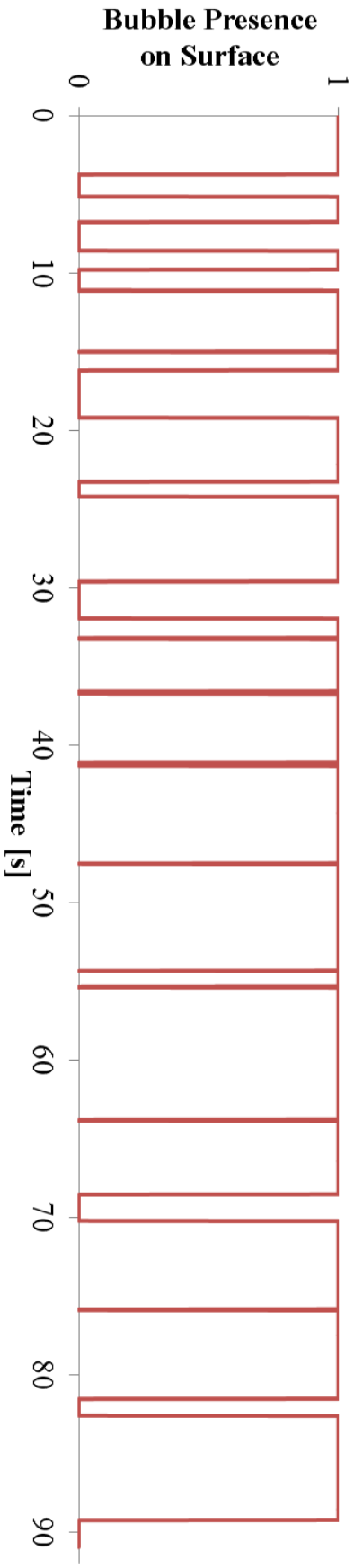

Figure 5-51: Manual analysis of the bubble presence for 215 kg/m^2-s.

Table 5-7: Summary of bubble accumulation frequency for high and medium flow rates.

	244 kg/m^2-s	**215 kg/m^2-s**
Downstream T_S	125.0 °C	127.6 °C
Downstream q''	3.11 MW/m^2	3.07 MW/m^2
Bubble Frequency	16 bubbles/min	12 bubbles/min
Presence ratio	≈ 68%	≈ 83%

Figure 5-52: Temperature profiles of three thermocouple locations inside the finned copper block during the bubble frequency experiments (vertical division: 30 seconds).

5.6 Summary: Subcooled Flow Boiling Experiments

The following summarizes the work performed in the subcooled experiments:

- Downward-facing flow boiling data was obtained. Such studies are not commonly found in literature.
- Experiments were performed for highly subcooled conditions, which are not commonly seen in flow boiling studies.
- Flow boiling heat transfer was investigated from a finned surface, and compared with a bare surface.

- Relatively low flow rates were applied to study the boiling behavior from downward-facing heated surfaces. Three mass flux were applied: 244 kg/m^2-s, 215 kg/m^2-s, and 177 kg/m^2-s.
- CHF conditions were only observed for the lowest flow rate (177 kg/m^2-s).

The following summarizes the conclusions from this chapter:

- A pin-fin was able to enhance the heat transfer from a downward-facing heated surface in subcooled flow boiling conditions.
- The ability of the fin to enhance the heat transfer was greater when the conditions were farther from CHF.
- An average heat transfer enhancement of 5% was observed for the high and medium flow rates for the upstream location, and 3% for the low flow rate.
- The heat transfer from the finned surface was reduced at low flow conditions. Even with the presence of a fin, a reduction in the local heat transfer coefficient for the downstream location was observed.
- The wake produced downstream caused bubble accumulation. The accumulation may have been the cause of CHF, thereby reducing it.

In short, an enhancement and reduction in the heat transfer was observed from a finned surface. Furthermore, bubble formation at a specific location for a substantial amount of time may cause local hot spots leading to high surface temperatures.

6. DOWNWARD-FACING SATURATED FLOW BOILING WITH BARE AND FINNED SURFACES

In this chapter, downward-facing flow boiling experiments were performed with bare and finned surfaces at reduced pressure saturated conditions. It is important to study flow boiling under saturated conditions since such conditions are believed to exist when ex-vessel cooling is applied to mitigate a severe accident. Again, the focus of this study is on the heat transfer effect from a finned surface in downward-facing flow boiling. The results are compared with a bare surface to observe the improvement obtained from the finned surface.

6.1 Experimental Loop

A completely new experimental facility was designed to perform saturated flow boiling experiments under reduced pressure conditions. The facility had heating capability, was well insulated, and provided closed conditions in which depressurization was performed. The reason for using reduced pressure conditions was to reach saturation at a lower temperature. Water reaches saturation at 100°C when at atmospheric pressure. If the pressure is reduced to half of atmospheric pressure, the saturation temperature becomes approximately 81°C. Such conditions were applied in the current experiments.

Figure 6-1 shows an image of the new experimental loop and Fig. 6-2 shows the detailed design. The flow loop facility is very compact with approximate dimensions of 1.70 m (length) x 0.70 m (width) x 1.40 m (height). Since it was designed for easy transportability, the entire flow loop structure had been placed on wheels. It was desired to move the flow loop facility to a different location for another type of experiment. The experiment, which is part of future work, is to perform live irradiation experiments related to Radiation Induced Surface Activation (RISA).

The flow loop consisted of a small pump, control valve to control the flow, a flow meter, an upstream tank (no heater), a flow channel with the test section, and a downstream tank (with heater). Each individual part of the flow loop is described in detail in the following sections.

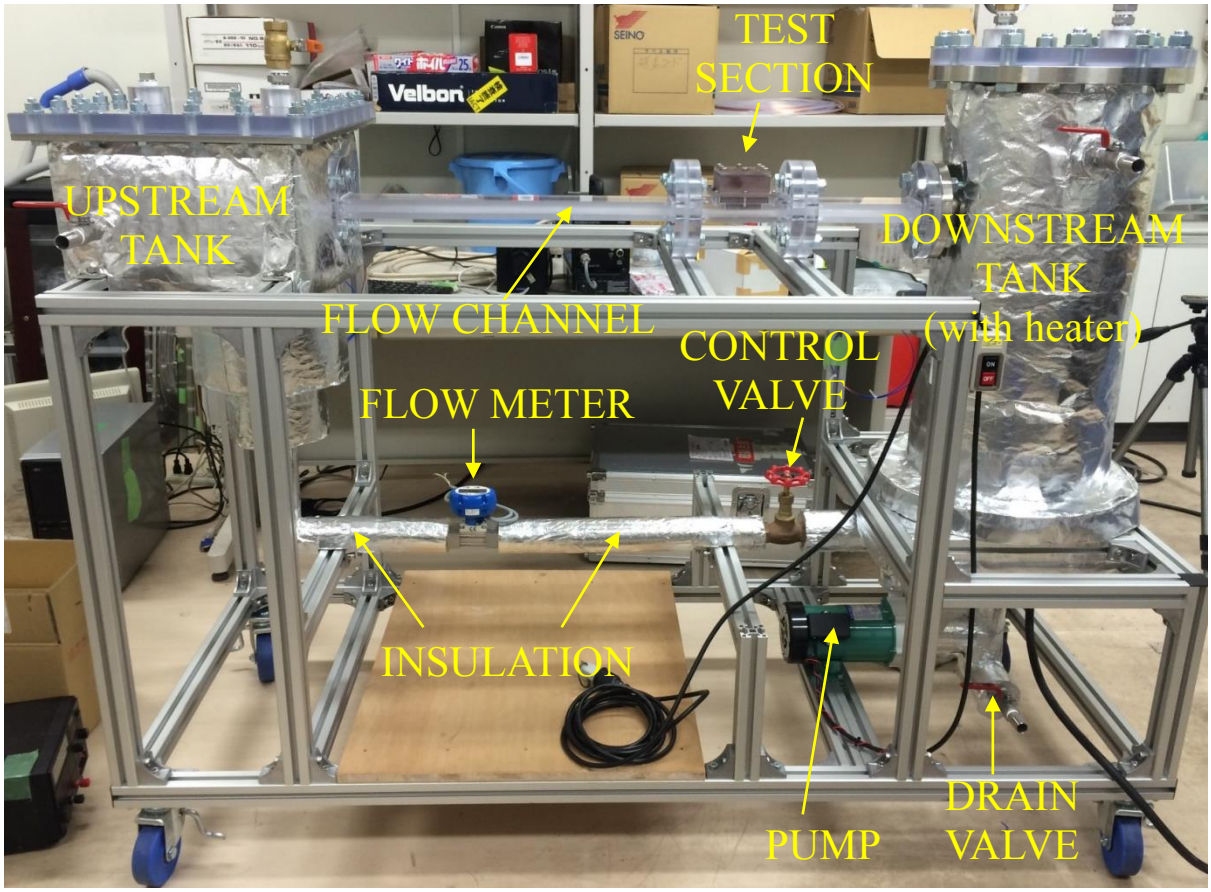

Figure 6-1: Reduced pressure flow boiling facility.

6.1.1 Pump

A 100V magnetic pump (Fig. 6-3) manufactured by Iwaki Co., Ltd. was used in the new experiment facility. The pump was smaller compared to the pumps in the previous subcooled experiments (Chapter 5). Since the facility was also smaller, the flow provided by the pump was sufficient for current experiments. The pump was directly installed onto the facility structure. The pipe leading from the bottom of the downstream tank was connected to the inlet of the pump. The outlet from the pump was connected to the pipe leading to the control valve, flow meter, and the upstream tank. Unlike before, the current pump did not have any controller devices. When power was applied to the pump, a switch was used to operate the pump. The flow rate was controlled via the control valve. The specifications of the pump are given in Table 6-1.

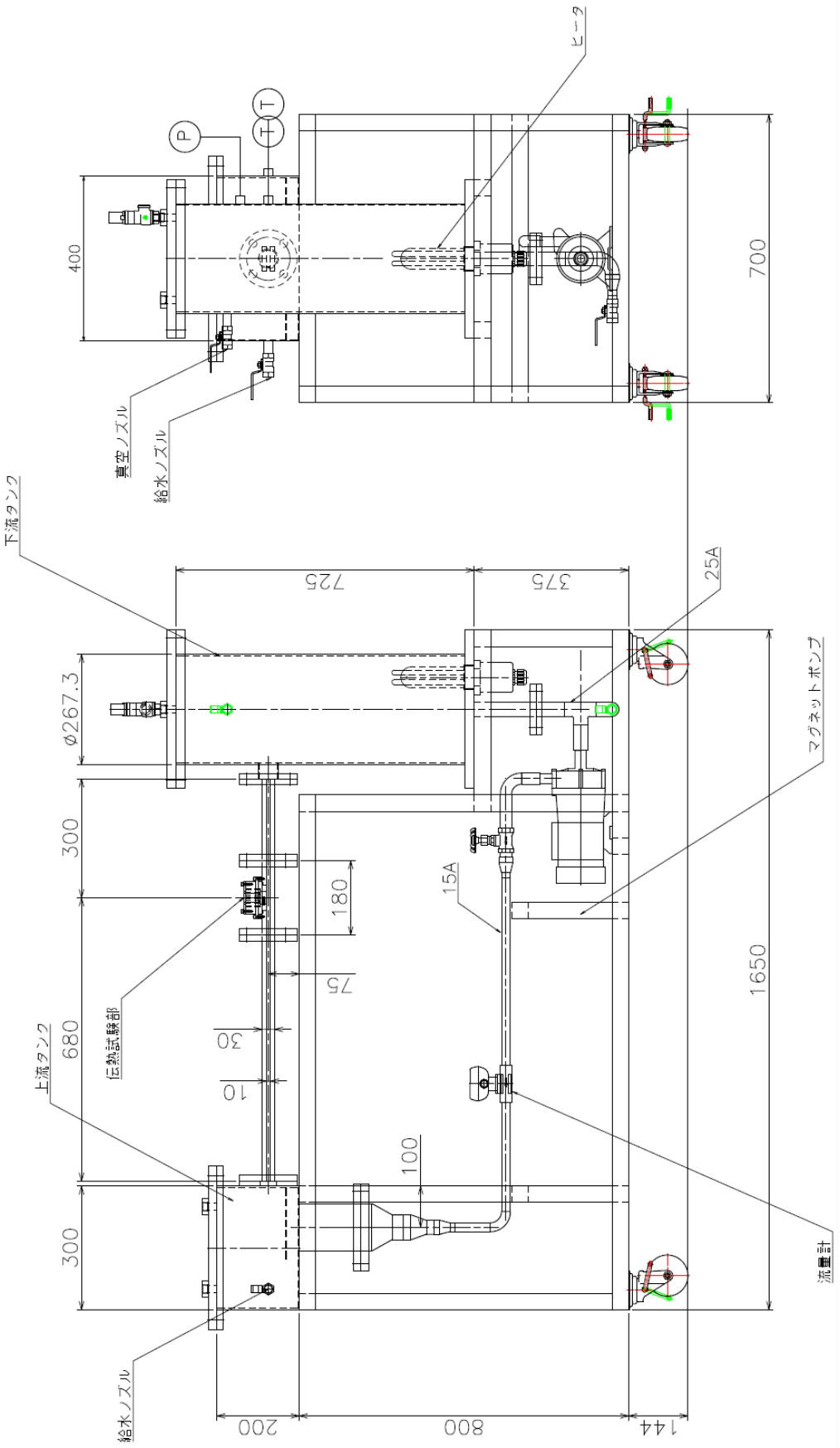

Figure 6-2: CAD design of new flow boiling facility (dimensions in mm).

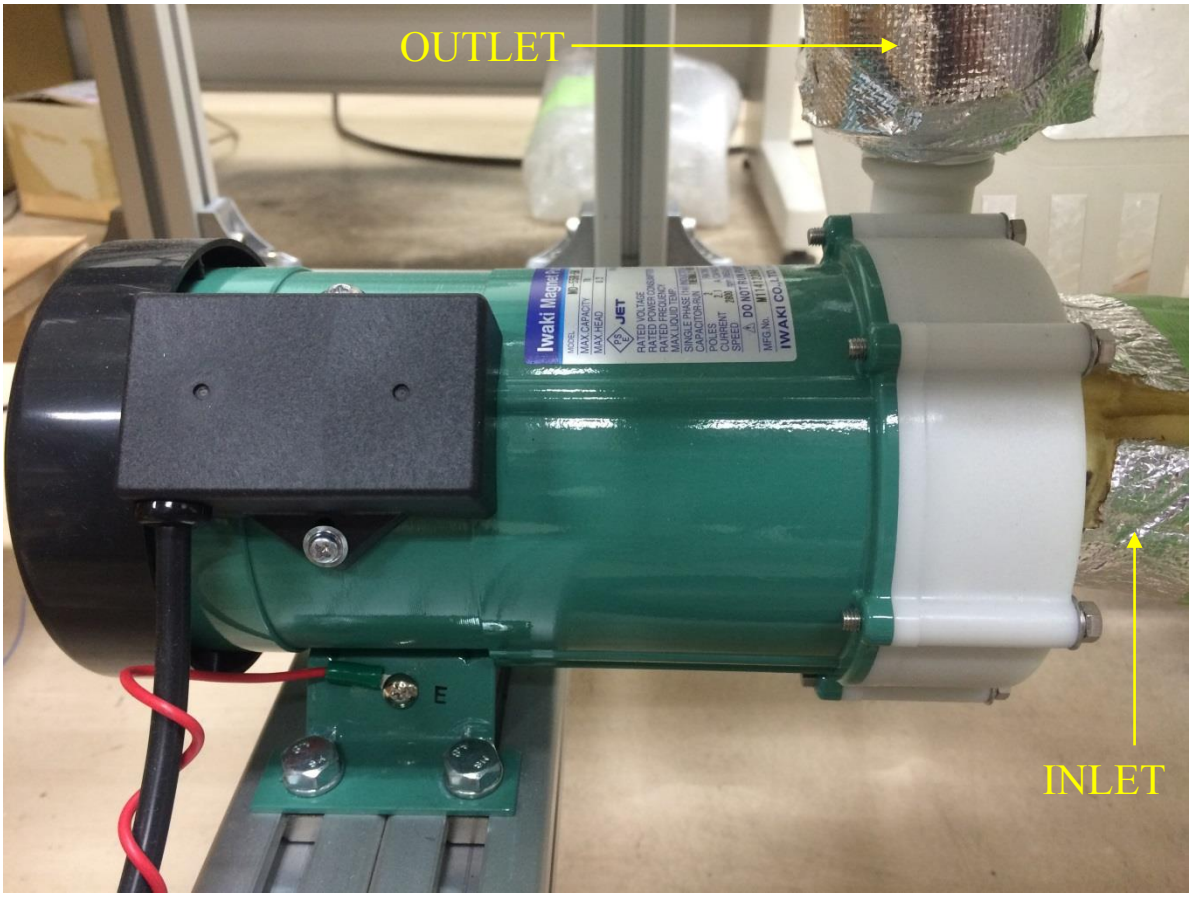

Figure 6-3: Magnetic pump installed in new facility.

Table 6-1: Specifications of the magnetic pump used in the new facility.

MODEL NO.	MD-55R-5M
TYPE	Canned Motor Pump
SPEED	2800 RPM
MAX. HEAD	8.2 m
MAX. CAPACITY	70 L/min
MAX. LIQUID TEMP.	80°C

6.1.2 Control Valve

The control valve was a necessary component of the new facility. Since the pump did not have a separate controller to set a certain speed for the pump (see previous section), the flow conditions for the experiment were controlled by the control valve. Without the control valve, only one flow rate would be available for all experiments.

6.1.3 Flow Meter

A flow meter was installed downstream from the control valve (Fig. 6-4). An Eggs Delta Vortex Flow Meter provided the flow rate measurement for the current experiments. The flow meter was not capable of connecting to a DAQ system to record flow rate measurement data. The volumetric flow rates were displayed on the flow meter screen and were monitored visually. The flow meter required a 12-45V DC power supply in order to operate and display the flow rate measurements. The power supply is shown in Fig. 6-5. The specifications of the flow meter are given in Table 6-2.

Figure 6-4: Flow meter installation downstream from the control valve.

Figure 6-5: DC power supply unit showing connection from the flow meter.

Table 6-2: Specifications of vortex flow meter.

MODEL NO.	FLM21-12SCW
ACCURACY	± 3% of full scale
FLOW RANGE	2.8 – 45 L/min
FLUID TEMP. RANGE	-10 – 80°C

6.1.4 Upstream Tank

The upstream tank (Fig. 6-6) collected the pumped water before it entered the flow channel. The tank was manufactured from stainless steel. A diverting plate was installed inside the tank. to reduce the turbulent mixing of the flow before it entered the flow channel. The flow path for the water is shown in Fig. 6-6. The water entered the upstream tank from the bottom, was

diverted around the plate, and entered the flow channel. In the previous subcooled experiment, a funnel was inserted into the upstream buffer tank for the same purpose. Two valves were placed on the upstream tank. The valve on the side of the tank allowed for water drainage in case it was overfilled. The valve on the top of the tank was used during the depressurization process (see section 6.2). Since experiments were conducted at saturated conditions, it was necessary to monitor the temperature of the water. A K-type thermocouple was inserted from the back side of the upstream tank (Fig. 6-7). The height of the thermocouple was at the same level as that of the center of the flow channel.

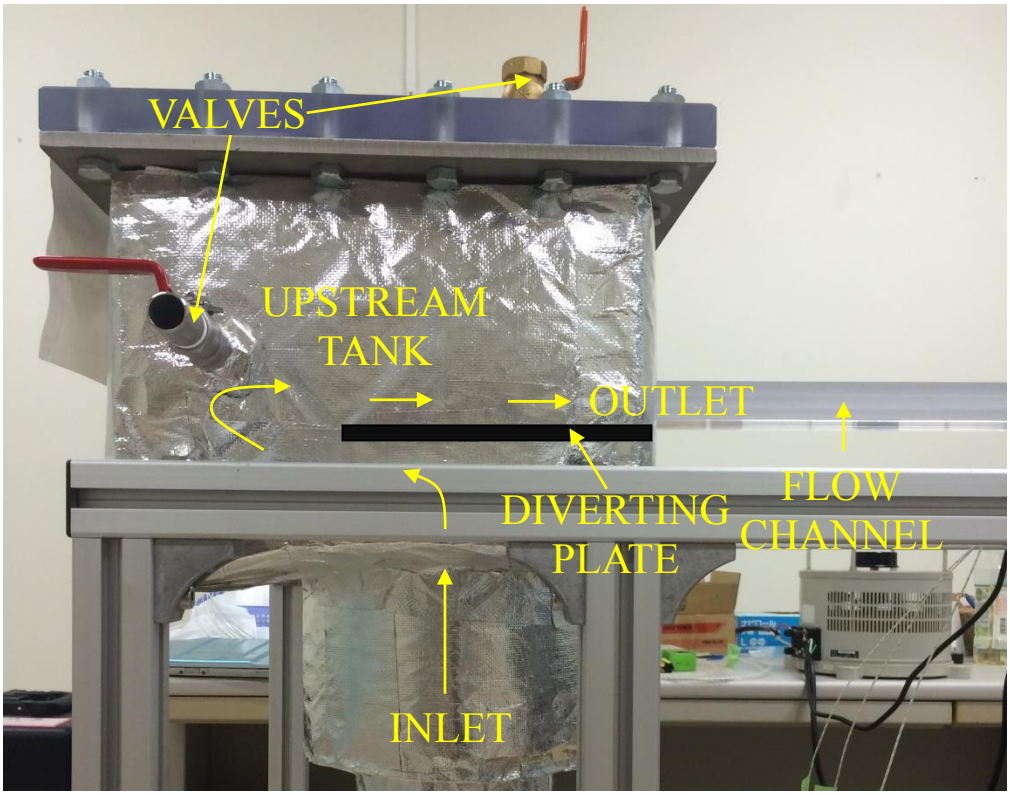

Figure 6-6: Image of upstream tank shown with the water flow path.

6.1.5 Flow Channel

The flow channel (Fig. 6-8) used in the new facility was smaller in size and cross-section that the channel used in previous experiments. The channel was fabricated from polycarbonate in order to withstand high temperatures during saturated boiling conditions. The dimensions of

the flow channel are given in Table 6-3. The channel consisted of three portions: entry portion, test section portion, and exit portion. The test section portion was slightly wider and thicker to accommodate the larger test section. The height of the flow cross-sectional area was smaller compared to previous subcooled experiments. It was desired to perform the current experiments in a thin channel since such type of geometry may be applied for severe accident ex-vessel cooling on the exterior of the vessel surface. For example, confined flow is created in the IVR scenario for the AP1000 when water flows in between the RPV exterior surface and the thermal insulation.

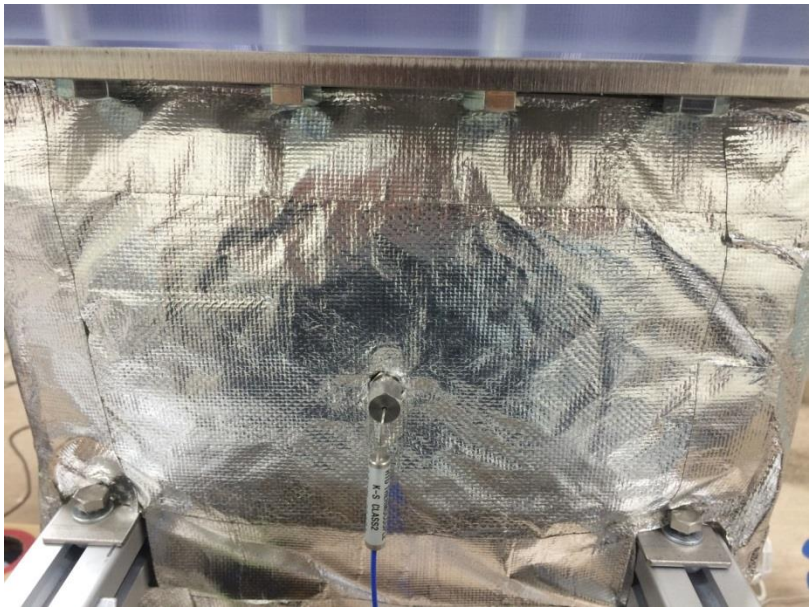

Figure 6-7: Thermocouple inserted in the upstream tank to monitor temperature of the water.

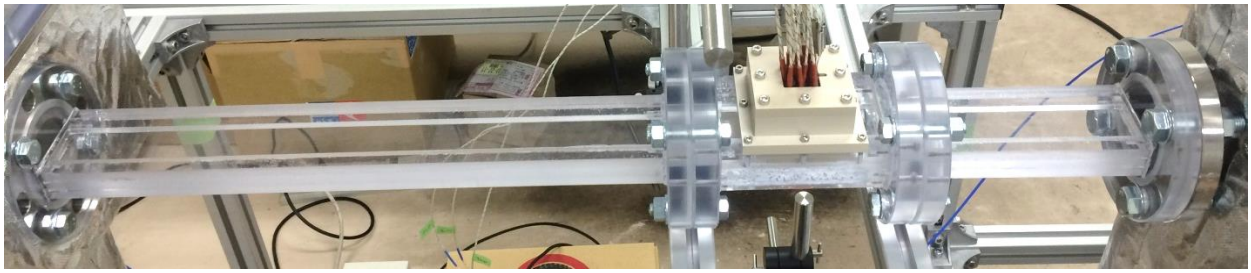

Figure 6-8: Polycarbonate flow channel in the new flow boiling facility.

Table 6-3: Dimensions of polycarbonate flow channel.

Length (L)	980 mm
Width (W)	80 mm
Height (H)	30 mm
Flow Cross-Section	40 mm (W) x 10 mm (H)

6.1.6 Test Section

The test section used in the new facility was designed similar to the test section used previously in the subcooled experiments. Two copper blocks were designed, each with a different surface. Copper was chosen for its excellent thermal conductivity. One block was designed with a bare surface, and the other with a fin located at the center. A comparison of the two surfaces was desired for heat transfer comparison. The copper blocks were designed to be smaller in height and large in surface area. The smaller height would allow more of the generated heat to reach the boiling surface and reduce heat loss. The larger surface area was designed primarily to resolve an issue observed in previous subcooled experiments. Due to a small heated area in the previous experiments, bubbles accumulated outside of the boiling surface and often interfered with the experiment. The total height of the copper blocks was 50 mm, and the boiling surface was a 30 mm x 30 mm square shape. The finned copper block had a similar design, except for the fin protruding from the center of the surface. The fin had a diameter of 6 mm and a length of 9.5 mm. Some design details and images of the test section are shown in Figs. 6-9 to 6-13.

The copper blocks were insulated mainly on the sides to reduce heat loss. PEEK was chosen as the insulation material for its low thermal conductivity. When placing the copper block inside the PEEK insulation, high temperature silicone was applied in the lower portion between the copper block and the PEEK. This was done to prevent water leakage. Also, the silicone provided a seal to prevent air from entering the facility when the system was depressurized. Some properties of copper and PEEK are listed in Table 5-3.

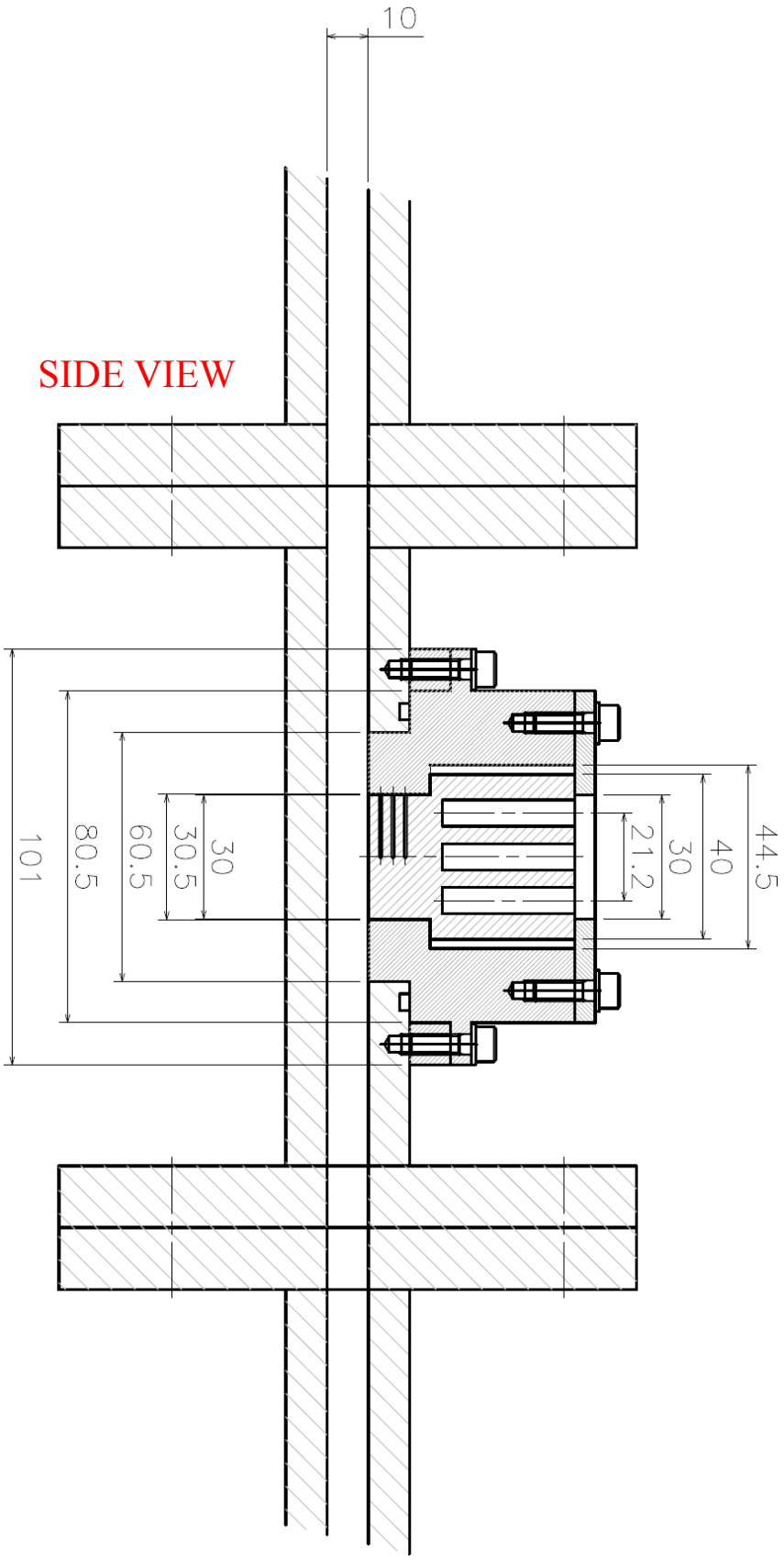

Figure 6-9: Side view of the test section design used in the new facility (dimensions in mm).

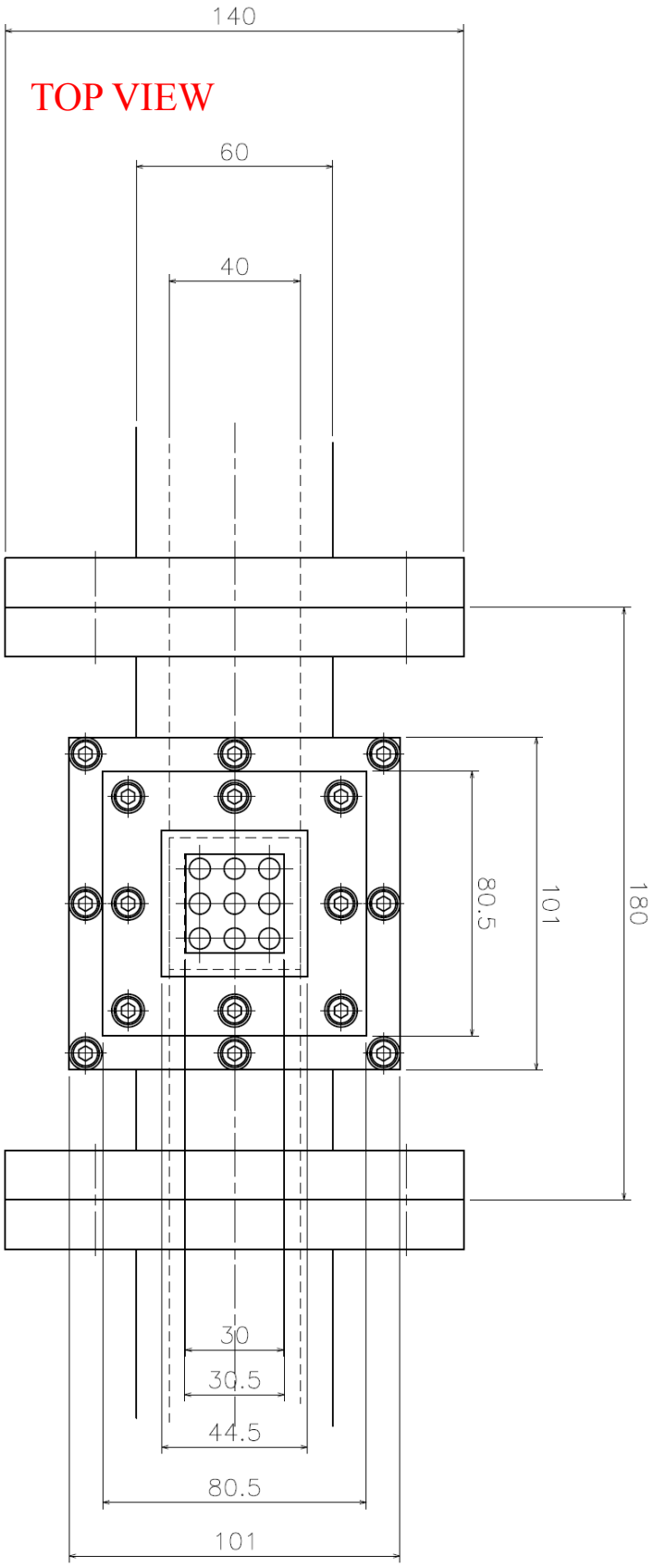

Figure 6-10: Top view of the test section design used in the new facility (dimensions in mm).

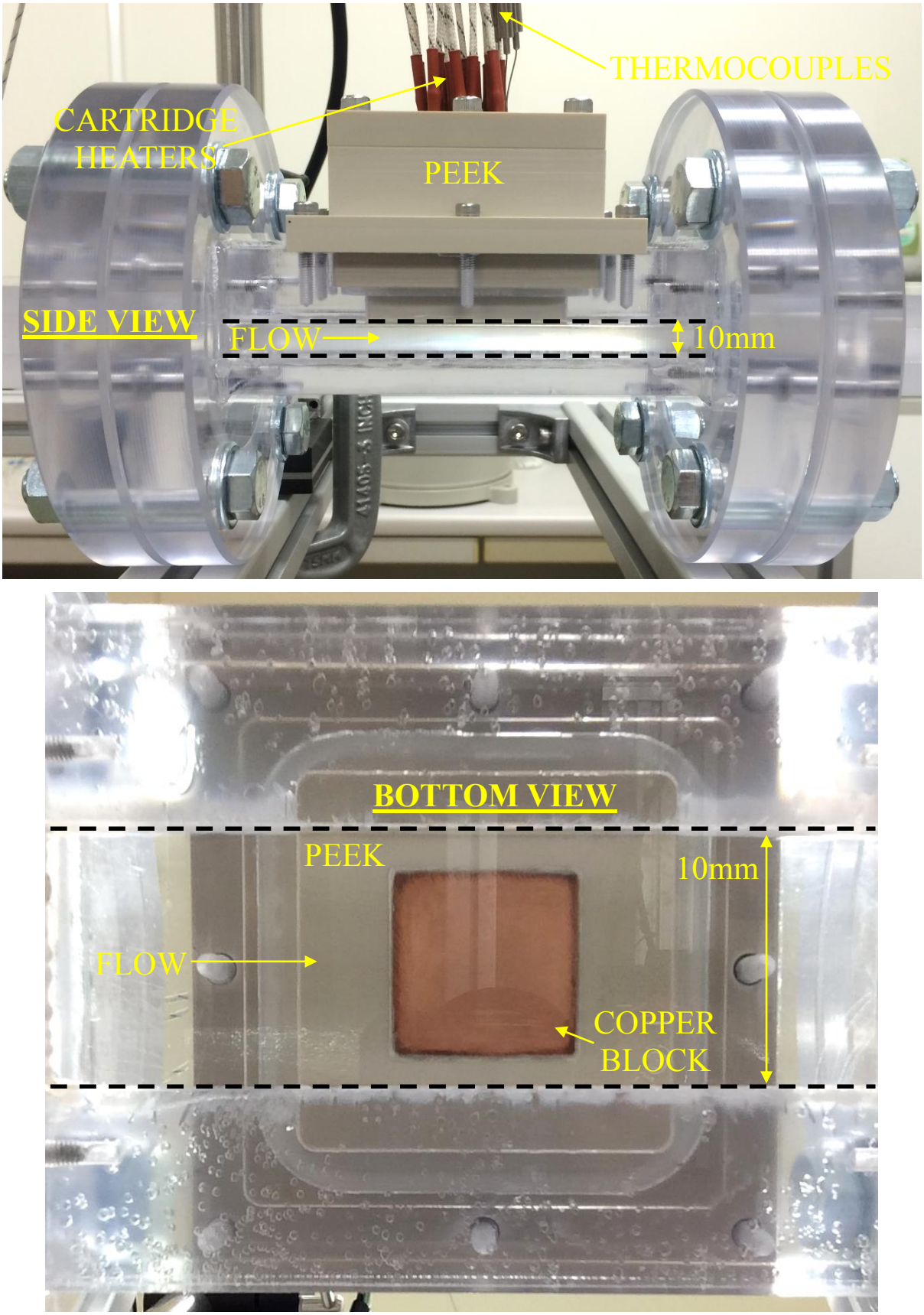

Figure 6-11: Images of side and bottom views of the bare surface test section.

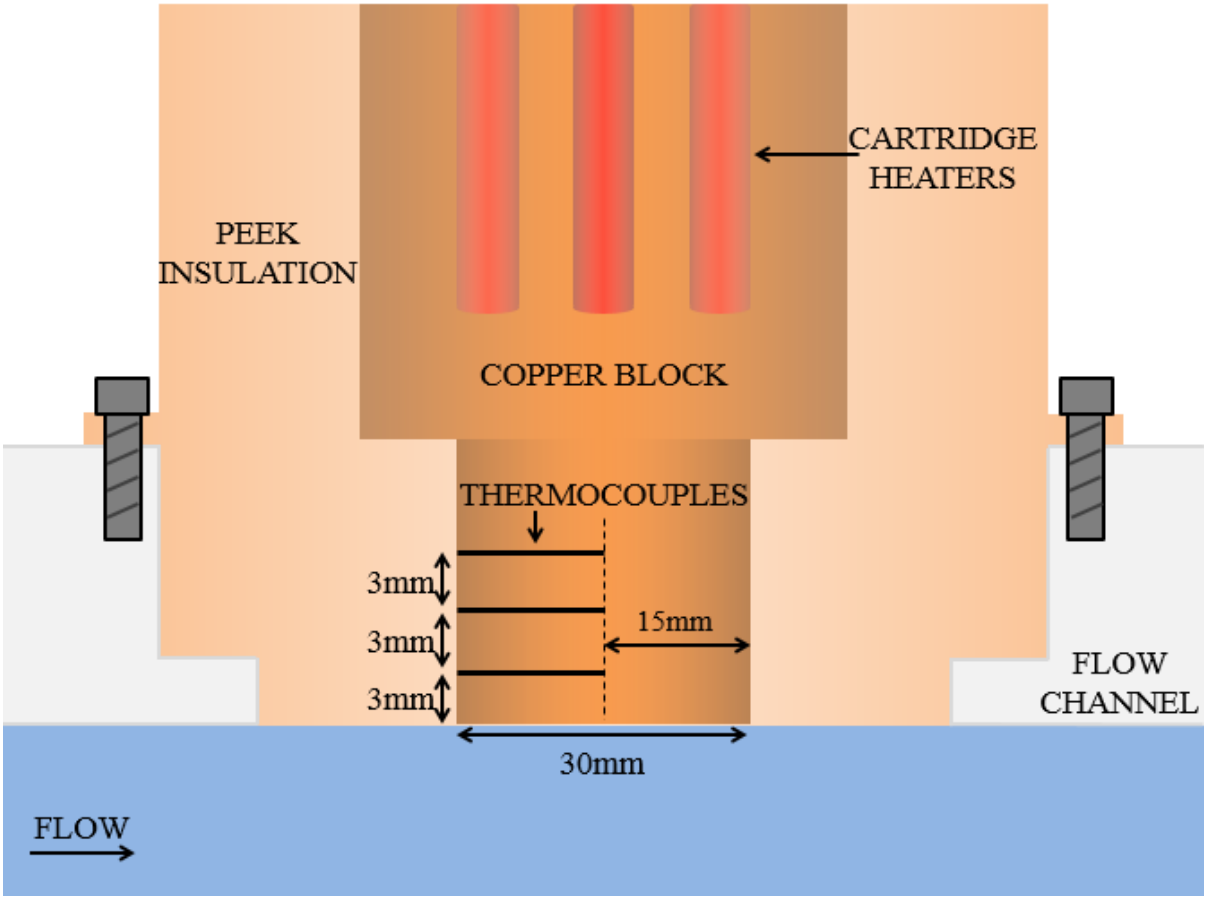

Figure 6-12: Mid-section schematic of bare surface copper block test section (not to scale).

Figure 6-13: Image of PEEK enclosing the bare surface copper block.

6.1.7 Cartridge Heaters

As in previous subcooled experiments, the heat was applied to the copper blocks via cartridge heaters. For the new test section, nine 200V Watlow Firerod cartridge heaters were inserted from the top of the copper blocks (Fig. 6-11). Each cartridge heater was rated at 225W. The heaters had a diameter of 6.25 mm and a length of 31.8 mm. The heater wires were connected to power cables, which were then connected to a slidac (Fig. 6-14). The Yamabishi Electric Co., LTD 200V slidac drew its power from the main power box. The heating for the current test section was provided by nine heaters in order to reach CHF conditions even at relatively high flow rates. Higher power was also required due to the increase in the boiling surface area.

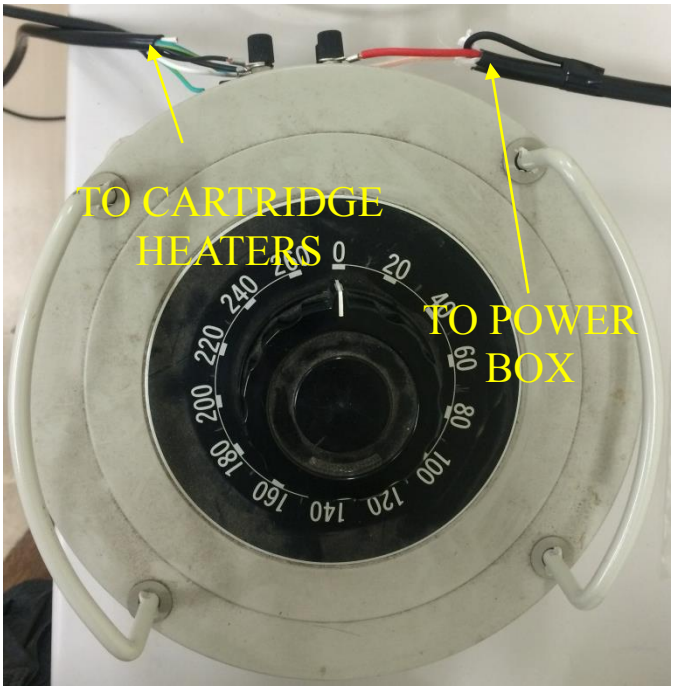

Figure 6-14: Slidac used to power the cartridge heaters.

6.1.8 Temperature Measurement

Temperature measurements were made in a similar manner as in the subcooled experiments. K-type thermocouples (0.5 mm diameter) were inserted in the lower region of the copper blocks (Fig. 6-12) and connected to a Keyence DAQ system (6-15). The measurement uncertainty of

the thermocouples was ± 0.75% of the measured temperature. The closest thermocouple was set at a distance of 3 mm from the boiling surface for both copper blocks. The same height was kept between consecutive thermocouples. For the bare surface, three thermocouples measured the temperatures in the center of the copper block. For the finned surface, three thermocouples measured the temperature before the fin (upstream location) and three thermocouples measured the temperature after the fin (downstream location). The thermocouples were kept at a location of 6 mm from the outer edge (close to PEEK) of the lower cylindrical region of the block. The distance was chosen based on simple simulations performed with ANSYS software. Grooves were manufactured on the inside of the PEEK to provide sufficient space for the thermocouples to exit between the copper block and PEEK. Refer to section 5.1.9 for further clarification.

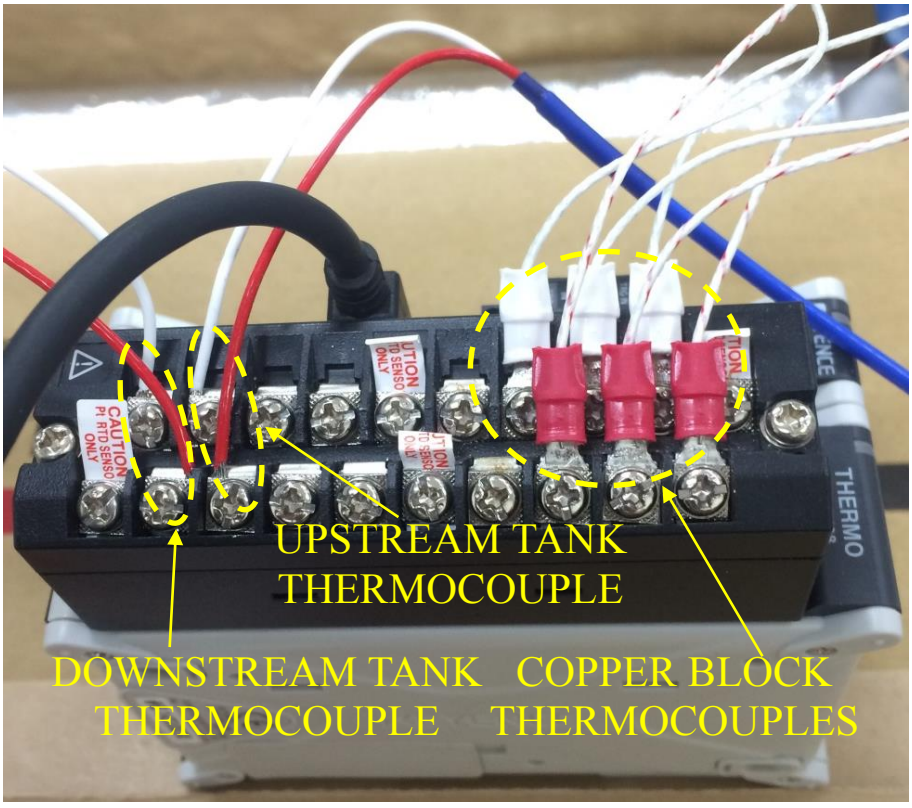

Figure 6-15: Keyence DAQ system used for data recording.

6.1.9 Downstream Tank

After the flow channel, the water returned to the downstream tank (Fig. 6-16). Like the upstream tank, the downstream tank was also manufactured from stainless steel. A 2 kW heater was placed inside the bottom of the tank to heat the water. A separate slidac controller was manufactured to control the heater power. Note that it is not the same slidac used to control the cartridge heaters as shown in Fig. 6-14. At the bottom center of the tank, a hole allowed water to enter into the pipe leading to the pump.

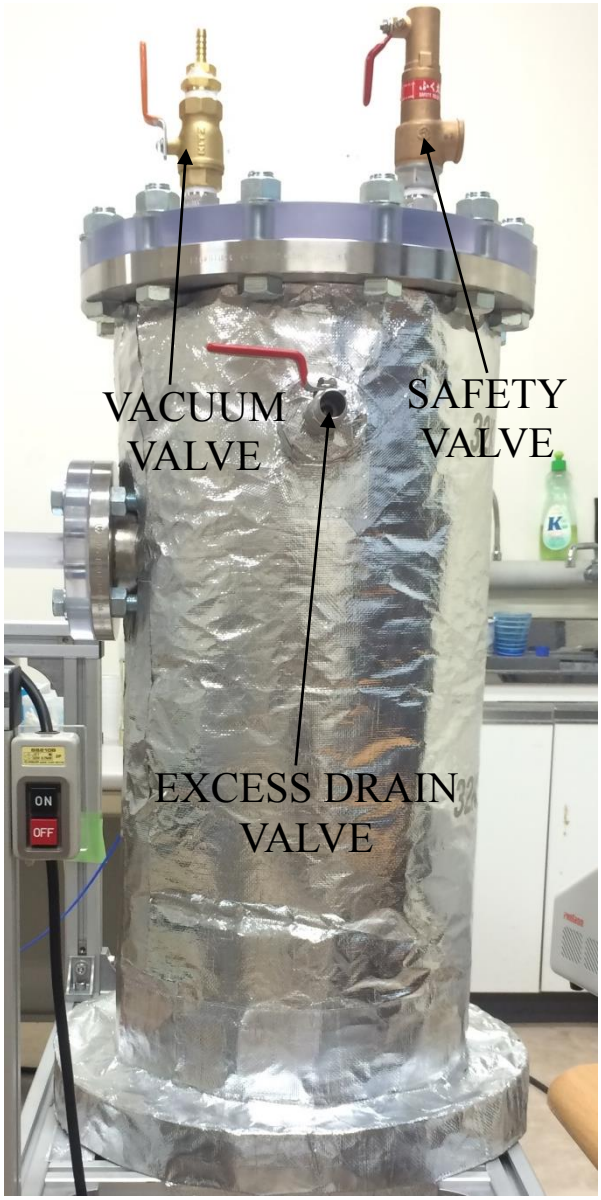

Figure 6-16: Image of downstream tank.

The downstream tank had three valves: safety valve, vacuum valve, and the excess water drain valve. The safety valve opened if the system over-pressurized (not applied to current experiments). A hose designed for vacuum purposes was connected to the vacuum valve and the vacuum pump. The vacuum process was conducted from the downstream tank. The excess water drain valve was inserted in case the water level went above a certain desired level. On the backside of the downstream tank (Fig. 6-17), a K-type thermocouple and pressure sensor monitored the water temperature and system pressure, respectively. The measurement uncertainty of the pressure sensor was 0.8% of the measured output. The pressure sensor was connected to a different Keyence DAQ system (Fig. 6-18) for data measurement, and required a 12V DC power supply to function. Similar to the upstream tank, the height of the thermocouple was at the same level as the center of the flow channel.

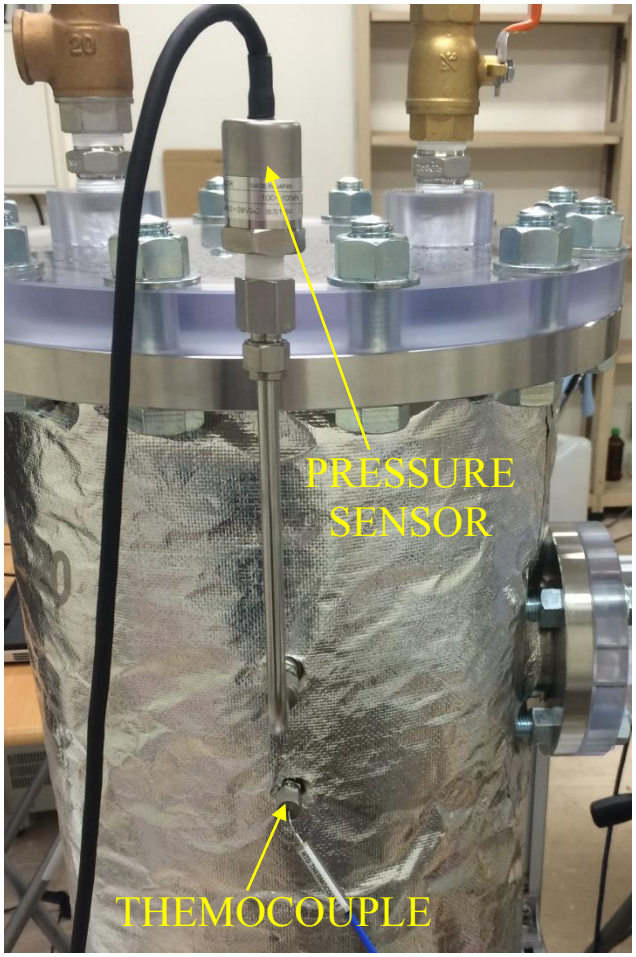

Figure 6-17: Temperature and pressure monitoring in downstream tank.

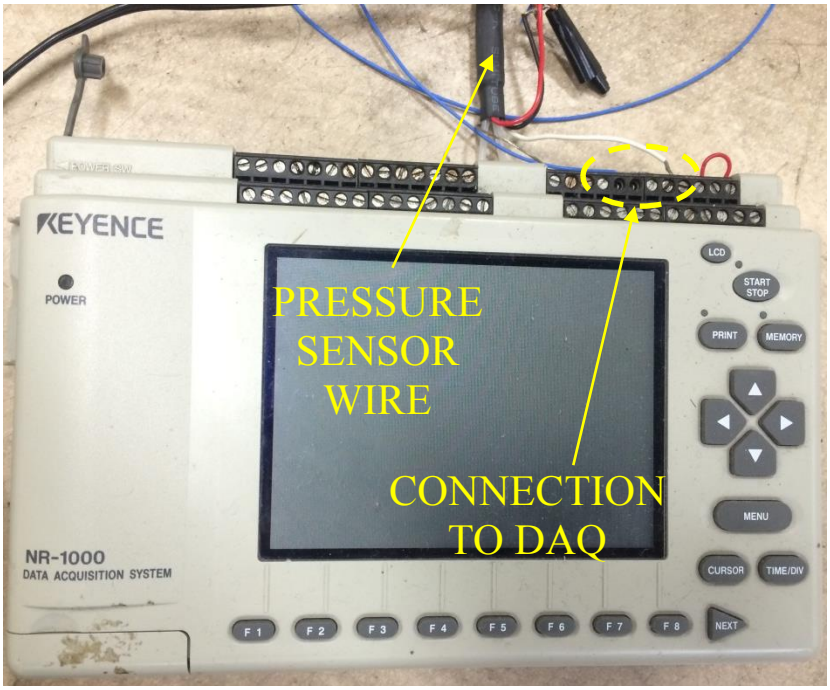

Figure 6-18: Pressure sensor connection to Keyence DAQ system.

6.1.10 Vacuum Pump

A 100V vacuum pump (Fig. 6-19) manufactured by ULVAC Kiko, Inc was used to reduce the system pressure before beginning the experiments. Since the pump did not have an on/off switch, it was connected to a surge protector which operated as the switch. Some specifications of the vacuum pump are given in the table below.

Table 6-4: Specifications of the ULVAC vacuum pump.

Model No.	DOP-80S
Pumping Speed	80 L/min
Ultimate Pressure	5.33 kPa

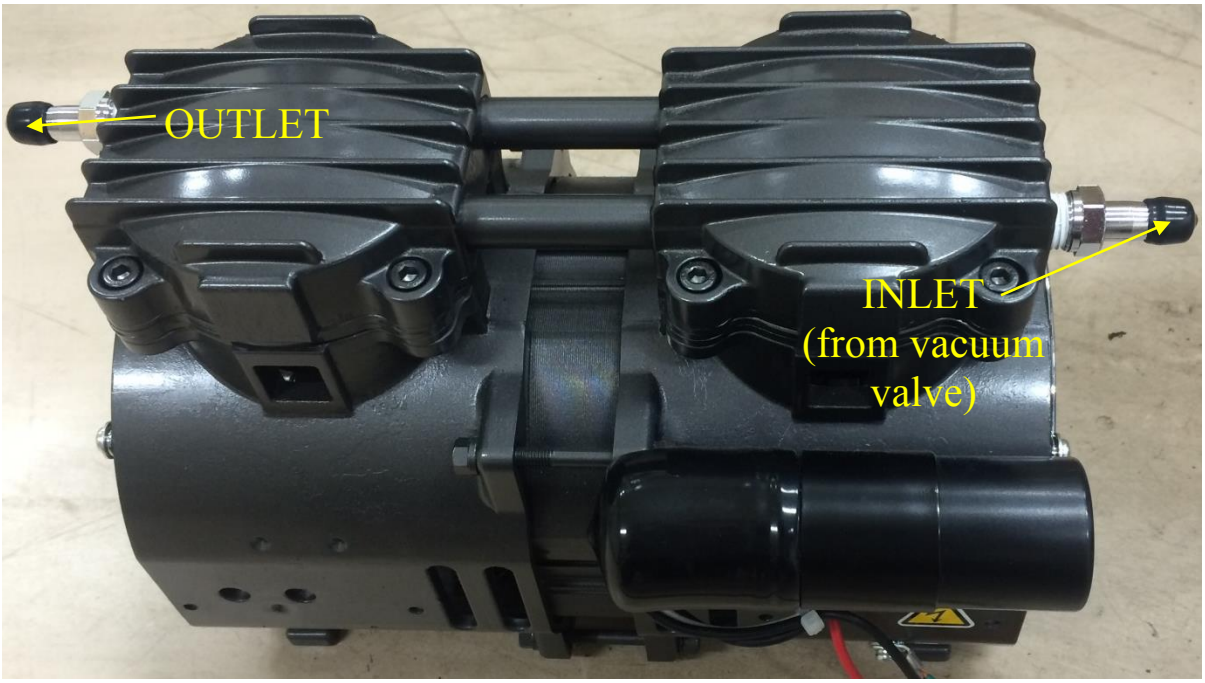

Figure 6-19: Vacuum pump used to reduce pressure in current experiments.

6.1.11 Experiment Visualization

Visualization of both block types was performed mainly for qualitative reasons. The boiling experiments were visualized from below the channel (Fig. 6-20). The visualization during the experiments was performed with the same camera used in the subcooled experiments. Due to limited space in the new facility, the boiling surface was illuminated from only one side by a powerful Photron HVC-SL lamp (Fig. 6-21). Although in the current experiments the resolution always remained at 1024 pixels x 1024 pixels, the frame rate altered between 1000 or 2000 frames per second based on the flow rate.

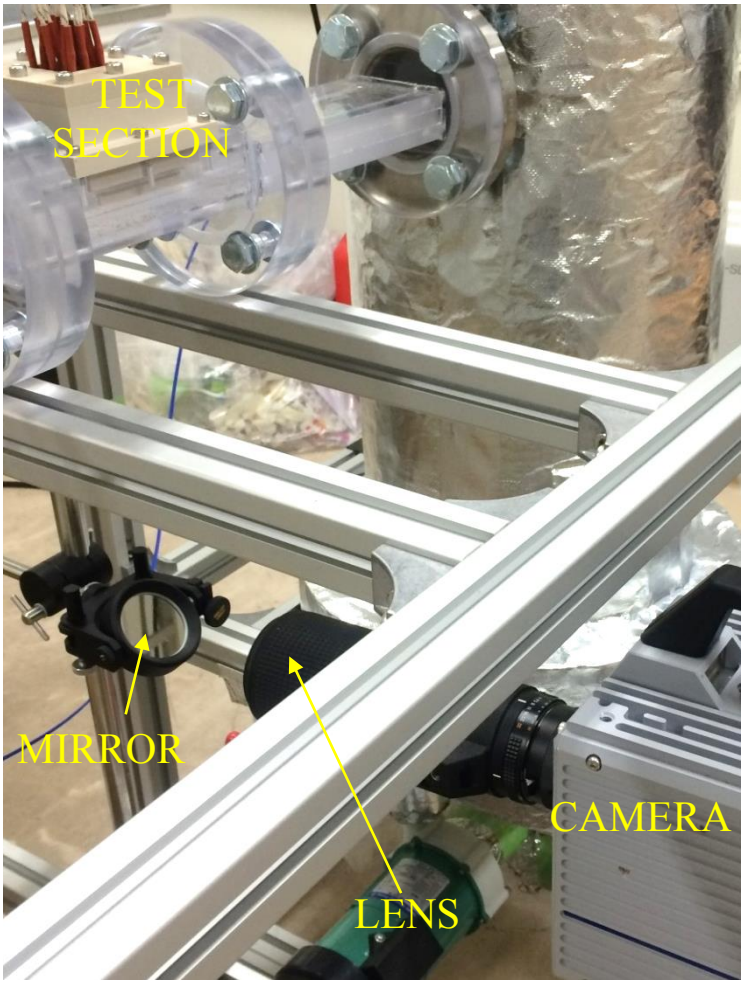

Figure 6-20: Visualization arrangement for new experimental facility (lamp not shown).

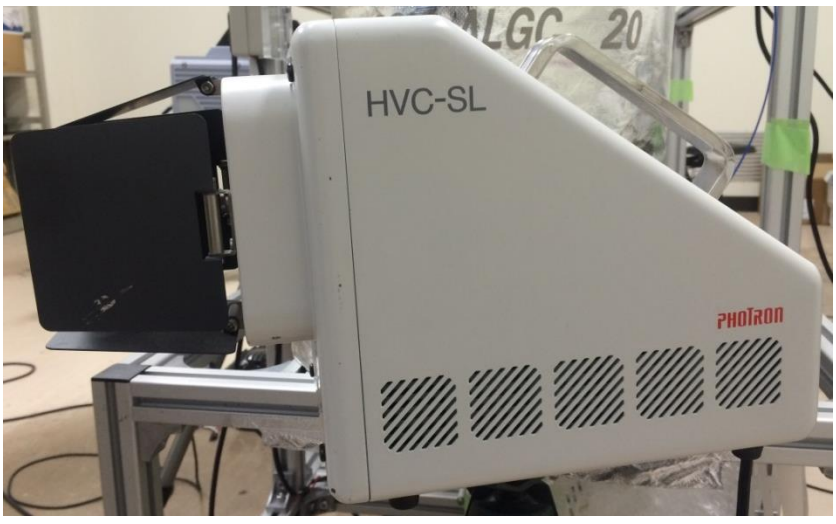

Figure 6-21: Powerful Photron lamp used during the experiments.

6.1.12 Experimental Conditions

The experimental conditions differed from previous subcooled experiments. Distilled water was used for all of the current experiments, whereas tap water was used for the subcooled experiments. It was desired to perform the current experiments at saturated conditions. In order to reach saturation at lower water temperatures, the pressure of the system was reduced to approximately half that of atmospheric pressure. During the experiments, the water temperature was maintained at approximately 81°C. Specific details of the condition of each experiment are shown in the results section.

Due to higher applicable power available, all experiments were capable of reaching CHF conditions even at higher flow rates. Seven different flow rates were applied in the current study. Once again, the current experimental conditions are compared with postulated accident conditions in Table 6-5.

Table 6-5: Conditions of current experiments vs accident conditions.

	Subcooled Experiment	**ULPU(Conf. V)***	**BWR SA Scenario**
Fluid Temperature	≈ 81°C	≈ 90-100°C	≈ 90-100°C
Fluid Pressure	≈ 0.05 MPa	> Atmosphere	> Atmosphere
Boiling Surface	Downward facing: Bare & Fin	Curved (0-90°), Slab	Hemisphere
Surface Size	Bare & Fin: 30mm (square) Fin: D=6mm, L=9.5mm	W=152mm, L≈2500mm	Lower Head with CRGT penetrations
Channel Size	40mm (W) x 10mm (H)	152mm (W) x 76mm (H)	Not Applicable
Reynolds No.	See Table 5-5	2.56×10^5	Unknown

* From: Dinh et al. (2003).

6.2 Experimental Procedure

6.2.1 Boiling Surface Preparation

Prior to performing the experiment, both boiling surfaces were polished with P1200 sandpaper (Fig. 6-22). It was necessary to polish the surface since only one copper block was available for each type of surface. Section 5.2.1 summarizes the preparation for the boiling surface. The same procedure was applied in the current experiments. A detailed description is shown in the Appendix.

6.2.2 General Experiment Procedure

In this section a detailed description is given of the experiment procedure. Before beginning the experiments, the test section had to be removed to polish the boiling surface (described in previous section). In order to do that, the water inside the facility was drained through the drain valve (Fig. 6-1) into a temporary container. Then, the thermocouple wires were disconnected from the DAQ system and the cartridge heaters were removed from the top of the copper block (Fig. 6-23). This step was necessary to prevent damage to the thermocouple and cartridge heater wires. The test section was removed from the flow channel and placed upside down to easily allow for the polishing of the boiling surface.

Figure 6-22: Front (left) and back (right) of P1200 sandpaper used to polish boiling surfaces.

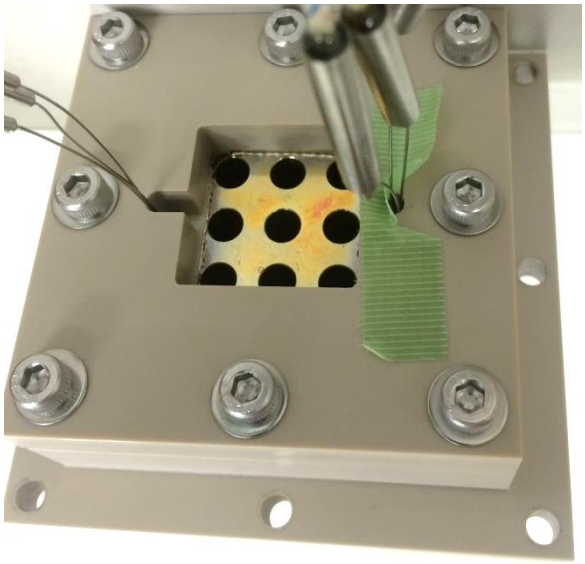

Figure 6-23: Top of the finned test section showing holes designed for cartridge heaters.

After preparing the boiling surface the test section was fixed back onto the flow channel. The cartridge heaters were reinserted into the copper block, and the thermocouples were reconnected to the DAQ system. The facility was refilled with water. An external pump was used during the refilling, as it was more efficient than manually inserting water. The refilling was performed from one of the valves on top of the upstream tank. Once the refilling was complete the valves were closed and the water heating process began. The pump (installed on the facility) was turned on multiple times to circulate the water inside the facility since the water heater was located in the downstream tank.

When the desired water temperature was reached, the control valve was adjusted to set the desired flow rate for the given experiment. Afterwards the valve on the upstream tank was opened to allow air to escape and water to fill up the upstream tank, decreasing the water level below the flow channel height in the downstream tank. This was done so that when depressurization would occur, the water level in both tanks would be above the flow channel height. Otherwise, the water level height in the downstream tank became much higher than the flow channel height and the opposite was observed for the upstream tank. This was experienced during trial experiments, and was not ideal for the experiments.

Next, the depressurization process began. The special vacuum hose was connected to the vacuum valve on top of the downstream tank (Fig. 6-16) and the inlet on the vacuum pump (Fig. 6-19). The facility water pump was terminated and the vacuum pump was started. As the vacuum pump removed air from inside the downstream tank, the water level in the upstream tank decreased and the water level in the downstream tank began to increase. The vacuum process continued until the pressure sensor measurement reached a steady state value, implying that vacuum conditions had been reached for that certain water temperature. The vacuum was shut down when the steady state pressure sensor value was observed. If the vacuum process was allowed to continue, the water level in the upstream tank would fall below the flow channel height. Again, knowledge of the correct water height before beginning the vacuum process was gained from experience during the trial experiments. The water pump was started again after the vacuum process was complete.

The experiments began once the facility was at the desired water temperature and pressure conditions. It should be clarified that preparation for all electronic equipment (computers, camera, DAQ, DC power supply, etc.) was done beforehand. The Photron lamp and the main power for the cartridge heater slidac were the only equipment turned on prior to beginning the experiments. The water temperature was maintained by controlling the water heater slidac.

The slidac supplying power to the cartridge heaters always began at 30V for all experiments. The final voltage value depended on the flow rate applied for that specific experiment, and whether the boiling surface was a bare or finned surface. As the results will show, there was a difference in the final voltage level for the bare and finned surface at the same flow rate. This was not observed in the previous subcooled experiments, where the final voltage was the same for both surfaces at a given flow rate. The voltage levels were incremented in intervals of 10V. The procedure for performing the flow boiling experiments is as follows:

1) A certain voltage is applied.
2) Time is given to reach steady state temperatures.
3) The visualization of the boiling phenomenon is performed during the steady state period.
4) The power is increased to the next voltage level, and steps 2) and 3) are repeated.
5) Step 4) continues until CHF conditions are observed.

All experiments were repeated twice for repeatability purposes, and the averaged results are presented. Figure 6-24 shows an example of a temperature profile for one of the bare

experiments. At CHF the temperatures increased very rapidly. At the occurrence of CHF the slidac voltage was suddenly turned to 0V and the flow rate was increased quickly to reduce the surface temperatures to prevent any damage to the components of the test section, specifically the PEEK insulation.

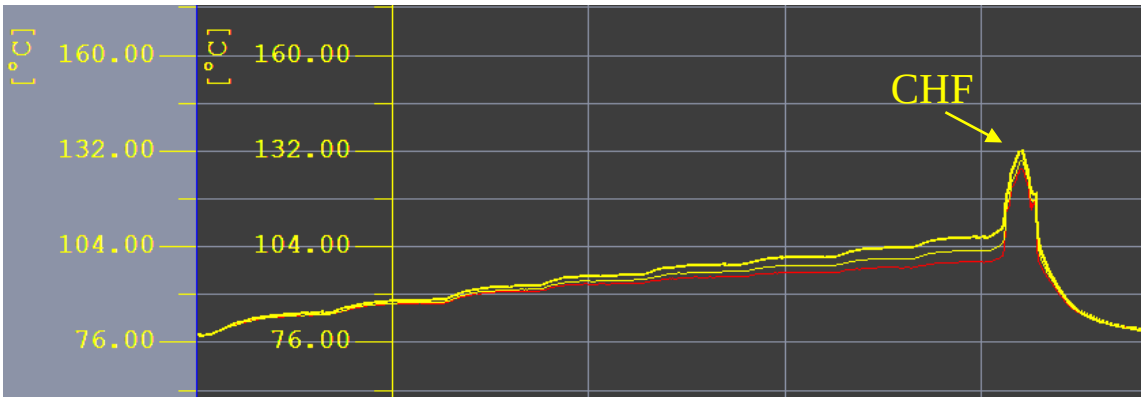

Figure 6-24: Typical temperature profile during B – 3 experiments (vertical division: 5 mins).

The shutdown procedure was performed after reaching CHF conditions. After saving all recorded data, the facility pump was terminated and the valves on top of both upstream and downstream tanks were opened. All equipment was turned off and the facility was allowed to cool down until the next set of experiments.

6.3 Data Post-processing

The data was analyzed in a similar manner as shown in the previous subcooled experiments. The reader is advised to refer to section 5.3 for calculation details. The boiling curves were obtained by calculating the surface temperature with equation (5-2) and the surface heat flux with equation (5-3). The heat transfer coefficient was calculated by

$$h_{\exp} = \frac{q''}{(T_S - T_{SAT})} \tag{6-1}$$

where

T_{SAT} = water saturated temperature at the given pressure during the experiment [°C]

In previous subcooled experiments, T_{film} was used instead of T_{SAT}.

6.4 Bare Surface Results

The bare surface results are the reference case to which a comparison is made of the finned surface results. Therefore, they are presented first. The flow rates will be referred to as the experiment references listed in Table 6-6. The emphasis of the results is on the higher heat flux values where nucleate boiling is assumed to be dominant. CHF conditions were observed in all experiments.

Table 6-6: Experiment reference number and equivalent flow rates for current experiments.

Exp. Reference[1]	**Volumetric Flow**	**Mass Flux**	**Reynolds No.**[2]	**Velocity**
B – 1	36 L/min	1456 kg/m^2-s	6.67x10^4	1.50 m/s
B – 2	32 L/min	1295 kg/m^2-s	5.93x10^4	1.33 m/s
B – 3	28 L/min	1133 kg/m^2-s	5.19x10^4	1.17 m/s
B – 4	24 L/min	971 kg/m^2-s	4.45x10^4	1.00 m/s
B – 5	16 L/min	647 kg/m^2-s	2.97x10^4	0.67 m/s
B – 6	8 L/min	324 kg/m^2-s	1.48x10^4	0.33 m/s
B – 7	5 L/min	202 kg/m^2-s	0.93x10^4	0.21 m/s

[1] B: bare surface.
[2] Based on hydraulic diameter.

The boiling curves for the bare surface are shown in Fig. 6-25 and the average conditions for all experiments are given in Table 6-7. Figures 6-26 to 6-32 are images taken from the

visualization of B-1 to B-7 experiments, respectively. Note that the last data point for each flow rate in the Fig. 6-25 is the CHF value. No specific pattern was observed in the data in Fig. 6-25. For B-6 and B-7 experiments, CHF occurred relatively soon after starting the experiments due to high power input and relatively low flow rates. Comparing the images from the current visualization to the previous subcooled images (Fig. 5-20 to 5-22), a significant difference is apparent in the bubble size. The bubbles are smaller for the subcooled experiments and larger for the current experiments. The reason for this is believed to be the conditions of the experiments. The high subcooling causes bubble collapse to occur. In current experiments, the saturated condition will not cause the bubble collapse. Notice from Figs. 6-26 to 6-32 that many single nucleation sites can be seen, which were not observed in the subcooled experiments.

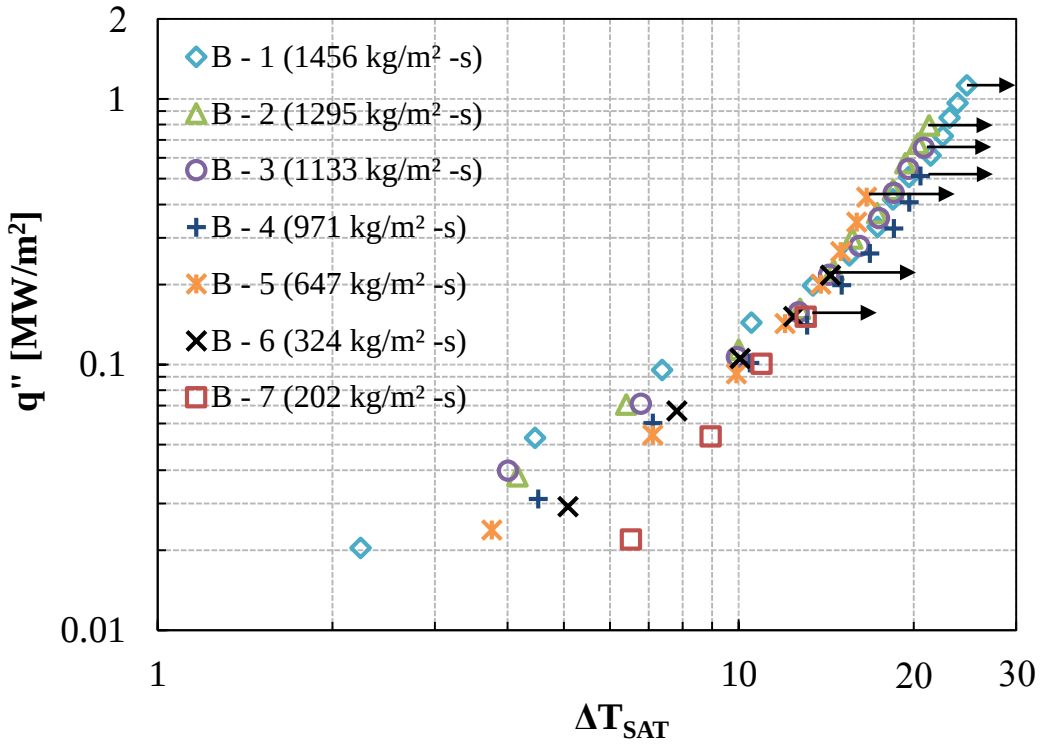

Figure 6-25: Boiling curves for the bare surface in reduced pressure experiments.

Table 6-7: Pressure and temperature conditions for the all bare surface experiments.

	B-1	**B-2**	**B-3**	**B-4**	**B-5**	**B-6**	**B-7**
Pressure	49 kPa	49 kPa	51 kPa	51 kPa	49 kPa	48 kPa	49 kPa
T_{SAT}	80.8°C	80.8°C	81.7°C	81.7°C	80.8°C	80.3°C	80.8°C
US-Tank	81.0°C	81.0°C	82.0°C	82.0°C	81.1°C	80.9°C	80.7°C
DS-Tank	81.1°C	81.0°C	82.1°C	82.0°C	81.1°C	81.2°C	81.4°C

The visual observation made at CHF conditions was slightly different from previous subcooled experiments. In previous experiments the bubble completely covered the boiling surface after the bubble front oscillated many times (Fig. 5-23). The oscillation was not observed in the current experiments. Film boiling conditions are assumed at CHF for current experiments, as the vapor film covers the boiling surface causing rapid rise in thermocouple temperatures. For experiments B-1 to B-5, the relatively high flow rates cause strong fluctuations of the vapor-liquid interface at CHF, so it cannot be confirmed visually whether a film is covering the boiling surface. Due to the relatively low flow rates for experiments B-6 and B-7, weaker fluctuation at the interface allows for clearer visualization of film boiling on the surface. In some cases outbursts of large vapor bubbles were observed at CHF (Fig. 6-33).

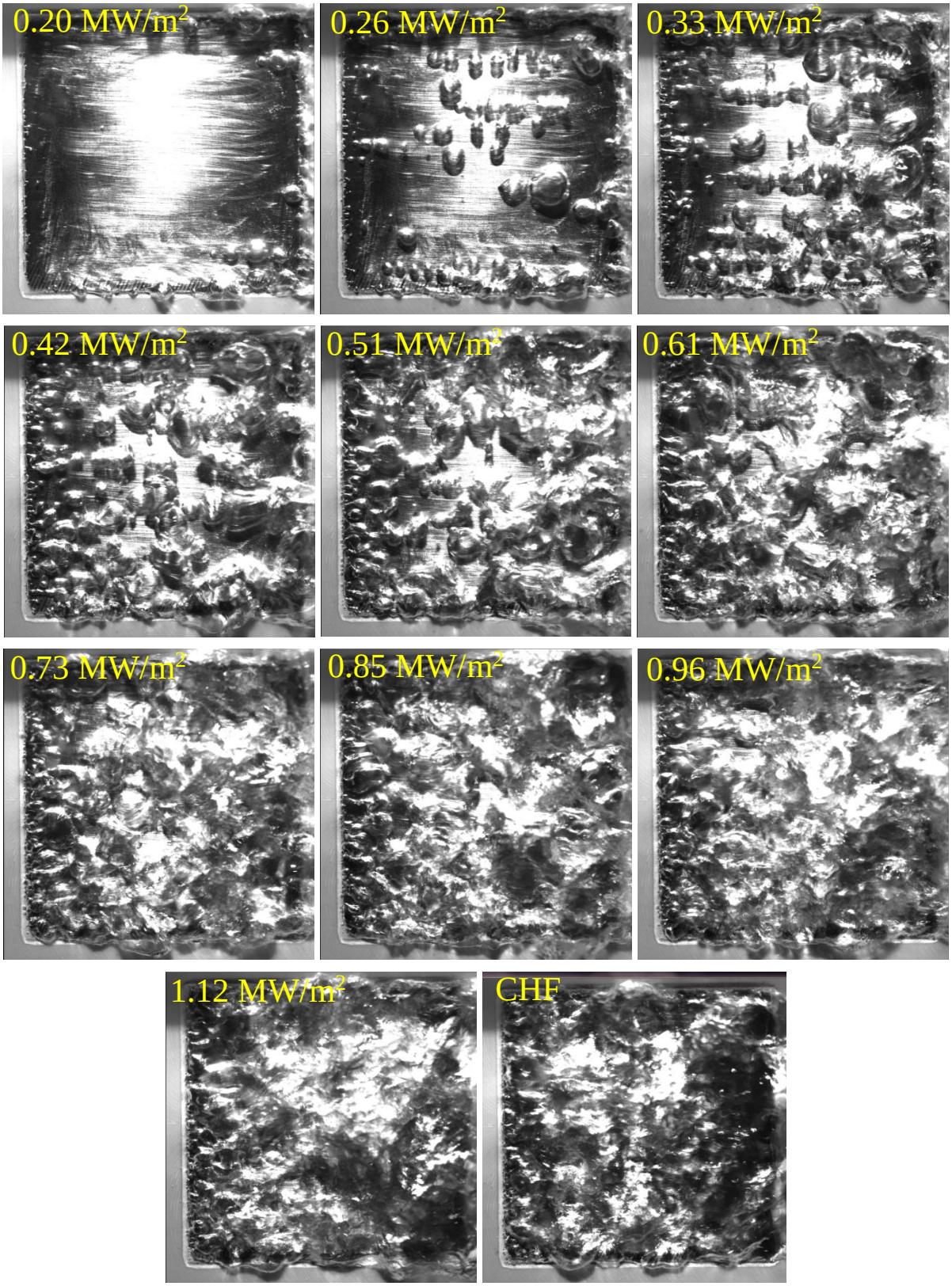

Figure 6-26: Visualization of B – 1 (1456 kg/m^2-s) experiments.

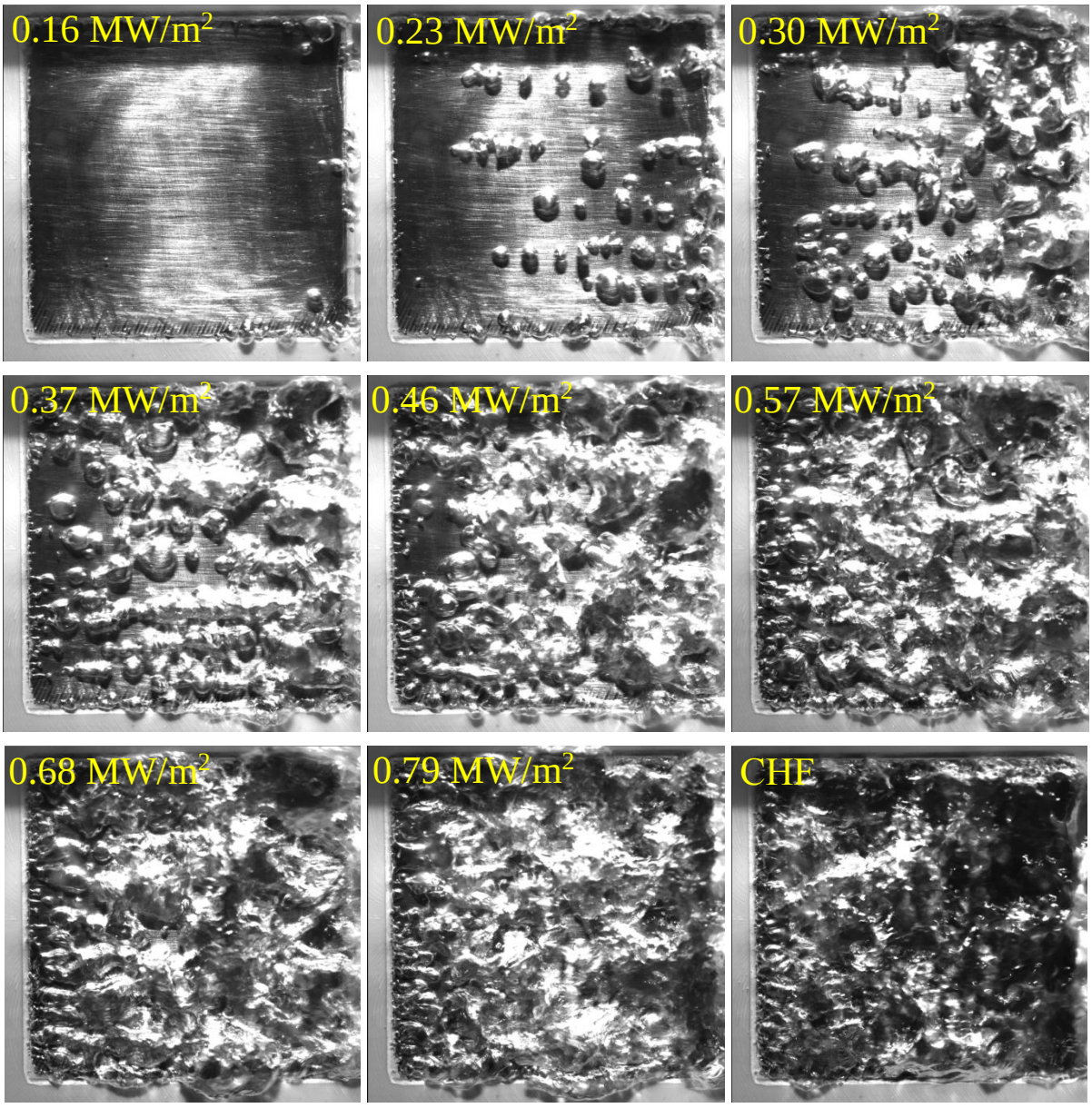

Figure 6-27: Visualization of B – 2 (1295 kg/m^2-s) experiments.

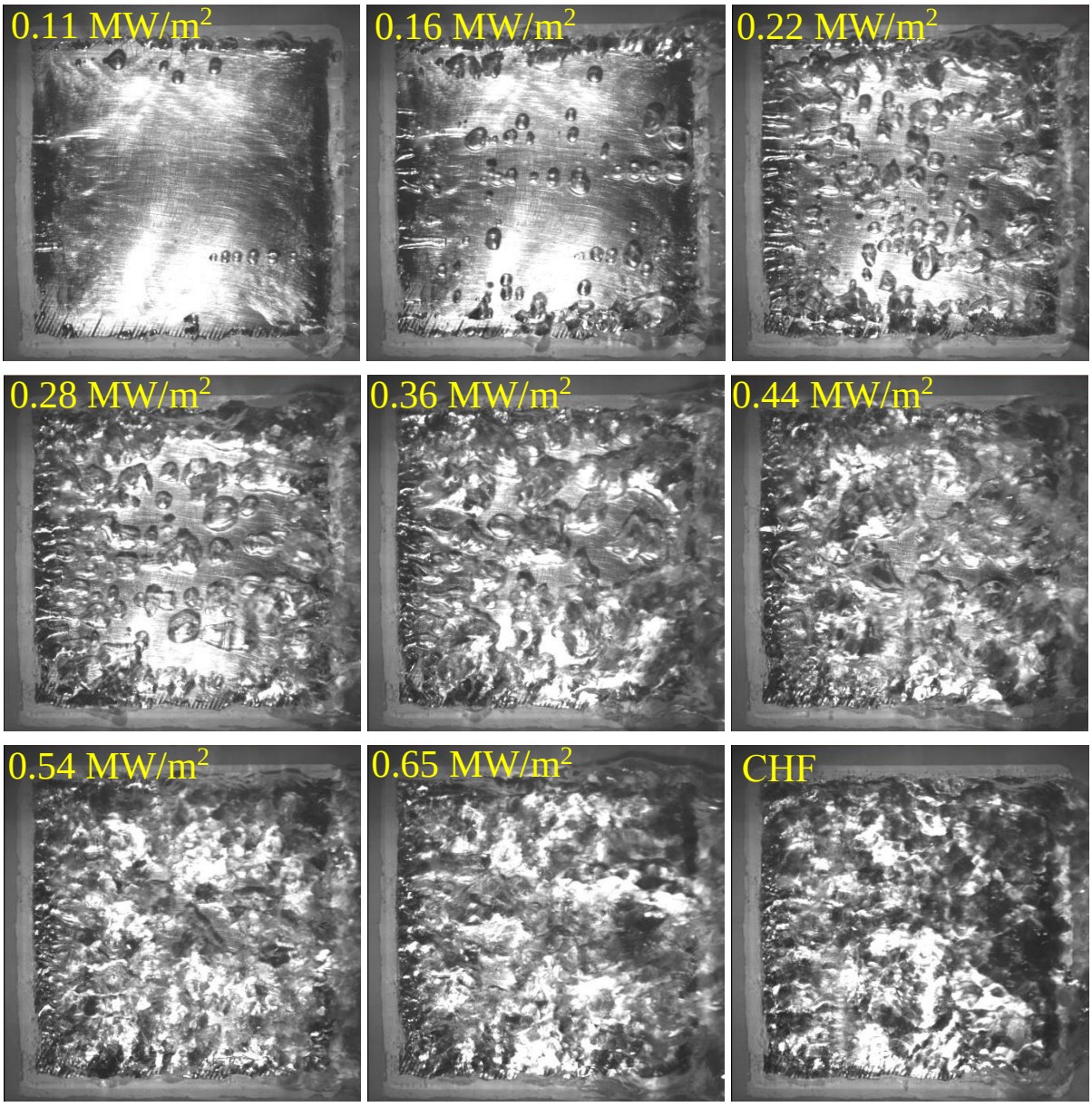

Figure 6-28: Visualization of B – 3 (1133 kg/m^2-s) experiments.

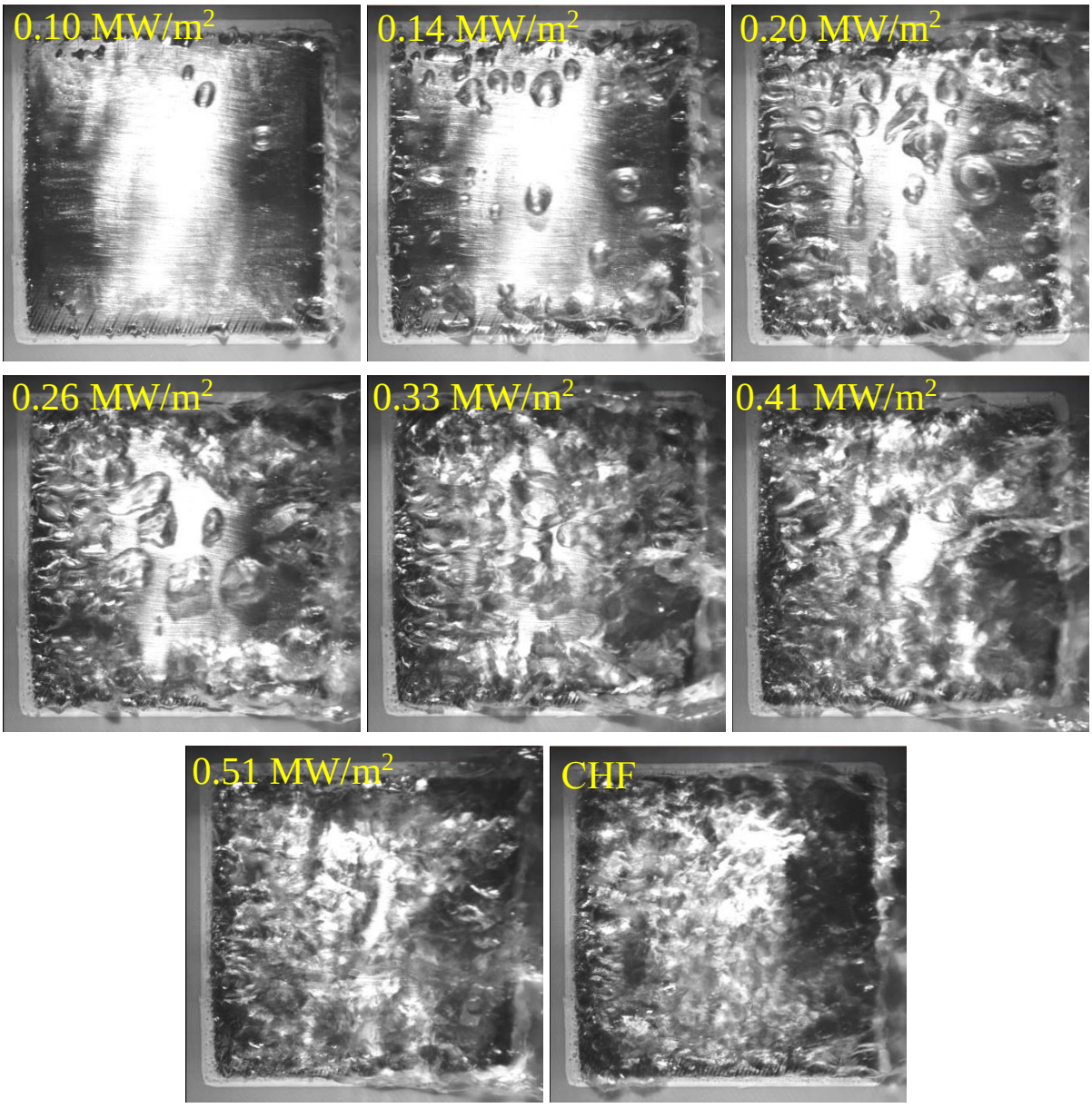

Figure 6-29: Visualization of B – 4 (971 kg/m^2-s) experiments.

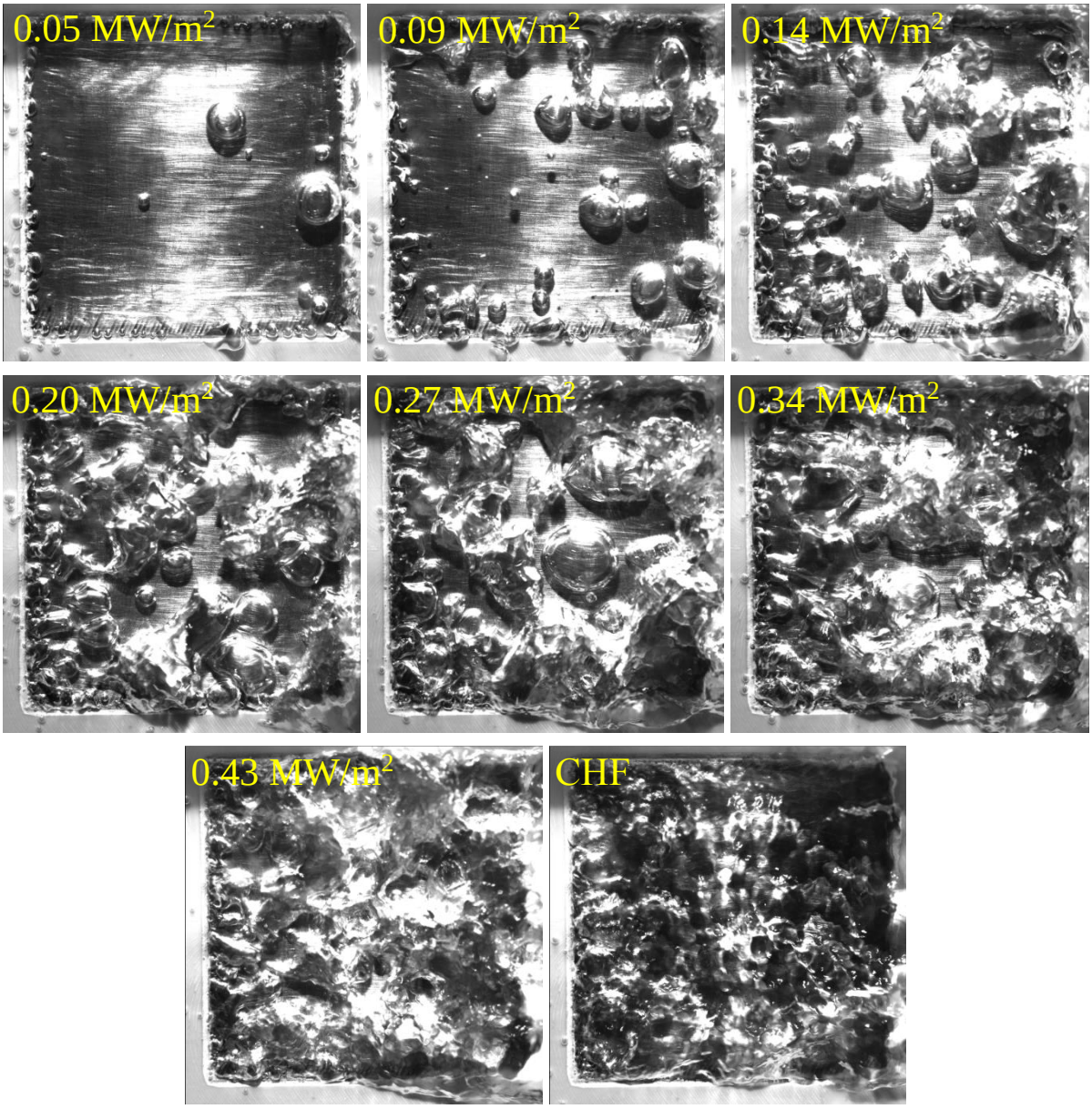

Figure 6-30: Visualization of B – 5 (647 kg/m^2-s) experiments.

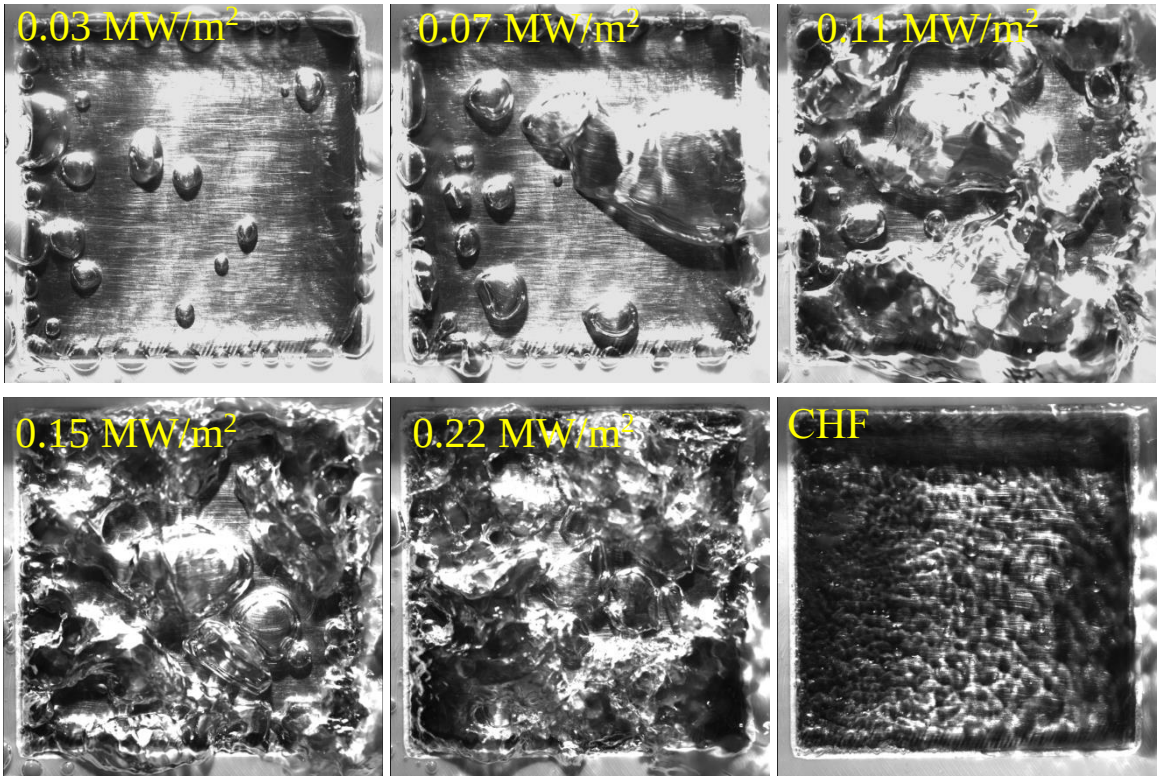

Figure 6-31: Visualization of B – 6 (324 kg/m^2-s) experiments.

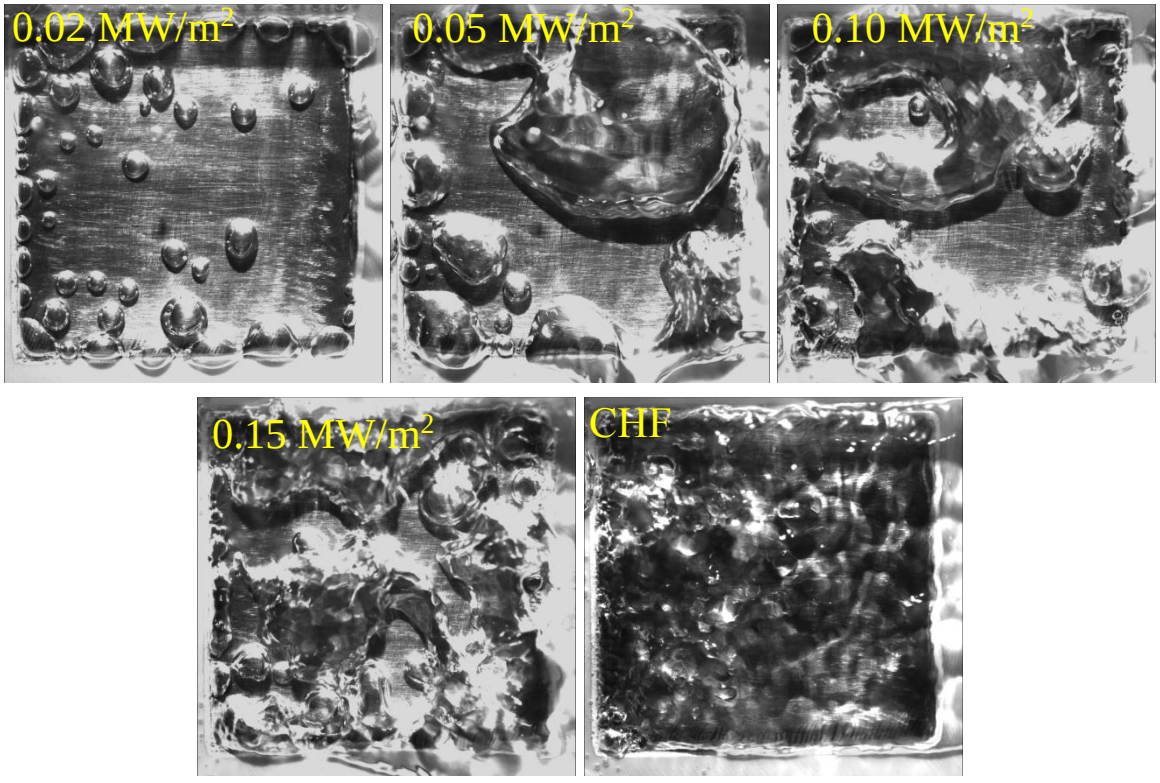

Figure 6-32: Visualization of B – 7 (202 kg/m^2-s) experiments.

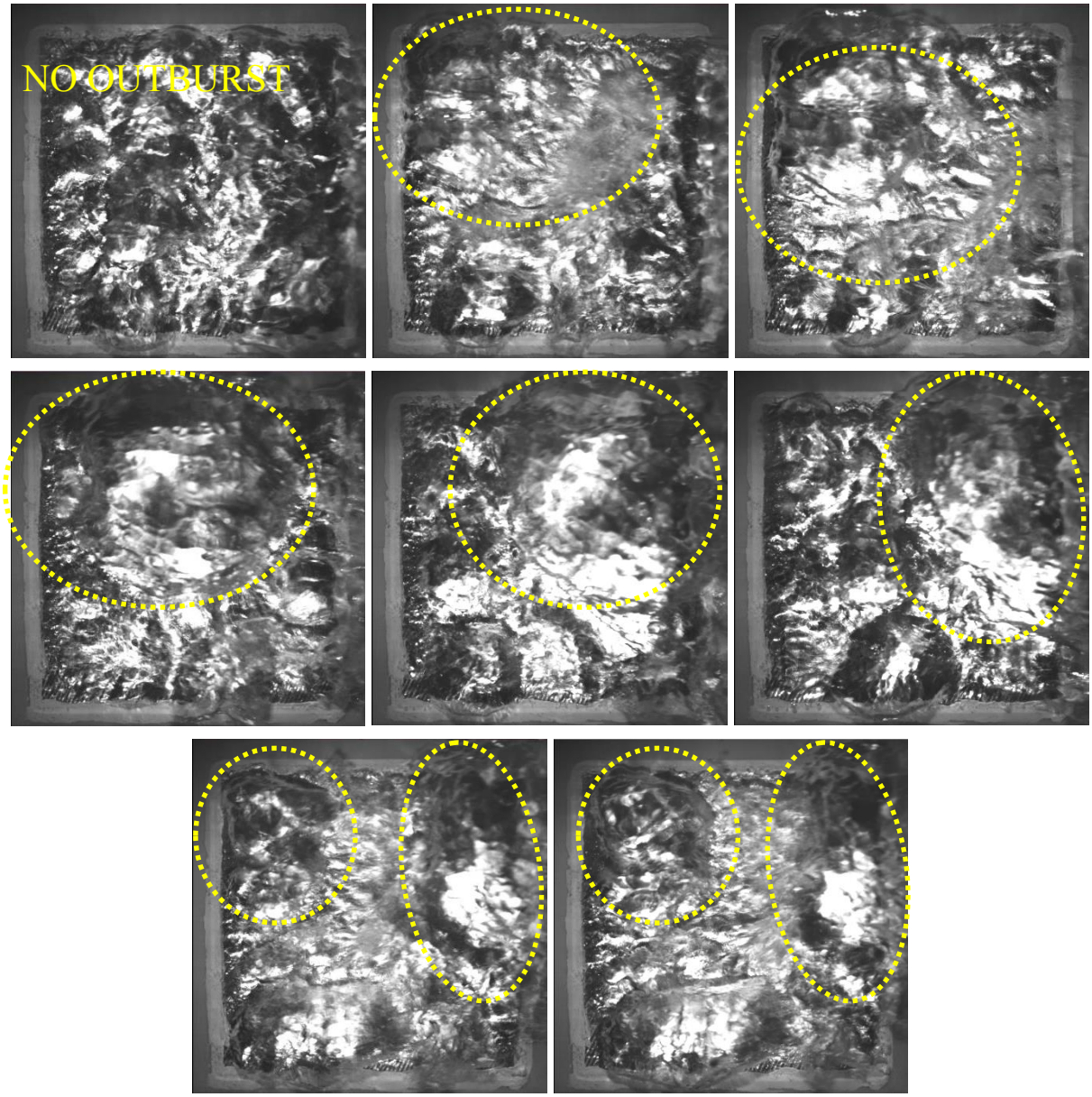

Figure 6-33: Visualization of bubble outburst during CHF (image sequence: left to right).

It is noteworthy to mention that the pressure will have an effect on CHF during boiling experiments. Since the current experiments were performed under reduced pressure conditions, the CHF is reduced for such conditions when compared to atmospheric conditions. On the other hand, the CHF will increase if pressurized conditions exist. Some previous studies have clearly shown that CHF decreases as the pressure is reduced (McGillis and Carey, 1992; Oh and Englert, 1993; Kosar et al., 2005; Kuo and Peles, 2008; Chan et al., 2010; Kwark et al., 2010;

Hu et al., 2011). A similar trend was not observed in the current study, since the pressure conditions were not varied for the experiments.

The bare surface CHF data obtained from the current experiments showed a linear trend, also seen in the works of Oh and Englert (1992), Kosar et al. (2005), and Kuo and Peles (2008). It was desired to compare the experimental data with a correlation to confirm the reliability of the experiments. A correlation proposed by Katto and Kurata (1980) was chosen to compare the bare surface data. Their experiments were performed for saturated water at atmospheric pressure on a vertically-oriented rectangular heated surface. The velocity ranged from 1.5 – 10 m/s in their experiments. Table 6-8 shows a comparison between the experimental conditions of Katto & Kurata and the current study. Their proposed CHF correlation is given as

$$\frac{q_{CHF}}{G\,h_{fg}} = 0.186\left(\frac{\rho_g}{\rho_l}\right)^{0.559}\left(\frac{\sigma\,\rho_l}{G^2\,l}\right)^{0.264} \tag{6-2}$$

where

σ = liquid surface tension [N/m]

l = length of heater [m]

A comparison of the bare surface data with equation (6-2) is shown in Fig. 6-34. The correlation shows a slightly similar trend, but overestimates the data. The reasons for the overestimation are believed to be due to the differences in the velocity and heated surface orientation. Figure 6-35 shows the experimental (measured) and correlated (predicted) CHF plotted against each other. The solid line represents an exact agreement between the correlated and experimental data. It is obvious from Fig. 6-35 that the correlation disagrees with the experimental data.

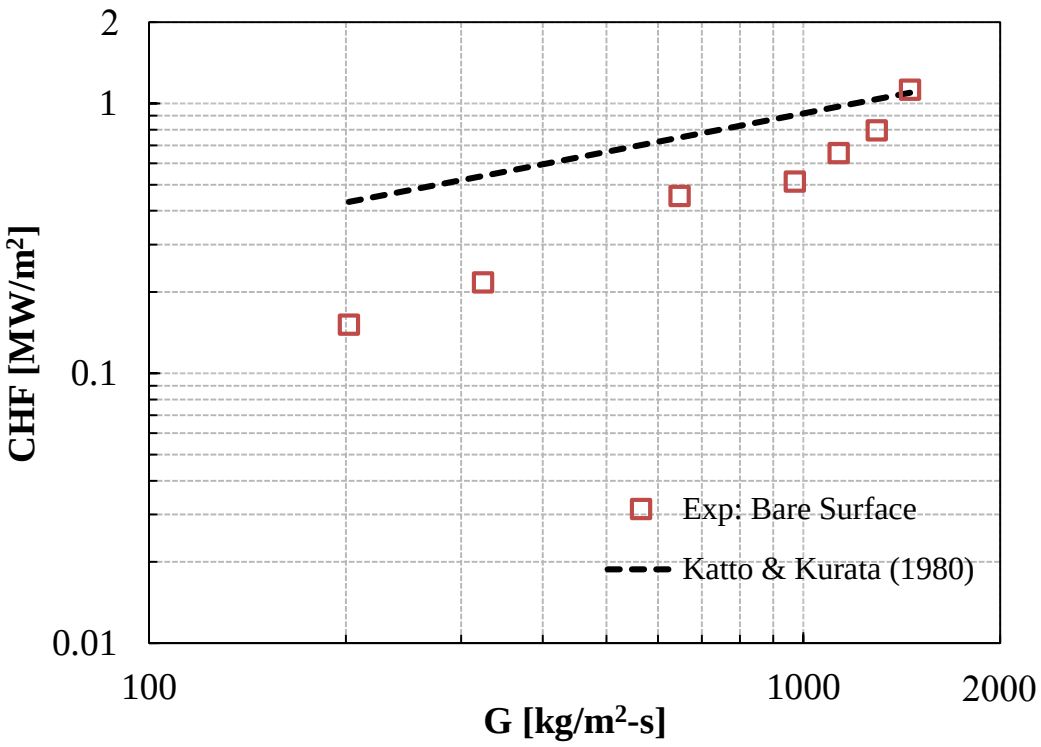

Figure 6-34: Comparison of correlation (equation (6-2)) and bare surface data.

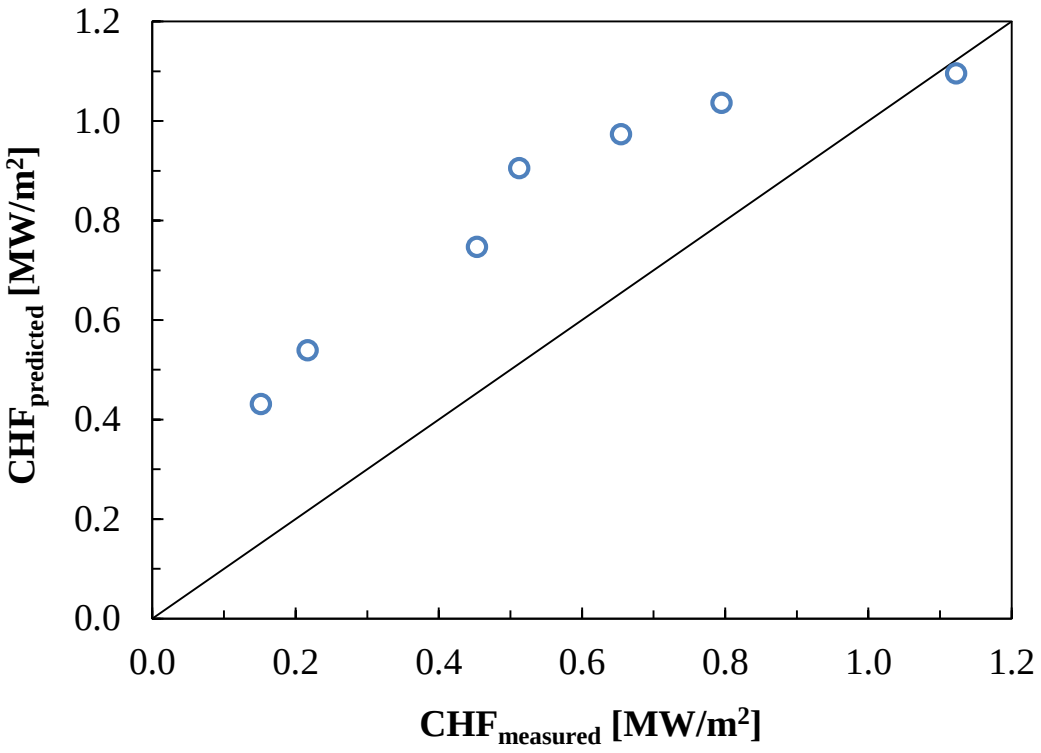

Figure 6-35: Comparison of predicted (equation (6-2)) and measured CHF.

Table 6-8: Comparison of conditions between Katto & Kurata and current study.

	Katto & Kurata	**Current Study**
Fluid Temperature	97 – 100 °C	~81 °C
Fluid Pressure	Atmosphere	~50kPa
Flow Rate Range	1.5 – 10 m/s	0.21 – 1.5 m/s
Surface Orientation	Vertical	Horizontal
Surface Size	Width = 10mm, Length = 10,15,20mm	Width = 30mm Length = 30mm
Nozzle/Channel Size	Width = 15mm Height = 5,10mm	Width = 40mm Height = 10mm

An attempt was made to better predict the experimental data after a modification was made to the correlation shown in equation (6-2). The modification was made to the exponent of the term ($\sigma \rho_l / G^2 l$), which is the modified inverse Weber (We) number. The term has been modified to include the mass flux, G, instead of the velocity. The We number is the ratio of the surface tension forces to the inertial force. The correlation is modified by following the same step shown in Katto and Kurata (1980), except the current experimental data was used. The term on the left hand side in equation (6-2) was divided by $(\rho_g/\rho_l)^{0.559}$, and then plotted against the We number. Once the two quantities were plotted, an equation was obtained from a least-squares fitted curve. The equation provided a modified exponent for the We number and a new constant for the correlation. As a result, the modified Katto & Kurata correlation is

$$q_{CHF} = 0.031 G \, \mathrm{h}_{\mathrm{fg}} \left(\frac{\rho_g}{\rho_l} \right)^{0.559} \left(\frac{\sigma \rho_l}{G^2 l} \right)^{0.036} \tag{6-3}$$

Figure 6-36 shows the original correlation from equation (6-2) and the modified correlation from equation (6-3) plotted with the experimental data.

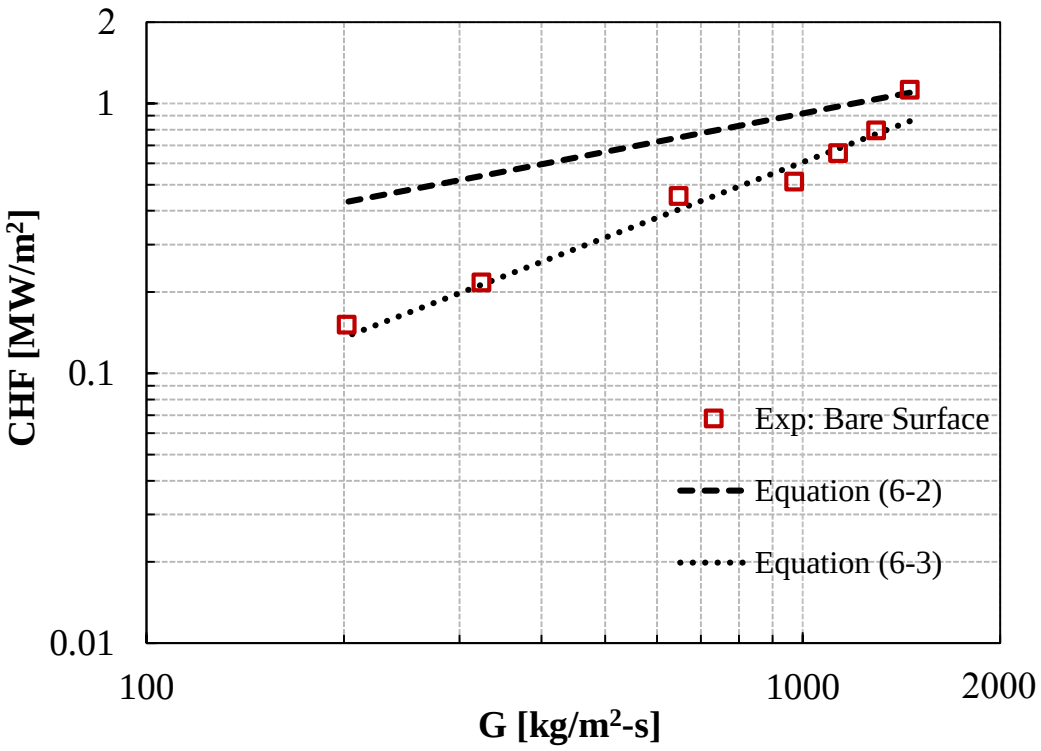

Figure 6-36: Comparison of original and modified correlations with bare surface data.

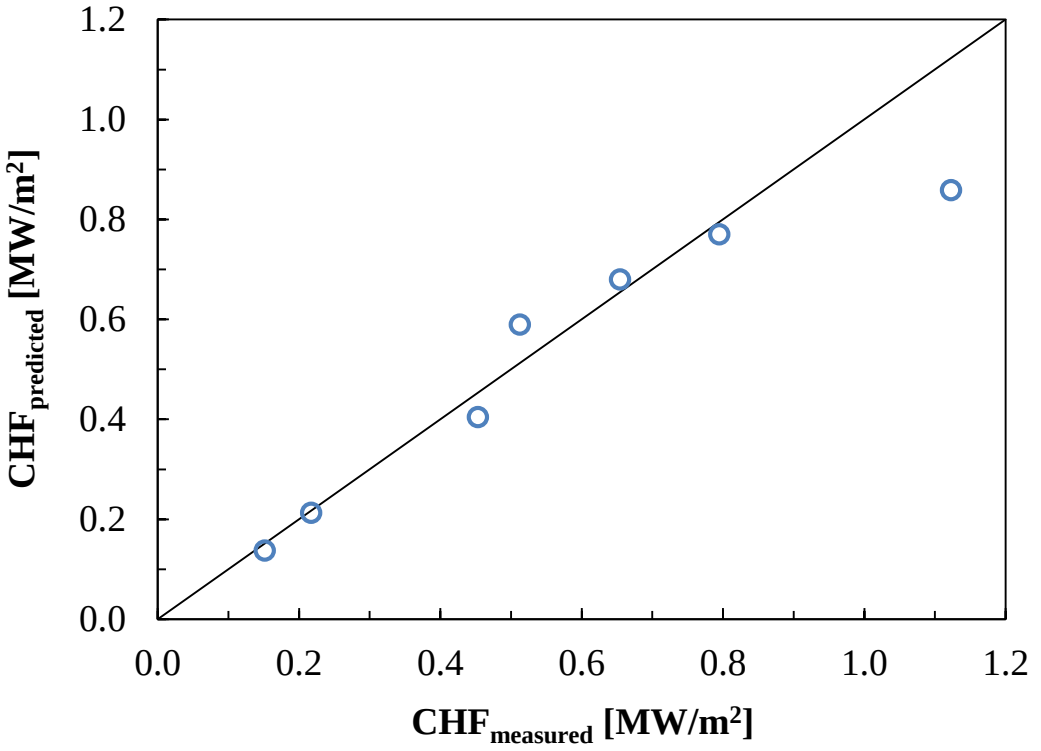

Figure 6-37: Comparison of predicted (equation (6-3)) and measured (bare) CHF.

The modified correlation shows better agreement with the experimental data than the original correlation. In comparison to Fig. 6-35, Fig. 6-37 shows that the predicted CHF (from modified correlation) agrees well with the measured CHF (from experimental data).

It is believed that the modified Katto & Kurata correlation in equation (6-3) agrees well with the experimental data due to the effect of the We number, the last term in the equation. The effect of the We number can be seen when comparing of equations (6-2) and (6-3). In equation (6-2) the exponent of the We number is 0.264, which is approximately seven times greater than the exponent for the We number in equation (6-3). Actually, the We number in the latter may be considered insignificant i.e. $We^{0.036} \approx 1$. The insignificance in the We number in equation (6-3) is believed to be the result of the orientation of the heated surface. The original Katto & Kurata correlation, equation (6-2), was developed from experiments performed using a vertically heated surface. The modified Katto & Kurata correlation, equation (6-3), is proposed for a downward-facing surface. Even at the same flow rate, the bubble removal from a vertically heated surface will be different when compared to a horizontally heated surface. For a vertically heated surface the bubble removal will depend on the flow rate and the size of the bubble, where the size is related to the surface tension forces i.e. the We number. On the other hand, bubble removal for a downward-facing surface will mainly depend on the flow rate. The bubble size (We number) will not assist in the bubble removal for a downward-facing surface since the bubble will expand and cannot be removed unless there is convective force.

6.5 Finned Surface Results

In this section the finned surface results for the reduced pressure experiments are presented and simultaneously compared with the bare surface experiments. All the conditions, procedures, and analyses for the finned surface experiments were performed in the same manner as they were for the bare surface experiments. Only the test section differed slightly (Figs. 6-38 and 6-39). Again, the upstream (US) and downstream (DS) surface temperatures and heat flux were calculated separately.

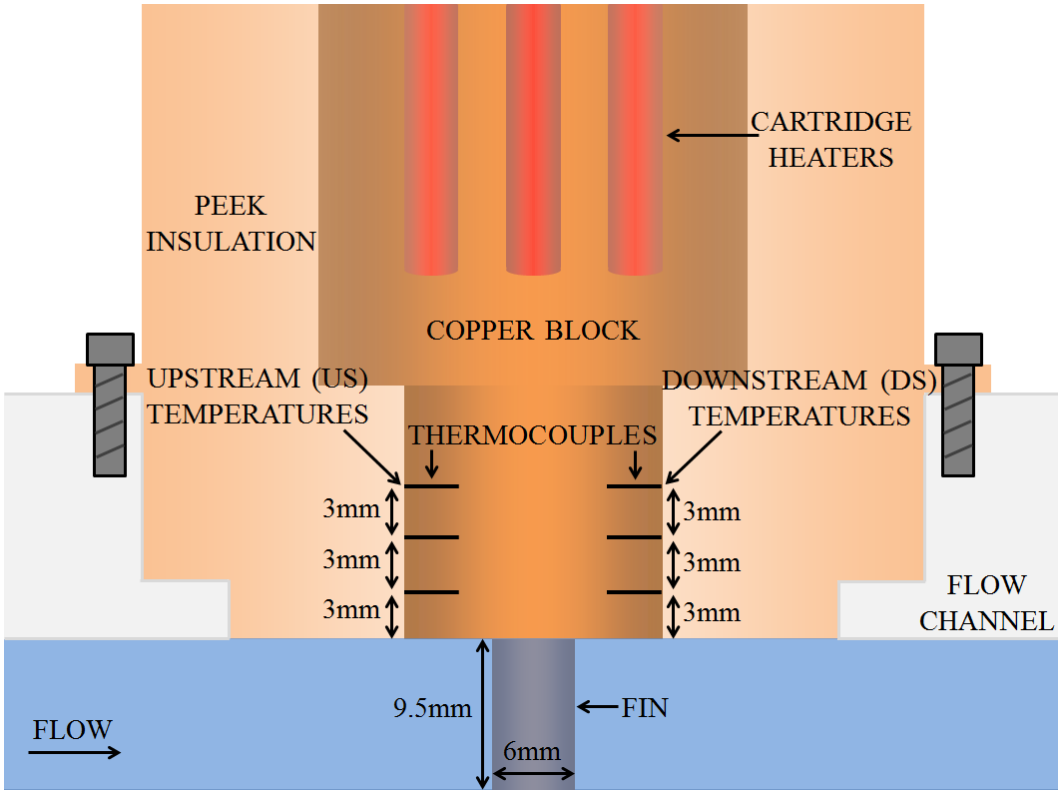

Figure 6-38: Mid-section schematic of finned surface copper block test section (not to scale).

Figure 6-39: Image of PEEK enclosing the finned surface copper block.

6.5.1 Heat Transfer from Both Surfaces

The flow rates for the finned surface are shown again for convenience in Table 6-9, and Table 6-10 lists the average conditions of the finned surface experiments. In Figs. 6-40 to 6-46 the boiling curves compare the upstream (US) and downstream (DS) data with the bare surface. Images from the visualization performed during the experiments are shown in Figs. 6-47 to 6-53. Although the fin may not be clearly visible in some images, it is located at the center of the boiling surface. In the previous subcooled experiments, it was observed that the largest heat flux value occurred at the same voltage level for both surfaces. The same was not observed in the current experiments. From the boiling curves it can be seen that for all experiments except F-7, the finned surface heat flux has been enhanced compared to the bare surface. Also, the surface temperatures are lower for the finned surface when compared to the bare surface. This implies that heat transfer has been improved by the presence of the fin. Notice that in most of the experiments the downstream temperatures for the finned surface are greater than upstream temperatures. Such results were seen in the subcooled experiments as well. It is assumed from the boiling curves that the flow rate for F-7 experiments did not allow for nucleate boiling conditions to be reached since CHF occurred soon after the experiments were started. Therefore, no clear trend is seen in Fig. 6-46.

The observations made at CHF are similar to those made for the bare surface. Film boiling conditions are assumed at CHF as the film covers the boiling surface and temperatures increase rapidly. For experiments F-1 to F-5, the relatively high flow rates also cause strong fluctuations of the vapor-liquid interface at CHF, so it cannot be confirmed visually whether a film is covering the boiling surface. It is assumed from the thermocouple data that film boiling is present at CHF. Due to the relatively low flow rates for experiments F-6 and F-7, weaker fluctuation at the interface allows for clearer visualization of the film boiling phenomenon on the surface. Regarding the rapid increase in temperatures, they were observed in F-1 to F-3 experiments. In F-4 and F-5 experiments, only the downstream location showed rapid temperature increase. The upstream temperature increased slightly, but did not increase rapidly like the downstream temperatures. In this case, it was assumed that CHF will occur for the upstream location if the experiment was undisturbed. To prevent any damage to the test section, the slidac power was turned off and the flow rate increased when the temperatures increased rapidly for the downstream location. For F-6 and F-7 experiments, a sharp increase in temperature was not observed. Rather, the temperature increase occurred slowly. Since such

conditions were not steady state and the boiling surface was constantly covered by vapor, CHF was assumed at such conditions. Figure 6-54 shows an example of the delay in CHF for F-1 experiments. The downstream temperatures (gray, purple, green data lines) increased before the upstream temperatures (yellow, orange, red data lines). Each vertical division is 20 seconds in the figure.

Table 6-9: Experiment reference number and equivalent flow rates for current experiments.

Exp. Reference[1]	**Volumetric Flow**	**Mass Flux**	**Reynolds No.**[2]	**Velocity**
B,F – 1	36 L/min	1456 kg/m^2-s	6.67x10^4	1.50 m/s
B,F – 2	32 L/min	1295 kg/m^2-s	5.93x10^4	1.33 m/s
B,F – 3	28 L/min	1133 kg/m^2-s	5.19x10^4	1.17 m/s
B,F – 4	24 L/min	971 kg/m^2-s	4.45x10^4	1.00 m/s
B,F – 5	16 L/min	647 kg/m^2-s	2.97x10^4	0.67 m/s
B,F – 6	8 L/min	324 kg/m^2-s	1.48x10^4	0.33 m/s
B,F – 7	5 L/min	202 kg/m^2-s	0.93x10^4	0.21 m/s

[1] B: bare, F: finned surface.
[2] Based on hydraulic diameter.

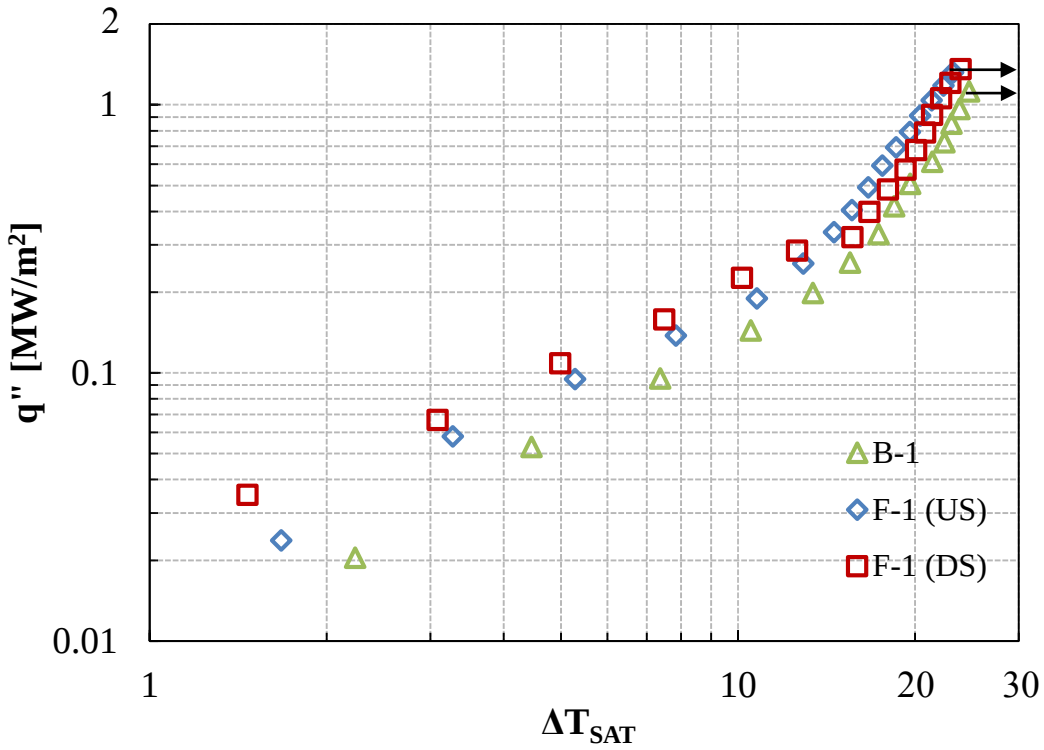

Figure 6-40: Boiling curves for B – 1 and F – 1 (1456 kg/m^2-s).

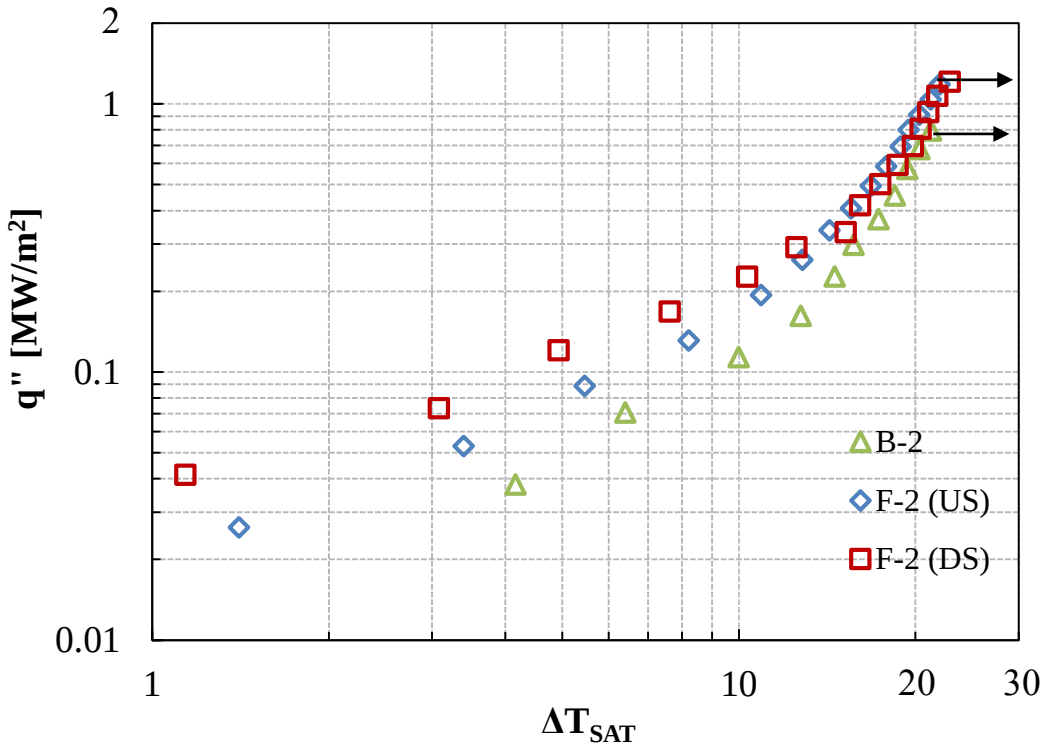

Figure 6-41: Boiling curves for B – 2 and F – 2 (1295 kg/m^2-s).

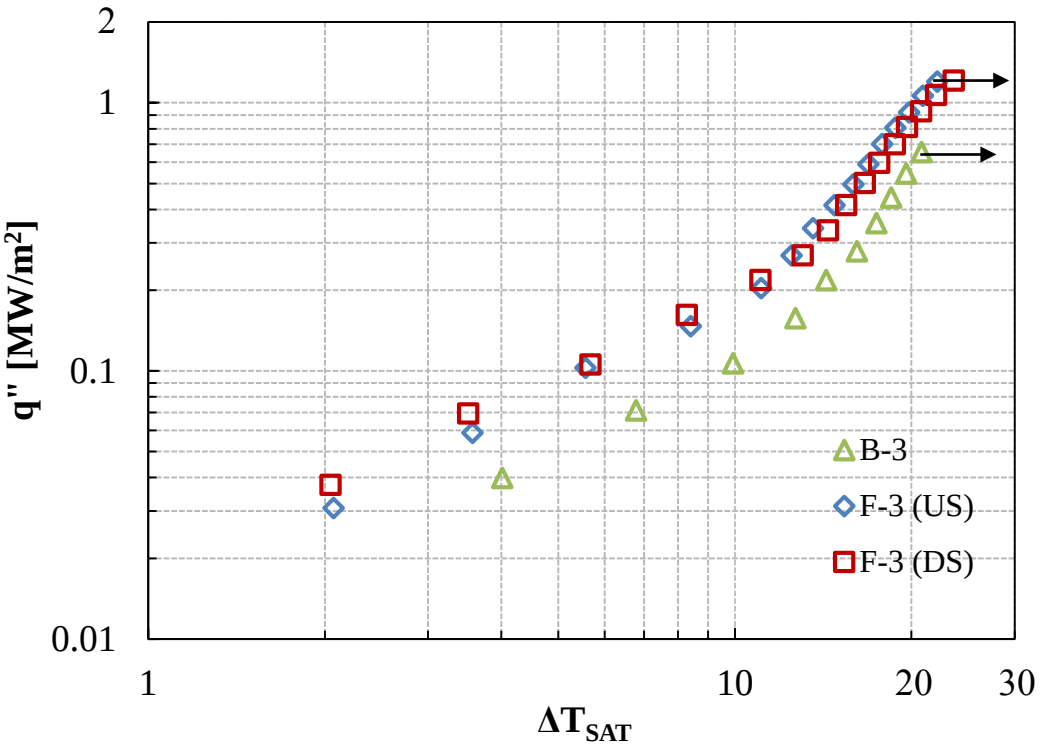

Figure 6-42: Boiling curves for B – 3 and F – 3 (1133 kg/m^2-s).

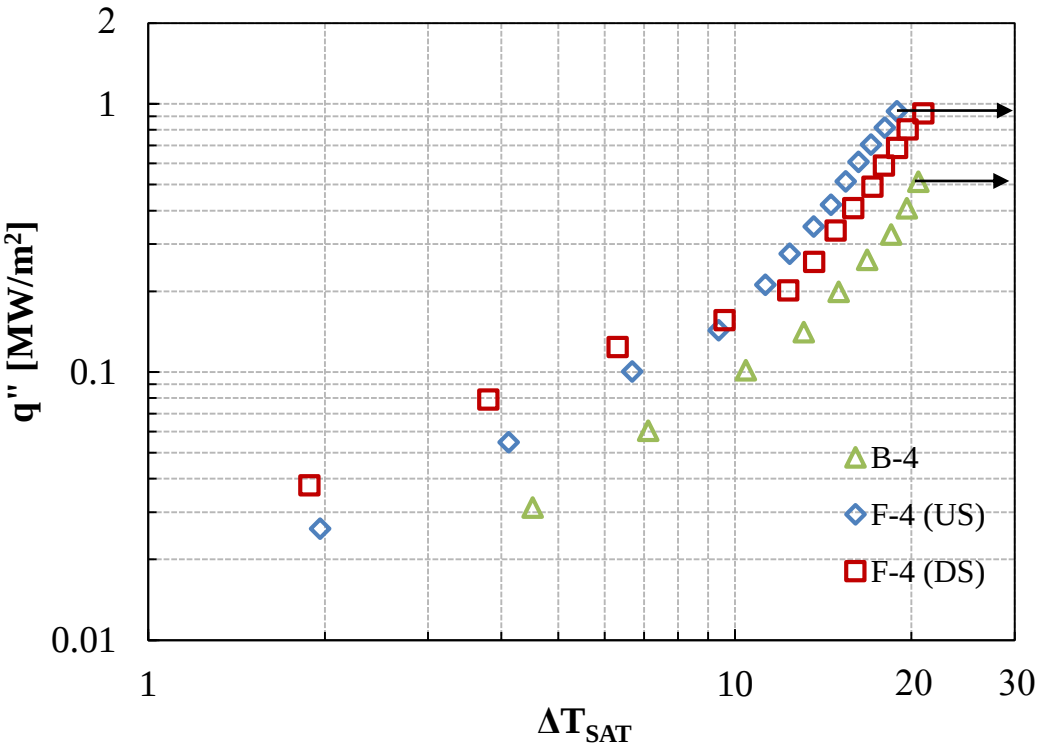

Figure 6-43: Boiling curves for B – 4 and F – 4 (971 kg/m^2-s).

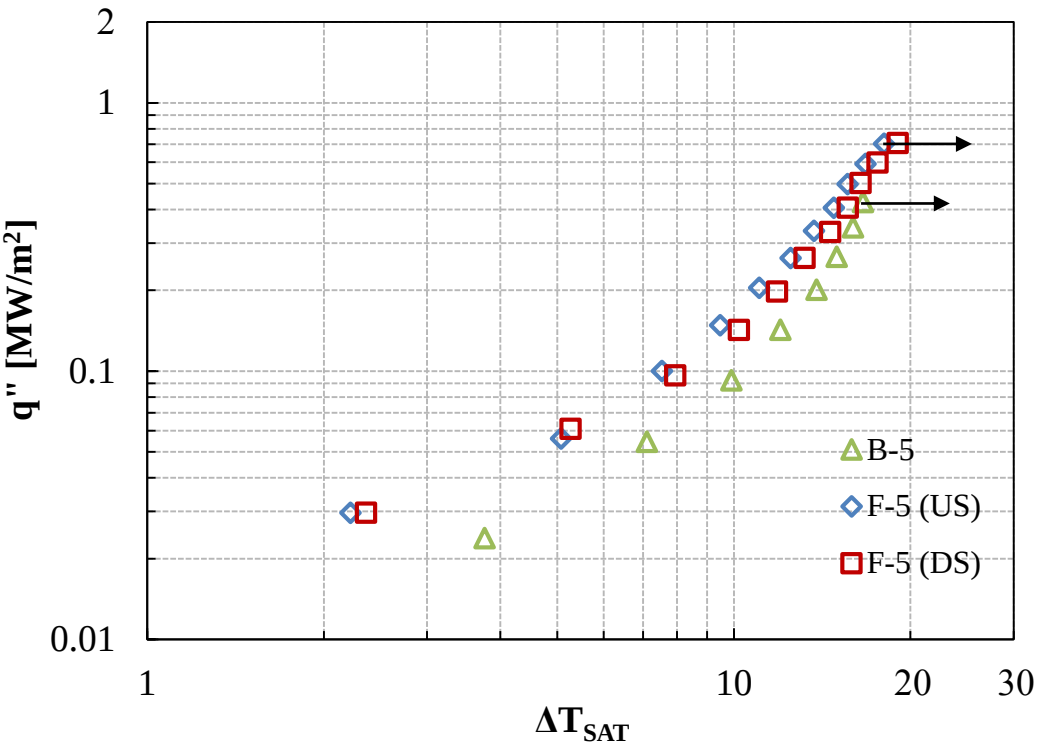

Figure 6-44: Boiling curves for B – 5 and F – 5 (647 kg/m^2-s).

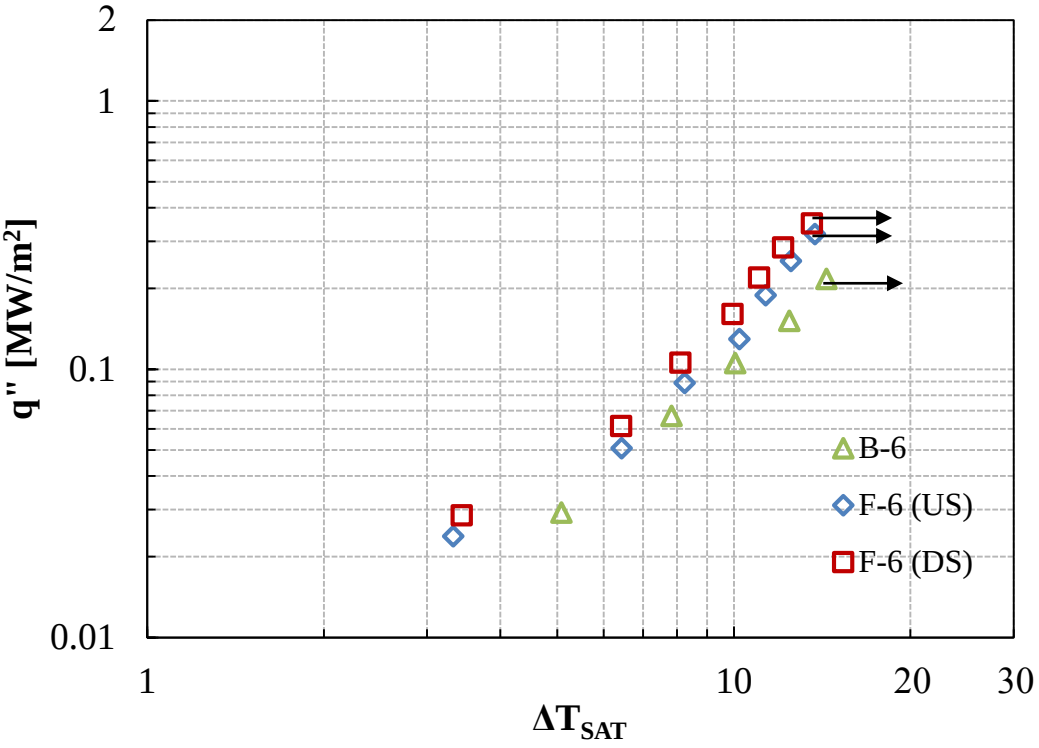

Figure 6-45: Boiling curves for B – 6 and F – 6 (324 kg/m^2-s).

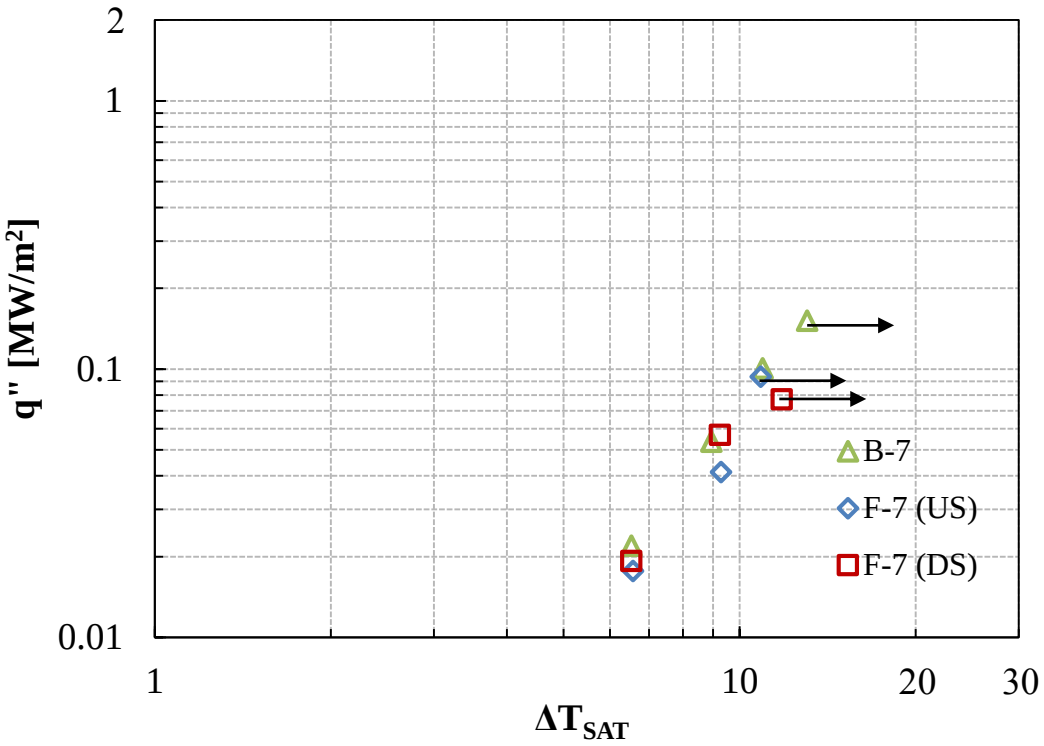

Figure 6-46: Boiling curves for B – 7 and F – 7 (202 kg/m^2-s).

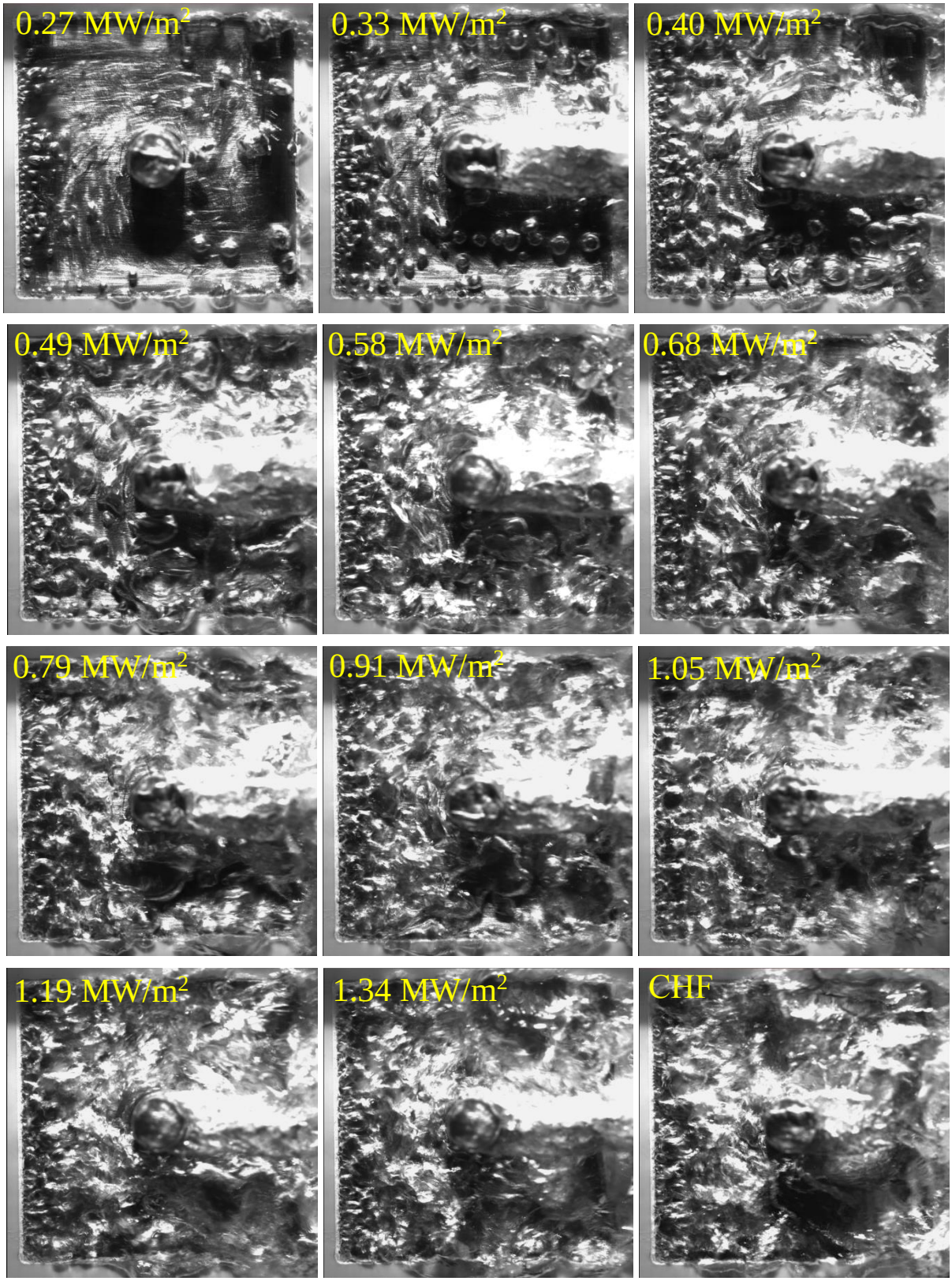

Figure 6-47: Visualization of F – 1 (1456 kg/m^2-s) experiments.

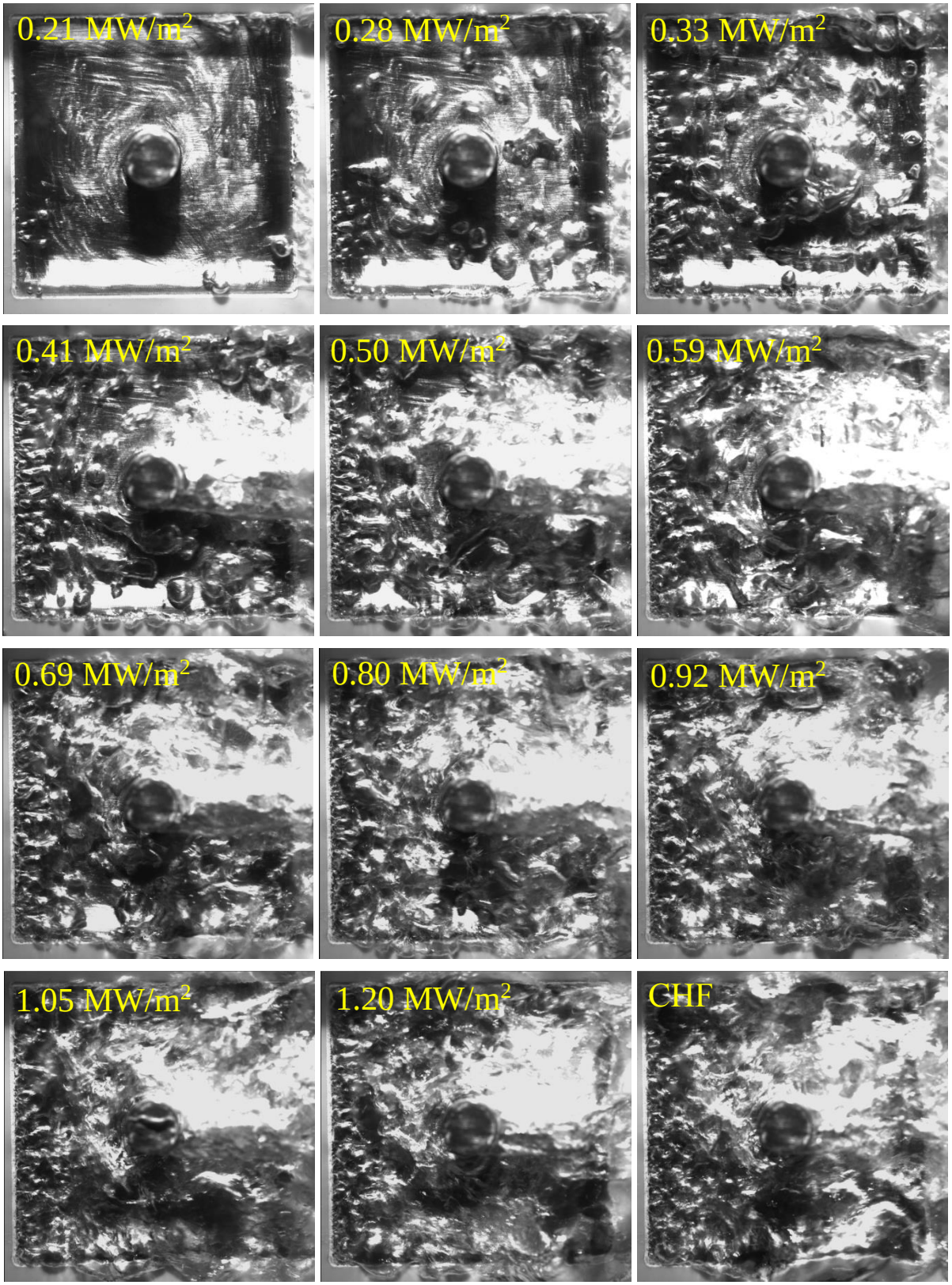

Figure 6-48: Visualization of F – 2 (1295 kg/m^2-s) experiments.

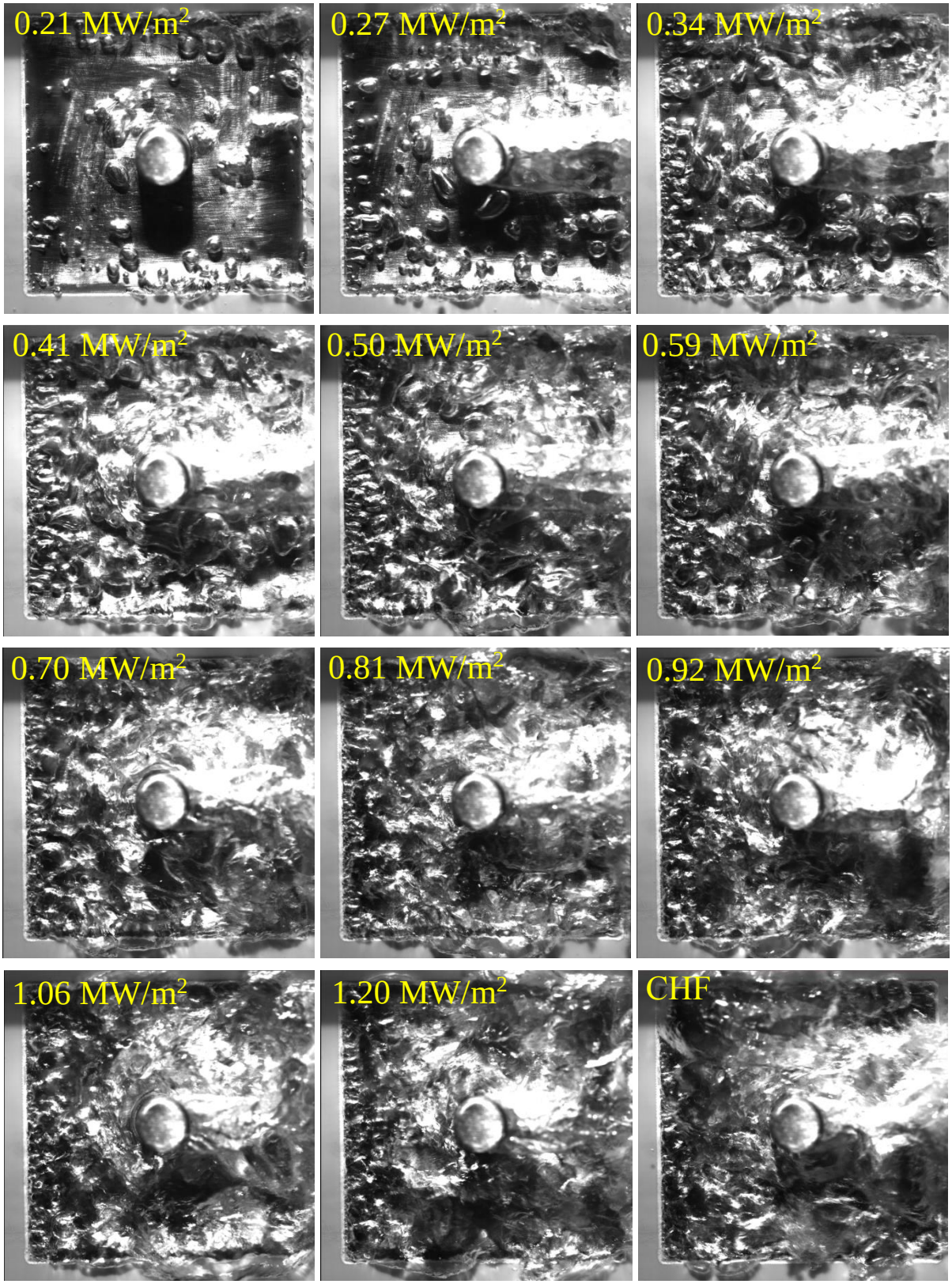

Figure 6-49: Visualization of F – 3 (1133 kg/m^2-s) experiments.

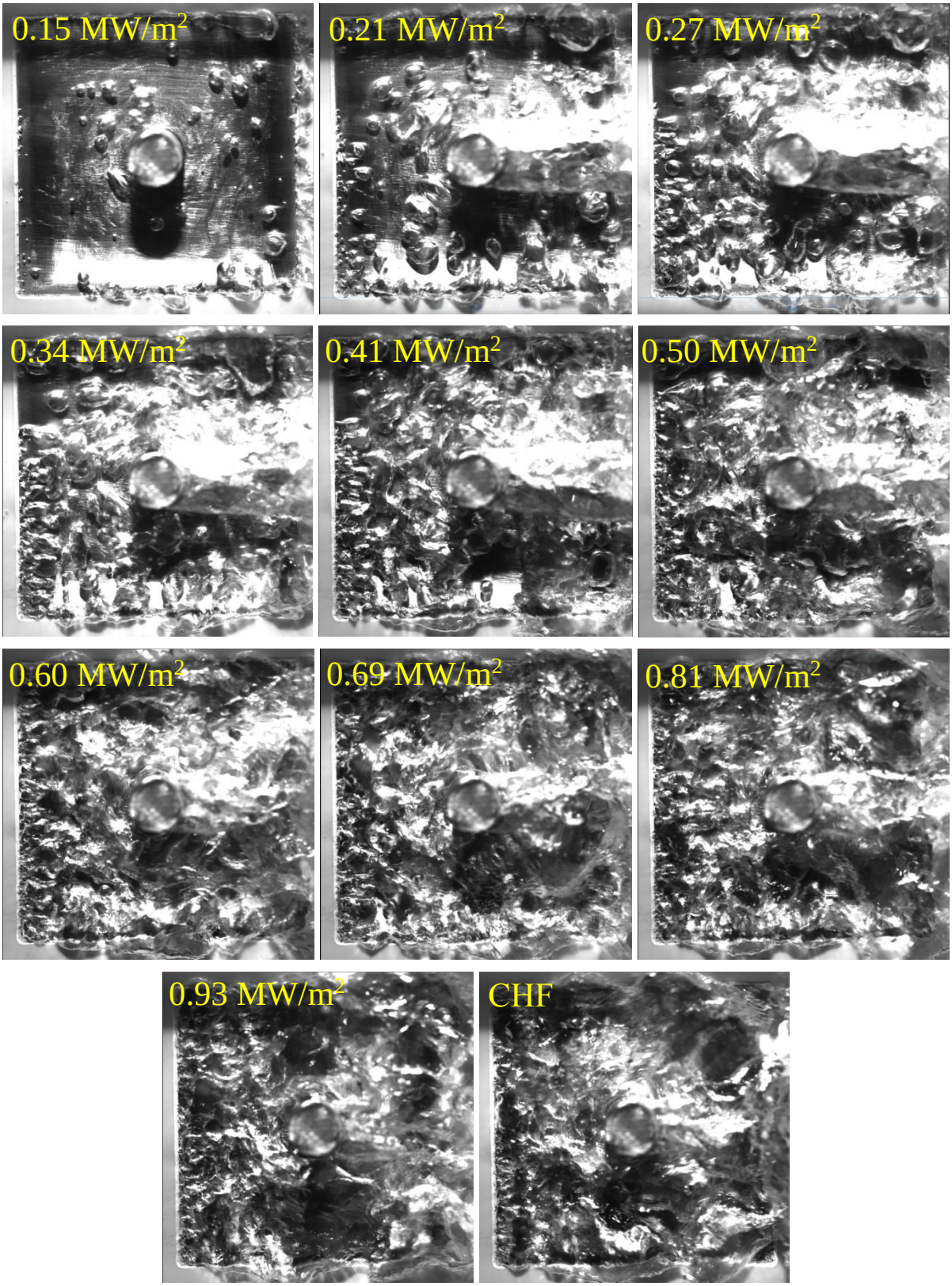

Figure 6-50: Visualization of F – 4 (971 kg/m^2-s) experiments.

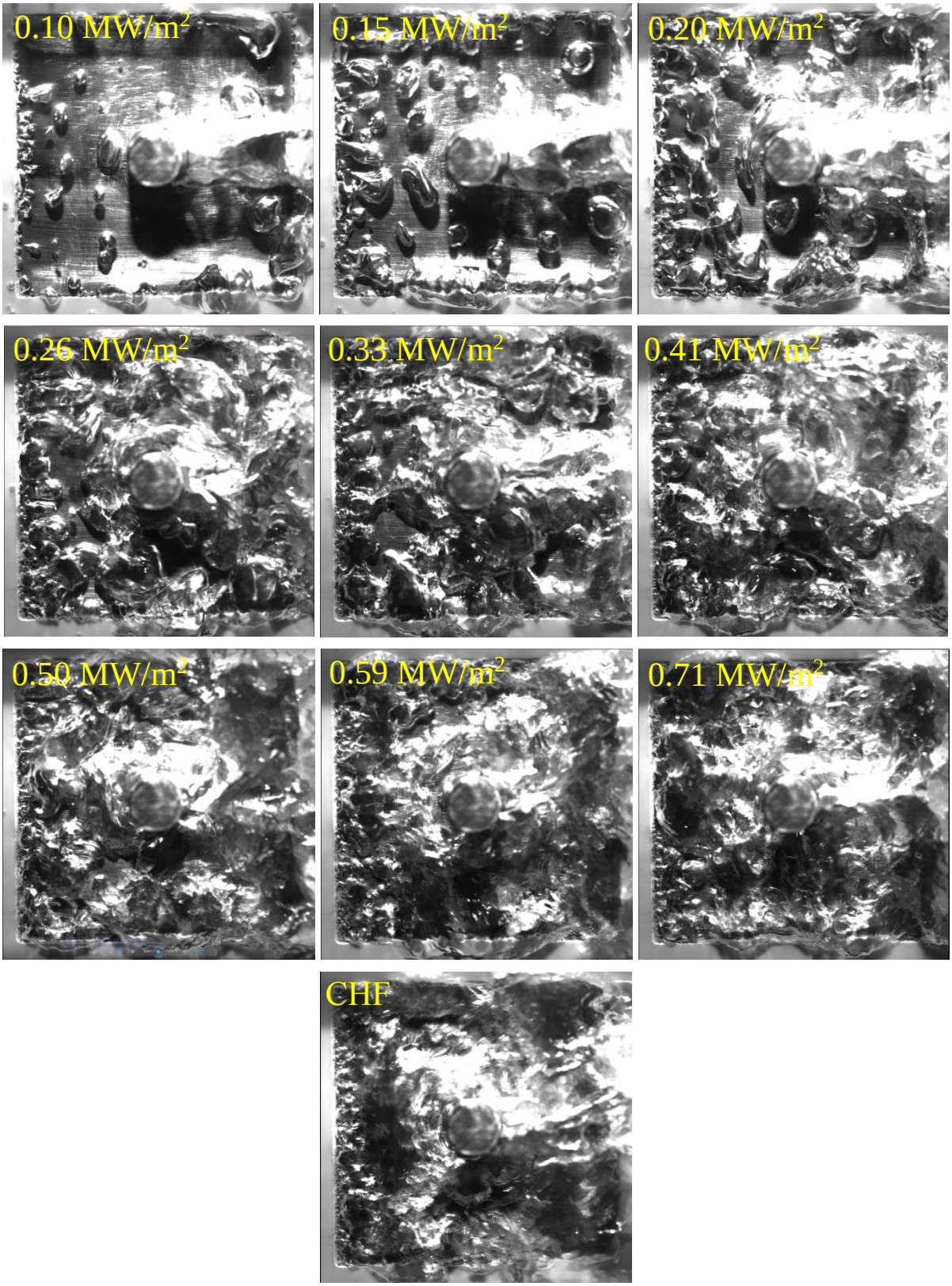

Figure 6-51: Visualization of F – 5 (647 kg/m^2-s) experiments.

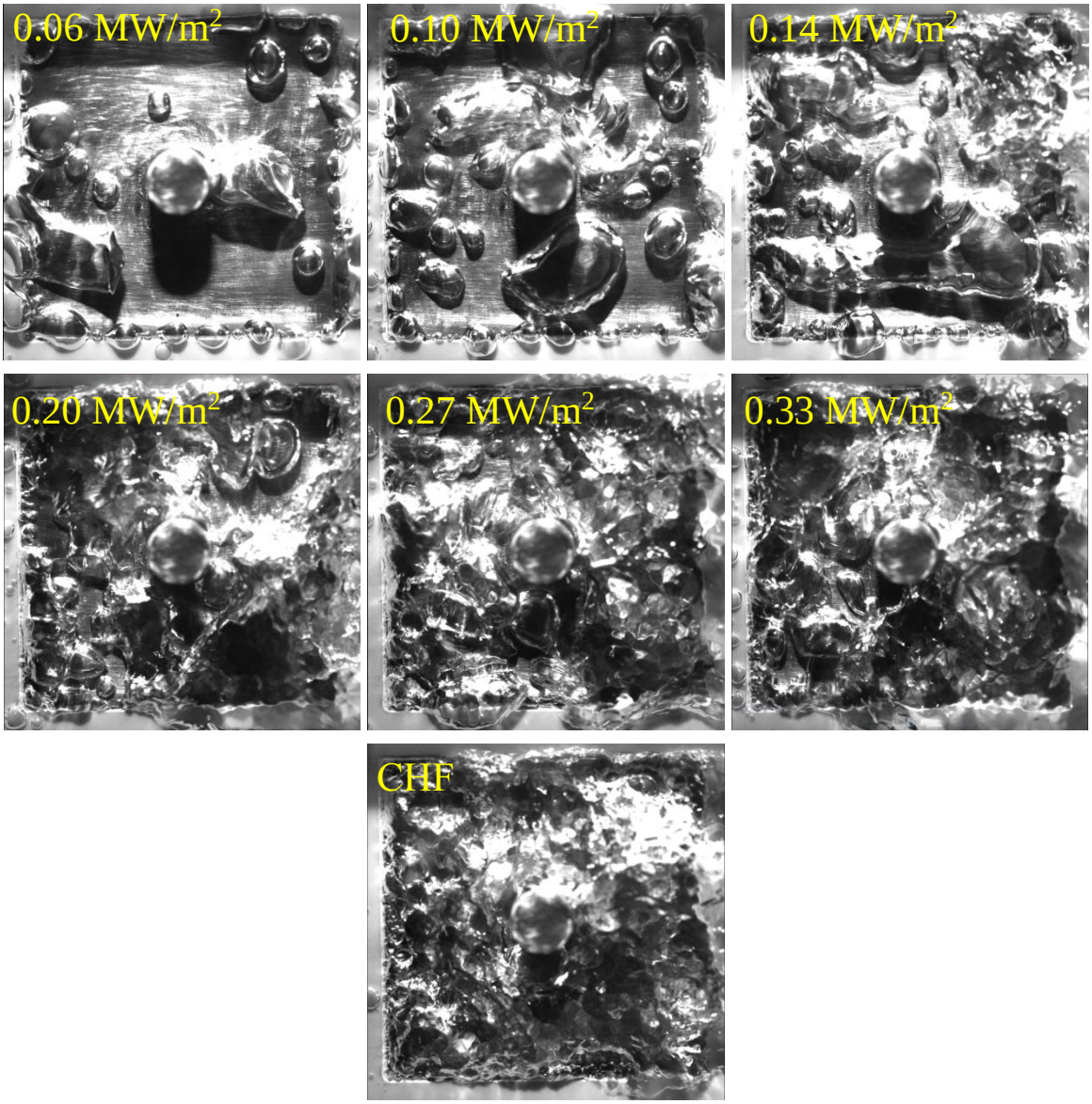

Figure 6-52: Visualization of F – 6 (324 kg/m^2-s) experiments.

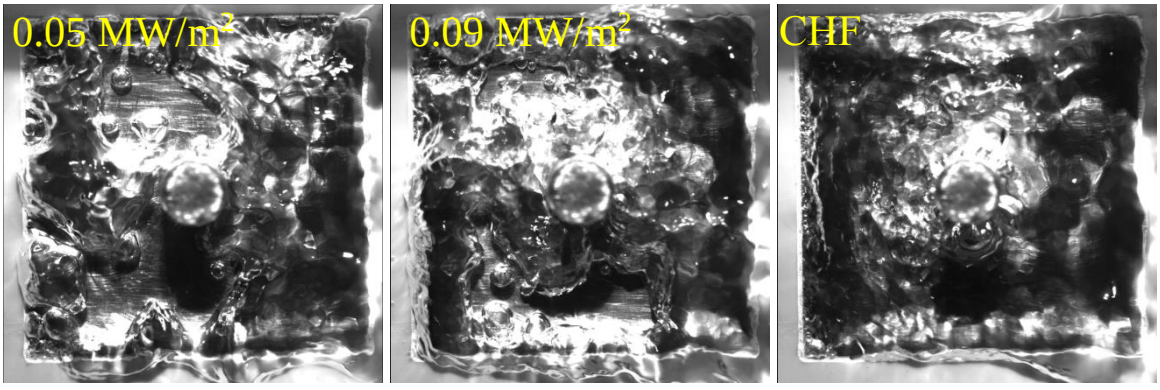

Figure 6-53: Visualization of F – 7 (202 kg/m^2-s) experiments.

Table 6-10: Pressure and temperature conditions for the all finned surface experiments.

	B-1	**B-2**	**B-3**	**B-4**	**B-5**	**B-6**	**B-7**
Pressure	49 kPa	49 kPa	49 kPa	49 kPa	49 kPa	50 kPa	49 kPa
T_{SAT}	80.8°C	80.8°C	80.8°C	80.8°C	80.8°C	81.3°C	80.8°C
US-Tank	81.1°C	80.9°C	81.1°C	81.0°C	80.9°C	80.8°C	80.6°C
DS-Tank	81.2°C	81.1°C	81.2°C	81.2°C	81.1°C	81.2°C	81.4°C

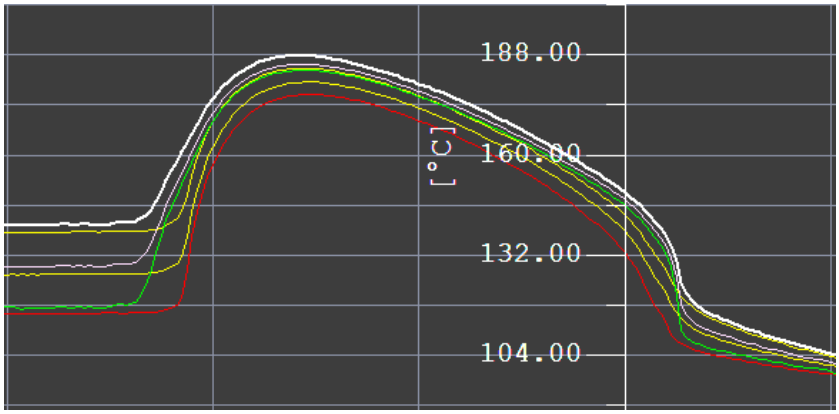

Figure 6-54: Delay in upstream CHF for F-2 experiments (vertical division: 20 seconds).

An interesting observation made at CHF was the delay in the CHF for the upstream and downstream locations. Again, CHF was defined as the conditions causing rapid increase in surface temperatures (Fig. 6-24). The rapid increase in surface temperatures was observed first for the downstream location, and then the upstream location. From the thermocouple data it seems as though there is a bubble front similar to the subcooled experiments (Fig. 5-23), but it was not visually confirmed.

Recall that bubble accumulation was found to occur at the downstream location for the subcooled finned surface experiments. In the current saturated reduced pressure conditions, no bubble accumulation was observed. The temperature and pressure of the liquid used in the experiments may have an impact on whether bubbles will accumulate in the downstream

location. Different experimental conditions of the fluid may help to verify the effect on bubble accumulation. Since only two different conditions were applied in this thesis, they are not deemed sufficient to make any conclusions regarding the conditions for bubble accumulation.

Figure 6-55 compares the CHF data obtained from the finned surface with the bare surface data. Considering only the finned surface data, there is no significant difference between the upstream and downstream CHF values. In Fig. 6-55, positive and negative effects of the fin can be seen. An increasing trend is observed in the CHF as the flow rate is increased, except two different slopes are observed at different flow rates. F-1 to F-6 data displays a very similar trend to the bare surface, although the values are greater. This finned surface data shows the positive effect: an increase of the CHF compared to the bare surface. The lowest flow rate data (F-7) does not follow the same trend. Therefore, it is part of another trend that shows degradation of the finned surface CHF; it shows the negative effect, which is reduction in the CHF compared to the bare surface. A transition occurs from the positive effect of the fin to the negative effect between F-6 and F-7 experiments. Due to only one data value for the negative effect, a clear transitioning point was not observed.

It is worthwhile mentioning the cause believed to enhance the CHF for the finned surface. One reason an enhancement in the CHF is observed is due to the increased heat transfer. The fin has reduced the surface temperatures, implying an improvement in the heat transfer. The reduction in the finned surface temperatures is clearly seen in the boiling curves shown earlier. Another reason believed to cause an increase in the CHF is due to the turbulent mixing caused by the fin, which removes the bubble accumulation. The flow agitation caused downstream by the fin leads to mixing of the fluid. In return, the mixing causes a delay in CHF. Again, as found in the case of subcooled flow boiling, CHF started downstream and slowly moved upstream. If the fluid is more turbulent in the downstream location, that will delay CHF conditions. On the other hand, the opposite was observed at the lowest flow rate. The transition may be described as follows. For the bare surface the CHF is directly dependent on the flow rate since higher convective conditions will allow for greater heat transfer. While the same is true for the finned surface, the fin presence will cause disturbance in the flow. From the subcooled experiments it was found that the fin presence causes bubble accumulation at the downstream location, which was believed to reduce the CHF. As mentioned earlier, no bubble accumulation occurred for the saturated finned surface experiments. Therefore, the flow conditions may be affecting the transition. The same turbulent mixing that causes a positive effect (increase in CHF) at higher

flow rates may be causing a negative effect (decrease in CHF) at the lowest flow rate. Video observations from B-6 & F-6 and B-7 & F-7 reveal a small difference in the rate at which bubbles are removed from the surface. Comparing the observations made for B-7 and F-7 shows that the large vapor slugs on the bare surface have slightly greater momentum than those on the finned surface, resulting in a higher CHF for the bare surface. The observations made for B-6 & F-6 show that the large vapor slugs on the finned surface are removed slightly faster than those on the bare surface, resulting in a higher CHF for the finned surface.

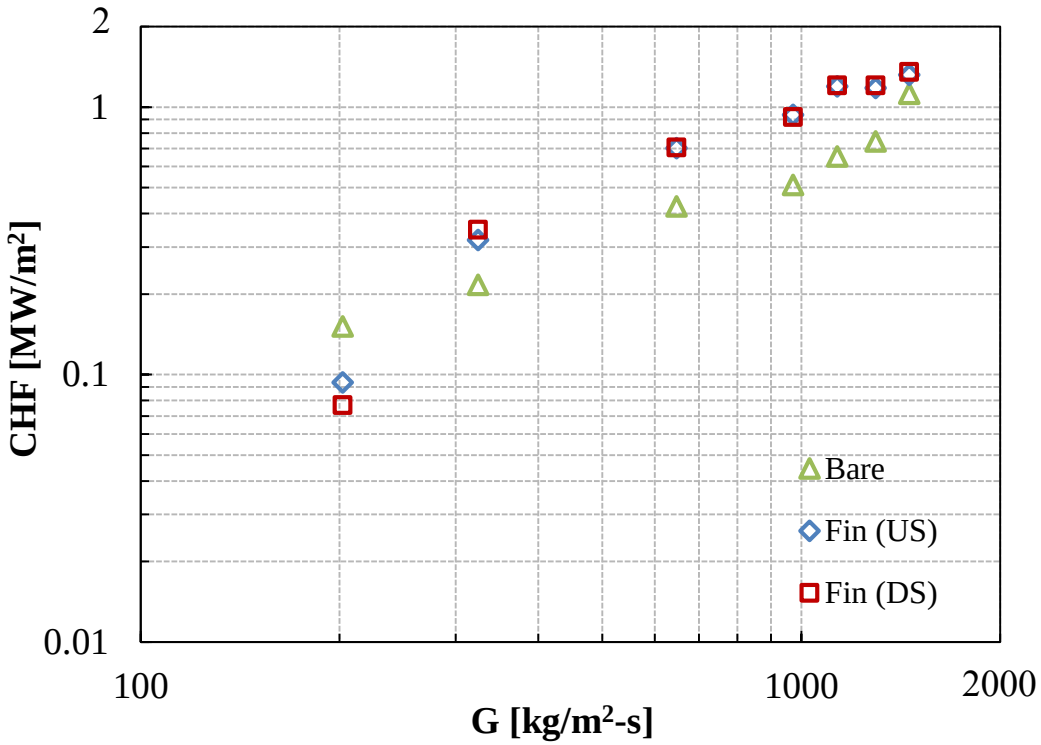

Figure 6-55: Bare and finned surface CHF data.

Figure 6-56 shows the CHF ratio from the finned surface compared to the bare surface. The same values are given in Table 6-11. In the figure, the ratios of the finned surface (both locations) to the bare surface are plotted. The Fin-US/Bare data is the ratio of the fin-upstream location CHF to the bare surface CHF, and the Fin-DS/Bare data is the ratio of the fin-downstream location CHF to the bare surface CHF. A value greater than 1.0 implies enhancement in the CHF from the finned surface, and a value below 1.0 implies a reduction. The lowest flow rate shows a reduction in the finned surface CHF, while all other flow rates

shown an improvement in the CHF. The average and maximum enhancements obtained from the finned surface are 61% and 85%, respectively.

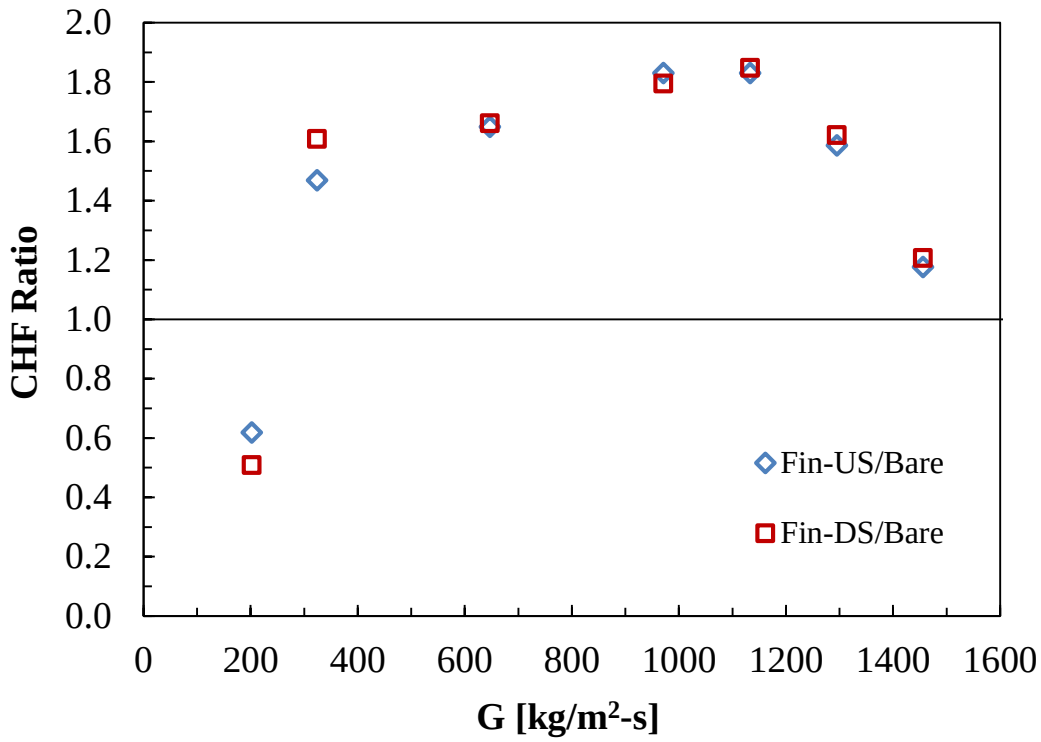

Figure 6-56: CHF enhancement from the finned surface.

Table 6-11: Values of the ratios from Fig. 6-55.

	CHF Ratio*			**CHF Ratio**	
G [kg/m^2-s]	*Fin-US/bare*	*Fin-DS/Bare*	**G [kg/m^2-s]**	*Fin-US/bare*	*Fin-DS/Bare*
1456	1.18	1.21	647	1.65	1.66
1295	1.59	1.62	324	1.47	1.61
1133	1.83	1.85	202	0.62	0.51
971	1.83	1.79			

* CHF Units: [MW/m^2].

The finned surface data was compared with the modified bare surface correlation, given in equation (6-3). The comparison is shown in Fig. 6-57. There is some disagreement between

the correlation of equation (6-3) and the finned surface experimental data (Fig. 6-58). A similar trend is shown between the correlation and the finned surface data, except the data is slightly greater. The constant in equation (6-3) was modified to improve the difference between the correlated and experimental data. There is no significant difference in the CHF for the upstream and downstream locations. Therefore, instead of plotting the correlation for both upstream and downstream locations, an average correlation for the two locations is presented. From Fig. 6-56, it can be seen that the average CHF enhancement from the fin surface is about 61%. Therefore, the CHF fin factor is 1.61 i.e. the approximate fin surface CHF can be given by multiplying the bare surface CHF by a factor of 1.61. Using the fin factor, the modified correlation for the finned surface was given as

$$q_{CHF,\,Fin} = 1.61\, q_{CHF,\,Bare} \tag{6-4}$$

The comparison of the finned surface data and equation (6-4) is shown in Fig. 6-59, along with the bare surface data and equation (6-3). The CHF fin factor applied in equation (6-4) results in good agreement of the finned surface data and equation (6-4). The same is observed when comparing Figs. 6-58 and 6-60.

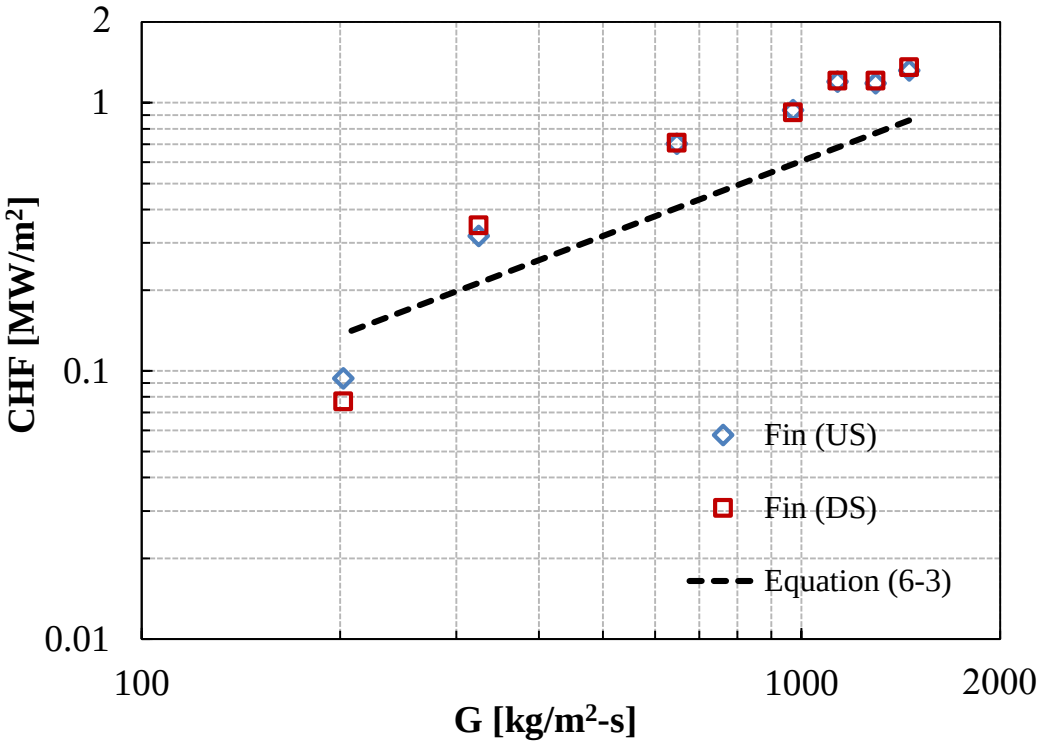

Figure 6-57: Comparison of modified Katto & Kurata correlation with finned surface data.

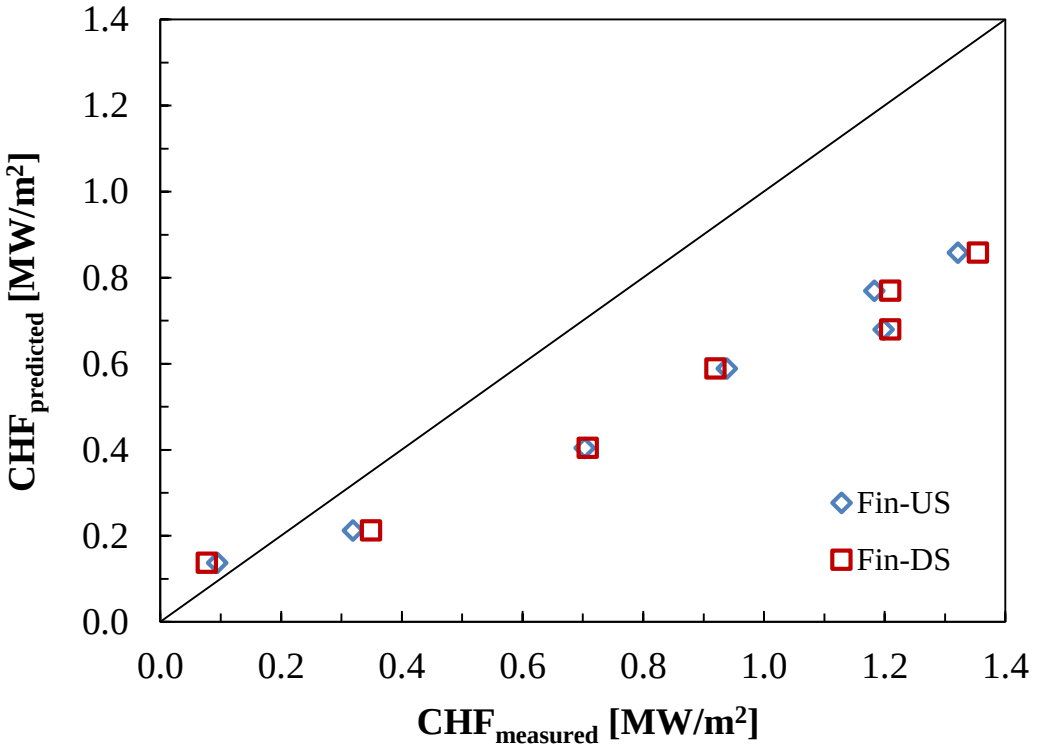

Figure 6-58: Comparison of predicted (equation (6-3)) and measured (fin) CHF.

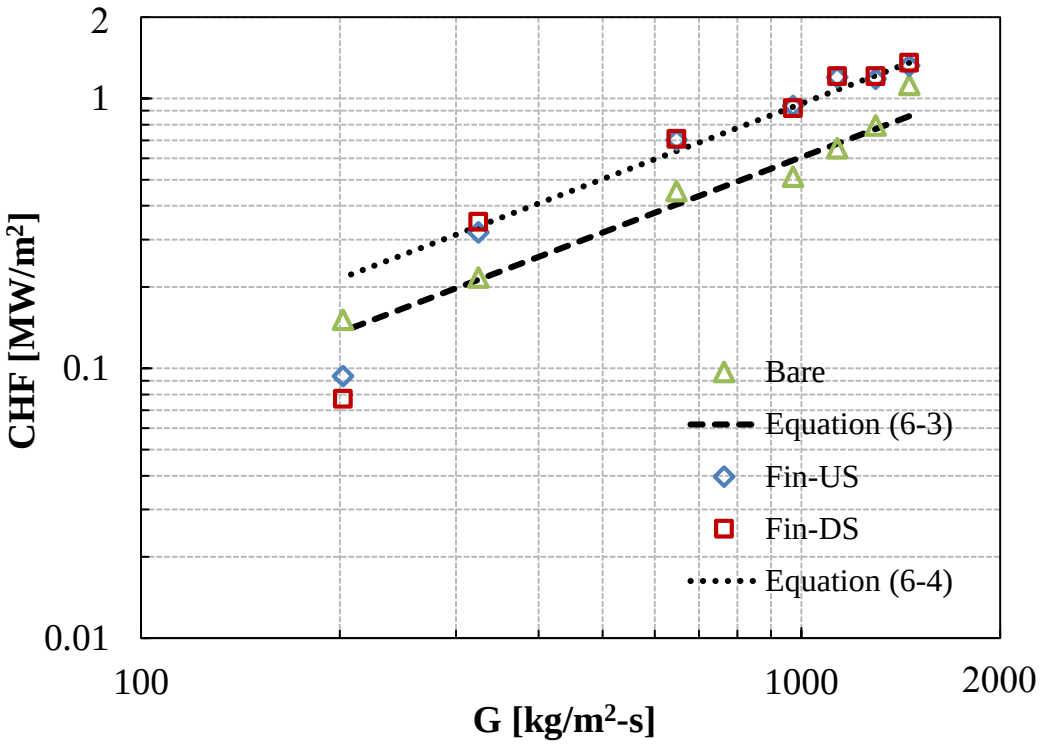

Figure 6-59: Comparison of equations (6-3) and (6-4) with bare and finned surface data.

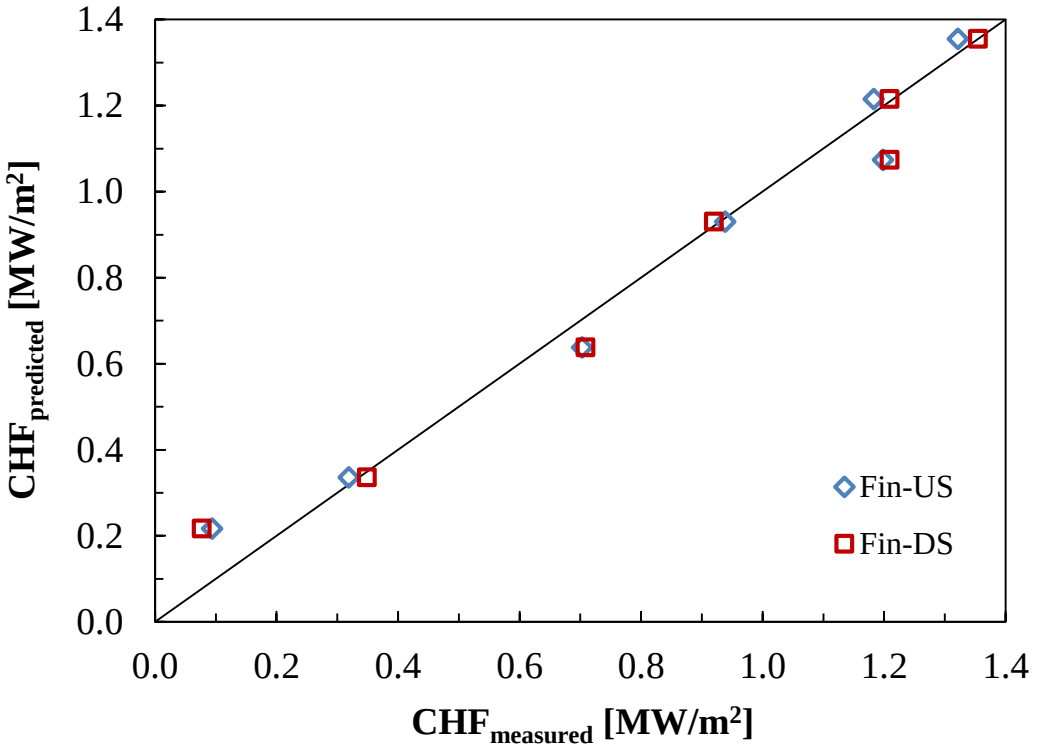

Figure 6-60: Comparison of predicted (equation (6-4)) and measured CHF.

As mentioned earlier, two trends were seen from the finned surface data: positive effect (CHF enhancement) and negative effect (CHF reduction). The positive effect has been estimated rather well by equation (6-4). It is believed that a separate correlation is required to estimate the trend of the negative effect. In the current experiments, data showing the reduction in the CHF for the finned surface is only available for the lowest flow rate. Therefore more data is required in proposing and estimating the negative effect at lower flow rates.

The heat transfer coefficients for both surfaces were calculated by equation (6-1). In the subcooled experiments, the final voltage level was the same for the bare and finned surfaces. Therefore, the improvement in the heat transfer coefficient from the finned surface was observed by calculating a ratio of the finned surface heat transfer coefficient to the bare surface heat transfer coefficient. In the current reduced pressure experiments the final voltage level for the bare surface experiments differed from the finned surface experiments. As a result, the ratio could not have been calculated. Instead, the heat transfer coefficients are shown as a function of the heat flux for each flow rate (Figs. 6-61 to 6-67). All figures except Fig. 6-67 show that the heat transfer coefficient is greater for the finned surface compared to the bare surface at the same voltage level, even though in some cases the coefficient has increased only slightly. This implies that the fin has improved the heat transfer for all but the lowest flow rate. Notice in the figures below that some experiments display a larger improvement in the heat transfer coefficient between the bare and finned surfaces, and between the upstream and downstream locations for the finned surface. For example when comparing Figs. 6-63 and 6-64, it is observed that the difference between the finned and bare surface heat transfer coefficients in Fig. 6-63 is larger than the same difference shown in Fig. 6-64. Also note that the difference between the upstream and downstream coefficients in Fig. 6-63 is larger than the same difference shown in Fig. 6-64. The difference in the data may be caused by some uncertainty in the experimental conditions, specifically the voltage level and the flow rate. Small variations in the applied voltage (for the cartridge heaters) will cause some difference in the heat flux and surface temperature calculations. Similarly, small variations in the flow rates will also cause some differences in the heat transfer from the boiling surface. It is believed that the discrepancy in the data was caused by such uncertainty.

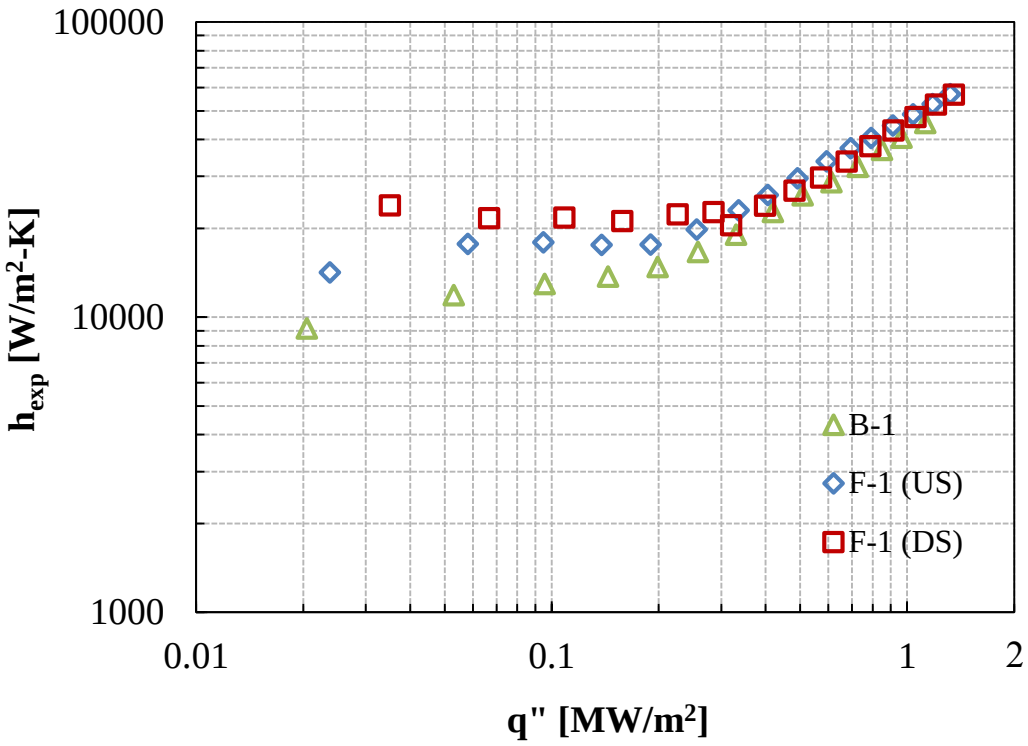

Figure 6-61: Heat transfer coefficients for B – 1 and F – 1 (1456 kg/m^2-s) experiments.

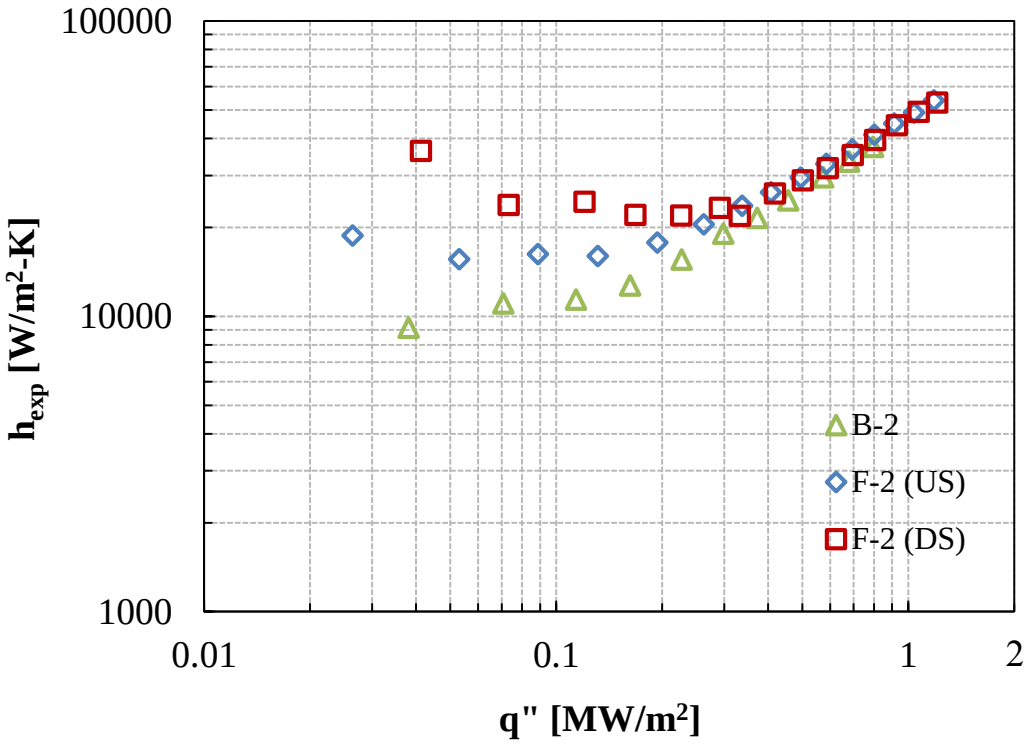

Figure 6-62: Heat transfer coefficients for B – 2 and F – 2 (1295 kg/m^2-s) experiments.

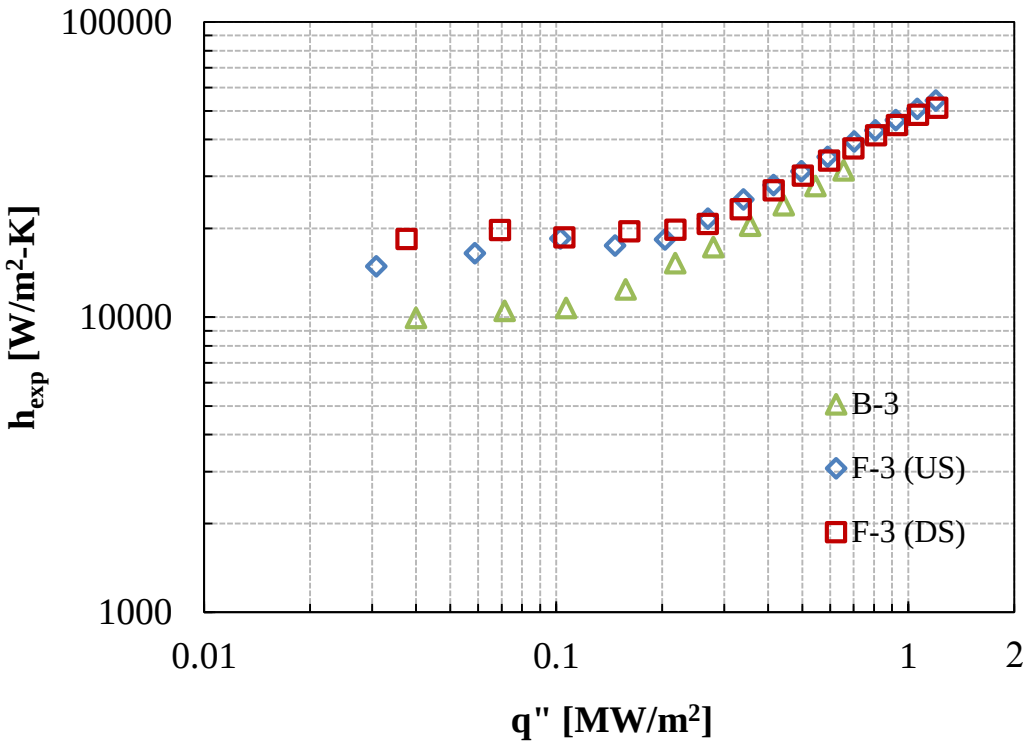

Figure 6-63: Heat transfer coefficients for B – 3 and F – 3 (1133 kg/m^2-s) experiments.

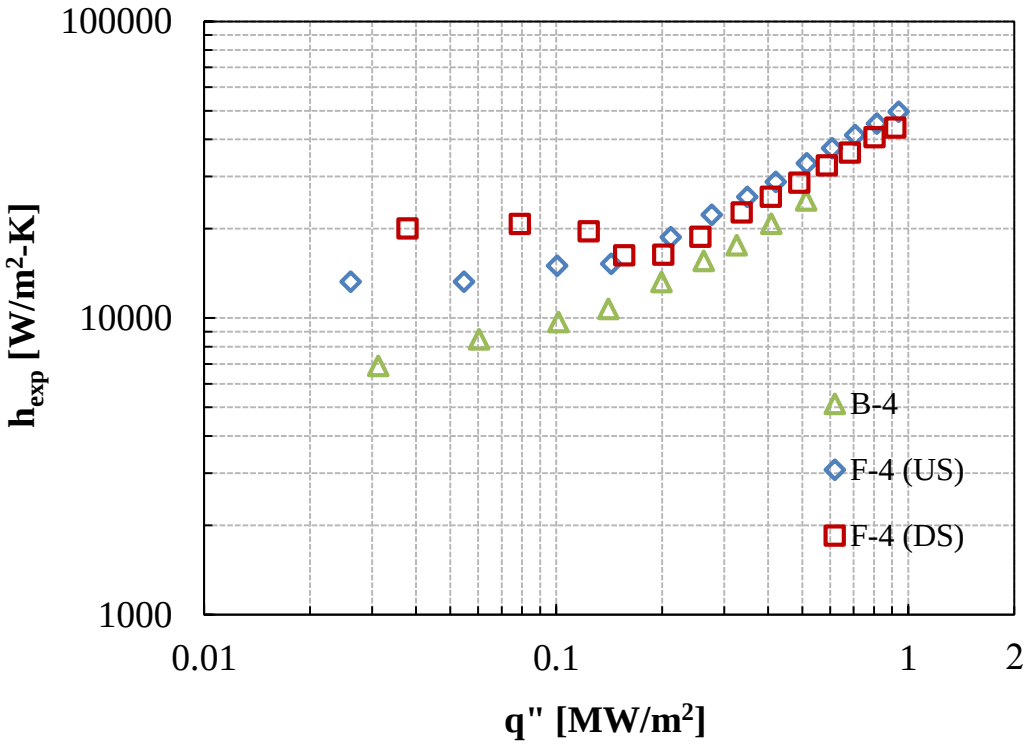

Figure 6-64: Heat transfer coefficients for B – 4 and F – 4 (971 kg/m^2-s) experiments.

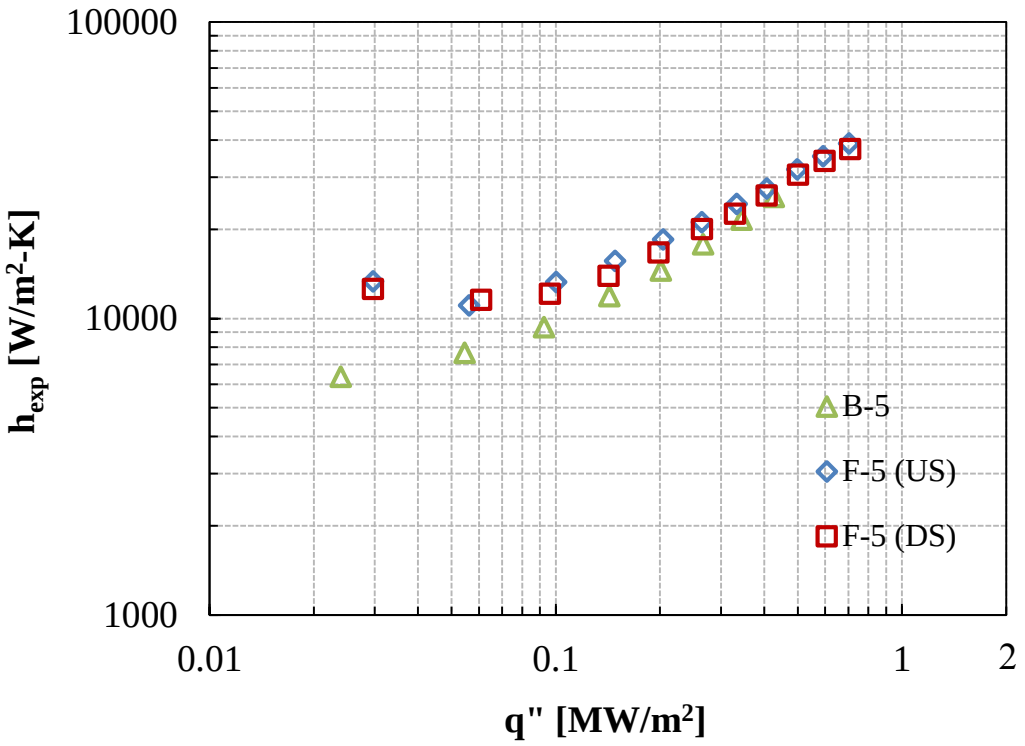

Figure 6-65: Heat transfer coefficients for B – 5 and F – 5 (647 kg/m^2-s) experiments.

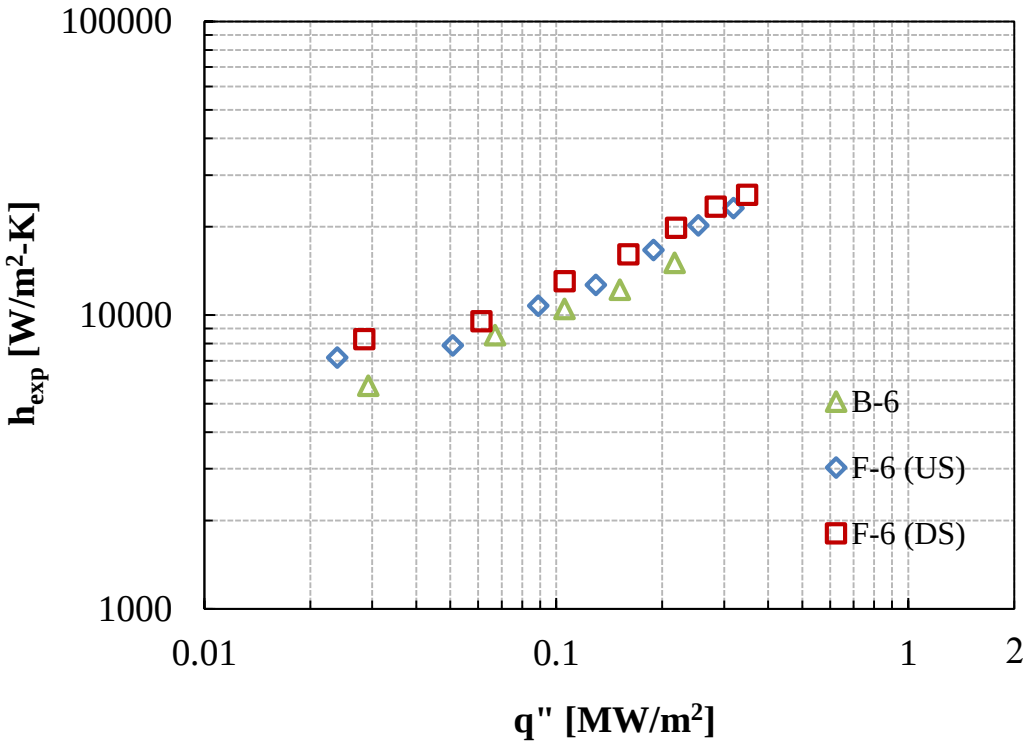

Figure 6-66: Heat transfer coefficients for B – 6 and F – 6 (324 kg/m^2-s) experiments.

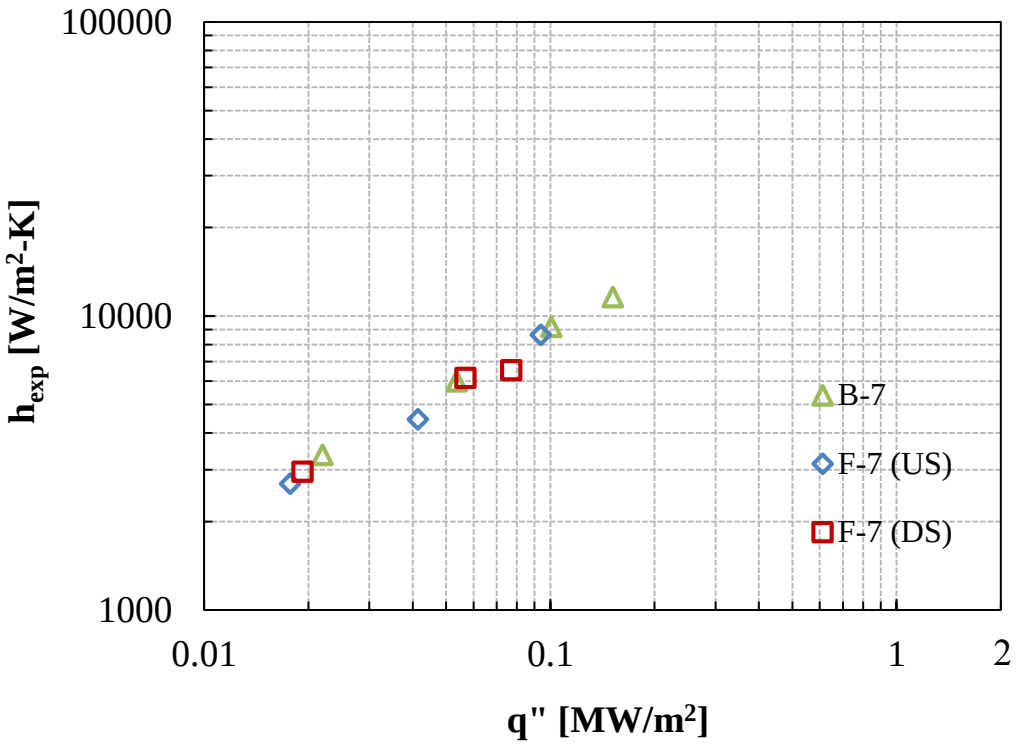

Figure 6-67: Heat transfer coefficients for B – 7 and F – 7 (202 kg/m^2-s) experiments.

6.5.2 Heat Transfer Coefficient Comparison: Experiment & Correlation

The heat transfer coefficients obtained from the finned surface experiments were compared with a heat transfer correlation. The correlation presented in the previous chapter was proposed for subcooled conditions, and was not applicable for the conditions of the current experiments. A heat transfer correlation for saturated conditions was desired.

As mentioned in the previous chapter in section 5.5.3, correlations often include dimensionless parameters which account for the physics of the experiment. Comparing such a correlation with the experimental data was desired. Hu et al. (2011) presents various heat transfer coefficient correlations for flow boiling. Three of the correlations presented in their work were of interest, since they consisted entirely of dimensionless parameters. The three correlations listed in their work were proposed by Lazarek and Black (1982), Tran et al. (1996), and Yu et al. (2002). The correlations, in the same order, are

$$h_{tp} = 30 Re^{0.857} Bo^{0.714} \left(\frac{k_f}{d_h} \right) \tag{6-5}$$

$$h_{tp} = 8.4x10^5 \left(Bo^2 We \right)^{0.3} \left(\frac{\rho_g}{\rho_f} \right)^{-0.4} \tag{6-6}$$

$$h_{tp} = 6.4x10^6 \left(Bo^2 We \right)^{0.27} \left(\frac{\rho_g}{\rho_f} \right)^{-0.2} \tag{6-7}$$

where

We = Weber number: $\frac{\rho_l v^2 D}{\sigma}$ [dimensionless]

Since equation (6-7) is very similar to equation (6-6), only the latter was considered for comparison. Equations (6-5) and (6-6) were compared with the finned surface heat transfer coefficients. Equation (6-5) showed good agreement with the data without any modification and equation (6-6) significantly over predicted the heat transfer coefficient. Even though equation (6-6) did not show good agreement with the data, it was chosen as the correlation for the comparison. The reason being it accounts for the experimental conditions at reduced pressure by including the density ratio. The correlation by Tran et al. was proposed for refrigerants (R-12) at a saturation pressure of approximately 0.82 MPa. Their experiments were conducted in small circular (2.46 mm diameter) and rectangular (4.06 mm x 1.70 mm) channels, applying a range of mass flux (44 – 832 kg/m^2-s). The difference in the experimental conditions between the current study and Tran et al. are believed to cause the disagreement between equation (6-6) and current experimental data.

Slight modifications were made to the correlation since it did not agree well with the experimental data. It is seen in Figs. 6-61 to 6-67 that a small difference is present in the upstream and downstream coefficients. For simplification, the average correlated values of the upstream and downstream heat transfer coefficients and corresponding heat flux were calculated and plotted. Additionally, a change in the correlation constant was also necessary in equation (6-6). The hydraulic diameter required for the *We* number was calculated by equation (5-15). The modified correlation for the finned surface was obtained as

$$h_{tp} = 3.7x10^4 \left(Bo^2 We\right)^{0.3} \left(\frac{\rho_g}{\rho_f}\right)^{-0.4} \tag{6-8}$$

A comparison of equation (6-8) and the finned surface experimental data is presented in Figs. 6-68 to 6-74. Simultaneously in the same figures the bare surface heat transfer coefficients are plotted with a modified version of equation (6-8) for the bare surface. Only the constant in equation (6-8) was modified to obtain the bare surface correlation, given by

$$h_{tp} = 3.1x10^4 \left(\mathrm{Bo}^2 We\right)^{0.3} \left(\frac{\rho_g}{\rho_f}\right)^{-0.4} \tag{6-9}$$

The emphasis of the comparison is on higher heat flux where nucleate boiling conditions are present. All figures show that the correlations are in good agreement with the experimental data. Notice that not only does the correlation agree well with the data, but it accounts for the trend of the experimental data. This may imply that the correlation incorporates the correct dimensionless parameters and exponents to predict the heat transfer coefficient for both surfaces. Figure 6-75 shows the comparison of the correlated and finned surface experimental heat transfer coefficients. The experimental data at high heat flux (greater heat transfer coefficients) agrees well with the correlated data. At lower heat flux the experimental values are greater than those predicted by the correlation, especially for the downstream data. This may be the cause of the wake effect at low applied voltages. The mixing of the flow in the wake of the fin is believed to cause higher heat transfer at low heat flux.

The purpose for presenting the bare surface correlation is to show and calculate the average enhancement in the heat transfer coefficient from the finned surface. One method of calculating the average heat transfer enhancement was through a comparison of the correlations. In order to obtain an average heat transfer enhancement from the correlations, all the data was compared to the average correlation for each surface type. Figures 6-76 and 6-77 show the heat transfer coefficients as a function of the heat flux for the bare and finned surfaces, respectively. From the figures it is evident that at higher heat flux the correlations show good agreement with the experimental data.

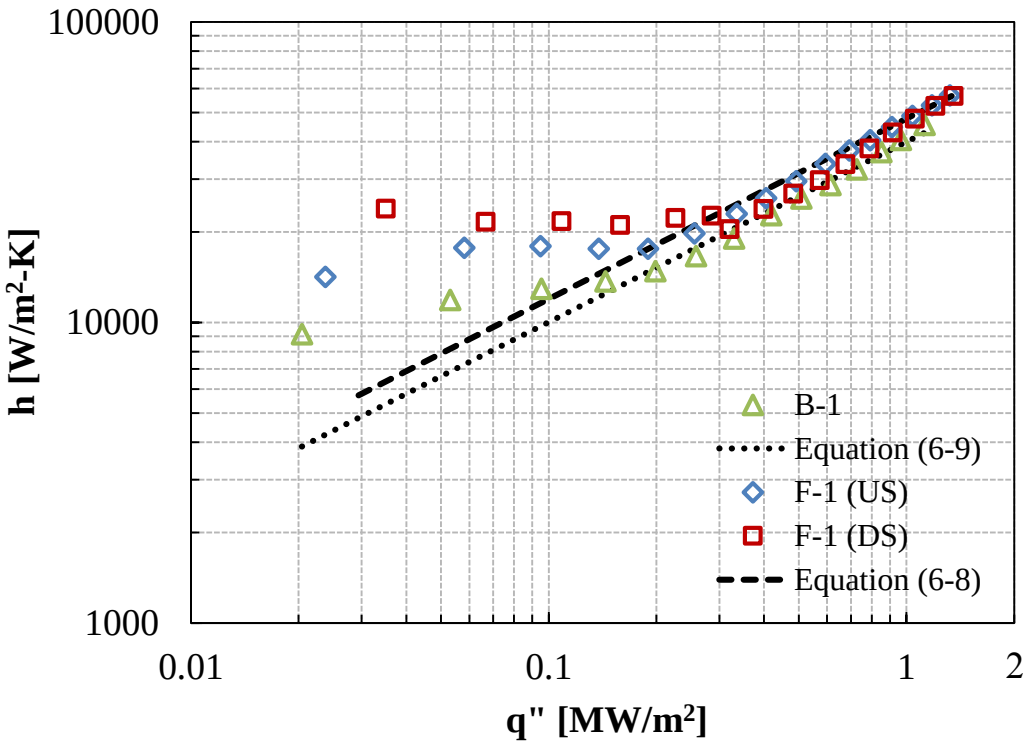

Figure 6-68: Comparison of correlations with B,F – 1 (1456 kg/m^2-s) experimental data.

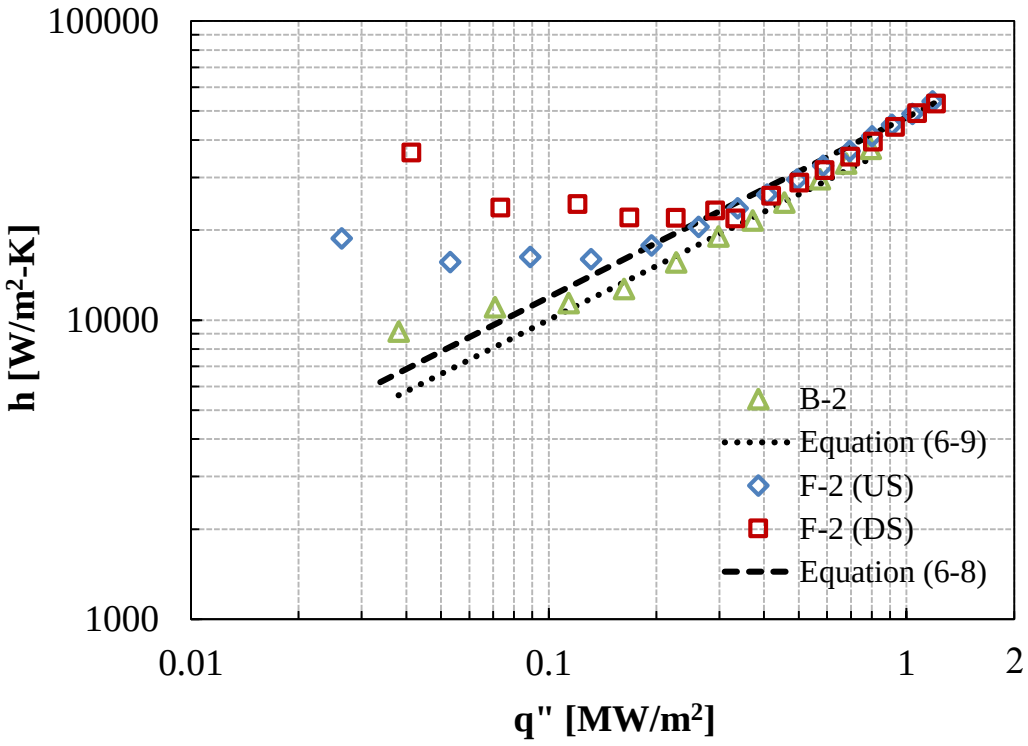

Figure 6-69: Comparison of correlations with B,F – 2 (1295 kg/m^2-s) experimental data.

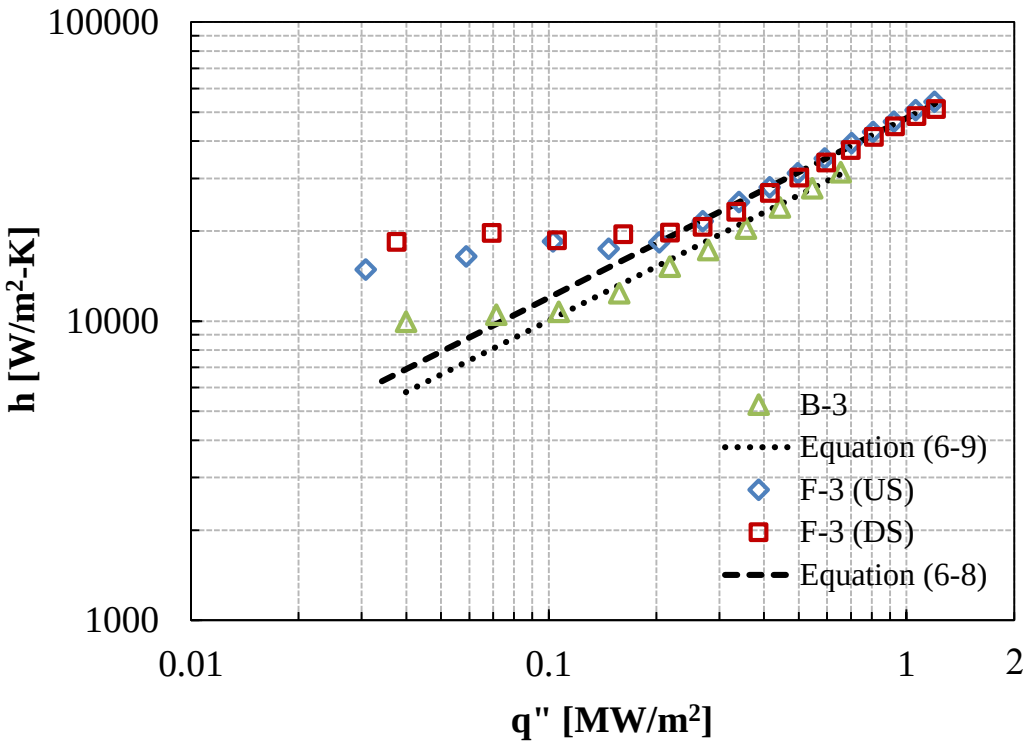

Figure 6-70: Comparison of correlations with B,F – 3 (1133 kg/m^2-s) experimental data.

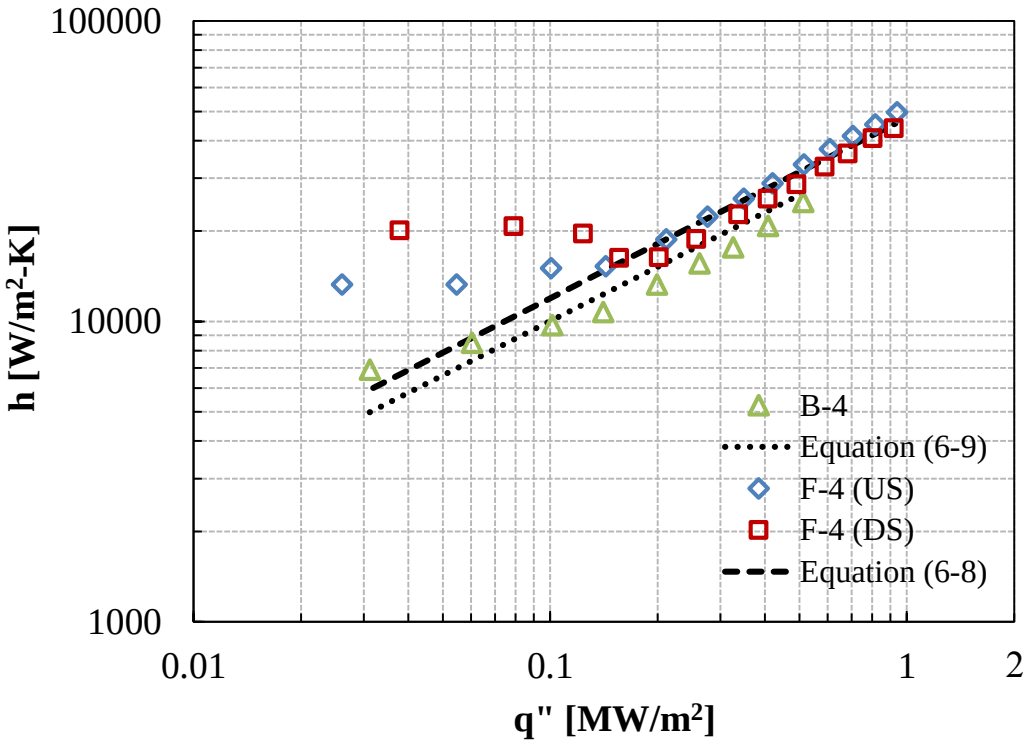

Figure 6-71: Comparison of correlations with B,F – 4 (971 kg/m^2-s) experimental data.

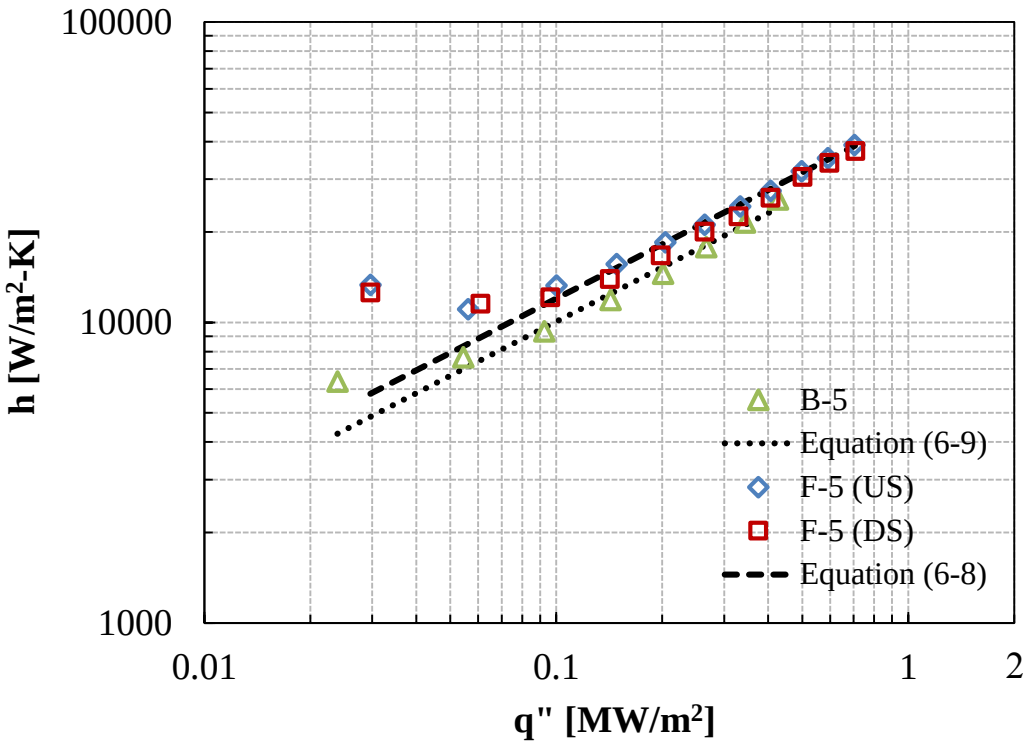

Figure 6-72: Comparison of correlations with B,F – 5 (647 kg/m^2-s) experimental data.

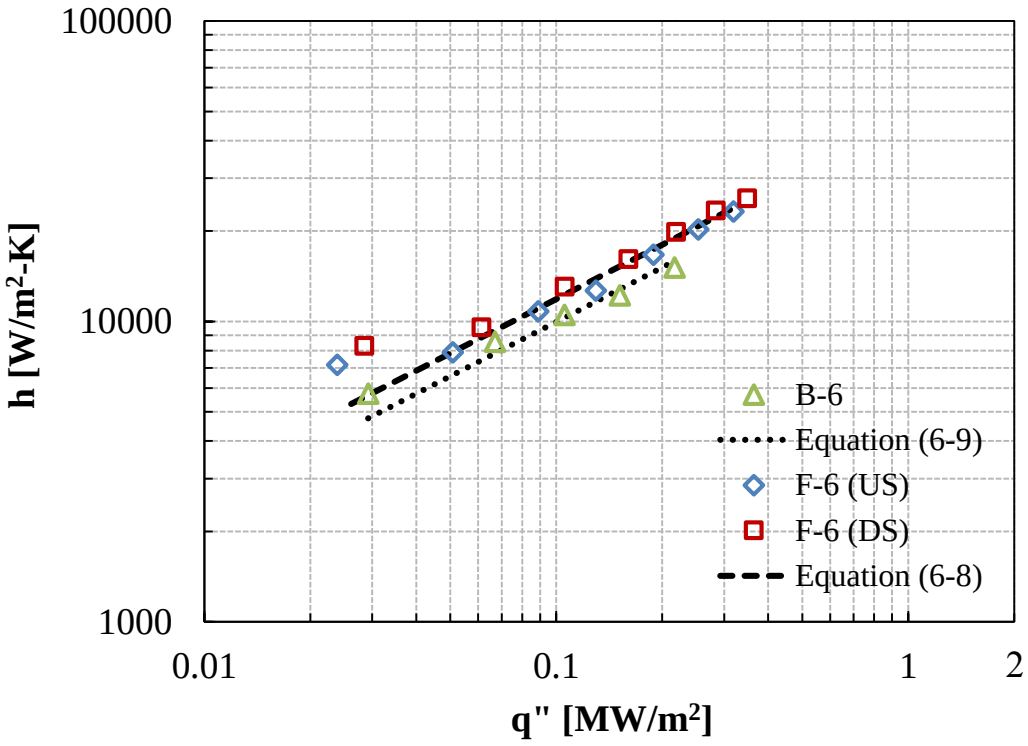

Figure 6-73: Comparison of correlations with B,F – 6 (324 kg/m^2-s) experimental data.

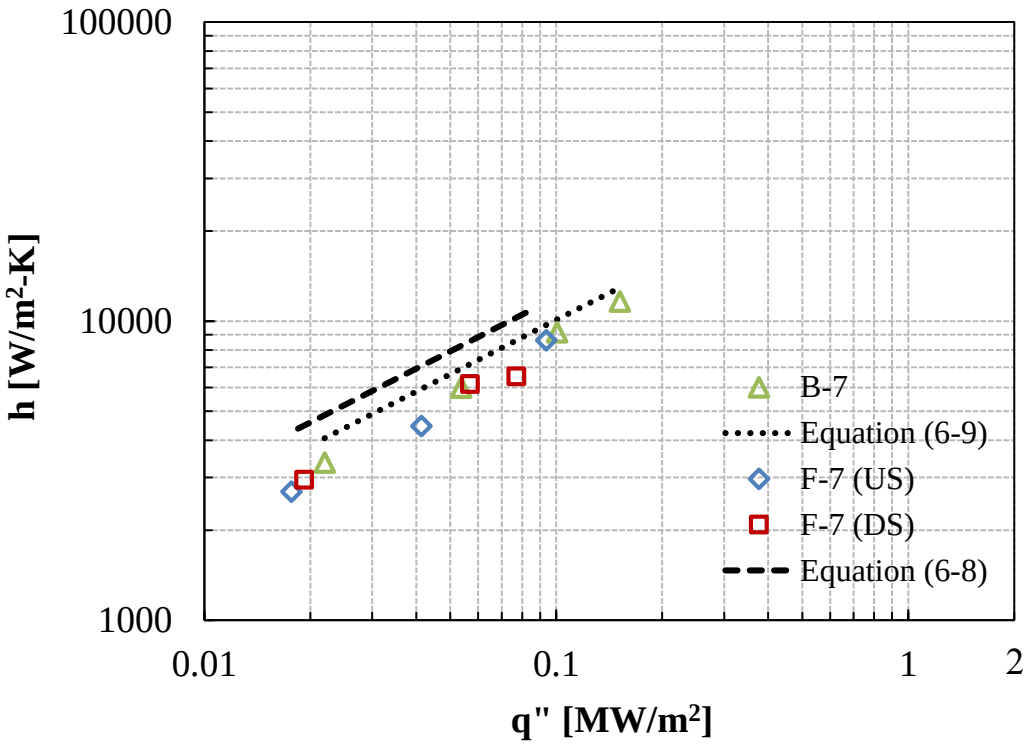

Figure 6-74: Comparison of correlations with B,F – 7 (202 kg/m^2-s) experimental data.

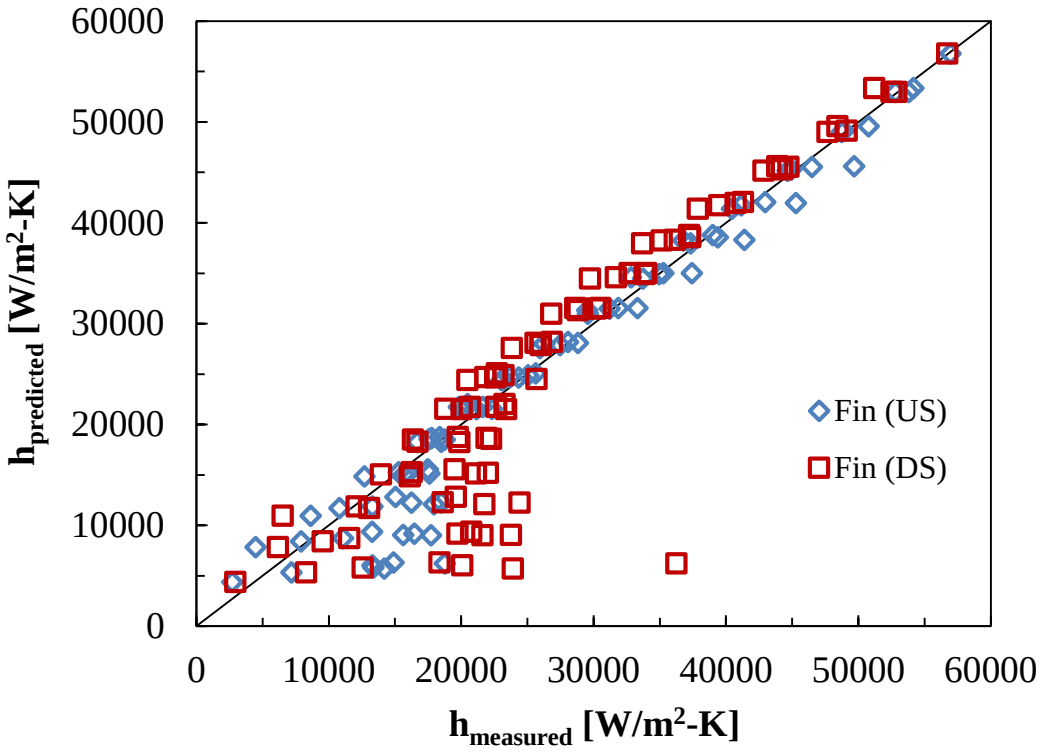

Figure 6-75: Comparison of predicted (equation (6-8)) and measured coefficients.

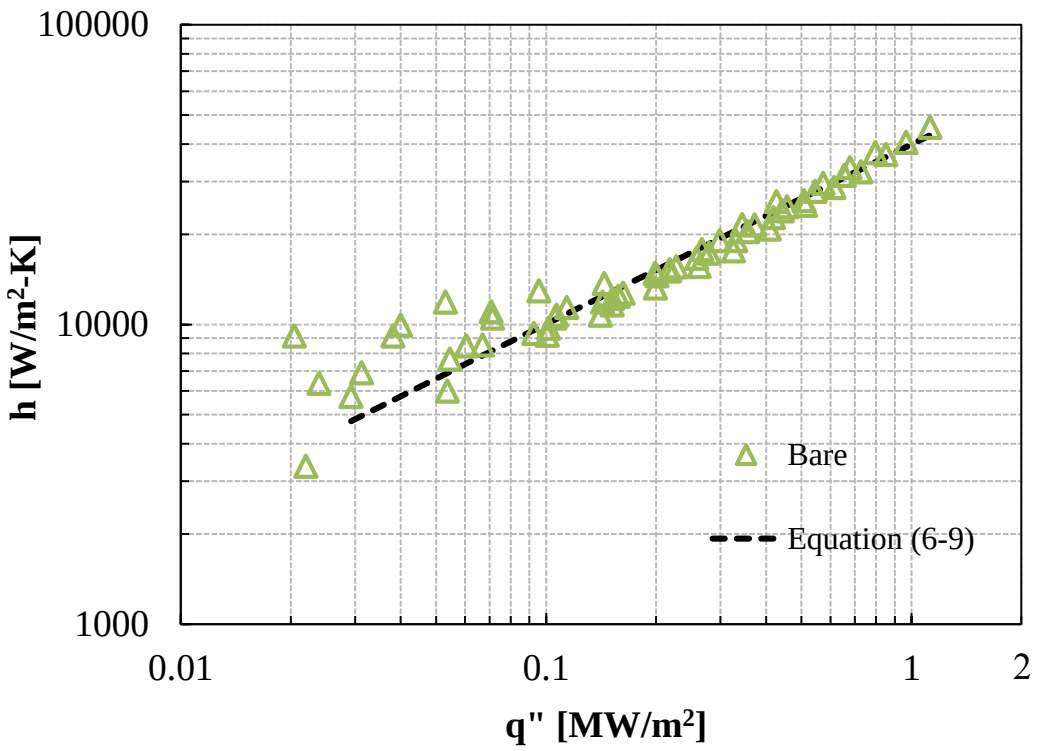

Figure 6-76: Comparison of average bare surface correlation with all bare experimental data.

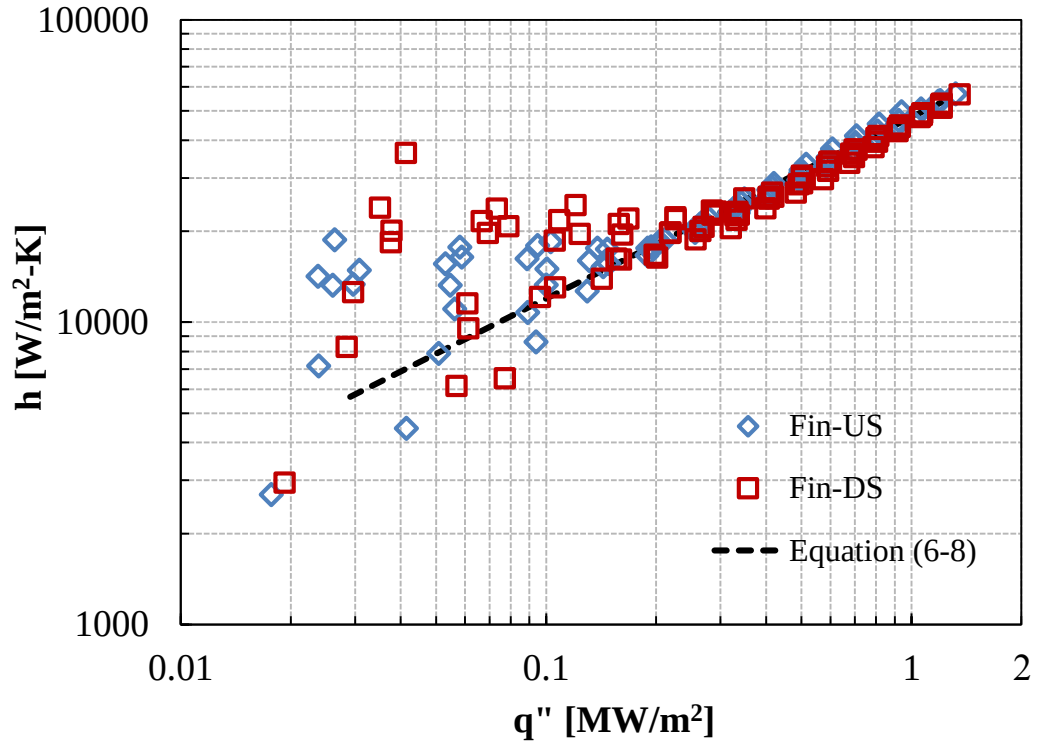

Figure 6-77: Comparison of average fin surface correlation with all fin experimental data.

When Figs. 6-76 and 6-77 are combined, the average enhancement in the heat transfer is seen from the increase in the correlations (Fig. 6-78). The modified Tran et al. correlations express the heat transfer coefficients well. There is no dependency on the flow rate at higher heat flux. The average heat transfer enhancement was obtained by taking the ratio of the fin correlation to the bare correlation. Dividing equation (6-8) by (6-9) yields a ratio of approximately 1.19, which is the heat transfer enhancement factor i.e. $h_{fin} = 1.19 h_{bare}$. Thus, the average heat transfer enhancement obtained from the finned surface is about 19%.

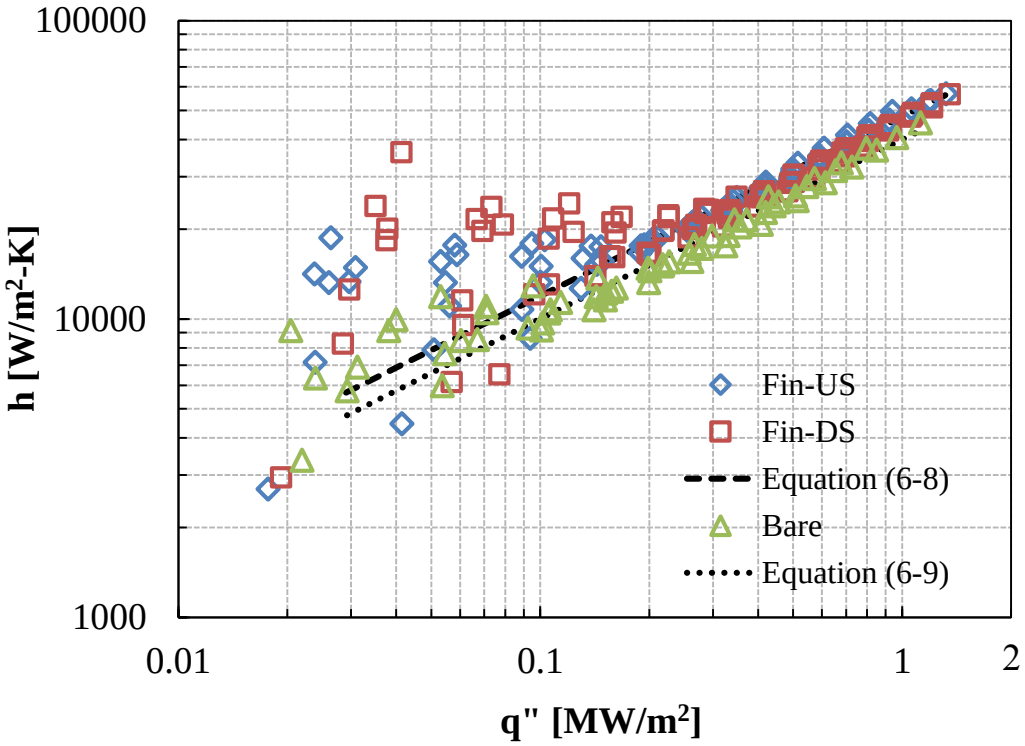

Figure 6-78: Heat transfer coefficients for both surfaces compared with both correlations.

6.5.3 Heat Transfer and CHF Enhancement

The enhancement in the heat transfer is believed to occur due to two reasons. Theoretically, an increase in the surface area allows for an increase in the heat transfer by increasing the area through which convection occurs. Consider the heated surface area of the finned surface and the bare surface. The ratio of the finned to bare surface area (A_{fin}/A_{bare}) is approximately 20%.

The average heat transfer enhancement as found from Fig. 6-78 is approximately 19%. The increase in the surface area is believed to increase the heat transfer. Another reason for the increase in the heat transfer is due to the conduction into the fin. When the fin is present on the surface, the increase in the surface area also allows heat to be transferred into the fin from the surrounding base area. Since heat is transferred into the fin, the surface temperatures will be reduced. The reduction of the surface temperatures can be seen in the boiling curves (Figs. 6-40 to 6-46). The fin causes a shift in the boiling curves as it reduces the surface temperatures.

An average CHF enhancement of approximately 61% was observed from the fin (Fig. 6-56). As mentioned earlier, one of the reasons for CHF enhancement is believed to occur due to the enhancement in the heat transfer. As mentioned above the presence of the fin reduces the surface temperatures, causing a shift in the boiling curve. The shift in the curve causes an enhancement of approximately 19% in the heat transfer. The shift also allows for an enhancement of approximately 61% in the CHF. Figure 6-79 shows an illustration of the boiling curve shift and its effects.

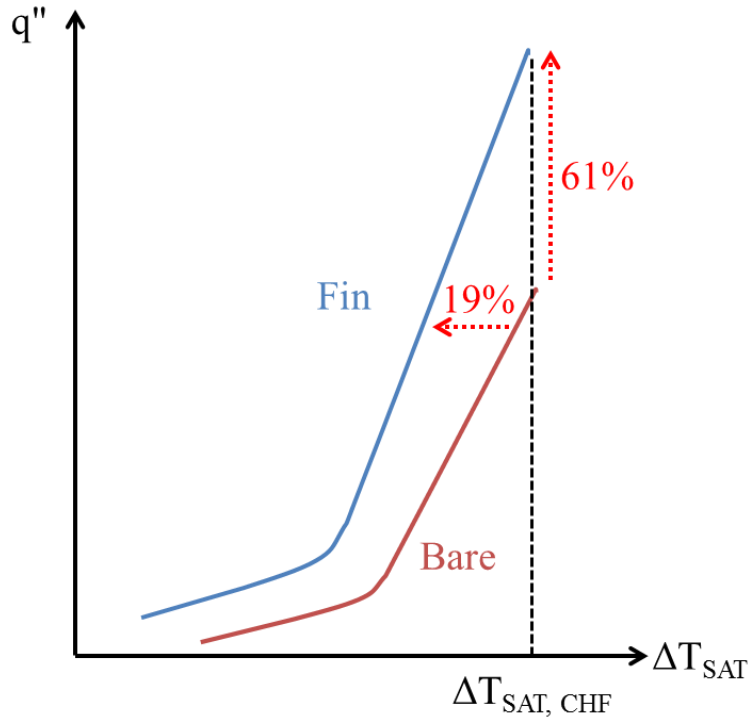

Figure 6-79: Illustration of boiling curve shift causing heat transfer and CHF enhancement.

In Fig. 6-79 the vertical dashed line represents the excess heat at CHF ($\Delta T_{SAT,CHF}$) for both bare and finned surfaces. When the $\Delta T_{SAT,CHF}$ was plotted for both surfaces, approximately same excess heat is observed for the bare and finned CHF. Figure 6-80 shows that even though there are some differences between the bare and finned surface excess heat, the temperatures are approximately within a standard deviation of two degrees for all flow rates. Moreover, the general observation made from Figs. 6-79 and 6-80 is that the fin allows for a greater increase in the CHF compared to the heat transfer at approximately similar excess heat temperatures. In other words, the presence of the fin has increased the CHF significantly (three times greater than the heat transfer) without causing large differences in the excess heat. Another reason for the increase in the CHF is believed to be the result of no bubble accumulation on the surface. In the previous chapter, bubble accumulation was found to occur on the boiling surface. The reduction in the heat transfer and CHF in the subcooled experiments was believed to be the result of the bubble accumulation. No bubble accumulation occurred in the current saturated experiments. This was believed to be due to the higher flow rates applied in the experiments. If some accumulation occurred, the relatively higher flow rates would be able to remove the bubble accumulation on the surface.

It was observed from the current experiments that with an appropriate fin design, a large enhancement in the CHF can be obtained. The enhancement in the heat transfer results from the reduction in the surface temperatures, which causes a shift in the boiling curve. The shift in the boiling curve was the result of an average enhancement of approximately 19% in the heat transfer. The shift in the curve also resulted in an average CHF enhancement of 61% at approximately similar excess heat (ΔT_{SAT}). It should be clarified that although an enhancement is observed in the CHF, a reduction can also occur in the CHF. Bubble accumulation on the boiling surface may cause reduction in the CHF.

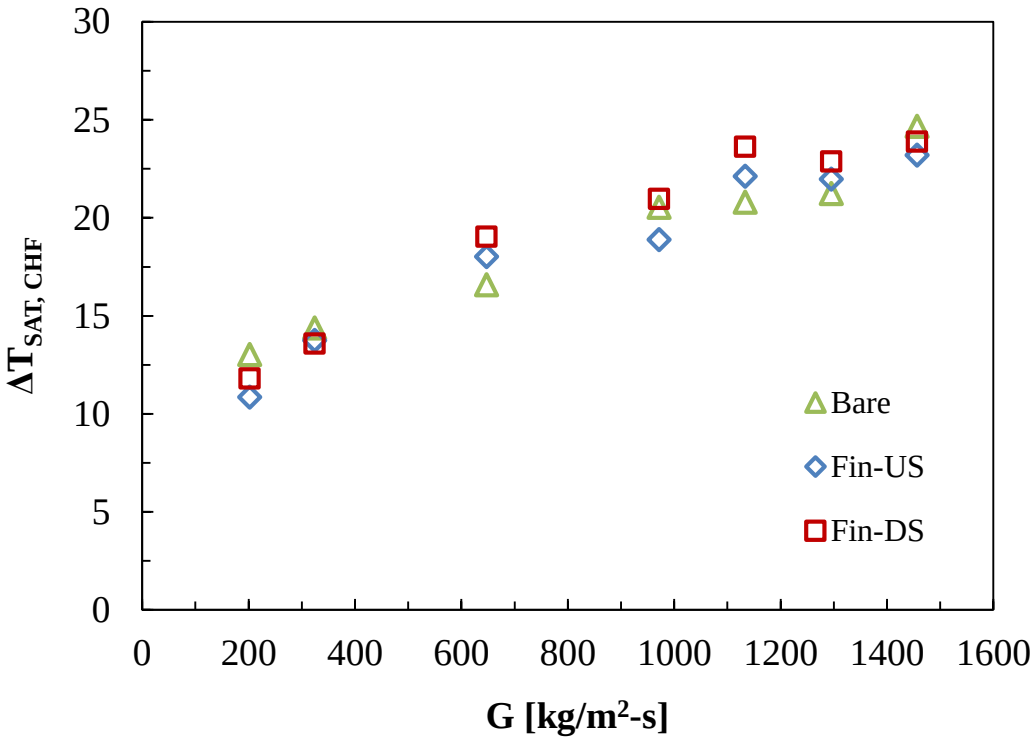

Figure 6-80: Excess heat at CHF ($\Delta T_{SAT,CHF}$) for bare and finned surfaces.

6.6 Summary: Saturated Flow Boiling Experiments

The following summarizes the work performed in the saturated experiments:

- Reduced pressure flow boiling data was obtained for downward-facing surfaces. Downward-facing flow boiling experiments have not been frequently studied.
- Experiments were performed for reduced pressure of approximately 50 kPa at which the saturated temperature was approximately 81°C.
- Flow boiling heat transfer was investigated from a finned surface, and compared with a bare surface.
- A range of flow rates were applied to study the boiling behavior from downward-facing heated surfaces. The mass flux applied were: 202 kg/m^2-s, 324 kg/m^2-s, 647 kg/m^2-s, 971 kg/m^2-s, 1133 kg/m^2-s, 1295 kg/m^2-s, and 1456 kg/m^2-s.
- CHF conditions were observed for all flow rates.

The following summarizes the conclusions from this chapter:

- The heat transfer was enhanced in saturated flow boiling conditions by the presence of a pin-fin.
- Both positive and negative effects from the fin were observed in the experiments.
- The finned surface was able to increase the heat transfer and CHF compared to a bare downward-facing surface for all but the lowest flow rate applied. An average heat transfer enhancement of approximately 19%, an average CHF enhancement of approximately 61%, and a maximum CHF enhancement of 85% were obtained from the current experiments.
- The lowest flow rate applied resulted in lower CHF for the finned surface compared to the bare surface.
- Fin-downstream temperatures were greater than upstream temperatures.
- No bubble accumulation was observed in the wake region.

The knowledge obtained from this study was useful in determining the applicability of a finned surface design to enhance heat transfer. The effect of one fin on forced convection boiling heat transfer was studied. To better understand the applicability of a finned surface design, a sensitivity study on the fin diameter, length, and spacing is proposed as future work.

7. CONCLUSIONS & FUTURE WORK

7.1 Conclusions

Current ex-vessel cooling capability may not provide sufficient cooling during a severe accident for future larger-powered LWRs implementing ex-vessel cooling as an accident management strategy. Additional improvement may be required in the heat transfer from the vessel surface. One method proposed is to apply a structured design on the exterior of the RPV, specifically a finned surface design. In order to observe the effect of a finned surface during forced convection conditions, an experimental study was performed to understand the effect of a pin-fin on flow boiling heat transfer from a downward-facing surface.

Experiments were performed at highly subcooled and saturated conditions with separate facilities for each condition. Positive and negative effects were observed from the finned surface. The enhancement in the heat transfer and CHF was achieved at higher flow rates, whereas the reduction in the heat transfer and CHF was observed at the lowest flow rate conditions. From both experiments, it was found that the fin is a capable method of improving the heat transfer from a boiling surface during forced convection conditions. Previously, no data was found to confirm quantitatively the ability of a fin to enhance heat transfer in flow boiling conditions. Only for the subcooled experiments bubble accumulation was found to occur in the wake of the fin. The accumulation was believed to cause the greater downstream surface temperatures. Even though the fin was able to enhance the heat transfer in both cases, the enhancement was only observed at certain conditions. If the conditions do not favor improving the heat transfer, reduction can be observed even with the presence of a fin. The presence of the fin itself does not guarantee enhancement in the heat transfer.

In the beginning (Chapter 2) a hypothesis was stated about CHF enhancement through a finned surface design. From the work performed as part of this thesis, the hypothesis was conformed. It was found that the pin-fin is an applicable design to improve the heat transfer and CHF from a boiling surface. During subcooled conditions, approximately 4 – 5% enhancement in the heat transfer was observed. An average of 19% enhancement in the heat transfer and an average of 61% enhancement in the CHF were observed for saturated conditions. It is believed that such

a design can be applied on the outer surface of the RPV to improve CHF during ex-vessel cooling. Further studies are necessary to investigate an optimized finned design for application.

Although an oversimplification, the results from this study may be extrapolated and applied to the submerged lower head section of a BWR under severe accident. If bubble accumulation occurs around the CRGTs in the lower head of a BWR, it may cause high surface temperatures. If bubble accumulation cannot be removed, the occurrence of CHF may eventually cause RPV failure. Therefore, such phenomenon should be considered as a safety issue for the submerged BWR lower head. On the other hand, RPV failure may be prevented if the CRGTs are able to dissipate heat, like fins, on the lower head of a submerged BWR.

7.2 Considerations for Future Work

Three recommendations are made regarding the future work of this study. The first proposal is to continue the current finned surface experiments and apply an array of fins instead of just one fin. As mentioned earlier, an optimized design for the finned surface will assist in the application of such a design. In order to propose an optimized design, the heat transfer effect from an array of fins on a boiling surface should be investigated during forced convection conditions. Therefore, it is important to investigate which combination of the fin diameter, length, and spacing will offer the greatest enhancement in the heat transfer at certain flow conditions.

The next recommendation is regarding a different type of structured surface design: porous honeycomb structured surface. This type of surface has been previously studied by Mori and Okuyama (2009) and Mori et al. (2015). The porous honeycomb design has shown promising results in heat transfer enhancement. The concept of this design is to wick water onto the boiling surface through the pores and release the generated vapor through the large openings created on the porous honeycomb. The above mentioned studies have not performed experiments at forced convection conditions. If such a design is to be implemented on the outer surface of a RPV, the design should be tested under flow boiling conditions. Therefore, the porous honeycomb design will be tested using the new test facility mentioned in this thesis.

Instead of performing downward-facing experiments only, experiments at different angular positions is desired.

The final recommendation is a method related to changing the surface characteristics, and is not a structured design. Radiation Induced Surface Activation (RISA) is a method that has been shown to increase heat transfer from a boiling surface (Imai et al., 2002; Koga et al, 2002; Okamoto et al, 2002; Takamasa et al., 2005). A change in the surface characteristics occurs when the surface is irradiated for a certain amount of time, and enhancement in the boiling performance is observed. Previous studies have investigated RISA in pool boiling conditions. If this technique is applied to enhance the heat transfer on the outer vessel of a RPV, experiments performed at forced convections conditions are required. The experiments will provide quantitative information necessary for the application of this technique.

APPENDIX

The following steps show the boiling surface preparation for the saturated experiments.

1) Remove the test section from the channel and place upside down.

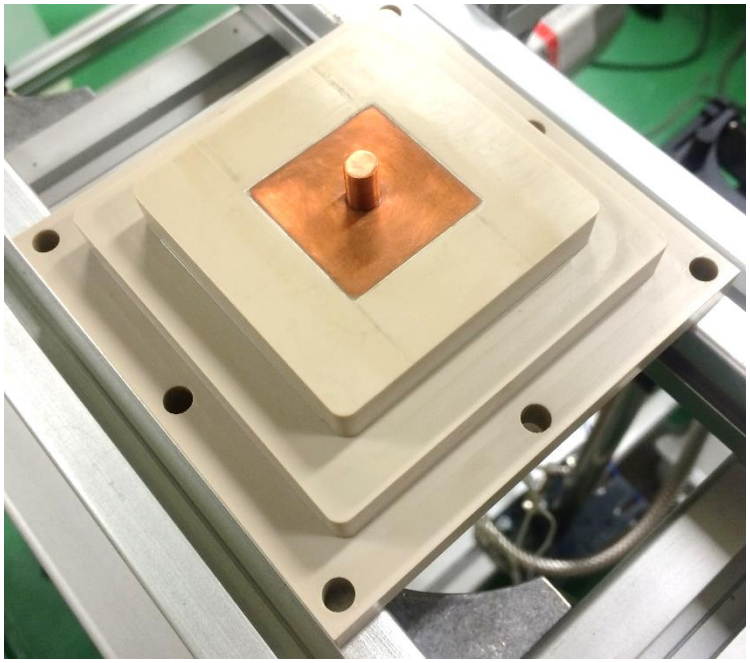

2) Remove previously applied silicone on surface.

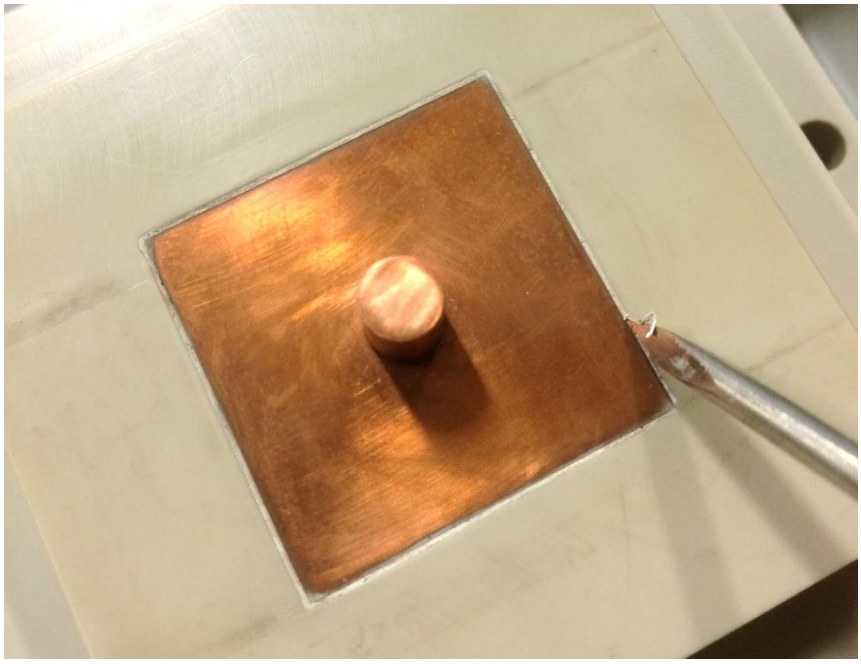

3) Apply new silicone on the boundary of boiling surface, ensuring to cover the gap between the edge of the copper boiling surface and the edge of PEEK.

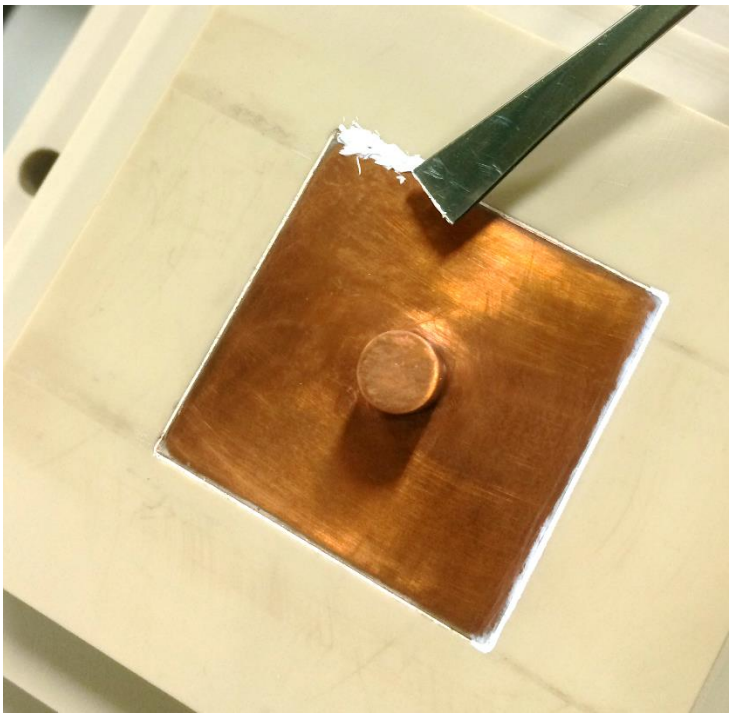

4) Remove excess silicone applied on the boiling surface and PEEK.

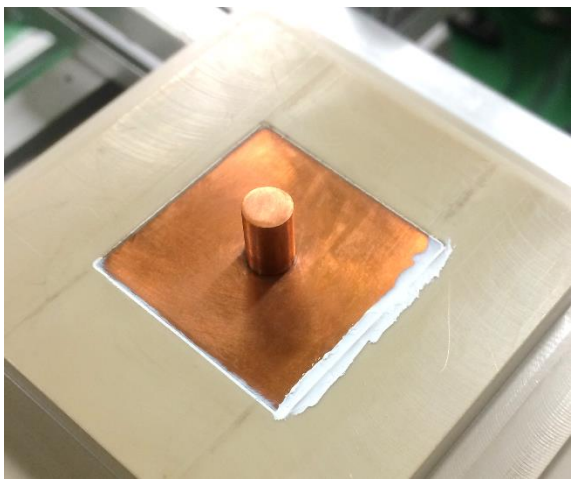

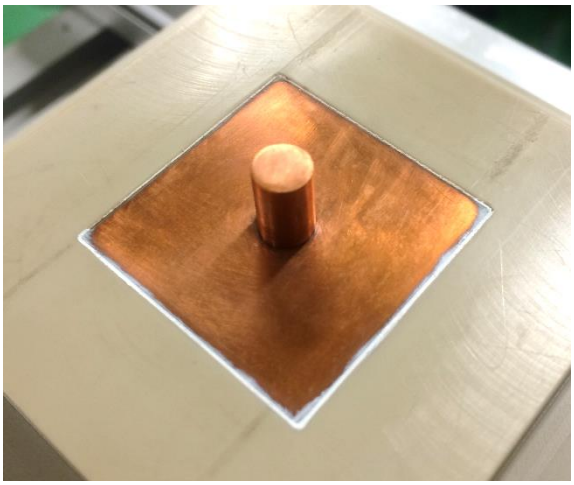

5) Repeat steps 3) and 4) for all four sides.

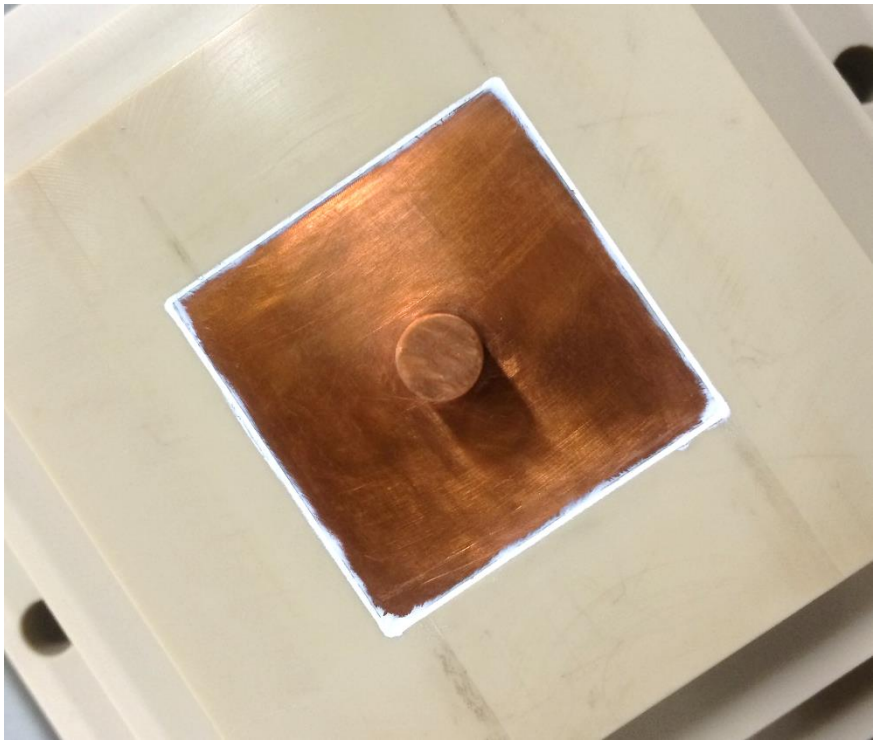

6) Apply lubricating oil on the boiling surface.

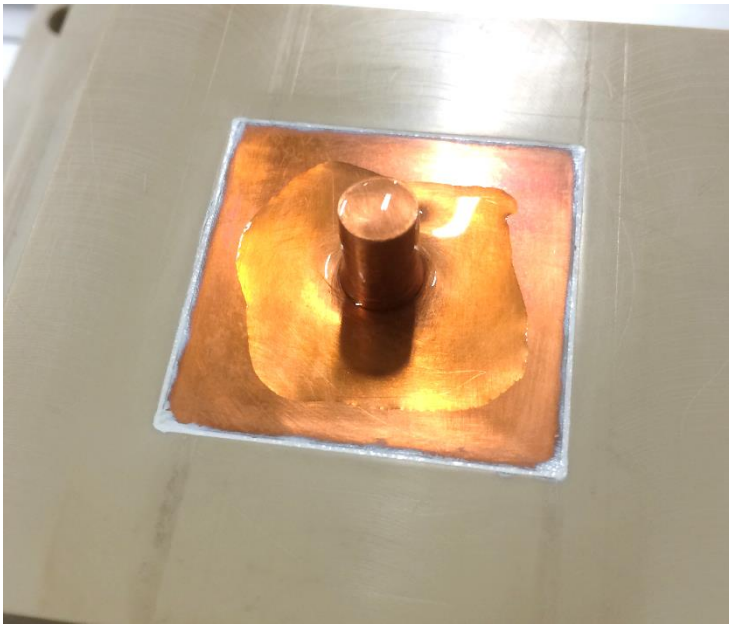

7) Cut a small portion of the P1200 sandpaper and polish boiling surface (and fin) completely.

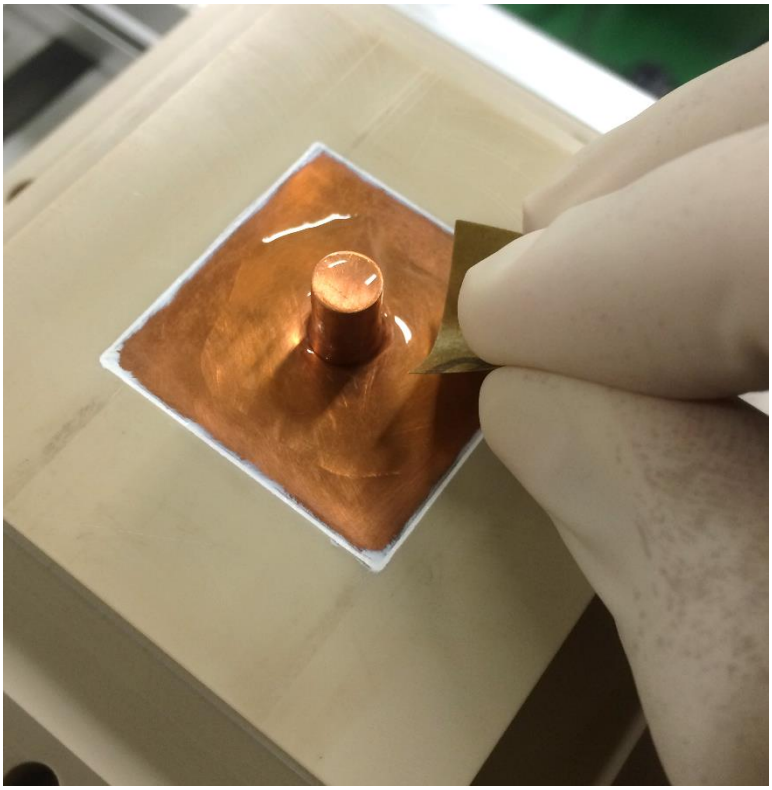

8) Wipe off excess oil and surface products and clean surface with acetone.

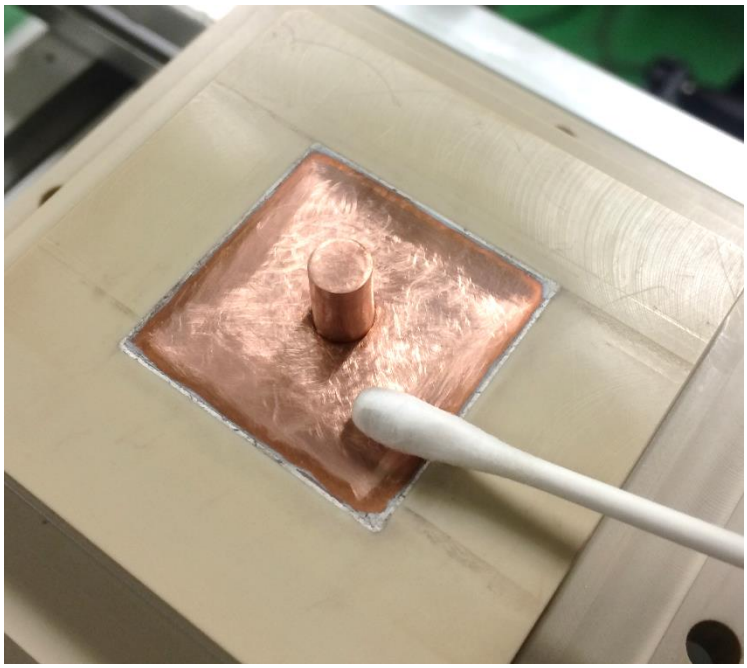

9) Clean surface with distilled water.

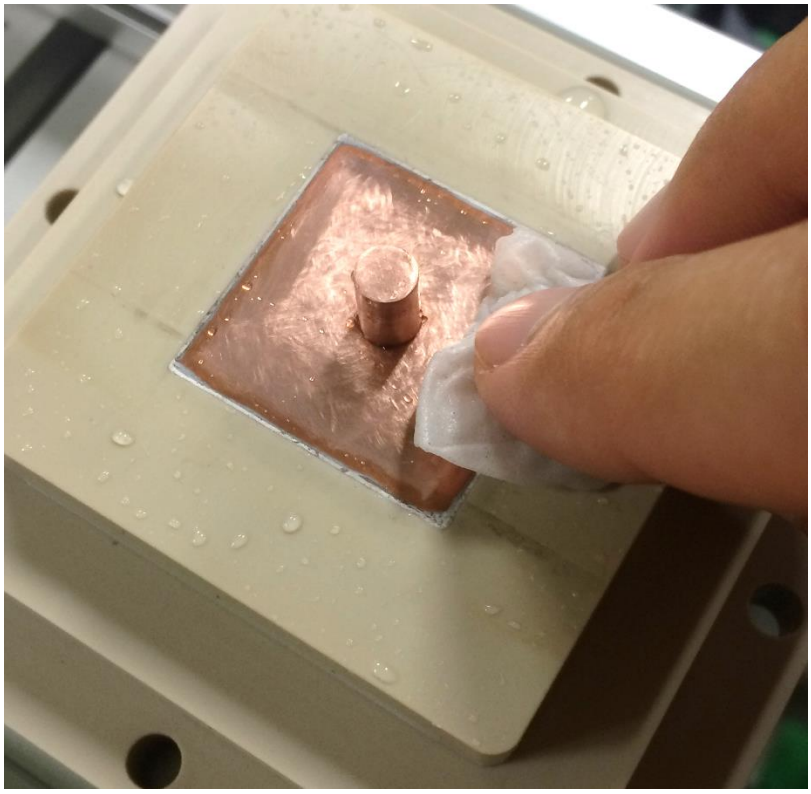

10) Wipe off excess water, then place test section back into channel.

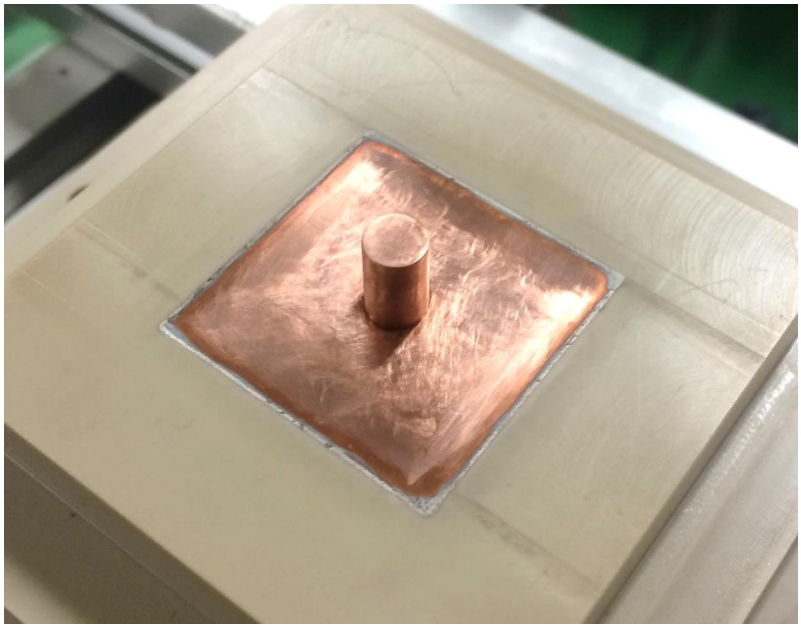

REFERENCES

1. AP1000 Design Control Document, Tier 2 Material – Revision 19: Chapter 4.

2. APR1400 Design Control Document, Tier 2 – Revision 0: Chapter 4.

3. Balasubramanian, K., Lee, P. S., Teo, C. J., Chou, S. K. "Flow boiling heat transfer and pressure drop in stepped fin microchannels." International Journal of Heat and Mass Transfer, 67 (2013) 234-252.

4. BWR design image in Figure 2-3: http://www.ge-energy.com/products_and_services /products/ nuclear_energy/advanced_boiling_water_reactor_abwr.jsp

5. Chan, M. A., Yap, C. R., Ng, K. C. "Pool boiling heat transfer of water on finned surfaces at near vacuum pressures." Journal of Heat Transfer, 132 (2010) 031501: 1-6.

6. Cheung, F. B., Haddad, K. H., Liu, Y. C. "Critical heat flux (CHF) phenomenon on a downward facing curved surface." NUREG/CR-6507, PSU/ME-97-7321 (1997).

7. Collier, J. G., Thome, J. R. "Convective boiling and condensation." Oxford University Press, 1994.

8. Copper properties taken from: http://www.copper.org/resources/properties/db/basic-search.php.

9. Dinh, T-N., Tu, J. P., Salmassi, T., Theofanous, T. G. "Limits of coolability in the AP1000-related ULPU-2400 configuration V facility." CRSS-03/06 (2003).

10. Divavin, V., Tanchuk, V., Shrubok, A., Watson, R., Gonzalez, J. "An experimental and numerical investigation of post-CHF heat transfer for one-sided heat load with highly sub-cooled flow boiling." Fusion Engineering and Design, 31 (1996) 189-200.

11. El-Genk, M. S., Guo, Z. "Transient boiling form inclined and downward-facing surfaces in a saturated pool." Int. J. Refrig., 16: No. 3 (1993) 414-422.

12. Guglielmini, G., Misale, M., Schenone, C. "Experiments on pool boiling of a dielectric fluid on extended surfaces." Int. Comm. Heat Mass Transfer, 23 (1996) 451-462.

13. Haley, K. W., Westwater, J. W. "Heat transfer from a fin to a boiling liquid." Chemical Engineering Science, 20 (1965) 711.

14. Hodge, S. A., Cleveland, J. C., Kress, T. S., Petek, M. "Identification and assessment of BWR in-vessel severe accident mitigation strategies." NUREG/CR-5869, ORNL/TM-12080 (1992).

15. Hu, X., Lin, G., Cai, Y., Wen, D. “Experimental study of flow boiling of FC-72 in parallel minichannels under sub-atmospheric pressure.” Applied Thermal Engineering, 31 (2011) 3839-3853.
16. Imai, Y., Koga, T., Takamasa, T., Okamoto, K., Uematsu, S. “Radiation induced surface activity phenomenon (1st report: Surface wettability on metal oxides).” Proceedings of ICONE 10 (2002) ICONE10-22747.

17. Incropera, F. P., Dewitt, D. P., Bergman, T. L., Lavine, A. S. “Fundamentals of Heat and Mass Transfer.” John Wiliey & Sons, 2007.

18. Katto, Y., Kurata, C. “Critical heat flux of saturated convective boiling on uniformly heated plates in parallel flow.” Int. J. Multiphase Flow, 6 (1980) 575-582.

19. Koga, T., Imai, Y., Takamasa, T., Okamoto, K., Mishima, K. “Radiation induced surface activity phenomenon (2st report: Radiation induced boiling enhancement).” Proceedings of ICONE 10 (2002) ICONE10-22746.

20. Kosar, A., Kuo, C.-J., Peles, Y. “Reduced pressure boiling heat transfer in rectangular microchannels with interconnected reentrant cavities.” Journal of Heat Transfer, 127 (2005) 1106-1114.

21. Kuo, C.-J., Peles, Y. “Critical heat flux of water at subatmospheric pressures in microchannels.” Journal of Heat Transfer, 130 (2008) 072403: 1-7.

22. Kwark, S. M., Amaya, M., Kumar, R., Moreno, G., You, S. M. “Effects of pressure, orientation, and heater size on pool boiling of water with nanocoated heaters.” International Journal of Heat and Mass Transfer, 53 (2010) 5199-5208.

23. Kymalainen, O., Tuomisto, H., Theofanous, T. G. “In-vessel retention of corium at the Loviisa plant.” Nuclear Engineering Design, 169 (1997) 109-130.

24. Launay, S., Fedorov, A. G., Joshi, Y., Cao, A., Ajayan, P. M. “Hybrid micro-nano structured thermal interfaces for pool boiling heat transfer enhancement.” Microelectronics Journal, 37 (2006) 1158-1164.

25. Lazarek, G. M., Black, S. H. “Evaporative heat transfer, pressure drop and critical heat flux in a small vertical tube with R-113.” Int. J. Heat Mass Transfer, 25 No. 7 (1982) 945-960.

26. Liaw, S. P., Yeh, R. H. “Fins with temperature dependent surface heat flux – II. Multi-boiling heat transfer.” Int. J. Heat Mass Transfer, 37 (1994) 1517-1524.

27. McGillis, W. R., Carey, V. P. “Boiling binary mixtures at subatmospheric pressure.” InterSociety Conference on Thermal Phenomena, CH3096-5/92/0000 (1992) 127-136.

28. Mori, S., Okuyama, K. “Enhancement of the critical heat flux in saturated pool boiling using honeycomb porous media.” International Journal of Multiphase Flow, 35 (2009) 946-951.
29. Mori, S., Aznam, S. M., Okuyama, K. “Enhancement of the critical heat flux in saturated pool boiling of water by nanoparticle-coating and a honeycomb porous plate.” International Journal of Heat and Mass Transfer, 80 (2015) 1-6.

30. Noh, S. W., Suh, K. Y. “Critical heat flux in various inclined rectangular straight surface channels.” Experimental Thermal and Fluid Science, 52 (2014) 1-11.

31. Oh, C. H., Englert, S. B. “Critical heat flux for low flow boiling in vertical uniformly heated thin rectangular channels.” Int. J. Heat Mass Transfer, 36 No.2 (1993) 325-335.

32. Okamoto, K., Akiyama, H., Madarame, H., Takamasa, T. “Experimental study on radiation induced boiling enhancement for stainless steel plate.” Proceedings of ICONE 10 (2002) ICONE10-22548.

33. Park, R. J, Ha, K. S., Kim, S. B., Kim, H. D. “Two-phase natural circulation flow of air and water in a reactor cavity model under an external vessel cooling during a severe accident.” Nuclear Engineering and Design, 236 (2006) 2424-2430.

34. Park, R., Kang, K., Hong, S. Kim, S., Song, J. “Corium behavior in the lower plenum of the reactor vessel under IVR-ERVC condition: Technical Issues.” Nuclear Engineering and Technology, 44 No. 3 (2012) 237-248.

35. PEEK properties taken from: http://www.goodfellow.com/E/Polyetheretherketone.html.

36. PWR design image in Figure 2-3: http://www.nucleartourist.com/type/pwr_cycle.htm

37. Sato, T., Kojima, Y. “Variations of a passive safety containment for a BWR with active and passive safety systems.” Nuclear Engineering and Design, 237 (2007) 74-86.

38. Sato, T., Akinaga, M., Kojima, Y. “Two types of a passive safety containment for a near future BWR with active and passive safety systems.” Nuclear Engineering and Design, 239 (2009) 1682-1692.

39. Sehgal, B. R. “Nuclear Safety in Light Water Reactors: Severe Accident phenomenology.” Academic Press (Elsevier), 2012.

40. Takamasa, T., Hazuku, T., Okamoto, K., Mishima, K., Furuya, M. “Radiation induced surface activation on Leidenfrost and quenching phenomena.” Experimental Thermal and Fluid Science 29 (2005) 267-274.

41. Theofanous, T. G., Liu, C., Additon, S., Angelini, S., Kymalainen, O., Salmassi, T. “In-vessel coolability and retention of a core melt.” Nuclear Engineering and Design, 169 (1997) 1-48.

42. Theofanous, T. G., Syri, S. “The coolability limits of a reactor pressure vessel lower head.” Nuclear Engineering and Design, 169 (1997) 59-76.

43. Tian, L. “CAP1400 Design & Construction.” Presentation: Shanghai Nuclear Engineering Research & Design Institute, June 2013.

44. Tong, L.S. “Core cooling in a hypothetical loss of coolant accident. Estimate of heat transfer in core meltdown,” Nuclear Engineering and Design, 8 (1968) 309-312.

45. Todreas, N. E., Kazimi, M. S. “Nuclear Systems I: Thermal Hydraulic Fundamentals.” Taylor & Francis, 1990.

46. Tran, T. N., Wambsganss, M. W., France, D. M. “Small circular-and rectangular-channel boiling with two refrigerants.” Int. J. Multiphase Flow, 22 No. 3 (1996) 485-498.

47. Warui, H. M., Fujisawa, N. “Feedback control of vortex shedding from a circular cylinder by cross-flow cylinder oscillations.” Experiments in Fluids, 21 (1996) 49-56.

48. Wei, J. J., Honda, H. “Effects of fin geometry on boiling heat transfer from silicon chips with micro-pin-fins immersed in FC-72.” International Journal of Heat and Mass Transfer, 46 (2003) 4059-4070.

49. Wei, J. J., Guo, L. J., Honda, H. “Experimental study of boiling phenomena and heat transfer performances of FC-72 over micro-pin-finned silicon chips.” Heat Mass Transfer, 41 (2005) 744-755.

50. Yang, S. H., Baek, W., Chang, S. H. “Poo-boiling critical heat flux of water on small plates: effects of surface orientation and size.” Int. Comm. Heat Mass Transfer, 24 No. 8 (1997) 1093-1102.

51. Yang, J., Dizon, M. B., Cheung, F. B., Rempe, J. L., Suh, K. Y., Kim, S. B. “Critical heat flux for downward facing boiling on a coated hemispherical surface.” Experimental Heat Transfer, 18 (2005) 223-242.

52. Yu, W., France, D. M., Wambsganss, M. W., Hull, J. R. “Two-phase pressure drop, boiling heat transfer, and critical heat flux to water in a small-diameter horizontal tube.” International Journal of Multiphase Flow, 28 (2002) 927-941.

53. Yu, C. K., Lu, D. C. “Pool boiling heat transfer on horizontal rectangular fin array in saturated FC-72.” International Journal of Heat and Mass Transfer, 50 (2007) 3624-3637.

54. Zhang, H., Mudawar, I., Hasan, M. M. “Experimental assessment of the effects of body force, surface tension force, and inertia on flow boiling CHF.” International Journal of Heat and Mass Transfer, 45 (2002a) 4079-4095.

55. Zhang, H., Mudawar, I., Hasan, M. M. “Experimental and theoretical study of orientation effects on flow boiling CHF.” International Journal of Heat and Mass Transfer, 45 (2002b) 4463-4477.

56. Zhang, M., Lian, K. “Using bulk micromachined structures to enhance pool boiling heat transfer.” Microsyst Technol, 14 (2008) 1499-1505.

57. Zhang, Y. P., Qui, S. Z., Su, G. H., Tian, W. X. “Analysis of safety margin of in-vessel retentions for AP1000.” Nuclear Engineering and Design, 240 (2010) 2023-2033.

58. Zheng, M. “Nuclear power in mainland China present situation and future perspective.” Presentation: Meeting of TWG-LWR, June 2013 (IAEA, Vienna).]